Tuning the architecture and luminescence of lanthanide doped rare-earth carbonate and tungstate nano- and micro- sized materials

Anna M. Kaczmarek

UNIVERSITEIT GENT

Tuning the architecture and luminescence of lanthanide doped rare-earth carbonate and tungstate nano- and micro- sized materials

By

Anna M. Kaczmarek

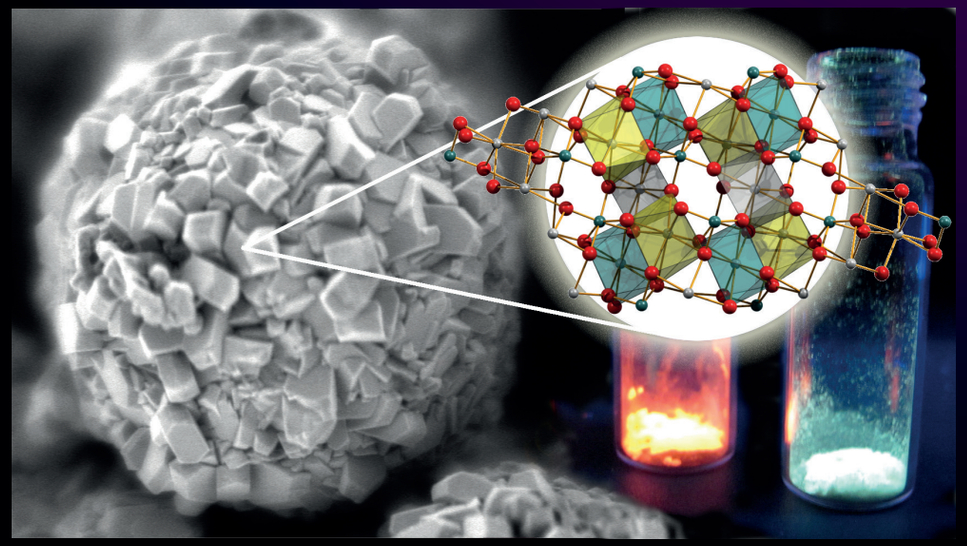

2015

Tuning the architecture and luminescence of lanthanide doped rare-earth carbonate and tungstate nano- and micro- sized materials

Dissertation submitted in fulfillment of the requirements for the degree of Doctor of Science: Chemistry

By

Anna M. Kaczmarek

Department of Inorganic and Physical Chemistry

Faculty of Sciences

Ghent University

2015

Promoter: Prof. dr. R. Van Deun

Composition of the reading and examination commission:

Prof. dr. P. Van Der Voort Ghent University (chairman)
Prof. dr. R. Van Deun Ghent University (promoter)
Prof. dr. D. Poelman Ghent University (reading committee)
Dr. D. Esquivel Merino Ghent University (examination committee)
Prof. dr. W. Radecka-Paryzek Adam Mickiewicz University, Poland (reading committee)
Prof. dr. P. Nockemann Belfast University, Ireland (reading committee)


UNIVERSITEIT
GENT
Luminescent
Lanthanide
Lab
f-element coordination chemistry

Preface

The research presented in this PhD work involves nano- and micro- sized rare-earth carbonate and tungstate materials doped with lanthanide ions. Research on both topics is very timely. This can be proved by the fact that in 2013 I published a 1st author tutorial review in Chemical Society Reviews on rare-earth tungstate and molybdate materials *(Rare earth tungstate and molybdate compounds - from 0D to 3D architectures*). At the time being less then 50 publications on the topic of nano-/micro- sized rare-earth tungstates and molybdates could be found in the Web of Science. Since then the interest in these topics has grown quite immensely. What is more, recently my second 1st author review on rare-earth carbonate nano-/micro-materials (*Nano- and micro- sized rare-earth carbonates and their use as sacrificial templates for the synthesis of new innovative materials*) has been accepted for publication also in Chemical Society Reviews. This highlights the importance and novelty of the up taken research during my PhD.

As a large part of this thesis work involved luminescence measurements, I have been very fortunate to have access to one of the most advanced spectrometers in Europe, which is available in the Luminescent Lanthanide Lab (Double Edinburgh Instruments FLSP920 / FSP920 spectrometer). Access and knowledge on how to operate such equipment has given me the opportunity for many interesting collaborations beyond the scope of my own PhD research.

In an attempt to keep this PhD thesis concise and somewhat enjoyable to read I have chosen not to describe all of the results obtained during the timeframe of my PhD. Additional results, not mentioned in this PhD work, have been published in some of the publications listed on the next pages.

Aknowledgements

I would like to thank the people who have contributed, directly or indirectly, to this PhD thesis.

First of all, I would like to express my sincere thanks to my promoter Prof. Rik Van Deun for giving me the opportunity of pursuing my PhD in his research group at Ghent University, for being my mentor in the field of lanthanide luminescence, and for teaching me many useful skills through out the years.

I would like to thank Prof. Isabel Van Driessche, for making it possible that I did not have to worry about financial matters during the last few months. I appreciate this very much.

I would also like to thank some of the S3 staff, especially Pierre, Tom, Pat and Bart. I am grateful for your help on many occasions. Many thanks to Pierre who makes the administrative task of the S3 staff members much easier. This was especially helpful during my first days in Belgium. To Tom, Pat and Bart, thank you for your help with measurements, organizing practicals, broken computers and equipment issues.

Also thanks to my colleagues from the Luminescent Lanthanide Lab for a nice and friendly atmosphere in the group. To Roel, thanks for making me feel welcome when I first joined the group in March 2011.

Also thanks to my colleagues from other research groups, above all the COMOC group, with which I have had several fruitful scientific collaborations and made several friends. Most of all thanks to Dolores for being a great friend at all times.

On a more personal level, thank you to my parents for supporting me in all of my endeavors throughout the years. To mom for always being there to listen. And to dad

for giving me a great example of what a scientist should be like. In general thank you to my family for being there for me, it hardly ever feels like I live 1000 km away from you all.

And thanks to Kristof, for making this last year a good one despite some odds. Thanks for your constant support and advice (among others with preparations for my PhD reception and for making it all come together in a non stressful manner), for making me smile more often, and for making Belgium feel more like home.

Samenvatting in het Nederlands

I. Introductie en doelen

Nanotechnologie is een onderzoeksdomein waarbij men doorgaans terugvalt op de welbekende lezing van fysicus Richard Feynman uit 1959. In deze lezing werd discussie gevoerd rondom de enorme mogelijkheden die miniaturisatie kan geven. Diepgaand onderzoek heeft uitgewezen dat materialen nieuwe eigenschappen kunnen verkrijgen door een aanpassing van de dimensies van deze materialen.[1] Deze wijziging in eigenschappen kan als volgt verklaard worden: wanneer de deeltjesgrootte verkleint, stijgt de oppervlakte tot volume ratio, wat resulteert in een verhoogde fractie aan atomen die op (of nabij) het oppervlak liggen. In de wereld van nanomaterialen is het essentieel om te weten dat dit type materialen ingedeeld kunnen worden als 0D, 1D, 2D, en 3D materialen (zie Figuur I). Er werd waargenomen dat deeltjesaggregaten collectieve eigenschappen hebben die verschillend zijn van deze van individuele deeltjes, alsook van het bulk materiaal. Het is deze observatie die zeer veel interesse heeft gewekt naar 3D gestructureerde materialen. Het zijn dan ook dit type materialen die voornamelijk verkregen zijn gedurende het onderzoek dat beschreven wordt in deze thesis.

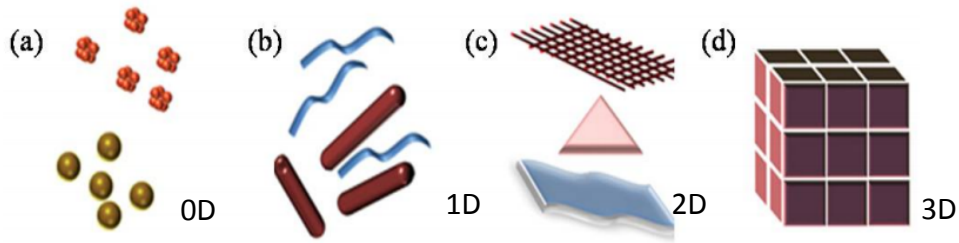

Figuur I: Classificatie van nanomaterialen volgens Richard Siegal.[2]

Gedurende deze doctoraatsthesis werd voornamelijk toegespitst op zeldzame-aarde bevattende door de unieke intra 4f-transities, welke slechts zwak beïnvloed worden door de coördinatieomgeving of het kristalveld. Dit aangezien de 4f-orbitalen afgeschermd worden van de omgeving door de gevulde 5s- en 5p-orbitalen.[8] Vele zeldzame-aarde bevattende nano- en micromaterialen werden al intensief onderzocht, vooral als matrix voor luminescente fosforen. De meest bestudeerde materialen zijn onder andere lanthanide gedoteerde LaF_3,[9] $NaYF_4$,[10] Gd_2O_3,[11] en Y_2O_3[12] matrices.

Het doel van deze doctoraatsthesis was de synthese van verschillende nieuwe lanthanide gedoteerde anorganische materialen van nano- en/of microgrootte en een gedetailleerde studie van hun luminescente eigenschappen. Hiervoor werden twee materiaalfamilies gekozen: zeldzame-aarde gedoteerde carbonaten en zeldzame-aarde gedoteerde tungstaten. Deze keuze werd gebaseerd op de relatief lage hoeveelheid aan publicaties in deze velden, vergeleken met andere anorganische matrices, met nochtans veelbelovende resultaten. De zeldzame-aarde bevattende carbonaat deeltjes werden ontwikkeld met 'bioimaging' als mogelijk toepassingsgebied, aangezien dit type materialen niet giftig is. Op vlak van luminescentie was het doel om intense zichtbare emissie te krijgen van stabiele colloïdale suspensies van deze materialen in water, met luminescente levensduren in de µs of ms regio. De zeldzame-aarde bevattende tungstaat materialen werden gesynthetiseerd om mogelijks gebruikt te worden in verlichtingstoepassingen en beeldschermen. Deze materialen zijn gekend om hun uitstekende chemische stabiliteit, zelfs bij hogere temperaturen (die men typisch verkrijgt in een LED). Bovendien is geen extra activatiestap nodig door de aanwezigheid van een W-O

ladingstransferband. Deze materialen absorberen energie in het verre UV-gebied, welke op een efficiënte manier overgedragen wordt naar de Ln^{3+}-ionen in het materiaal. Het verkrijgen van intense wit licht emitterende materialen was een van de hoofddoelen van dit deel van het onderzoek. Naast de synthese van nieuwe, nog niet gepubliceerde materialen was een belangrijk aspect van dit onderzoek het vinden van manieren om de architectuur en luminescente eigenschappen van deze materialen aan te modificeren.

Gedurende het verloop van mijn doctoraat werden verscheidene zeldzame-aarde bevattende carbonaten en zeldzame-aarde bevattende tungstaten verkregen met groottes in de nano- en micro-regio: $LaOHCO_3$, $Ce_2O(CO_3)_2 \cdot H_2O$, $La_2O(CO_3)_2 \cdot H_2O$, $La_2O_2CO_3$, Y_2WO_6, $Ce_2(WO_4)_3$, $Ce_{10}W_{22}O_{81}$, $La_2(WO_4)_3$, en $Y(WO_3)_2(OH)_3$. De meerderheid van deze materialen wordt beschreven in deze thesis.

II. Zeldzame-aarde bevattende carbonaten gedoteerd met Eu^{3+} and Tb^{3+}

Hoofdstuk 4 beschrijft de synthese en karakterisatie van verscheidene zeldzame-aarde bevattende carbonaat materialen: $LaOHCO_3$, $La_2O(CO_3)_2 \cdot H_2O$ en $Ce_2O(CO_3)_2 \cdot H_2O$. Twee verschillende synthetische technieken werden gebruikt om deze materialen te verkrijgen: een lage temperatuur, urea gebaseerde homogene precipitatie methode en een hydrothermale methode.[13] Andere factoren, zoals de bron van lanthanide-ionen (het nitraat- of acetaat-zout), de bron van carbonaat, en de aan- of afwezigheid van stabiliserende liganden werden ook aangepast met als doel het verkrijgen van verschillende morfologieën. Bijvoorbeeld: wanneer het $LaOHCO_3$ materiaal gesynthetiseerd werd via de hydrothermale route, vertrekkende van $La(OAc)_3$ en urea, werden kleine nanodeeltjes van 30-50 nm grootte verkregen (**A1**, Figuur II). Wanneer urea vervangen werd door Na_2CO_3, en alle andere reactieomstandigheden constant bleven, werden grotere sferen van 100-200 nm in grootte gevormd (**A3**, Figuur II). Wanneer glucose en fructose gebruikt werden als stabiliserende liganden voor de synthese van $La_2O(CO_3)_2 \cdot H_2O$, werden materialen met zeer verschillende morfologieën verkregen. Bij de lage temperatuur, urea gebaseerde homogene precipitatie synthese, met $La(OAc)_3$ als de lanthanumbron en aanwezigheid van glucose in het reactiemengsel, werden sferoïden van 50-200 nm in grootte geobserveerd met SEM (**A10**, Figuur III). In het geval dat fructose gebruikt werd in plaats van glucose, werden microsferen van 4 μm grootte, opgebouwd uit nanoplaten verkregen (**A12**, Figuur III).

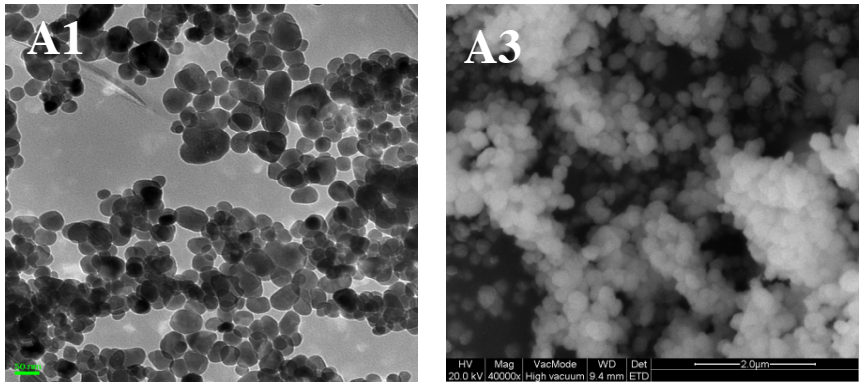

Figuur II: TEM en SEM afbeeldingen van stalen A1 and A3 ($LaOHCO_3$ deeltjes verkregen van twee verschillende bronnen van carbonaat-ionen).

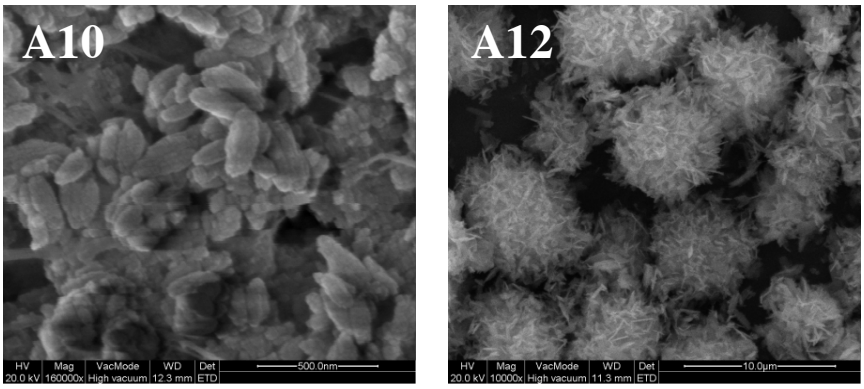

Figuur III: SEM afbeeldingen van stalen A10 and A12 ($La_2O(CO_3)_2 \cdot H_2O$ deeltjes verkregen in de aanwezigheid van twee verschillende liganden).

De luminescente eigenschappen van Eu^{3+} en Tb^{3+} gedoteerde, zeldzame-aarde bevattende carbonaat materialen werden in detail onderzocht, zowel in de vaste toestand als in colloïdale suspensies. De luminescente eigenschappen van de Ln^{3+} gedoteerde $LaOHCO_3$ deeltjes bleken zeer verschillend te zijn van deze van de Ln^{3+} gedoteerde $La_2O(CO_3)_2 \cdot H_2O$ deeltjes. Verschillen in vooral de fijnstructuur van de pieken in de emissiespectra, alsook de kwantumopbrengsten werden geobserveerd.

Hoogst waarschijnlijk wordt het verschil in kwantumopbrengst veroorzaakt door de verandering in radiative lifetime in de twee matrices, aangezien de luminescente levensduren van beide materialen gelijkaardig waren.

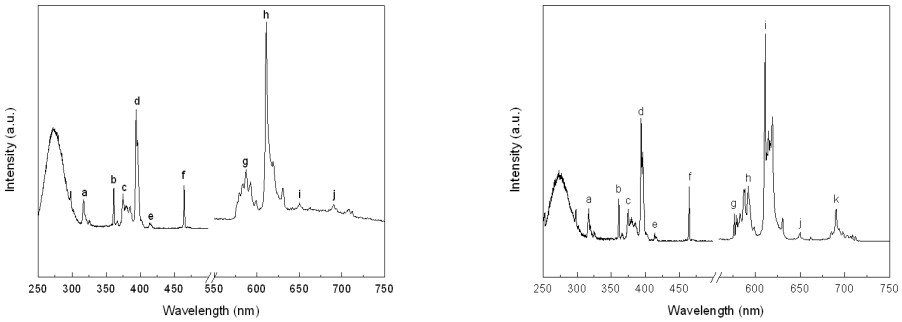

Figuur IV: Gecombineerde excitatie-emissiespectra voor 5% Eu gedoteerd A1 (links) en 5% Eu gedoteerd A6 (rechts), welke de verschillen tonen tussen de luminescente eigenschappen van beide materialen.

Zoals verwacht tonen deeltjes welke gesynthetiseerd werden in de aanwezigheid van een ligand lagere luminescente levensduren en kwantumopbrengsten, vergeleken met deeltjes van hetzelfde carbonaatmateriaal welke gesynthetiseerd werden in de afwezigheid van een organisch ligand. Deze afname in luminescente levensduur en kwantumopbrengst kan hoogst waarschijnlijk verklaard worden door het dovende effect van OH-groep van het ligand. Een vergelijking van de emissiesprectra opgemeten in de vaste toestand en in colloïdale suspensie toont een verlaging in intensiteit (ongeveer 25%), maar geen verandering in relatieve piekintensiteiten. Er werd geen significant verschil geobserveerd voor de lengte van de luminescente levensduren. Hieruit kan geconcludeerd worden dat de deeltjes na dispersie in water geen aanpassingen ondergaan. Alle Eu^{3+} en Tb^{3+} gedoteerde zeldzame-aarde

bevattende carbonaat stalen tonen een sterke rode en groene emissie, respectievelijk na excitatie met een UV-lamp geschikt voor laboratoriumgebruik, bij een excitatiegolflengte van 365.0 nm (Figuur V). Aangezien vele van deze deeltjes stabiele colloïdale suspensies vormen in water en niet toxisch zijn voor het menselijk lichaam, zijn dit veelbelovende materialen voor gebruik in biolabeling.

Figuur V: Foto's genomen onder een UV-lamp (bij 365.0 nm excitatie) van Eu^{3+} en Tb^{3+} gedoteerde $LaOHCO_3$ stalen (links) en $La_2O(CO_3)_2 \cdot H_2O$ (rechts). De Eu^{3+} gedoteerde stalen tonen rode emissie en de Tb^{3+} gedoteerde stalen tonen groene emissie.

III. Zeldzame-aarde bevattende tungstaten gedoteerd met Sm^{3+}, Eu^{3+}, Gd^{3+}, Tb^{3+} and Dy^{3+}-ionen

Hoofdstukken 5, 6 en 7 van deze doctoraatsthesis beschrijven de synthese, karakterisatie en luminescentie eigenschappen van verscheidene Ln^{3+} gedoteerde zeldzame-aarde bevattende tungstaat materialen.

Een van de tungstaat fases die verkregen werd was $Y(WO_3)_2(OH)_3$. Dit materiaal werd gesynthetiseerd via een hydrothermale syntheseroute (200°C) in aan- en afwezigheid van natriumdioctylsulfosuccinaat (DSS).[14] Gedurende deze thesis werd aangetoond dat de morfologie van het $Y(WO_3)_2(OH)_3$ materiaal gewijzigd kan worden

door de volgende factoren te modificeren: reactietijd, hoeveelheid surfactant, en de bron van Y^{3+}-ionen. Figuur VI geeft weer hoe het gebruik van $Y(NO_3)_3$ of $Y(OAc)_3$ als Y^{3+}-bron een invloed heeft op de morfologie van de materialen. Significante veranderingen in de luminescente eigenschappen van de materialen werden ook geobserveerd voor stalen die een warmtebehandeling ondergingen bij 900°C gedurende 3 u en wanneer het doteringspercentage van het Ln^{3+}-ion veranderd werd.

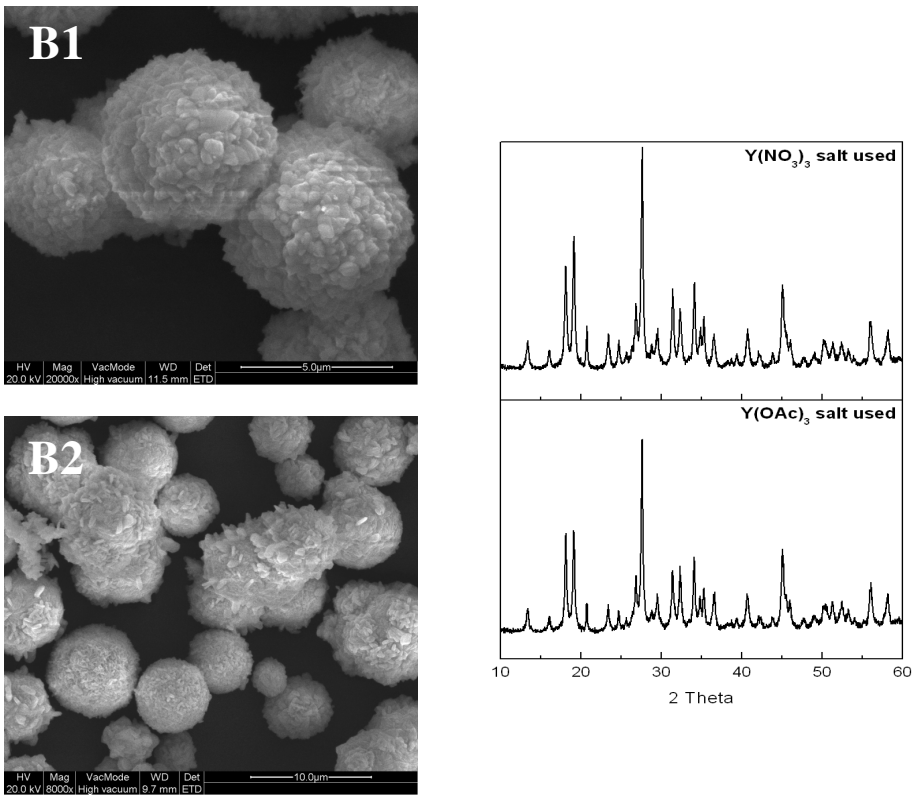

Figuur VI: SEM afbeeldingen van stalen B1 en B2 - $Y(WO_3)_2(OH)_3$ materialen gesythetiseerd uit $Y(NO_3)_3$ en $Y(OAc)_3$, in de afwezigheid van DDS (links). XRD patronen van stalen B1 en B2 (rechts).

Figuur VII geeft een voorbeeld van de invloed die het Ln^{3+}-doteringspercentage heeft op de luminescente eigenschappen van een materiaal, gebaseerd op een Eu^{3+}:$Y(WO_3)_2(OH)_3$ staal, gedoteerd met 1%, 3% en 5% Eu^{3+}. Het is duidelijk dat de intensiteit van de brede ladingstransferband stijgt, en de emissie van de Eu^{3+}-ionen zwakker wordt, met de afname in Eu^{3+} concentratie van 5% naar 1%. In het CIE kleurdiagram worden de CIE-coördinaten weergegeven. Een verandering in emissiekleur werd geobserveerd bij verschillende doteringspercentages.

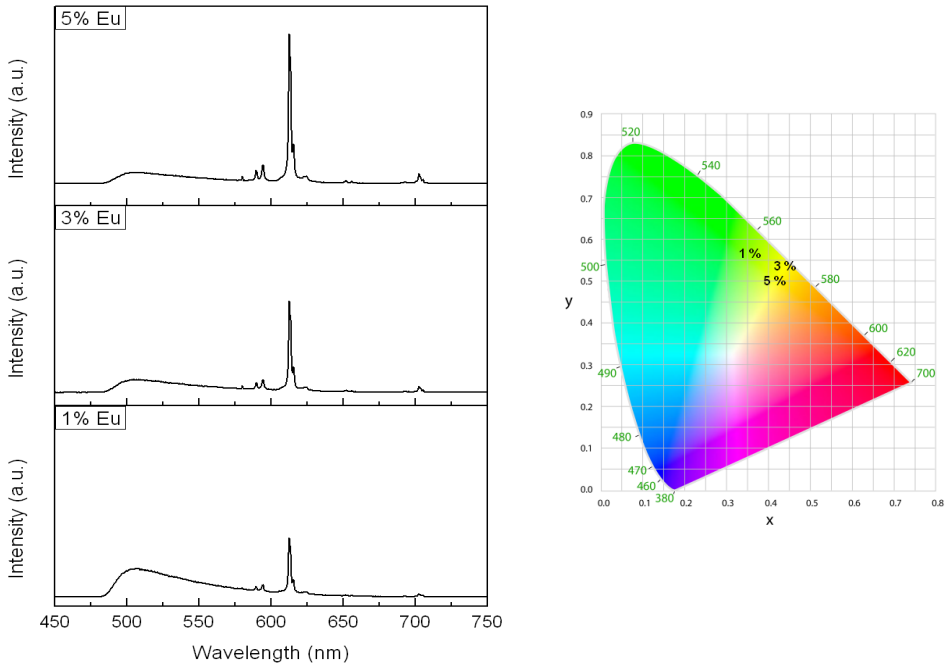

Figuur VII: Rechts – emissiespectra van 1%, 3% en 5% gedoteerd $Y(WO_3)_2(OH)_3$ staal (B6 precursor_24u). Links – CIE chromaticiteitsdiagram welke de verandering in kleur toont wanneer een verschillend doteringspercentage aan Eu^{3+} gebruikt wordt (1% Eu: x = 0.33, y = 0.58; 3% Eu: x = 0.41, y = 0.53; 5% Eu: x = 0.41, y = 0.51).

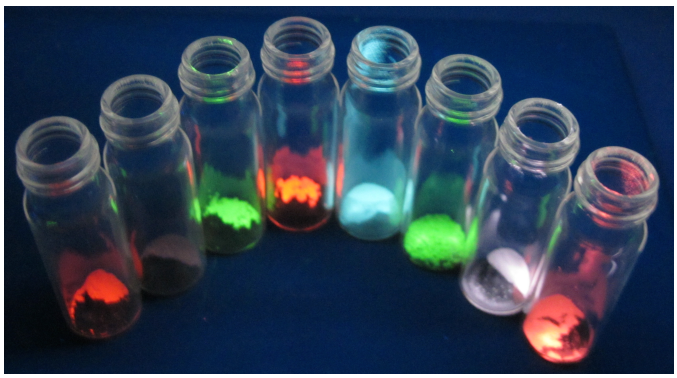

Figuur VIII: Foto van verschillende Ln^{3+}-gedoteerde nano- en microgroottes van $Y(WO_3)_2(OH)_3$ materialen, onder een UV-lamp (302.0 nm excitatie golflengte).

Andere tungstaat materialen, die beschreven worden in deze thesis zijn Ln^{3+}-gedoteerde Y_2WO_6 materialen, gesynthetiseerd in hydrothermale omstandigheden en in aanwezigheid van natriumdodecylsulfaat (SDS).[14] Dit materiaal bleek zeer gevoelig te zijn voor de pH gedurende de reactie. Enkel bij de geschikte pH werd een pure fase verkregen. Bij pH = 3 werden sferische microstructuren (2-5 µm), opgebouwd uit regelmatige nano bouwblokken geobserveerd via SEM. De gedetailleerde luminescente eigenschappen van Sm^{3+}, Eu^{3+}, and Dy^{3+} gedoteerde Y_2WO_6 sferische 3D microstructuren, welke opgebouwd zijn uit nanodeeltjes, werden bestudeerd. Bovendien werd ook de luminescente intensiteitsverhoging via co-dotering met Gd^{3+}-ionen onderzocht voor dit materiaal. Verscheidene wit licht emitterende materialen met hoge kwantumopbrengsten werden verkregen. Voor de Y_2WO_6 fase, die gedoteerd werd met Dy^{3+} (2.5%, 5% en 10%) emitteerden alle stalen, voor en na warmtebehandeling wit licht. Uit deze groep toonde de 2.5% Dy^{3+} gedoteerde Y_2WO_6 fase de langste levensduur en hoogste kwantumopbrengst, welke dan ook verder cogedoteerd werd met Gd^{3+}-ionen om de invloed hiervan op de luminescente

eigenschappen te onderzoeken (Figuur X). Het 2.5% Dy^{3+}, 10% Gd^{3+} gedoteerd Y_2WO_6 staal toonde de hoogste kwantumopbrengst (22%) en een levensduur van 160 µs. De kleurtemperatuur van dit staal bedraagt 3591 K. Het 2,5% Dy^{3+} gedoteerd staal, zonder cogedoteerde Gd^{3+}-ionen tonen een kleurtemperatuur van 4428 K, waaruit afgeleid kan worden dat co-dotering met Gd^{3+} resulteerde in een verschuiving van de emissiekleur richting een warmer wit (halogeen wit). Tabel I toont de CIE kleurcoördinaten, kwantumopbrengsten en levensduren van de besproken stalen.

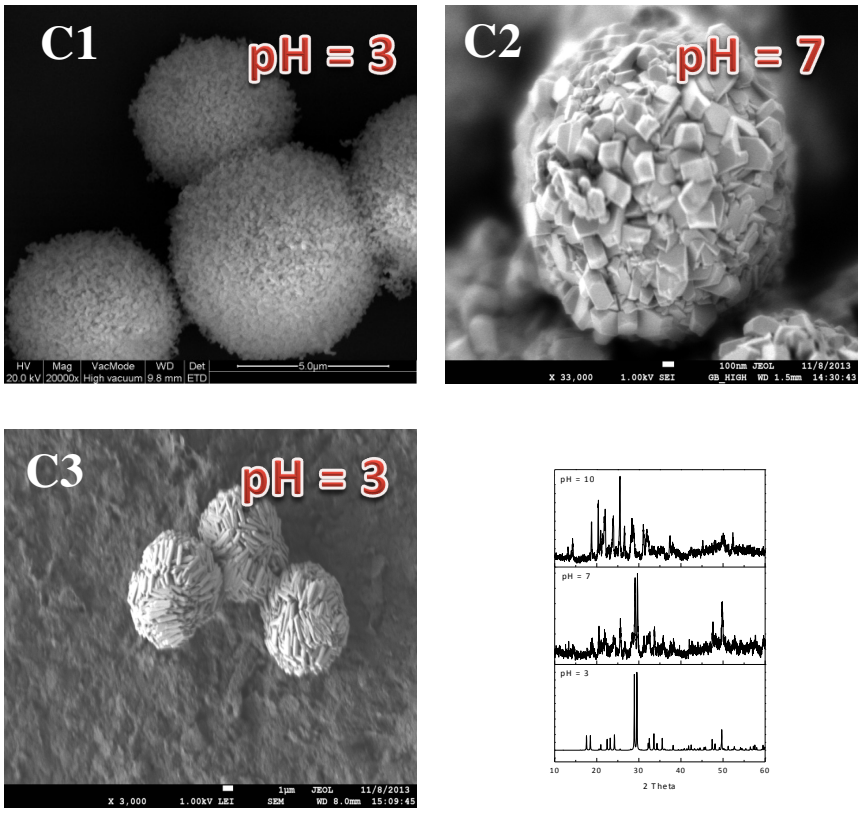

Figuur IX: SEM afbeeldingen en XRD patronen C1-C3 materialen, die verkregen werden bij verschillende pH waarden. Enkel bij pH = 3 werd een puur Y_2WO_6 materiaal verkregen.

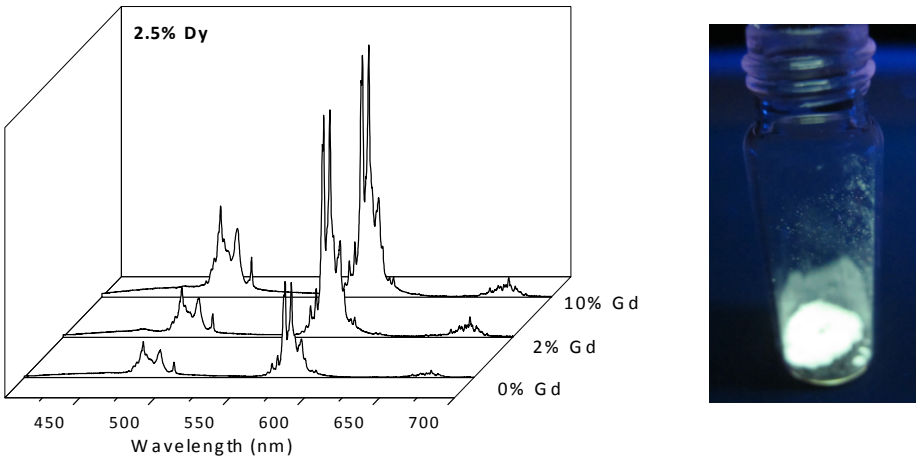

Figuur X: Verandering in emissie-intensiteit die geobserveerd werd voor 2.5% Dy: Y_2WO_6 staal gecodoteerd met 0%, 2%, and 10% Gd^{3+} -ionen (links). Foto van 2.5% Dy_10% Gd: Y_2WO_6 stalen, geëexciteerd onder een UV-lamp (302.0 nm excitatie).

Tabel I. CIE kleurcoördinaten, kwantumopbrengsten (QY) en levensduren van 2.5% Dy^{3+} gedoteerde Y_2WO_6 stalen.

Staal	CIE (x)	CIE (y)	Kleur	QY	Levensduur (µs)
2.5% Dy	0.324	0.353	wit	17%	119
2.5% Dy_2% Gd	0.408	0.415	wit	21%	155
2.5% Dy_10% Gd	0.372	0.390	wit	22%	160

De syntheseroute en luminescente eigenschappen van de 5% Tb^{3+} gedoteerde $Ce_2(WO_4)_3$ en $Ce_{10}W_{22}O_{81}$ materialen wordt ook beschreven. Deze materialen werden gesynthetiseerd via een hydrothermale route, in aan- en afwezigheid van natriumdioctylsulfosuccinaat (DDS), door de pH en molaire ratio aan Ce : W aan te

passen. Figuur XI geeft twee voorbeelden weer van de verkregen materialen. Al deze materialen toonden een efficiënte ladingstransfer van de tungstaat groepen naar de Tb^{3+}-ionen. Groene, blauwe of groen-blauwe emissie was zichtbaar bij UV excitatie.

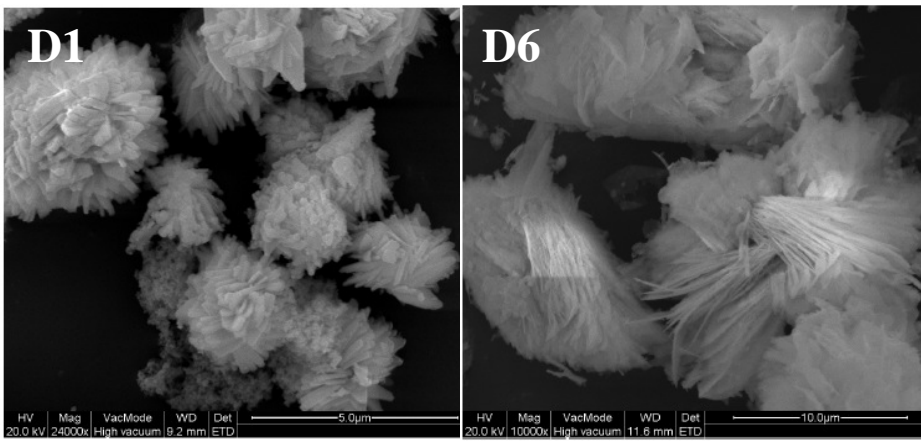

Figuur XI: SEM afbeeldingen met voorbeelden van $Ce_2(WO_4)_3$ (D1) en $Ce_{10}W_{22}O_{81}$ (D6) materialen.

Figuur XII toont het emissiespectrum van 5% Tb^{3+} gedoteerd $Ce_2(WO_4)_3$ (**D1**), voorgesteld met een regenboogcurve met als doel de verschillende kleurcomponenten van het staal weer te geven. Bij excitatie onder de UV-lamp emitteerde het staal groen licht. De kleurcoördinaten van dit materiaal zijn x = 0.31 en y = 0.51. Figuur XIII geeft het emissiespectrum van een 5% Tb^{3+} gedoteerd $Ce_{10}W_{22}O_{81}$ staal (**D6**) waaronder een regenboogcurve getekend werd die de verschillende kleurcomponenten van het staal toont. Dit staal toonde een blauwe emissiekleur bij excitatatie onder UV-licht. De kleurcoördinaten werden berekend als x = 0.23 en y = 0.32.

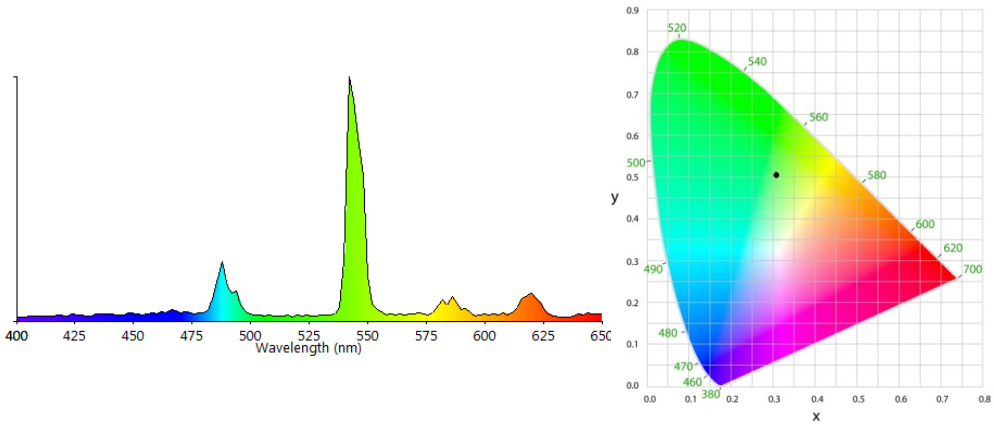

Figuur XII: Links – emissiespectrum van 5% Tb^{3+} gedoteerd $Ce_2(WO_4)_3$ (D1), geëxciteerd bij 260.0 nm waaronder de regenboogcurve getekend werd om de verschillende kleurcomponenten te tonen. Rechts – CIE kleurdiagram, waarbij de zwarte stip de locatie van de x en y coördinaten aanduidt.

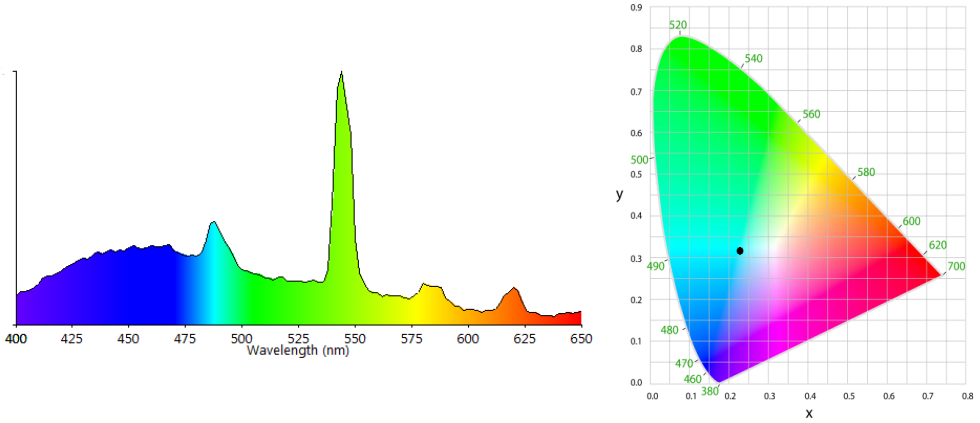

Figuur XIII: Links – emissiespectrum van 5% Tb^{3+} gedoteerd $Ce_{10}W_{22}O_{81}$ (D6), geëxciteerd bij 270.0 nm waaronder de regenboogcurve getekend werd om de verschillende kleurcomponenten te tonen. Rechts – CIE kleurdiagram, waarbij de zwarte stip de locatie van de x en y coördinaten aanduidt.

IV. Algemene conclusies

In deze doctoraatsthesis werden verschillende zeldzame-aarde bevattende carbonaat en zeldzame-aarde bevattende tungstaat nano- en microgroottes aan materialen gesynthetiseerd en gekarakteriseerd. Doorheen deze thesis werd aangetoond dat variabelen zoals de reactietijd, bron van zeldzame-aarde, hoeveelheid ligand, een invloed kunnen hebben op de morfologie van de materialen. Door deze factoren, alsook het doteringspercentage van het lanthanide, de warmtebehandelingstemperatuur en co-dotatie met Gd^{3+}-ionen te variëren, was het mogelijk om nieuwe luminescente eigenschapen van lanthanide gedoteerde materialen te verkrijgen. Deze observaties kunnen gebruikt worden om de morfologieën en luminescentie van andere lanthanide gedoteerde, zeldzame-aarde bevattende fosforen te controleren.

1. Colfen H.; Mann S. *Angew. Chem*., *Int. Ed*., **2003**, 42, 2350.
2. Siegel, R.W. 1994. Nanophase materials. In Encyclopedia of applied physics, Vol. 11, G.L. Trigg, ed. Weinheim: VCH, pp. 1-27.
3. Liu, G.; Chen, X. *Handbook on the Physics and Chemistry of Rare Earths*, Gschneidner, K.A. Jr.; Bünzli, J.-C.G.; Pecharsky, V. K. Elsevier Science: Amsterdam, **2007**; Vol. 37, Chapter 233, pp. 99–169.
4. Blasse, G.; Grabmaier, B. C.; *Luminescent Materials*, Springer Verlag, Berlin, 1994.
5. He, H.; Ma, H.; Sun, D.; Zhang, L.; Wang, R.; Sun, D. *Cryst. Growth Des.* **2013**, 13, 3154.
6. Li, C.; Lin, J. *J. Mater. Chem.* **2010**, 20, 6831.
7. Chakhmouradian, A. R.; Wall, F. *Elements*, **2012**, 8, 333.
8. Binnemans, K. *Chem. Rev.* **2009**, 109, 4283.
9. Stouwdam, J. W.; Van Veggel. F. C. J. M. *Nano Letters* **2002**, 206, 733.
10. Boyer, J.-C.; Van Veggel, F. C. J. M. *Nanoscale* **2010**, 2, 1417.
11. Li, J.-G.; Li, X.; Sun, X.; Ikegami, T.; Ishigaki, T. *Chem. Mater.* **2008**, 20, 2274.
12. Jun-Ming, L.; Yong-Xiu, L.; Li-Ping, D.; Yong-Rui, Y.; Wei-Fan, C. *J. Nanosci. Nanotechnol.* **2008**, 8, 1211.
13. Kaczmarek, A. M.; Miermans, L.; Van Deun, R. *Dalton. Trans.* **2013**, 42, 4639.
14. Kaczmarek, A.M.; Liu, Y.-Y.; Van Der Voort, P.; Van Deun, R. *Dalton Trans.*, **2013**, 42, 5471.
15. Kaczmarek, A.M.; Van Hecke, K.; Van Deun, R. *Inorg. Chem.,* **2014**, 53, 9498.

Scientific activities

Publications covered in this thesis:

1) Nano and micro sized Eu^{3+} and Tb^{3+} doped lanthanide hydroxycarbonates and oxycarbonates. The influence of glucose and fructose as stabilizing ligands.

Anna M. Kaczmarek, Linde Miermans, Rik Van Deun, *Dalton Trans.*, **2013**, *42*, 4639-4649.

2) Tuning the architecture and properties of micro structured yttrium tungstate oxide hydroxide and lanthanum tungstate

Anna M. Kaczmarek, Ying-Ya Liu, Pascal Van Der Voort, Rik Van Deun, *Dalton Trans.*, **2013**, *42*, 5471-5479.

3) Rare earth tungstate and molybdate compounds - from 0D to 3D architectures

Anna M. Kaczmarek, Rik Van Deun, *Chem. Soc. Rev.*, **2013**, 42, 8835-8848.

4) Enhanced luminescence in Ln^{3+}- doped Y2WO6 (Sm, Eu, Dy) 3D microstructures through Gd^{3+} co-doping

Anna M. Kaczmarek, Kristof Van Hecke, Rik Van Deun, *Inorg. Chem.*, **2014**, 53, 9498-9508.

5) Nano- and micro- sized rare-earth carbonates and their use as sacrificial templates for the synthesis of new innovative materials

Anna M. Kaczmarek, Kristof Van Hecke, Rik Van Deun, *Accepted to Chem. Soc. Rev.*

6) Green and blue emitting 3D structured Tb: $Ce_2(WO_4)_3$ and Tb: $Ce_{10}W_{22}O_{81}$ micromaterials

Anna M. Kaczmarek, Dorine Ndagsi, Isabel Van Driessche, Kristof Van Hecke, Rik Van Deun , *To be submitted to Dalton Trans.*

Other publications (written during the timeframe of the PhD):

7) Bipyridine based nanosized Metal-Organic Framework with tuneable luminescence by a postmodification with Eu(III): an experimental and theoretical study
Ying-Ya Liu, Roel Decadt, Thomas Bogaerts, Karen Hemelsoet, Anna M. Kaczmarek, Dirk Poelman, Michel Waroquier, Veronique Van Speybroeck, Rik Van Deun, Pascal Van Der Voort, *J. Phys. Chem. C*, **2013**, *117*, 11302-11310.

8) Eu^{3+}@PMO: synthesis, characterization and luminescence properties.
Maria Dolores Esquivel Merino, Anna M. Kaczmarek, Cesar Jimenez-Sanchidrian, Rik Van Deun, Francisco Romero-Salguero, Pascal Van Der Voort, *J. Mater. Chem. C*, **2015**, DOI: 10.1039/C4TC02553A

9) Layered exfoliable crystalline materials based on Sm-, Eu- and Eu/Gd- 2-phenylsuccinate frameworks. Crystal structure, topology and luminescent properties
German E. Gomez, Maria C. Bernini, Elena V. Brusau, Griselda E. Narda, Daniel Vega, Anna M. Kaczmarek, Rik Van Deun, Marcelo Nazzarro, *Dalton Trans.,* **2015**, *44*, 3417-3429.

10) Highly Photoluminescent Europium Tetraphenylimidodiphosphinate Ternary Complexes with Heteroaromatic co- Ligands. Solution and Solid State Studies
Marek Pietraszkiewicz, Oksana Pietraszkiewicz, Jerzy Karpiuk, Alina Majka, Grzegorz Dutkiewicz, Teresa Borowiak, Anna M. Kaczmarek, Rik Van Deun

Submitted to J. Lumin. on 23.12.2014; Manuscript ID: LUMIN-D-14-01663

11) Dynamic orientational disorder in 4, 4'- Diaminoazobenzene

Anna M. Kaczmarek, Rik Van Deun, Patrick Bultinck, Koen Robeyns, Kristof Van Hecke,

To be submitted

Table of Contents

Abbreviations

0D	zero – dimensional
1D	one – dimensional
2D	two – dimensional
2Na-EDTA	disodium ethylenediaminetetraacetate
3D	three – dimensional
BET	Brunauer-Emmett-Teller
BJH	Barrett, Joyner & Halenda
CCT	correlated color temperatures
Ce	cerium
CIE	Commission Internationale de l'Eclairage (International Commission on Illumination)
CTAB	cetyltrimethylammonium bromide
DRIFTS	diffuse reflectance infrared fourier transform spectroscopy
DSS	dioctyl sodium sulfosucciate
Dy	dysprosium
ED	electric dipole
EDTA	ethylenediaminetetraacetic acid
EG	ethylene glycol
Er	erbium
Eu	europium
Gd	gadolinium

H_3cit	citric acid
Ho	holmium
ICSD	Inorganic Crystal Structure Database
LED	light emitting diode
Ln	lanthanide
M	alkali metal
MD	magnetic dipole
Na_3cit	sodium citrate
Nd	neodymium
NIR	near infrared
Pr	praseodymium
PVP	polyvinyl pyrrolidone
QY	quantum yield
RE	rare-earth
SDBS	sodium dodecyl benzenesulfonate
SDS	sodium dodecyl sulfate
SEM	scanning electron microscopy
Sm	samarium
Tb	terbium
TEM	transmission electron microscopy
Tm	thulium
UV	ultra-violet
vis	visible
XRD	X-ray diffraction

Y	yttrium
Yb	ytterbium

Outline

The first two chapters provide a background and literature overview related to the PhD work presented in this thesis. Chapter 3 describes the employed measurement techniques as well as the procedures involved in the research work. Chapters 4 to 7 contain most of the experimental work and their results. Some additional experimental results can be found in the scientific publications published through the duration of the PhD. The general conclusions are provided in Chapter 8.

Chapter 1 gives a brief introduction to the world of nanotechnology and lanthanide luminescence materials. A general link between the change of a lanthanide doped inorganic material's size and its luminescence properties is made.

Chapter 2 overviews the so far reported literature on rare-earth carbonate and tungstate materials. The different synthetic techniques and methods of controlling the morphology are compared. For both families of materials the reported lanthanide doped materials are discussed.

Chapter 3 presents the different measurement techniques used throughout this PhD work and the procedures connected with it.

Chapter 4 described the synthesis and characterization of several rare-earth carbonate materials: $LaOHCO_3$, $La_2O(CO_3)_2$ and $Ce_2O(CO_3)_2$. The low temperature urea homogenous precipitation method is compared with the hydrothermal synthesis. The use of two different La^{3+}/Ce^{3+} sources and glucose/fructose as stabilizing ligands on the materials' morphology is investigated. A wide variety of morphologies is obtained. Next the luminescence properties of these materials doped with Eu^{3+} and Tb^{3+} ions are explored in detail.

Chapter 5 presents the hydrothermal synthesis of a $Y(WO_3)_2(OH)_3$ material in the presence and absence of a dioctyl sodium sulfosucciate surfactant. The different factors, which affect the size and shape of the particles such as reaction time, source of Y^{3+}, and amount of ligand, are investigated in depth. The luminescence properties of Eu^{3+}, Tb^{3+}, and Dy^{3+} doped $Y(WO_3)_2(OH)_3$ nanoparticles, nanorods, and 3D spheres are discussed. The influence of reaction time, doping concentration, and heat treatment on the luminescence properties of particles is presented in this chapter. Several white light emitting materials were obtained

Chapter 6 describes the hydrothermal synthesis of a Y_2WO_6 material in the presence of sodium dodecyl sulfate surfactant. The reaction pH was found to have a significant influence on the material formation. The detailed luminescence properties of Sm^{3+}, Eu^{3+}, and Dy^{3+} doped Y_2WO_6 spherical 3D microstructures built from nanosized particles are studied. The enhancement of luminescence through co-doping with Gd^{3+} ions is explored for this material. Several white light emitting materials, with quite high quantum yields, were obtained.

Chapter 7 compares two microsized materials: $Ce_2(WO_4)_3$ and $Ce_{10}W_{22}O_{81}$. These cerium tungstate materials were obtained in hydrothermal reactions, in the presence or absence of dioctyl sodium sulfosuccinate surfactant. The luminescence mechanisms of Tb^{3+} doped $Ce_2(WO_4)_3$ and $Ce_{10}W_{22}O_{81}$ are studied.

Chapter 8 summarizes the main findings of this PhD work and provides suggestions for further research.

Chapter 1: Introduction

In this chapter a brief introduction to the world of nanotechnology and lanthanide luminescence is given. The influence of size reduction on luminescence in lanthanide doped phosphors is presented.

1.1. Nanotechnology

According to the official definition announced by the European Commission a nanomaterial is: "A natural, incidental or manufactured material containing particles, in an unbound state or as an aggregate or as an agglomerate and where, for 50% or more of the particles in the number size distribution, one or more external dimensions is in the size range from 1 – 100 nm".[1]

The beginning of nanotechnology – a new era of technology – can be traced back to the famous lecture "There is plenty of room at the bottom" given by theoretical physicist Richard Feynman in 1959. In this talk Feynman discussed the problem of manipulating and controlling things on a (very) small scale and the immense possibilities that miniaturization could give.[2]

Years of research have shown that the properties of a material depend on factors such as size, shape, and dimensionality and that by miniaturization of materials it is possible to acquire novel or altered properties.[3] This change in properties can be explained by the fact that when a particle size decreases, the surface to volume ratio increases, resulting in an increasing fraction of atoms lying at or near the surface. Because of this, surface and interface effects become more important giving rise to new properties. To explain further, the ratio of surface area to volume is actually a measurement of the percentage of atoms or molecules that are present on the surface of a material compared to the total number of atoms or molecules in the entire 'piece' of material. The change of surface area with materials miniaturization has been visualized in Figure 1.1. For a given 'piece' of material as the material is broken into smaller and smaller pieces, the surface area (available for interactions) increases staggeringly.

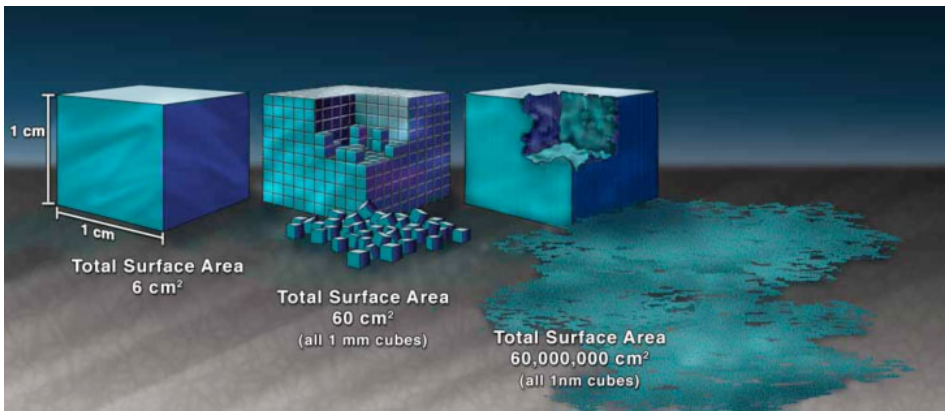

Figure 1.1: Illustration presenting the effect of increasing the surface area of a material by building it from nanosized building blocks.[4]

Nanosized particles often have unexpected properties because they are small enough to confine their electrons and produce quantum effects. To give a classic example, the color and catalytic properties of gold change with the decrease in size of the particles.[5] In its bulk form gold is considered an inert material. However, when a 'piece' of gold is broken down to nanosize it will become red or purple color and can act as a catalyst for example for oxidizing carbon monoxide. In bulk gold each gold atom is surrounded by twelve other gold atoms. The gold atoms on the surface of the materials are surrounded by six other gold atoms. In a nanosized gold material a much larger percentage of gold atoms are present on the surface, therefore a larger amount of gold atoms is surrounded by fewer gold atoms. This allows gold nanoparticles to catalyze reactions. Gold as we know it (in its bulk form) is a shiny yellow metal. It is shiny because light reflects of its surface. This is due to the fact that photons of light cannot get through clouds of electrons at the surface of the metal. Therefore the photons are reflected back to the eye. At nanoscale, depending on the size of the particles, the

electron cloud will be in resonance with a particular wavelength of light and absorb that wavelength. For example gold nanoparticles about 90 nm in size will absorb red and yellow light making the nanoparticles appear blue-green. Nanoparticles about 10 nm in size will absorb blue and green light resulting in a red appearance.

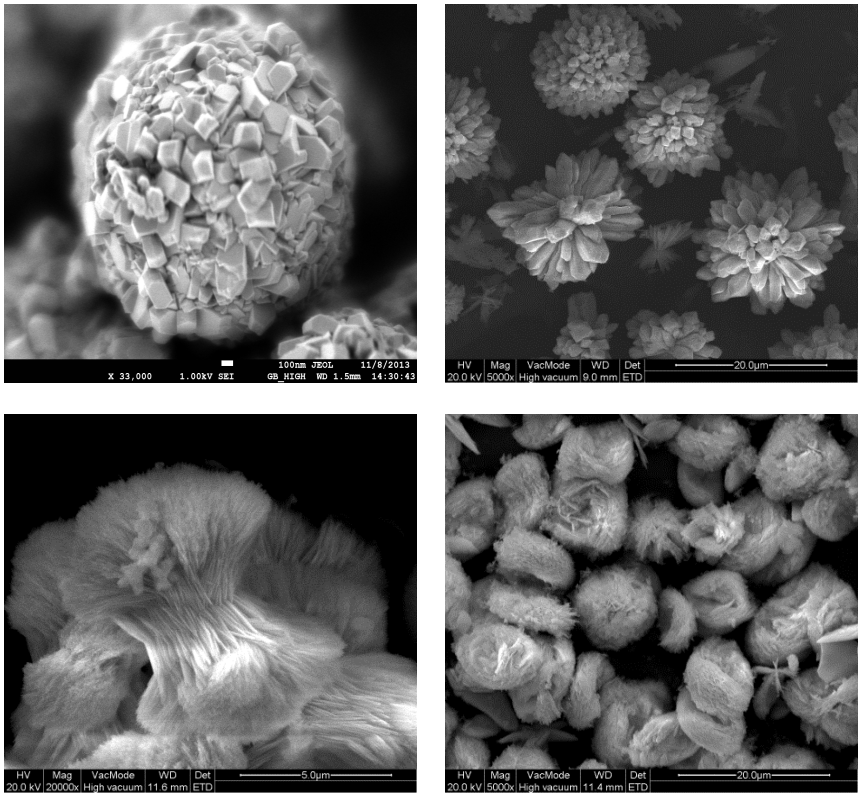

Figure 1.2: Examples of 3D structured materials synthesized during this PhD.

According to Richard Siegal, nanomaterials can be classified as zero dimensional (0D), one dimensional (1D), two dimensional (2D), and three dimensional (3D).[6] Zero dimensional nanomaterials are materials wherein all the dimensions are measured within the nanoscale (no dimensions are larger than 100 nm). Nanoparticles and nanoclusters are examples of 0D materials. One dimensional nanomaterials are

materials with one dimension outside the nanoscale (e.g. nanorods, nanowires, nanotubes). Two dimensional nanomaterials are materials with two dimensions outside the nanoscale (e.g. nanofilms, nanolayers). Three dimensional nanomaterials are composed of multiple 0D, 1D or 2D crystals arranged in various ways. 3D nanomaterials have gained interest after it was observed that particle aggregates can have collective properties different from those displayed by the individual particles as well as the bulk material.

1.2. Lanthanides and their luminescence properties

The lanthanides (Ln) are the elements with atomic numbers 57 to 71 (lanthanum to lutetium). Together with scandium and yttrium they are known as rare-earth elements (RE). The word "lanthanide" has its origins in Greek and means "lying hidden" which has its roots in the fact that up until efficient separation techniques were established the lanthanides were difficult to separate from other minerals. You could say that they were "hiding" behind each other in minerals.

In the lanthanides the 4f orbitals are gradually filled with electrons.[7-8] These elements usually exist as trivalent cations with an electronic configuration of [Xe] $4f^n$, where n varies from 1 (Ce^{3+}) to 14 (Lu^{3+}). In lanthanum the 5d subshell is lower in energy than 4f and therefore the electron configuration of this element is [Xe] $5d^1$ $6s^2$. Some of the lanthanides exist also as divalent or tetravalent ions (e.g. Eu^{2+}, Sm^{2+}, Ce^{4+}, Tb^{4+}). A characteristic feature of trivalent lanthanide ions are their sharp (atom like) electronic transitions. This is caused by the fact that 4f orbitals penetrate the xenon core significantly. They are isolated from the influence of ligands and therefore crystal-field effects are very small (because of this electronic spectra as well as

magnetic properties are essentially unaffected by the environment). This is very different compared to d transition metals, where crystal field splittings are large.

When a Ln^{3+} ion absorbs light it is excited from the ground state to one of its excited states. The energy of the photon that is absorbed matches the energy difference between the specific excited state and ground state. The f-f transitions of lanthanides are actually forbidden by the Laporte selection rule (as other transitions between energy levels with the same parity, such as d-d transitions). The f-f transitions can be excited by both magnetic dipole (MD) and electric dipole (ED) radiation. The ED transitions are Laporte forbidden. The MD transitions are allowed by the selection rules, yet they are very weak. Only because the ED transitions are weak (due to their forbidden nature) are the MD transitions also seen in the electronic spectra. Figure 1.3 shows the energy levels of the 4f configurations. Due to the good shielding of the 4f electrons this energy level diagram can be used for lanthanide ions in very different host materials.

One of the main problems with lanthanides considering their luminescence properties is the fact that lanthanide ions suffer from weak light absorption (they have very low molar absorption coefficients ε).[9] Therefore a very limited amount of radiation is absorbed when exciting directly into the 4f levels of the lanthanides. If the energy is transferred from a host material or other ion with a higher absorption coefficient this can lead to stronger luminescence. This can be overcome for example by the so-called antenna sensitization. As organic ligands have allowed absorption transitions they can absorb more light then the forbidden 4f-4f absorption transitions. Therefore often in lanthanide complexes energy is harvested by the organic ligand., and the energy is next transferred from the organic ligand to the lanthanide ion

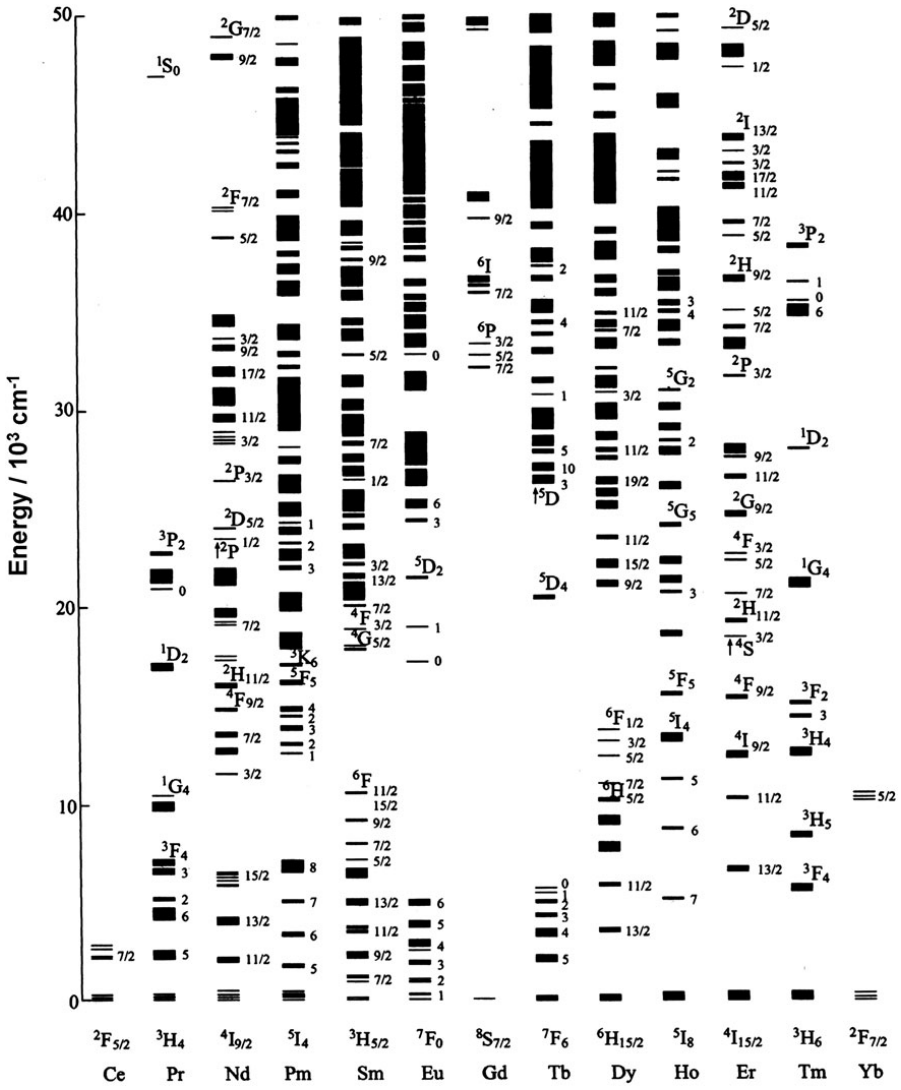

Figure 1.3: Energy level diagram for lanthanide ions doped into a LaF_3 matrix.

through intramolecular energy transfer. In some inorganic materials, such as rare-earth vanadates, tungstates or molybdates, the doped lanthanide ions can be excited via the charge-transfer transition (from the 2p orbitals of the oxygens to the 5d orbitals of the metal). The energy is then transferred to the lanthanide ion. As the

absorption coefficients of these charge-transfer transitions in the mentioned materials are several orders of magnitude higher than those of the lanthanide 4f transitions, therefore in most cases it is possible to transfer energy from the charge-transfer band to most lanthanide ions (they have energy levels high enough to accept energy from the charge-transfer band). Other indirect excitation options are also possible. For example it is feasible to excite Tb^{3+} ions by energy-transfer from Ce^{3+} ions (Ce^{3+} has allowed 4f-5d absorption in the UV). Yet this sensitization process is only efficient for Ce-Tb systems, and in some cases slightly efficient in Ce-Sm and Ce-Dy systems.

Most of the lanthanides (excluding La^{3+}, Gd^{3+}, and Lu^{3+}) show luminescence in the visible or near-infrared spectral region upon excitation with ultraviolet radiation.[9] Each of the lanthanides emits a specific color, for example Eu^{3+} emits red light, Sm^{3+} emits orange light, Dy^{3+} emits yellow light, and Tb^{3+} emits green light. Europium and terbium are often chosen as the doping ions to investigate the luminescence properties of a material because they show strong emissions in the visible region. What is more, Eu^{3+} ions can be used as a structural probe for investigating the local environment in a host material.[10] The $^5D_0 \rightarrow {}^7F_1$ transition is a pure MD transition, the total integrated intensity of which is practically independent of the symmetry of the surroundings. The $^5D_0 \rightarrow {}^7F_2$ transition is a pure ED transition and is strongly dependent on the symmetry of the environment. The relative intensities of the $^5D_0 \rightarrow {}^7F_1$ and $^5D_0 \rightarrow {}^7F_2$ transitions give information about the symmetry of the crystal sites in which Eu^{3+} ions are located. If the MD transition ($^5D_0 \rightarrow {}^7F_1$) is dominant in the spectrum, this gives information about europium being located in a site with inversion symmetry. On the contrary if the ED transition ($^5D_0 \rightarrow {}^7F_2$) is dominant this

means that the europium is located in a site without inversion symmetry. Additionally the $^5D_0 \rightarrow {}^7F_0$ transition can also give information about the environment. In theory this transition can give rise to only one line. Therefore if more than one peak is observed for this transition this would indicate the presence of more than one europium site.

Transitions which are very sensitive to changes in the symmetry of the coordination sphere are referred to as hypersensitive transitions.[11] Depending on the ion's environment they can have different intensities or splittings. Besides europium's $^5D_0 \rightarrow {}^7F_2$ transition other ions also have hypersensitive transitions, such as Nd^{3+} ($^4G_{5/2} \leftarrow {}^4I_{9/2}$), Dy^{3+} ($^6F_{11/2} \leftarrow {}^6H_{15/2}$), Er^{3+} ($^2H_{11/2} \leftarrow {}^4I_{15/2}$, $^4G_{11/2} \leftarrow {}^4I_{15/2}$) and others. These transitions can be useful tool in the analysis of lanthanide spectroscopic data.

1.3. Influence of size reduction on luminescence in lanthanide doped rare-earth inorganic materials

When the size and shape of a lanthanide doped rare-earth inorganic material are modified changes in the luminescence properties can be observed. Most often changes in the emission spectra (different peak intensity, peak position, and splitting), luminescence lifetimes, quantum yield, and concentration quenching are observed. Many of these changes can be linked to the structure distortions and surface defects caused by the size reduction – these structure distortions and surface defects affect the local environment of the lanthanide ion giving rise to different site symmetry, crystal field strength, and index of refraction compared to the bulk material.[12] In lanthanide doped rare-earth inorganic matrixes quantum size effects are usually not expected. This is due to the localized nature of the electrons of the 4f orbitals. Some exceptions can be observed for nanoparticles smaller than 10 nm.[14-15] Yet, because the

materials presented in this thesis are well above 10 nm (and usually hundreds of nanometers or several micrometers in size) the quantum effects and their influence on luminenescence properties will not be discussed.

As mentioned above the size reduction of a material may cause a change in the luminescence lifetime.[16] Usually the smaller the size of the particle, the shorter the lifetime, though some exceptions have also been reported. The decrease of luminescence lifetime with size decrease can be explained by the fact that both radiative and nonradiative relaxation rates affect the luminescence lifetime. When the material is reduced in size surface defects and quenching centers are formed, which results in an increased nonradiative relaxation rate. An increase in radiative lifetime can also be observed in nanoparticles, which will cause the increase of their luminescence lifetime compared to the bulk material. This can be caused for example by size dependent spontaneous emission increases. A change in quantum yield is another very important change in luminescence properties observed after the size reduction of a material. Most often after reducing a material to nanosize the quantum yield is lower than for the bulk material. This can be a result of energy transfer to quenching centers at the surface. A known way to overcome both the drop in luminescence lifetime and quantum yield at nanosize is to grow undoped inorganic shells around the nanoparticles, which has been done for a variety of rare-earth inorganic nanoparticles.[17]

1.4. References

1. European Commission, "COMMISSION RECOMMENDATION of 18 October **2011** on the definition of nanomaterial (2011/696/EU)," **2011**.

2. Feynman, R. P. *Engineering and Science*, **1960**, 22.

3. Colfen H.; Mann S. *Angew. Chem*., *Int. Ed*., **2003**, 42, 2350.

4. http://www.nano.gov/nanotech-101/special

5. Yeh, Y.-C.; Creran, B.; Rotello, V. M. *Nanoscale*, **2012**, 4, 1871.

6. Siegel, R.W. **1994**. Nanophase materials. In Encyclopedia of applied physics, Vol. 11, G.L. Trigg, ed. Weinheim: VCH, pp. 1-27.

7. Bünzli, J.-C.,G.; Piguet, C. *Chem. Soc. Rev.* **2005**, 34, 1048.

8. Werts, M.H.V. *Science Progress*, **2005**, 88, 101.

9. Binnemans, K. *Chem. Rev.*, **2009**, 109, 4283.

10. Bünzli, J.-C.,G.; Plancherei, D.; Pradervand G.O. *J. Phys. Chem.*, **1989**, 93, 980.

11. Henrie, D.E.; Fellows, R.L.; Choppin, G.R. *Coord. Chem. Rev.*, **1976**, 18, 199.

12. Liu, G.; Chen, X. *Handbook on the Physics and Chemistry of Rare Earths*, Gschneidner, K.A. Jr.; Bünzli, J.-C.G.; Pecharsky, V. K. Elsevier Science: Amsterdam, **2007**; Vol. 37, Chapter 233, pp. 99–169.

13. Bhargava, R. N.; Gallagher, D.; Hong, X.; Nurmikko, A. *Phys. Rev. Lett.* **1994**, 72, 416.

14. Bhargava, R. N. *J. Lumin.* **1997**, 72, 46.

15. Bhargava, R. N. *J. Lumin*. **1996**, 70, 85.

16. Tissue, B. M. *Chem. Mater.* **1998**, 10, 2837.

17. Abel, K. A.; Boyer, J. C.; Van Veggel, F. C. J. M. *J. Am. Chem. Soc.* **2009**, 131, 14644.

Chapter 2: Lanthanide doped nano- and micro- sized inorganic rare-earth materials

In this chapter the literature on rare-earth carbonates and rare-earth tungstates, which are the host materials employed in this PhD work, is overviewed. Last the aims of the research work presented in this PhD are outlined.

2.1. Rare-earth carbonates as hosts for lanthanide ions

The rare-earth carbonate family, which includes rare-earth carbonates $RE_2(CO_3)_3$, hydroxycarbonates $REOHCO_3$, oxycarbonate hydrates $RE_2O(CO_3)_2 \cdot H_2O$, and dioxycarbonates $RE_2O_2CO_3$ is an interesting family of compounds. At the origin of the studies on rare-earth carbonates particles lies the important work carried out by Matijevic and co-workers, which dates back to the 1980's and early 1990's.[1-6] Matijevic reported the synthesis of colloidal rare-earth carbonate particles, prepared by employing a facile low temperature urea ($(NH_2)_2CO$) precipitation reaction. Ever since then the rare-earth carbonate materials have been studied quite intensively at the nano- and micro- scale. The most interest has been focused on the luminescence properties of lanthanide doped rare-earth carbonates (especially rare-earth dioxycarbonates), as well as the potential to use the rare-earth carbonate particles as precursors for rare-earth oxide materials with various morphologies.

For the synthesis of rare-earth carbonate materials the low temperature urea homogenous precipitation method (synthesis used by Matijevic) and the hydrothermal reaction are most frequently used. Aside from these synthetic routes also microwave assisted hydrothermal reaction, sonochemical reaction, microemulsion synthesis, thermolysis, and flux method have been successful techniques in the synthesis of rare-earth carbonate nano- and micro- sized materials. In Table 1.1. examples of rare-earth carbonate materials prepared in each of the mentioned synthetic techniques, as well as their strengths and weaknesses are presented.

Table 2.1. Typical synthetic routes to obtain rare-earth carbonate nano- and micro-materials

Method	Examples (host material)	Ref.	Remarks
Low temperature urea homogenous precipitation method	$YOHCO_3$ $CeOHCO_3$ $GdOHCO_3$ $LaOHCO_3$ $Gd_2(CO_3)_3$ $Gd_2O(CO_3)_3$	7 8 9 10 11, 12 12	Simple, cheap raw materials. Short reaction time. Use of high temperature not required. Good control over particle size and shape. No need for costly equipment and complex procedures.
Hydrothermal/ solvothermal synthesis	$CeOHCO_3$ $LaOHCO_3$ $Gd_2O(CO_3)_3$ $YOHCO_3$ $Y_2(CO_3)_3$ $Eu_2O(CO_3)_3$ $SmOHCO_3$	13, 14, 15 16, 17, 18 19 20 21 21 22, 23	Simple, cheap raw materials. Good control over particle size and shape. Reaction vessel (autoclaves) required.
Microwave assisted hydrothermal synthesis	$(Y,Gd)_2(CO_3)_3$ $(Y,Gd)OHCO_3$ $Ce_2O(CO_3)_3$	24 24 25	Very short reaction time. Simple, cheap raw materials. Good control over particles size and shape. Costly equipment required.
Sonochemical synthesis	$La_2(CO_3)_3$ $Dy_2(CO_3)_3$ $La_2O(CO_3)_3$ $CeOHCO_3$	26 27 28 29	Simple, cheap raw materials. Short reaction time. Good control over particle shape and size. Costly equipment required.
Microemulsion synthesis	$La_2(CO_3)_3$ $Ce_2(CO_3)_3$ $Pr_2(CO_3)_3$ $Nd_2(CO_3)_3$ $Ho_2(CO_3)_3$ $Er_2(CO_3)_3$ $Yb_2(CO_3)_3$ $Y_2(CO_3)_3$	30, 31 31 31 31, 32 31 31 31 31	Cheap raw materials. No costly equipment required.
Thermolysis	$LaOHCO_3$ $Eu_2O_2CO_3$ $Pr_2O_2CO_3$	33 34 35	High temperatures and autoclaves required. Cheap raw materials. Solvent, catalyst and template-free synthesis.
Flux method	$Gd_2O_2CO_3$ $Y_2O_2CO_3$ $La_2O_2CO_3$ $(Gd,Y)_2O_2CO_3$	36, 37 36, 37 38 39	Cheap raw materials. Use of high temperature required.

Some of the most important factors which affect the size, shape and distribution of rare-earth carbonate particles are: the carbonate source, reactant concentration, presence of ligands, reaction temperature and time, pH of the reaction and presence of doping ions. In the low temperature urea homogenous precipitation synthetic technique (which is up to date the most commonly used synthesis for the preparation of these materials) urea is added to a rare-earth salt (most often a nitrate or chloride salt) and the solution is aged at a temperature between 70 - 90 °C for several hours. The molar ratio of urea to rare-earth salt is one of the most important factors that influence the morphology of the products. This can be explained by the fact that the conversion of urea in aqueous solutions is very slow (for example in the concentration range of $6 \cdot 10^{-3}$ to 1.2 mol·dm^{-3} heated at 90 °C for 1 h gives a conversion of about 4%).[2] However the presence of lanthanide salts in the aqueous medium significantly accelerates the decomposition of urea. The amount of urea in a reaction medium influences both the amount of nuclei formed as well as the point when supersaturation will be reached, and precipitation will occur, and these factors influence the size of the formed particles. Another very important factor in this type of reaction is temperature. It has already been reported in the papers by Matijevic et al. that a temperature of around 85 °C is the best choice for rare-earth carbonate synthesis when using the urea homogenous precipitation method. At a temperature below 70 °C the decomposition of urea is too slow and no precipitation occurs. At aging temperatures above 100 °C the decomposition of urea is too fast, which can lead to secondary critical supersaturation conditions and as a result of this a broad size distribution of the particles. During the aging of the solution the hydrolysis of urea occurs producing NH_4^+, OH^- and CO_3^{2-}groups into the reaction system. This increases

the alkalinity of the system. The OH^- and CO_3^{2-} groups then react with the rare-earth salts forming rare-earth carbonates. The discussed reaction requires low temperature, is simple, convenient, cost-effective, green, and in most reported cases leads to homogenous particles with regular shapes and a narrow size distribution. Rare-earth carbonate particles obtained by employing this method are usually spherical, below 300 nm in size, and amorphous. They are most often reported to be rare-earth hydroxycarbonate particles. To give a few examples Eu: $GdOHCO_3$ amorphous, spherical particles, with an average diameter of 150 nm, and nearly monodispersed were prepared via the urea homogenous precipitation method.[40]

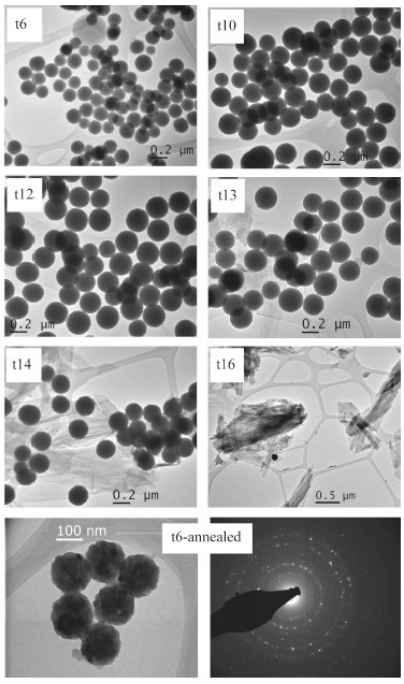

Figure 2.4: TEM images of samples measured at different reaction times (t6 = 2 h, t10 = 3 h, t12 = 4 h, t13 = 4.5 h, t14 = 5 h, t16 = 7 h). Reaction times up to around 4 h yielded spherical $GdOHCO_3$ particles, whereas prolonging the reaction time caused $Gd_2(CO_3)_3 \cdot 2H_2O$ platelets to form.[11]

Eu: $GdOHCO_3$ amorphous, spherical particles, with diameters of around 164 nm were obtained in this type of synthesis.[11] The reaction had to be carried out for 2 h to synthesize particles of this size, prolonging the reaction led to an increase in size. The urea homogenous precipitation method is most often carried out in the absence of a ligand, although several reports on the use of ligands in this type of reaction can be found in literature. For example Li et al. reported the formation of shuttle-like $CeOHCO_3$ microcrystals in a urea homogenous precipitation method carried out in the presence of polyvinylpyrrolidone (PVP).[8] The importance of the ligand is most often studied for the hydrothermal/solvothermal reaction. This type of reaction is carried out at high temperature, in a steel pressure vessel (autoclave) most often lined with Teflon. For the synthesis of rare-earth carbonate materials generally the autoclave is maintained at a temperature of 100 - 240 °C for different periods of time ranging up to 72 h. The use of ligands such as for example ethylenediaminetetraacetic acid (EDTA),[7] ethylene glycol (EG),[41] cetyltrimethylammonium bromide (CTAB),[42] polyvinyl pyrrolidone (PVP)[43] have been reported in literature for the hydrothermal synthesis.

A variety of carbonate sources can be used to synthesize rare-earth carbonate materials. Urea is the most often used source of the carbonate ions (employed in the urea homogenous precipitation method, hydrothermal synthesis, microwave assisted hydrothermal synthesis and some sonochemical synthesis). Urea is a very weak Brönsted base and its hydrolysis rate can be easily controlled by reaction temperature, as well as, as has been mentioned earlier, by the presence of a lanthanide salt. The decomposition of urea releases ions slowly and homogeneously into the reaction system. This way the localized distribution of the reactant is avoided.

The decomposition of urea increases the pH of the reaction medium, which is suitable for the formation of rare-earth carbonate particles. Other sources such as sodium carbonate (Na_2CO_3), thiourea ($SC(NH_2)_2$), sodium hydrogen carbonate ($NaHCO_3$), ammonium carbonate ($(NH_4)_2CO_3$), gelatin, and others have also been used in syntheses to obtain rare-earth carbonate materials. The different carbonate sources which have been reported in literature are gathered in Table 2.2.

Table 2.2: Most important sources of carbonate ions for the synthesis of carbonates.

Carbonate source	Examples of materials obtained from the carbonate source	Ref.	Reaction type
Urea $CO(NH_2)_2$	$YOHCO_3$	7	Urea homogenous precipitation method
	$Gd_2(CO_3)_2$	11	Urea homogenous precipitation method
	$GdOHCO_3$	11	Urea homogenous precipitation method
	$LaOHCO_3$	44	Hydrothermal
Sodium carbonate Na_2CO_3	$La_2(CO_3)_3$	26	Sonochemical synthesis
	$LaOHCO_3$	10	Mild reaction conditions
Sodium hydrogen carbonate $NaHCO_3$	$Dy_2(CO_3)_3$	27	Sonochemical synthesis
	$LaOHCO_3$	10	Mild reaction conditions
Ammonium carbonate $(NH_4)_2CO_3$	$LaOHCO_3$	10	Mild reaction conditions
Ammonium hydrogen carbonate NH_4HCO_3	$Ce_2(CO_3)_3$	31	Microemulsion synthesis
	$Nd_2(CO_3)_3$	31	Microemulsion synthesis
Thiourea $SC(NH_2)_2$	$LaOHCO_3$	45	Hydrothermal reaction
Sodium tartarate $Na_2C_4H_4O_6$	$CeOHCO_3$	13	Hydrothermal reaction
Gelatin	$LaOHCO_3$	16	Hydrothermal reaction
1,1,3,3-tetramethyl guanidinium lactate	$LaOHCO_3$	18	Hydrothermal reaction

For example Li et al. reported the synthesis of nano- and micro- particles of $LaOHCO_3$ using five different carbonate sources ($CO(NH_2)_2$, Na_2CO_3, $NaHCO_3$, $(NH_4)_2CO_3$, NH_4HCO_3) with all reaction conditions remaining the same.[10] Figure 2.5. shows that each carbonate source gave particles of different size and shape. Additionally the pH of the solution also played an important role in the formation of these particles. The reactions were carried out in covered beakers placed on a hot plate. The reactions were maintained at 90 °C for 2 h. When urea was used as the source of carbonate microflowers built from elliptical nanoflakes were formed at pH = 2, rhombic microplates were formed at pH = 7, and sandwich-like microspindles were formed at pH = 10. When $NaHCO_3$ was employed as the carbonate source in the reaction double-deck-like microhexagrams were observed at pH = 7. With the increase of pH to 10 double hexagrams were still obtained, yet it can be seen that the diameter and thickness shrunk compared to those obtained at lower pH. In the case when NH_4HCO_3 was the carbonate source at lower pH flower-like morphologies were obtained. At higher pH a mixture of irregular microhexagrams and microflowers was formed. When Na_2CO_3 was employed as the carbonate source at pH = 7 irregular two-double microrhombes were formed. At pH = 10 irregular microcrystals were collected. When $(NH_4)_2CO_3$ was used in the reaction at neutral pH peach-nucleus-shaped microcrystals were observed. At pH = 10 as in the case of Na_2CO_3 irregular microcrystals were the final product. These observations show that employing different carbonate sources, with all other reaction conditions remaining the same, have a huge influence on the morphology of the final products.

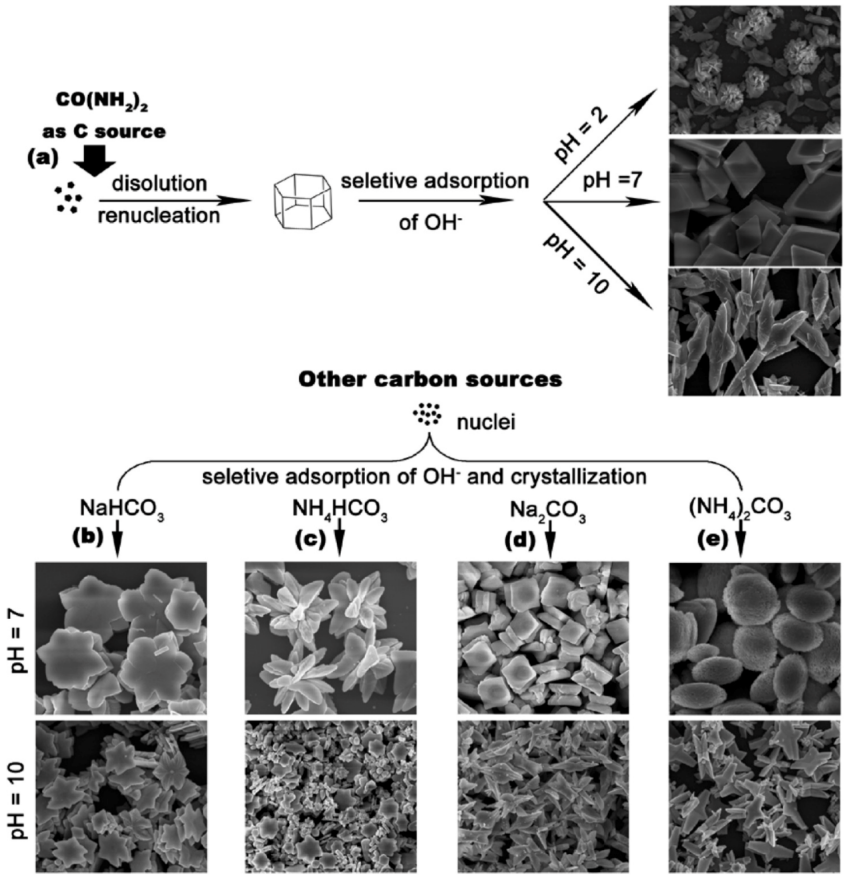

Figure 2.5: Schematic representation of the possible formation process of $LaOHCO_3$ particles when different sources of carbonate ions are used in the reaction.[10]

In the synthesis of rare-earth carbonates each reaction technique seems to be more favorable for the synthesis of a certain type of material. For example, up to date the successful preparation of $RE_2O_2CO_3$ materials in a direct synthesis has only been reported for the thermolysis and flux synthesis.[33,37] A major drawback of these routes is the preference to form larger, microsized particles, usually not very uniform in their size. Also the use of very high temperatures is required in these techniques. Another way to synthesize the $RE_2O_2CO_3$ materials is by employing a two step synthesis, where

first $REOHCO_3$ particles are formed, which are than transformed to $RE_2O_2CO_3$ particles.[10] This allows the preparation of nanosized $RE_2O_2CO_3$ materials. Although $REOHCO_3$ particles can easily be prepared both in the urea homogenous precipitation method as well as in hydrothermal synthesis, the prior one in most cases leads to spherical amorphous materials, which is not always desirable. On the other hand the hydrothermal synthesis of $REOHCO_3$ gives crystalline products, but the decomposition of urea occurs at a very high temperature which can cause, as mentioned before, secondary critical supersaturation conditions. The microemulsion method has been shown to be an ideal technique for obtaining pure $RE_2(CO_3)_3$ materials in a variety of shapes and sizes. This knowledge is of great importance as it is fundamental to know the best synthetic route to obtain the desired compound.

The photoluminescence properties of some lanthanide doped rare-earth carbonate nano- and micro- structured materials have been studied by researchers. Table 2.3. summarizes the typical dopant-host combinations, which can be found in literature for rare-earth carbonate materials at the nano- and micro- scale. The dopant concentration as well as quantum yield (QY) and luminescence decay time of a material has been included, if this information was available in the original articles. Up until now only Eu^{3+}, Tb^{3+} or mixed Eu^{3+}/Tb^{3+} doped rare-earth carbonate materials have been reported. Europium and terbium have been chosen as the doping ion to investigate the luminescence properties of a material due to the fact that they show strong emission in the visible region. Additionally as mentioned in Chapter 1 Eu^{3+} ions can be used as a structural probe for investigating the local environment in a host material.

Table 2.3: Typical dopant-host combinations for making multicolored rare-earth carbonate materials.

Dopant ion	Host material	Doping concentration	Sample form	QY [%][a]	Decay time [ms][a]	Ref.
Eu^{3+}	$CeOHCO_3$	10%	solid	-	-	13
	$GdOHCO_3$	5%	solid	<1	-	9
	$GdOHCO_3$	5%	solid	-	0.64	11
			suspension	-	0.60	
	$SmOHCO_3$	1%	solid	-	-	23
		5%		-	-	
	$La_2O_2CO_3$	5%	solid	24.2	0.87	10
	$La_2O_2CO_3$	7%	solid	-	-	38
	$La_2O_2CO_3$	x	solid	-	-	46
	$La_2O_2CO_3$	6%	solid	-	-	47
	$Y_2O_2CO_3$	7%	solid	-	-	38
	$Gd_2O_2CO_3$	7%	solid	-	-	38
	$Gd_2(CO_3)_3$	5%	solid	-	0.67	11
			suspension	-	0.59	
Tb^{3+}	$La_2O_2CO_3$	17%	solid	-	-	36
	$La_2O_2CO_3$	1%	solid	7.1	-	10
	$La_2O_2CO_3$	17%	solid	-	-	47
	$Gd_2O_2CO_3$	17%	solid	-	-	36
	$Gd_2O_2CO_3$	15%	solid	-	-	37
	$Y_2O_2CO_3$	7%	solid	-	-	36
	$(Gd,Y)_2O_2CO_3$	11%	solid	75	-	39
	$Gd_2(CO_3)_3$	5%	solid	-	-	48
Eu^{3+}/ Tb^{3+}	$LaOHCO_3$	5% Eu, 5% Tb	solid	-	-	16
		5% Eu, 2.5%Tb		-	-	
		2.5% Eu, 5% Tb		-	-	
		1% Eu, 5% Tb				

[a] If data available in original papers (data obtained for powder samples)

It has been observed that among the rare-earth carbonate materials the hexagonal rare-earth dioxycarbonate is the most suitable host for luminescent materials. Due to its thermodynamic stability and chemical durability against H_2O and CO_2 hexagonal dioxycarbonate is a good choice as host for luminescent lanthanide ions. Additionally the hexagonal $RE_2O_2CO_3$ show a close resemblance to the hexagonal A-type rare-earth

sesquioxide, which are known to be a very good host for phosphors.[49] In RE_2O_3 structures the REO_2 layers are stacked directly upon one another and share planes of oxygens, whereas in hexagonal $RE_2O_2CO_3$ the RE_2O_2 layers are separated by CO_3^{2-} groups. This type of layered structure is suitable as energy transfer from an excited lanthanide ion to another lanthanide ion across the CO_3^{2-} layer is restrained because of the distance between the Ln^{3+} ions. Due to this lanthanide doped hexagonal $RE_2O_2CO_3$ are resistant to concentration quenching and result in high emission intensities.

Many of the reported rare-earth carbonate nano-/micro- materials have very promising applications. For example $LaOHCO_3$ hierarchical nanostructures, synthesized in the presence of gelatine, and co-doped with Eu^{3+} and Tb^{3+} have been found to be efficient white light sources.[16] The $LaOHCO_3$ hierarchical nanostructures were co-doped with different concentrations of Eu^{3+} and Tb^{3+} ions. In the emission spectra peaks which can be assigned to both europium and terbium transitions can be distinguished. Peaks located at 487 nm and 541 nm correspond to Tb^{3+} transitions ($^5D_4 \rightarrow {}^7F_6$ and $^5D_4 \rightarrow {}^7F_5$, respectively). Peaks located at 581 nm, 619 nm, and 690 nm correspond to Eu^{3+} transitions ($^5D_0 \rightarrow {}^7F_0$, $^5D_0 \rightarrow {}^7F_2$, and $^5D_0 \rightarrow {}^7F_4$, respectively). For a 5% Eu, 5% Tb: $LaOHCO_3$ system the CIE chromaticity coordinates on excitation at different wavelengths are x = 0.312, y = 0.302 (260 nm); x = 0.276, y = 0.292 (277 nm); x = 0.259, y = 0.301 (290 nm); x = 0.244, y = 0.276 (310 nm); x = 0.231, y = 0.241 (330 nm); and x = 0.206, y = 0.213 (365 nm). This has been presented in Figure 2.6. As can be seen when the excitation wavelength is shorter than 330 nm, the CIE coordinates are located in the white light region. For a 5% Eu, 2.5% Tb: $LaOHCO_3$ material also at the right excitation wavelength (310 - 365 nm) white light emission

can be obtained. This work showed that in the case of doped $LaOHCO_3$ the emission color can be easily tuned by varying the doping concentration and choosing an appropriate excitation wavelength.

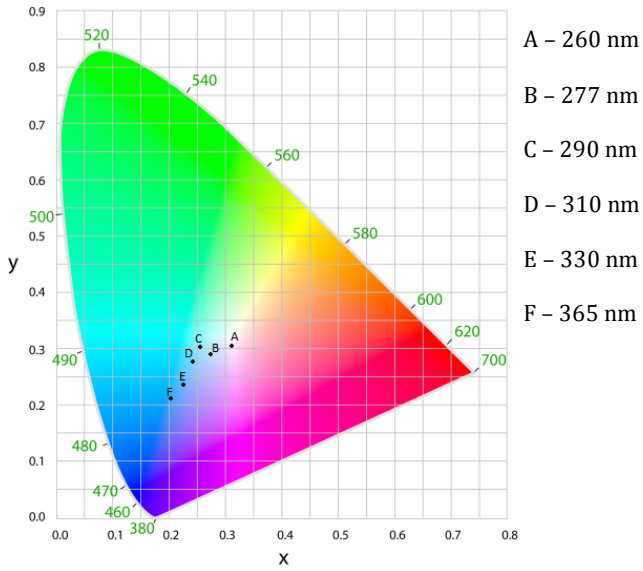

Figure 2.6: CIE chromaticity diagram of 5% Tb^{3+}, 5% Eu^{3+} co-doped $LaOHCO_3$ apple-like hierarchical structures excited with different wavelengths.[16]

The luminescence of Eu^{3+}: $GdOHCO_3$ spherical nanoparticles was investigated after their internalization by human cervical carcinoma (HeLa) cells, and were found to have adequate characteristics for biolabels.[11] Also extensive in vitro and in vivo toxicological studies have been carried out for water-stable spherical Gd^{3+}: $YbOHCO_3$ nanoparticles synthesized using a urea-based homogenous precipitation method.[50] The studies showed that these nanoparticles possess high biocompatibility and low toxicity, making them safe for clinical use. The nanoparticles showed excellent imaging efficiency and could be employed as dual-modal contrast agents in X-ray CT and MR imaging. Eu^{3+} and Tb^{3+} doped hexagonal rare-earth dioxycarbonate particles

have been reported by several researchers as highly luminescent red and green phosphors. For example Li et al. reported the luminescence properties of 5% Eu^{3+} and 1% Tb^{3+} doped $La_2O_2CO_3$ rhombic microplates.[10] These rhombic microplates had been obtained in a reaction carried out between urea and lanthanum nitrate at pH = 7 and 90 °C in a flask reaction. At first $LaOHCO_3$ particles were obtained, which after heat treating at the appropriate temperature (600 °C) for 4 h were transformed into $La_2O_2CO_3$ particles. Heat treatment of the $LaOHCO_3$ materials at 800 °C for the same amount of time led to the formation of La_2O_3. It was observed that doping Eu^{3+} or Tb^{3+} ions did not change the phase, crystallization or morphology of the materials. In Figure 2.7. the photoluminescence excitation and emission spectra of 5% Eu: $La_2O_2CO_3$ and 1% Tb: $La_2O_2CO_3$ are presented. They are compared with the emission and excitation spectra of the Ln^{3+}: La_2O_3 materials obtained when higher heat treatment temperature is applied to the $LaOHCO_3$ microstructures. Under UV light radiation at 254 nm the 5% Eu: $La_2O_2CO_3$ sample shows a bright red color (CIE color coordinates x = 0.612, y = 0.335) and the 1% Tb: $La_2O_2CO_3$ emits a green color (CIE coordinates x = 0.234, y = 0.515). The excitation spectrum of 5% Eu: $La_2O_2CO_3$ monitored at 610 nm shows two broad excitation bands, one centered at 226 nm and the other one at 280 nm. The strong band with a maximum at 280 nm is a Eu^{3+}-O^{2-} charge transfer transition band. The band with a maximum at 226 nm is assigned to the host absorption. Besides the two broad bands there are also several sharp peaks visible in the excitation spectrum, which can all be assigned to characteristic Eu^{3+} transitions. Upon excitation at 280 nm characteristic transitions of Eu^{3+} are visible in the emission spectrum: $^5D_1 \rightarrow {}^7F_1$ (535 nm), $^5D_0 \rightarrow {}^7F_0$ (580 nm), $^5D_0 \rightarrow {}^7F_1$ (590 nm), $^5D_0 \rightarrow {}^7F_2$ (610 nm), and $^5D_0 \rightarrow {}^7F_3$ (653 nm). The $^5D_0 \rightarrow {}^7F_2$ transition peak is the

strongest. The authors reported that this material showed a luminescence lifetime of 0.87 ms (measured at 300 K) and a quantum yield of 24.2 %. The differences in the excitation and emission spectra between Eu^{3+} doped $La_2O_2CO_3$ and La_2O_3 can be attributed to the different coordination environments and symmetries of Eu^{3+} ions in the two host lattices. Investigation of the splitting of the $^5D_0 \rightarrow {}^7F_0$ transition peak suggests that the Eu^{3+} ions occupy three different intrinsic crystallographic sites in the $La_2O_2CO_3$ matrix. The excitation spectrum of 1% Tb: $La_2O_2CO_3$, monitored at 542 nm, shows two broad bands centered at 236 and 274 nm. The band at 236 nm can be assigned to the host absorption, whereas the 274 nm one is due to the $4f^75d^1 \leftarrow 4f^8$ transitions of terbium. Upon excitation at 236 nm the material shows characteristic transition peaks for Tb^{3+} emission: $^5D_4 \rightarrow {}^7F_6$ (488 nm), $^5D_4 \rightarrow {}^7F_5$ (542 m), $^5D_4 \rightarrow {}^7F_4$ (588 nm), and $^5D_4 \rightarrow {}^7F_3$ (620 nm). The Tb^{3+} hexagonal dioxycarbonate showed a quantum yield of 7.1%. The luminescence lifetime was not reported in the paper. In the same study the influence of size, shape and morphology of the particles on the luminescence properties was investigated. 5% Eu^{3+} doped $La_2O_2CO_3$ samples obtained at different pH conditions were taken under consideration. At pH = 2 microflowers built from nanoflakes were formed. At pH = 7 the previously described rhombic microplates were obtained. Increasing the pH to 10 gave sandwich-like microspindles. Figure 2.8. shows the emission spectra of the three samples doped with Eu^{3+} ions. It can be seen that the rhombic microplates have the highest intensity of the investigated samples. The differences in emission intensities of the samples are related to surface areas and surface defects. From the spectra provided in the original paper it is difficult to determine if any change in the peak splitting was recorded for the materials synthesized at different pH. Yet, a very slight shift of the peak position

can be observed. Brunauer-Emmett-Teller measurements confirmed a large difference in the specific surface areas of the samples.

A very important application of rare-earth carbonate materials besides the already mentioned luminescence is their use as precursors/sacrificial templates for other inorganic materials such as rare earth oxides, vanadates, tungstates, and others.[41, 51-54]

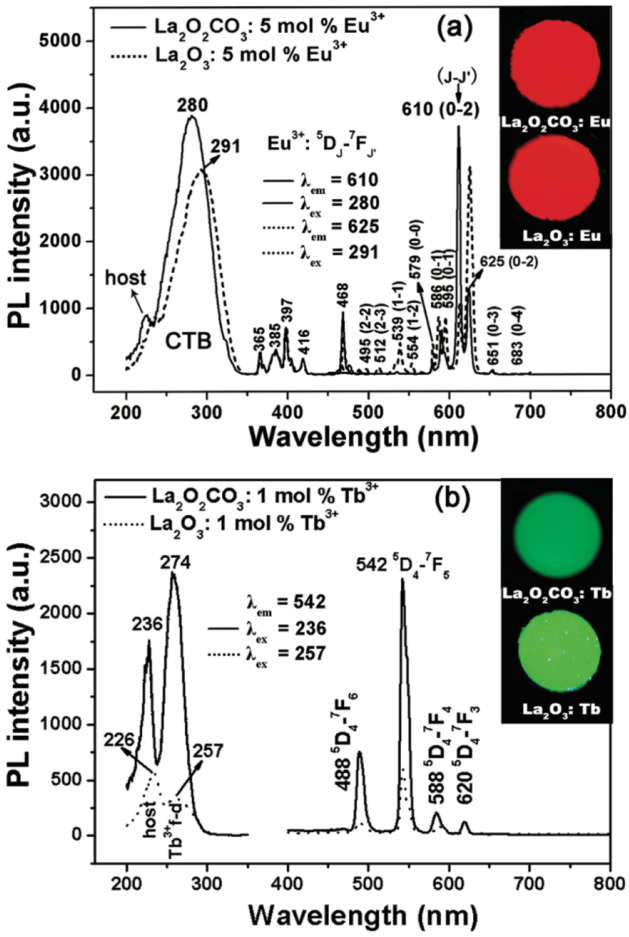

Figure 2.7: Excitation and emission spectra of a) 5% Eu: $La_2O_2CO_3$ (solid line) and 5% Eu: La_2O_3 (dashed line) and b) 1% Tb: $La_2O_2CO_3$ (solid line) and 1% Tb: La_2O_3 (dashed line).[10]

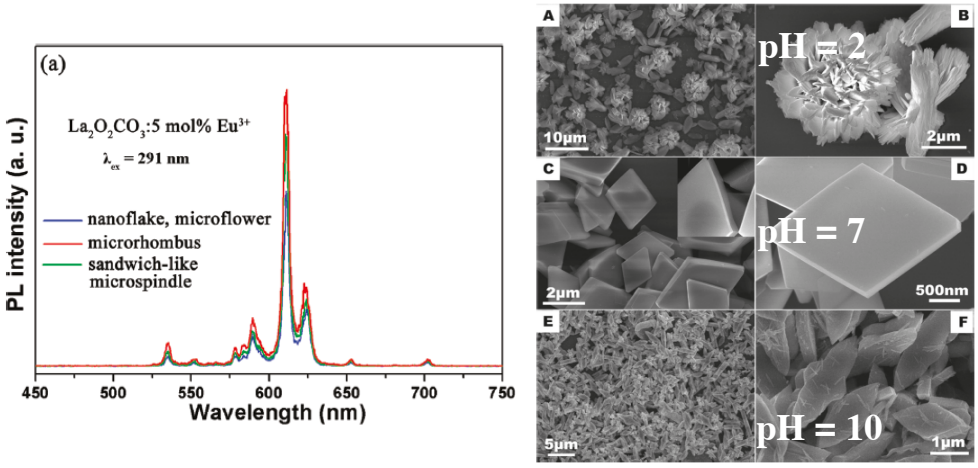

Figure 2.8: On the left: emission spectra of 5% Eu: $La_2O_2CO_3$ samples obtained at different pH values with three different morphologies (all samples were excited at 291 nm). On the right: SEM images of $La_2O_2CO_3$ samples obtained at different pH.[10]

2.2. Rare-earth tungstates as hosts for lanthanide ions

Compounds of the rare-earth tungstate family have a long history of practical applications due to their unique luminescence properties.[55] Undoped rare-earth tungstates emit blue-green light under ultraviolet excitation. When doped with visible emitting lanthanide ions this can lead to many interesting emission colors, including strongly emitting white light samples. In the last years there has been a renewed interest in rare-earth tungstate materials, this time at the nano- and micro- scale, as it was observed that by tuning the size, shape and dimensionality materials with new desirable luminescence properties can be obtained. Rare-earth tungstate materials such as RE_2WO_6, $RE_2(WO_4)_3$ and $MRE(WO_4)_2$ (M – alkali metal) have been obtained using a variety of synthetic techniques such as the hydrothermal method (which is the most often employed synthetic technique for these materials),[56] microwave assisted

hydrothermal method,[57] molten salt synthesis,[58] sol-gel synthesis,[59] and microemulsion synthesis.[60] An overview of the different synthetic methods, which can be employed for the synthesis of rare-earth tungstates, has been gathered in Table 2.4. Factors such as presence of ligand, reaction time and temperature, reaction pH, and source of rare-earth and tungstate ions were found to be the most important when trying to obtain a material with specific morphology.

Table 2.4: Typical synthetic routes to obtain rare-earth tungstate nano- and micro-materials.

Methods	Examples (host material)	Ref.	Remarks
Hydrothermal/solvothermal synthesis	$Gd_2(WO_4)_3$ Y_2WO_6 $Y_2(WO_4)_3$	56 61 62	Simple, cheap raw materials. Good control over particle size and shape. Calcinations at high temperatures sometimes required. Reaction vessels (autoclaves) required.
Microwave assisted hydrothermal synthesis	$NaY(WO_4)_2$	57	Very short reaction times, cheap raw materials. Good control over particles size and shape. Calcinations at high temperatures sometimes required. Costly equipment required.
Molten salt synthesis	Gd_2WO_6	58	Simple, short reaction times, cheap raw materials. Use of high temperatures required.
Sol-gel processing	$Tb_2(WO_4)_3$	59	Cheap raw materials. Calcinations at high temperatures required.
Microemulsion method	$Ce_2(WO_4)_3$	60	Cheap raw materials, no need for costly equipment and complex procedures. Small particles are obtained.

Many rare-earth tungstate materials with fascinating architectures have been reported. The rare-earth tungstate materials often show a tendency to form complex

3D microstructures which are built out of 0D or 1D nanobuilding blocks. For example microstructures (micro- belts, stars, and flowers) of $Gd_2(WO_4)_3$ were synthesized hydrothermally in the presence of CTAB,[56] $Tb_2(WO_4)_3$ nanowires of different thickness and structures were obtained in a combined sol-gel synthesis and electrospinning,[59] and $NaLa(WO_4)_2$ microspindles were synthesized hydrothermally in the presence of disodium ethylenediaminetetraacetate (2Na-EDTA).[63]

As in the case of rare-earth carbonates the morphology of rare-earth tungstates can be controlled by certain factors. In rare-earth tungstate materials the most important factors, which affect the size, shape and distribution of particles are the presence (and amount) of a ligand, reaction time and temperature, reaction pH, amount of tungstate salt used, and the source of the tungstate ions. For example, as has been schematically presented in Figure 2.9. the hydrothermal synthesis of $Y_2(WO_4)_3$ in the presence and absence of EDTA leads to products with two different morphologies.[62] In both cases spherical 3D structures several micrometers in size were formed. In the EDTA-free synthesis first 0D nanoparticles formed, which than change into 2D nanoflakes and eventually to 3D flowerlike architectures by means of self assembly. When EDTA was present in the reaction medium initially formed 0D nanoparticles undergo a transformation to nanospindles and eventually to dandelion-like microspheres. Other ligands which have been used in the synthesis of rare-earth tungstates are sodium dodecyl benzenesulfonate (SDBS), polyvinylpyrrolidone (PVP) and sodium citrate (Na_3cit).[64-65, 57] The amount of the used ligand also has a significant influence on the size and shape of the obtained material. This has been presented in Figure 2.10. for a $Y_2(WO_4)_3$ material synthesized in the presence of different amounts of SDBS surfactant.[64]

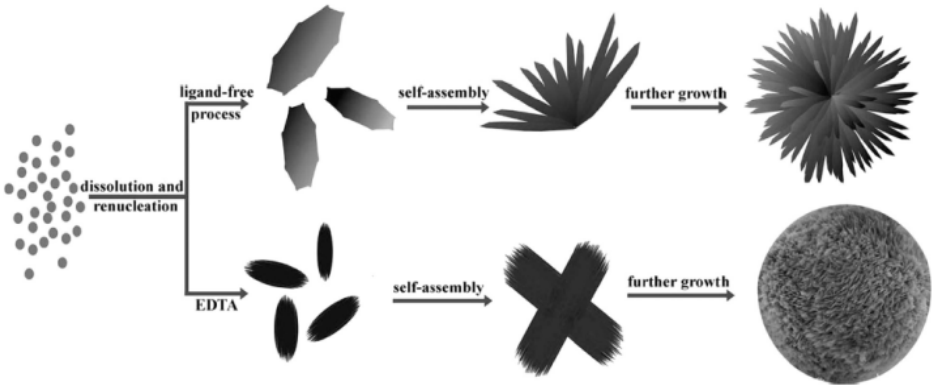

Figure 2.9: Possible morphological evolution of $Y_2(WO_4)_3$ 3D hierarchical architectures in the absence and presence of EDTA.[62]

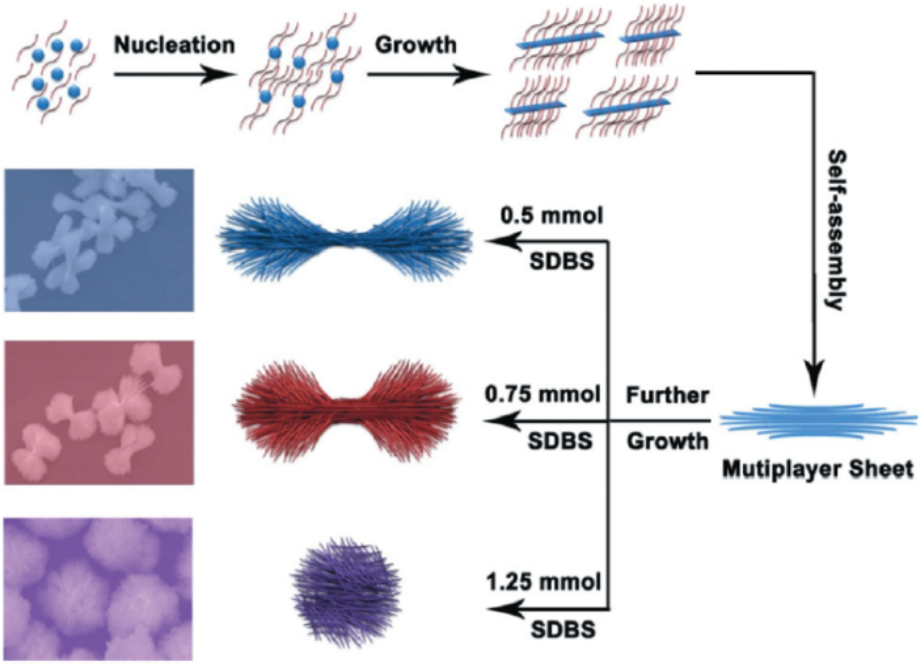

Figure 2.10: Schematic illustration of the formation process of $Y_2(WO_4)_3$ in the presence of different amounts of SDBS surfactant.[64]

Time dependent experiments were carried out by Tian et al. for the microwave-assisted hydrothermal synthesis of $NaY(WO_4)_2$ in the presence of Na_3cit to show the influence of time on particles morphology.[57] SEM images were taken of products obtained after a reaction time of 1 min, 3 min, 7 min, 15 min, and 30 min. The product obtained after 1 min was composed of many thin nanosheets and nanoparticles. After 3 min the nanosheets began to agglomerate together and form uniform clusters, although some single nanosheets were also present. With the increase of microwave irradiation time the number of single, not agglomerated nanosheets decreased and a larger amount of nanosheet clusters was formed. After carrying out the reaction for 15 min porous flower-like morphologies, with an average size of 1.5 μm, were formed. After increasing the reaction time to 30 min the flower-like morphologies had remained, however their average size had decreased to around 1.0 μm, and the borders of some particles were merged together. To give one last example, it was reported that using different molten salts does not have any influence on the crystal structure of the rare-earth tungstate materials, but that the morphology of the products can be significantly influenced by this.[58] When NaCl was employed in the synthesis sphere-like particles, about 100 nm in size, were obtained. When KCl was used instead, rod-like particles 200–400 nm in length had formed. The authors suggest that this difference in size and shape is caused by different electronegativities or the relatively larger distance between K^+ and Cl^-. The influence of the amount of the used molten salt compared to the source of lanthanide and tungstate was also investigated. It was observed that when the molar ratio of the raw materials (Gd_2O_3, WO_3, to NaCl was 1 : 1 or 1 : 3 pure phases of the products were obtained. When the amount of the molten salt was increased to 1 : 6 additional impurities were present.

The photoluminescence properties of some lanthanide doped rare-earth tungstate materials have been studied by researchers. Table 2.5. summarizes the typical dopant-host combinations, which can be found in literature for rare-earth tungstate materials at the nano- and micro- scale. The dopant concentration as well as quantum yield (QY) and luminescence decay time of a material has been included (if this information was given in the original article).

Nano- and micro- crystals doped with lanthanide ions play an important role in modern lighting and display field due to their unique optical and chemical properties.[66] Opposed to conventional luminescent materials (such as organic fluorescent dyes or semiconductor quantum dots) lanthanide doped materials show narrow emission bands, longer luminescence lifetimes and low photobleaching.[67, 68] Rare-earth tungstates (and similar to them rare-earth molybdates) have been proved to be good host lattices for the luminescence of lanthanide ions. They show good chemical and thermal stability. The use of rare-earth tungstates in light-emitting diodes (LEDs) is often discussed in literature. The micro-texture of rare-earth tungstate particles is in many cases highly porous and the particles have a large surface area, which is favorable for the manufacture of LEDs.[69] The large surface-to-volume ratio in nanosized particles leads to additional non-radiative decay paths (caused by surface defects), which can cause a decrease in quantum efficiency and thermal quenching behavior.[70] By employing microsized materials we avoid these drawbacks. In phosphor-converted white LEDs (pc-white-LEDs) a single LED light source (blue or near-UV) is combined with one or more conversion phosphors to obtain white light. One can either fully convert the emission from a near-UV LED by

Table 2.5: Typical dopant-host combinations for making multicolored rare-earth tungstate materials.

Dopant ion	Host material	Doping concentration[a]	QY [%][b]	Decay time [ms][b]	Ref.
Eu^{3+}	$NaY(WO_4)_2$	5%	-	1.04	71
	$NaY(WO_4)_2$	2-8%	-	-	72
	$NaY(WO_4)_2$	1%	-	1.03	57
		15%	-	0.94	
	$NaLu(WO_4)_2$	1-5%	-	-	73
	$AgLa(WO_4)_2$	2%	40	0.35	74
	$AgGd(WO_4)_2$	2%	27	0.88	74
	$AgY(WO_4)_2$	2%	21	0.84	74
	$AgLu(WO_4)_2$	2%	10	0.71	74
	$NaGdWO_4(OH)_x$	1-5%	-	-	75
	$Y(WO_3)_2(OH)_3$	5%	-	-	76
	$Y_2(WO_4)_3$	7%	-	0.37 (precursor) 0.49 (annealed)	64
	$Y_2(WO_4)_3$	5%	-	-	62
	Y_2WO_6	5%	-	-	61
	Y_6WO_{12}	5%	-	1.23	71
Tb^{3+}	$AgY(WO_4)_2$	2%	95	0.83	74
Eu^{3+}/Tb^{3+}	$Gd_2(WO_4)_3$	xEu + yTb = 5% (x, y = 0-5)	-	-	56
	$Tb_2(WO_4)_3$	5% Eu, 95% Tb	-	0.73	59
$Eu^{3+}/Tb^{3+}/Tm^{3+}$	$NaLa(WO_4)_2$	1.5%Eu, 4%Tb, 3%Tm	-	-	63
Sm^{3+}	Y_2WO_6	2%	-	-	61
	$AgY(WO_4)_2$	2%	15	0.34	74
Dy^{3+}	Y_2WO_6	2%	-	-	61
	$AgY(WO_4)_2$	2%	56	0.32	74
Yb^{3+}/Ho^{3+}	$Y_2(WO_4)_3$	3% Yb, 1% Ho	-	-	64
	$NaY(WO_4)_2$	3% Yb, 1% Ho	-	-	77
Yb^{3+}/Er^{3+}	$Y_2(WO_4)_3$	3% Yb, 1% Er	-	-	64
	$AgRE(WO_4)_2$ (RE = La, Gd, Y, Lu)	20% Yb, 2% Er	-	-	74
	$NaY(WO_4)_2$	3% Yb, 1% Er	-	-	77
Yb^{3+}/Tm^{3+}	$Y_2(WO_4)_3$	3% Yb, 1% Tm	-	-	64
	$NaY(WO_4)_2$	3% Yb, 1% Tm	-	-	77
	$AgRE(WO_4)_2$ (RE = La, Gd, Y, Lu)	20% Yb, 2% Er	-	-	74

[a] In some cases other doping % were also discussed; only the most significant ones are included in the table. [b] Unless indicated otherwise the values are given for the annealed materials

phosphors, or use a blue LED and convert part of the emitted light to longer wavelengths by using a phosphor. The majority of current LEDs combine phosphors with 460 nm-emitting chips. A red-emitting phosphor can be successfully used in white LEDs if it exhibits strong absorption at around 400 nm (which is the LED chips emission wavelength), and shows strong emission under excitation with near-UV light. Many of the rare-earth tungstate materials fulfill these requirements. Although the topic of using nano-/ micro- rare-earth tungstate materials in LEDs is often mentioned in literature, yet the scarcity of true performance data beyond comparing CIE coordinates of new materials with existing LEDs needs to be highlighted.

To give an example of the luminescence properties of Ln^{3+} doped rare-earth tungstates Zheng et al. reported the luminescence properties of Eu^{3+} doped $NaY(WO_2)_4$ bowknot-like structures, obtained hydrothermally in the presence of disodium ethylenediamine tetraacetate (Na_2EDTA), before and after heat treatment.[71] The excitation spectrum of as-prepared (before heat treatment) Eu^{3+} doped $NaY(WO_2)_4$ (monitoring the $^5D_0 \rightarrow {}^7F_2$ transition at 614 nm) consisted of a strong broad charge-transfer band, with a maximum at around 250 nm, and weak peaks which can be assigned to the typical intra 4f transitions of Eu^{3+} (Figure 2.11.). The charge-transfer band is a result of the charge-transfer absorption from the 2p orbitals of oxygen ligands to the 5d orbitals of tungsten atoms in tungstate groups. After excitation into the charge-transfer band the emission spectrum contained a broad band with a maximum at 450 nm, and sharp peaks at 593 nm and 614 nm. Under UV excitation at about 254 nm the as-prepared $NaY(WO_2)_4$ material emitted white light (CIE coordinates were determined to be x = 0.31, y = 0.26 and were close to the CIE

coordinates for standard white light x = 0.33, y = 0.33). After heat treatment the luminescence properties of the material changed significantly. The broad charge-transfer band in the excitation spectrum shifted from 250 nm to 276 nm, and the Eu^{3+} characteristic peaks were relatively more intensive. The intensity of the charge-transfer band in the emission spectrum was so weak that it could be neglected. The characteristic emission peaks of Eu^{3+} become dominant. Therefore it can be concluded that in the heat-treated material the energy absorbed by the charge-transfer transition is transferred more effectively to the Eu^{3+} ions. The heat treated Eu^{3+} doped $NaY(WO_2)_4$ bowknot-like structures emitted red light under a UV lamp (CIE coordinates were determined to be x = 0.60, y = 0.32).

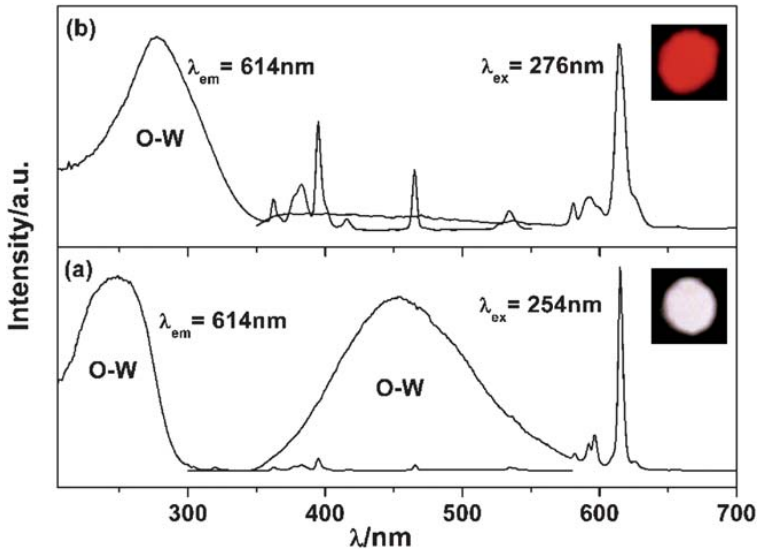

Figure 2.11: Excitation and emission spectra of Eu^{3+} doped $NaY(WO_4)_2$ bowknot-like structures before (a) and after (b) heat treatment.[71]

2.3. Aims of this PhD research

The aim of this PhD research was to develop several new lanthanide-doped inorganic materials of nano-/micro- size, and investigate their luminescence properties in detail. Two families of materials were chosen: rare-earth carbonates and rare-earth tungstates. This choice was based on the relatively small amount of published results (compared to other lanthanide-doped inorganic matrices at the time being), yet already quite promising data.

The idea behind this PhD research work was to develop rare-earth carbonate particles, which could potentially find application in the field of bio-imaging (rare-earth carbonates are non-toxic, therefore it seemed like a good choice of material). The aim was to synthesize carbonate particles, which would form stable colloidal suspensions in water, emit strongly in the visible region, and have luminescence lifetimes in the μs or ms range.

In the case or rare-earth tungstate materials they were synthesized for the purpose of potential use in lighting and displays. This group of materials is known to show excellent chemical stability, even at increased temperatures encountered in a typical illumination grade LED. Additionally these materials are self-activated due to the presence of a W-O charge transfer band. They absorb energy in the UV region, which can then be efficiently transferred to Ln^{3+} ions incorporated into the material. Strongly white-emitting materials were one of the main goals of this part of the research.

An important aspect of the research besides synthesizing new, previously not reported in literature materials, was finding ways to tune the architecture and luminescence properties of these materials.

2.4. References

1. Matijevic, E. *Pure Appl. Chem.,* **1988**, 60, 1479.

2. Matijevic, E.; Hsu, W. P. *J. Colloid Interface Sci.,* **1987**, 118, 506.

3. Her, Y.S.; Matijevic, E.; Wilcox, W.R. *J. Mater. Res.,* **1992**, 7, 2269.

4. Sprycha, R.; Jablonski, J.; Matijevic, E. *J. Colloid Interface Sci.* **1992**, 149, 561.

5. Her, Y.S.; Matijevic, E.; Wilcox, W.R. *Powder Technol.* **1990**, 61, 173.

6. Alken, B.; Matijevic, E. *J. Colloid Interface Sci.* **1988**, 126, 645.

7. Cress, C. D.; Redion, C. S.; Landi, B. J.; Raffaelle, R. P. *J. Solid State Chem.* **2008**, 181, 2041.

8. Li, Q.; Han, Z.; Shao, M.; Liu, X.; Qian, Y. *J. Phys. Chem. Solids* **2003**, 64, 295.

9. Di, W.; Ren, X.; Zhang, L.; Liu, C.; Lu, S. *CrystEngComm* **2011**, 13, 4831.

10. Li, G.; Peng, C.; Zhang, C.; Xu, Z.; Shang, M.; Yang, D.; Kang, X.; Wang, W.; Li, C.; Cheng, Z.; Lin, J. *Inorg. Chem.* **2010**, 49, 10522.

11. Lechevallier, S.; Lecante, P.; Mauricot, R.; Dexpert, H.; Dexpert-Ghys, J.; Kong, H.-K.; Law, G.-L.; Wong, K.-L. *Chem. Mater.* **2010**, 22, 6153.

12. Park, I. Y.; Kim, D.; Lee, J.; Lee, S. H.; Kim, K.-J. *Mater. Chem. Phys.* **2007**, 106, 149.

13. Qian, L.-W.; Wang, X.; Zheng, H.-G. *Cryst. Growth Des.* **2012**, 12, 271.

14. Han, Z. H.; Guo, N.; Tang, K. B.; Yu, S. H.; Zhao, H. Q.; Qian, Y. T. *J. Cryst. Growth* **2000**, 219, 315.

15. Li, K.; Zhao, P. *Mater. Res. Bull.* **2010**, 45, 243.

16. Zhong, S.-L.; Zhang, L.-F.; Jiang, J.-W.; Lv, Y.-H.; Xu, R.; Xu, A.-W.; Wang, S.-P. *CrystEngComm* **2011**, 13, 4151.

17. Zhang, Y.; Han, K.; Cheng, T.; Fang, Z. *Inorg. Chem.* **2007**, 46, 4713.

18. Li, Z.; Zhang, J.; Du, J.; Gao, H.; Gao, Y.; Mu, T.; Han, B. Mater. Lett. **2005**, 59, 963.

19. Yang, X.; Zhai, Z.; Xu, L.; Li, M.; Zhang, Y.; Hou, W. *RSC Advances*, **2013**, 3, 3907.

20. Raju, G. S. R.; Pavitra, E.; Yu, J. S. *Dalton Trans.*, **2013**, 42, 11400.

21. Zhang, Y.; Gao, M.; Han, K.; Fang, Z.; Yin, X.; Xu, Z. *J. Alloy Compd.* **2009**, 474, 598.

22. Li, Y.; Ge, M.; Li, J.; Wang, J.; Zhang, H. *CrystEngComm,* **2011**, 13, 637.

23.Yin, X.-B.; Zhang, Y.-J.; Fang, Z.-Y.; Xu, Z.-Y. *Chin. J. Chem.* **2010**, 23, 102.

24. Dai, S.-H.; Liu, Y.-F.; Lu, Y.-N. *J. Colloid Interface Sci.* **2010**, 349, 34.

25. Ikuma, Y.; Oosawa, H.; Shimada, E.; Kamiya, M. *Solid State Ionics*, **2002**, 151, 347.

26. Salavati-Niasari, M.; Hosseinzadeh, G.; Davar, F. *J. Alloy Compd.* **2011**, 509, 134.

27. Salavati-Niasari, M.; Javidi, J.; Davar, F. *Ultrason. Sonochem.* **2010**, 17, 870.

28. Jeevanandam, P.; Koltypin, Y.; Palchik, O.; Gedanken, A. *J. Mater. Chem.* **2001**, 11, 869.

29. Qi, R.-J.; Zhu, Y.-J.; Cheng, G.-F.; Huang, Y.-H. *Nanotechnology* **2005**, 16, 2502.

30. Guo, G.; Gu, F.; Wang, Z.; Guo, H. *J. Cryst. Growth* **2005**, 277, 631.

31. Gu, F.; Wang, Z.; Han, D.; Guo, G.; Guo, H. *Cryst. Growth Des.* **2007**, 7, 1452.

32. Zhu, W.; Ma, J.; Xing, X.; Xu, L.; Chen, Y. *Mater. Res. Bull.* **2011**, 26, 830.

33. Pol, V. G.; Thiyagarajan, P.; Calderon Moreno, J. M.; Popa, M. *Inorg. Chem.* **2009**, 48, 6417.

34. Pol, V. G.; Calderon Moreno, J. M.; Popa, M.; Acharya, S.; Ariga, K.; Thiyagarajan, P. *Inorg. Chem.* **2009**, 48, 5569.

35. Calderon Moreno, J. M.; Pol, V. G.; Suh, S.-H.; Popa, M. *Inorg. Chem.* **2010**, 49, 10067.

36. Koyabu, K.; Mayama, Y.; Masui, T.; Imanaka, N. *J. Alloy Compd.* **2006**, 418, 230.

37. Mayama, Y.; Masui, T.; Koyabu, K.; Imanaka, N. *J. Alloy Compd.* **2008**, 451, 132.

38. Mayama, Y.; Koyabu, K.; Masui, T.; Tamara, S.; Imanaka, N. *J. Alloy Compd.* **2006**, 418, 243.

39. Kim, S. W.; Masui, T.; Matsushita, H.; Imanaka, N. *J. Electrochem. Soc.* **2010**, 157, J181.

40. Di, W.; Ren, X.; Zhang, L.; Liu, C.; Lu, S. *CrystEngComm* **2011**, 13, 4831.

41. Yin, S.; Minamidate, Y.; Tonouchi, S.; Goto, T.; Dong, Q.; Yamane, H.; Sato, T. *RSC Adv.* **2012**, 2, 5976.

42. Wang, S.; Gu, F.; Li, C.; Cao, H. *Cryst. Growth Des.* **2007**, 307, 386.

43. Wu, M.; Zhang, Q.; Liu, Y. Fang, Q.; Liu, X. *Mater. Res. Bull.* **2009**, 44, 1437.

44. Yang, X.; Zhai, Z.; Xu, L.; Li, M.; Zhang, Y.; Hou, W. *RSC Advances*, **2013**, 3, 3907.

45. Han, Z.; Yang, Q.; Lu, G. Q. J. *Solid State Chem.* **2004**, 177, 3709.

46. Mao, G.; Zhang, H.; Li, H.; Jin, J.; Niu, S. *J. Electrochem. Soc.* **2012**, 159, J48.

47. Koyabu, K.; Masui, T.; Tamura, S.; Imanaka, N. *J. Alloy Compd.* **2006**, 408-412, 867.

48. Wu, Y.; Xu, X.; Tang, Q.; Li, Y. *Nanotechnology* **2012**, 23, 205103.

49. Olafsen, A.; Larsson, A.-K.; Fjellvasg, H.; Hauback, B.C. *J. Solid State Chem.* **2001**, 158, 14.

50. Jin, Y.; Liu, J.; Zheng, Q.; Xu, J.; Sharma, B. R.; He, G.; Yan, M.; Zhang, L.; Song, Y.; Li, T.; Yuan, Q.; Sun, Y.; Yang, H. *New J. Chem.* **2013**, 37, 3024.

51. Riccardi, C. S.; Lima, R. C.; dos Santos, M. L.; Bueno, P. R.; Varela, J. A.; Longo, E. *Solid State Ionics* **2009**, 180, 288.

52. Xu, Z.; Bian, S.; Wang, J.; Liu, T.; Wang, L.; Gao, Y. *RSC Adv.* **2013**, 3, 1410.

53. Huang, S.; Wang, D.; Wang, Y.; Wang, L.; Zhang, X.; Yang, P. *J. Alloy Compd.* **2012**, 29, 140.

54. Jia, Y.; Sun, T.-Y.; Wang, J.-H.; Huang, H.; Li, P.; Yu, X.-F.; Chu, P. K. *CrystEngComm* **2014** DOI:10.1039/c4ce00440j

55. Glorieux, B.; Jubera, V.; Apheceixborde, A.; Garcia, A. *Solid State Sci.*, **2011**, 13, 460.

56. Zheng, Y.; Li, Z.; Wang, L.; Xiong, Y. *CrystEngComm*, **2012**,14, 7043.

57. Tian, Y.; Chen, B.; Hua, R.; Yu, N.; Liu, B.; Sun, J.; Cheng, L.; Zhong, H.; Li, X.; Zhang, J.; Tian, B.; Zhong, H. *CrystEngComm*, **2012**, 14, 1760.

58. Lei, F.; Yan, B. *J. Am. Ceram. Soc*., **2009**, 92, 1262.

59. Hou, Z.; Cheng, Z.; Li, G.; Wang, W.; Peng, C.; Li, C.; Ma, P.; Yang, D.; Kang, X.; Lin, J. *Nanoscale*, **2011**, 3, 1568.

60. Pramanik, S.; Bhattacharya, S.C. *Mater. Chem. Phys*., **2010**, 121, 125.

61. Wang, J.; Zhang, Z.-J.;Zhao, J.-T.; Chen, H.-H.; Yang, X.-X. Tao, Y.; Huang, Y.

J. Wang, Z.-J. Zhang, J.-T. Zhao, H.-H. Chen, X.-X. Yang, *J. Mater. Chem*., **2010**, 20, 10894.

62. Xu, L.; Shen, J.; Lu, C.; Chen, Y, Hou, W. *Cryst. Growth Des*. **2009**, 9, 3129.

63. Liu, X.; Hou, W.; Yang, X.; Liang, J. *CrystEngComm* **2014**, 16, 1268.

64. Huang, S.; Zhang, X.; Wang, L.; Bai, L.; Xu, J.; Li, C.; Yang, P. *Dalton Trans*., **2012**, 5634.

65. Zhou, Y.; Yan, B.; He, X.-H. *J. Mater. Chem. C* **2014**, 2, 848.

66. Eliseeva, S.V.; Bünzli, J.-C.G. *Chem. Soc. Rev*., **2010**, 39, 189.

67. Bünzli, J.-C.G., Piguet, C. *Chem. Soc. Rev.*, **2005**, 34, 1048.

68. Binnemans, K. *Chem. Rev*., **2009**, 109, 4283.

69. Rao, R.P. *J. Electrochem. Soc*., **1996**, 143, 189.

70. Smet, P.F.; Parmentier, A.B.; Poelman, D. J. ELectrochem. Soc. 2011, 158, R37-R54.

71. Zheng, Y,; You, H.; Liu, K.; Song, Y.; Jia, G.; Huang, Y.; Yang, M.; Zhang, L.; Ning, G. *CrystEngComm*, **2011**, 13, 3001.

72. Lei, F.; Yan, B.; Chen, H.H.; Zhao, J.T. *Inorg. Chem.* **2009**, 48, 7576.

73. Lei, F.; Yan, B. *J. Mater. Res.* **2011**, 26, 88.

74. Zhou, Y.; Yan, B. He, X.-H. *J. Mater. Chem. C,* **2014**, 2, 848.

75. Lei, F.; Yan, B. *J. Phys. Chem. C*, **2009**, 113, 1074.

76. Xu, L.; Lu, C.; Shen, J.; Chen, Y.; Zhang, Z.; Hou, W. *CrystEngComm*, **2009**, 11, 1323.

77. Huang, S.; Wang, D.; Wang, Y.; Wang, L.; Zhang, X.; Yiang, P. *J. Alloys Compd*., **2012**, 529, 140.

Chapter 3: Instrumentation and procedures

In this chapter a description of the used instruments and procedures in this PhD work is overviewed.

3.1. Instrumentation

3.1.1. Powder X-Ray Diffraction (XRD)

X-ray diffraction is a non-destructive technique that creates a diffractogram (diffracted intensity vs. scattering angle 2θ) from crystalline materials. XRD is a primary analytical technique used for phase identification of a crystalline material, additionally it can provide information on unit cell dimensions. In an XRD measurement X-rays are generated by a cathode ray tube, filtered to produce monochromatic radiation, and directed toward the sample. When an X-ray beam interacts with a sample part of the beam is absorbed by the sample, part is transmitted, part is refracted and scattered, and part is diffracted. Only the diffracted X-rays that follow Bragg's Law and lead to constructive interference are detected. Bragg's Law states that $n\lambda = 2d\ \sin\theta$ (with n being the order of diffraction (integer), λ the wavelength of the incident wave, d the distance between the planes of the lattice and θ the angle between the incoming wave and the planes). The diffracted X-rays are detected, processed and counted. Recorded XRD patterns can then be compared with standard reference patterns to identify the phase of the obtained material. A limitation of using XRD for determining the structure of a material is that analyzed materials must have an ordered structure and cannot be amorphous. Additionally mixtures of phases that have low symmetry are difficult to distinguish between because of the large number of diffraction peaks.

XRD patterns presented in this PhD thesis have been recorded on a Thermo Scientific ARL X'TRA diffractometer equipped with a CuK_α (λ = 1.5405 Å) source, a goniometer and a Peltier cooled Si(Li) solid state detector.

3.1.2. Diffuse Reflectance Infrared Fourier Transform Spectroscopy (DRIFTS)

Absorption of electromagnetic radiation of the right wavelength can excite atoms in molecules to higher vibrational levels. This energy is absorbed from the infrared region of the electromagnetic spectrum. Every group of atoms vibrates at a specific wavelength. A spectrum is collected in which the absorption in function of the wavelength is monitored. When a solid sample is being irradiated, the energy reflects off the sample. There are two ways in which the light can be reflected: specular reflectance and diffuse reflectance. The specular component is the light that reflects directly off the surface of the sample. Diffuse reflectance is radiation that is scattered in all directions from a powder sample or rough surface. Before measurements the solid samples are finely ground and mixed with KBr, which functions as a non-absorbing matrix. This is done to increase the amount of diffuse reflectance. A KBr background file is used for corrections. In the DRIFTS technique the specular reflectance is minimized while the diffuse reflectance is maximized and this signal is detected by the infrared detector.

All samples analyzed during this PhD were measured under vacuum and at room temperature. A Thermo Scientific FT-IR spectrometer (type Nicolet 6700) equipped with a DRIFTS cell was used. Spectra were recorded from 4000 cm^{-1} to 650 cm^{-1} with a resolution of 4 cm^{-1}.

3.1.3. Elemental analysis (CHN)

Elemental analysis is a process where a sample is analyzed for its elemental composition. In the CHN analysis the amount of carbon, hydrogen and nitrogen in the sample is determined. The sample is first fully combusted in an oxygen rich environment. The carbon, hydrogen, and nitrogen present oxidize and form CO_2, H_2O, N_2 and NO_x. All nitrogen-containing products are finally reduced to N_2. The resulted

gases are carried by a helium flow to a layer filled with copper. These combustion products are analyzed using a gas chromatography column (provides the separation of the gases) and thermal conductivity detector.

For the analysis of the samples obtained during this PhD a Thermo Scientific FLASH 2000 Series CHNS/O Analyzer was used. The combustion reactor reached a temperature of 1800 °C and a thermal conductivity detector has been used.

3.1.4. Transmission Electron Microscopy (TEM)

TEM is a very frequently used technique for the characterization of nanosized materials. A large disadvantage of TEM is that high vacuum and very thin samples are required for the measurements. Also often the specimen can be damaged or destroyed by the intense, high-voltage electron beam. In TEM measurements an incident electron beam is transmitted through the specimen. The incident electrons then interact with the specimen and are transformed to unscattered, elastically scattered, or inelastically scattered electrons. The unscattered or scattered electrons are focused by a series of electromagnetic lenses and projected onto a screen. TEM makes it possible to observe samples at very high resolution and get information not only about their size, shape, size distribution, aggregation and dispersion, but also information about the crystallography of a material can be retrieved.

In this work the TEM images were recorded using a JOEL JEM2200FS transmission electron microscope with an accelerating voltage of 200 kV. Images were obtained digitally on a Gatan CCD camera. The samples for TEM were prepared on copper grids (size 200 mesh) coated with a carbon support film. The sample were prepared by placing a drop of aqueous solution of the product on a grid and allowing the solvent to evaporate.

3.1.5. Scanning Electron Microscopy (SEM)

SEM is another frequently employed technique for the characterization of nano- and micro- materials. SEM is a surface imaging technique, in which the incident electron beam scans across the sample surface and interacts with the sample to generate signals reflecting the atomic composition and topographic details of the specimen. The incident electrons cause emission from backscattered electrons, secondary electrons, and characteristic X-ray light called cathodoluminescence from atoms on the sample surface (or near the surface). Detection of secondary electrons is the most common mode in SEM. SEM is a very useful technique for acquiring information about the size/size distribution, shape and morphology of a material. Also the aggregation and dispersion of particles can be analyzed. A big disadvantage of the SEM technique is that samples which are nonconductive specimens tend to acquire charge and insufficiently deflect the electron beam. This leads to imaging faults. Therefore for nonconductive samples coating the specimen with an ultrathin layer of electrically conducting material is often required.

SEM images presented in this PhD thesis were performed with an FEI Quanta 200F SEM and an FEI Nova 600 Nanolab Dual-Beam focused ion beam in secondary electron mode.

3.1.6. N_2 adsorption-desorption measurements

Physical adsorption at the gas/solid interface is routinely measured in the laboratory. As adsorption of nitrogen occurs at the gas-solid interface, the weight of the solid increases and the pressure of the gas decreases. Thus, the amount adsorbed can be measured in at least two ways: by measuring the change in weight of the solid with a spring balance (gravimetric technique) or measuring the change in pressure of the gas in an accurately known volume (volumetric technique).

The nitrogen sorption experiments presented in this thesis were conducted at 77 K with a Micromeritics Tristar 3000. Samples were vacuum dried overnight at 80 °C prior to analysis. The surface area was calculated using the BET method. The data of the adsorption branch were used to calculate the pore diameter using the BJH method (the Barrett-Joyner-Halenda method is used for calculating pore size distributions based on a model of the adsorbent as a collection of cylindrical pores).

3.1.7. Luminescence

Photoluminescence measurements were done on an Edinburgh Instruments FLSP920 UV-vis-NIR spectrofluorimeter, using a 450W xenon lamp as the steady state excitation source and a Hamamatsu R928P PMT detector, which has a response curve between 200 and 900 nm. When recording an excitation spectrum, the emission monochromator is fixed at a certain wavelength, which is normally the most intense emissive peak. The excitation monochromator then scans the wavelength range of interest. From this spectrum the most efficient excitation wavelength can be found. In the case of an emission spectrum, the process is similar. The excitation monochromator is then fixed at a certain wavelength while the emission monochromator scans the wavelength-range. Luminescence decay times were recorded using a 60W pulsed Xe lamp, operating at a frequency of 100 Hz. The decay curves can be fitted to a single or higher exponential equation to obtain the decay time. Absolute quantum yields (QY) were measured in an integrating sphere, coated on the inside with BENFLEC®, provided by Edinburgh Instruments. The relative error on QY measurements is estimated to be around 10%. All of the luminescence measurements were recorded at room temperature. Solid powdered samples were put between quartz plates (Starna cuvettes for powdered samples, type 20/C/Q/0.2).

In order to compare the measurements the same amounts of powders were used as well as same settings of each measurement (same step, slit size and dwell time). In some cases the luminescence of both solid samples and colloidal suspensions was studied. The colloidal suspensions of particles were prepared by dispersing 0.01 g of the sample in 2 mL distilled water. All emission spectra included in manuscript have been corrected for detector sensitivity. The excitation spectra have not been corrected for lamp spectrum.

3.2. Procedures

3.2.1. Luminescence decay time

The luminescence decay time (τ) expresses the time in which the luminescence intensity decays to 1/e of the intensity immediately following the excitation pulse. In this PhD work all the decay curves could be well fitted using a single expotential equation (2.1):

$$I = I_0 \exp\left(-\frac{t}{\tau}\right) \quad (2.1)$$

where I and I_0 are the luminescence intensities at time t and 0, respectively, and τ is the luminescence lifetime. Some materials reported in literature show multi-expotential decay curves. No such materials were obtained during this PhD work.

3.2.2. Quantum yield (QY)

The absolute quantum yield (QY) is a measure of the ratio of the photons emitted by a sample with respect to the photons absorbed. Quantum yield can be calculated using equation (2.2):

$$\eta = \frac{\int L_{emission}}{\int E_{blank} - \int E_{sample}} \quad (2.2)$$

where $L_{emission}$ is the integrated area under the emission spectrum, E_{blank} is the integrated area under the "excitation" band of the blank, and E_{sample} is the integrated

area under the excitation band of the sample (as the sample absorbs part of the light, this area will be smaller than E_{blank}). To determine the QY the following steps are taken. First an emission spectrum of the excited light, with the "blank cuvette" (made from the same material BENFLEC® as the lining of the sphere) in place is recorded. This measurement is repeated three times. Next an emission spectrum of the excited light, with the sample in place is recorded (repeated three times). Last a complete emission spectrum of the sample is measured (repeated three times). All of the measurements are carried out with the background subtraction option. After the measurement all spectra are corrected for detector sensitivity. The spectra are then integrated. The calculation itself is performed using the Edinburg Instruments software provided with our Edinburgh Instruments FLSP920 spectrometer.

3.2.3. CIE coordinates and color temperature

The color that is perceived by the human eye can vary from the actual color of the material. In 1931 the Commission Internationale de l'Eclairage (CIE) developed the RGB CIE XYZ color spaces, which define colors in a mathematical way.

In order to calculate the CIE coordinates and correlated color temperatures (CCT) a ColorCalculater 4.97 freeware program provided by Osram Sylvania was used. These values are derived based on the emission spectra. The CIE coordinates for white light are x = 0.333, y = 0.333. For white light the temperature of a color is an important aspect. White light can be defined as warm or cold. Warm colors have a CCT < 3000 K, whereas cold colors have a CCT > 5000 K.

3.2.4. Data correction

During a measurement the detected signal is not correlated directly to the actual amount of light emitted from the sample. The sensitivity of the detector is not equal

for photons of different wavelength. Therefore the emission and excitation spectra should be corrected for detector sensitivity and lamp spectrum. The detector response can be measured by calibrated lamps. By comparing the measured intensity with the theoretical intensity of the lamp, the detector response curve R ($R = I_{measured}/I_{theorethical}$) can be calculated. Therefore the spectra are corrected for detector sensitivity by dividing the raw data by R.

All of the emission spectra presented in this thesis have been corrected for detector sensitivity. The presented excitation spectra have not been corrected for the lamp emission profile. To explain this, an uncorrected and corrected excitation spectrum of 5%Dy: Y_2WO_6 have been presented in Fig. 3.1. to show the effect of such correction. In the corrected spectrum the short wavelength part of the spectrum is blown out of proportion, because the Xe-lamp has almost no emission intensity at these short wavelengths.

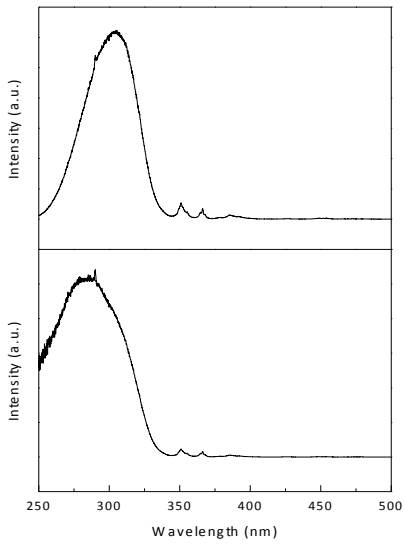

Figure 3.3. Uncorrected (top) and corrected (bottom) excitation spectra of 5% Dy: Y_2WO_6

Chapter 4: Nano- and micro- sized Eu^{3+} and Tb^{3+}doped $LaOHCO_3$ and $Ln_2O(CO_3)_2 \cdot H_2O$ (Ln = La^{3+}, Ce^{3+})

In this chapter the synthesis and characterization of two types of materials belonging to the rare-earth carbonate family – cerium and lanthanum hydroxycarbonates and oxycarbonate hydrates are presented. The low temperature urea homogenous precipitation method and hydrothermal reaction are compared as possible synthetic routes for these materials. The synthesis of lanthanum and cerium oxycarbonate hydrates in the presence of two stabilizing ligands - glucose and fructose is considered. The main focus of this chapter is on the luminescence properties of the Eu^{3+} and Tb^{3+} doped hydroxycarbonate and oxycarbonate hydrate nano- and micro- particles.

The results were published in 'Nano and micro sized Eu^{3+} and Tb^{3+} doped lanthanide hydroxycarbonates and oxycarbonates. The influence of glucose and fructose as stabilizing ligands.' Anna M. Kaczmarek, Linde Miermans, Rik Van Deun, *Dalton Trans.*, **2013**, *42*, 4639-4649.

4.1. Introduction

As mentioned in Chapter 2, doped lanthanide carbonates, hydroxycarbonates, oxycarbonate hydrates and dioxycarbonates are a family of luminescent materials not yet fully explored at the nano- and micro- scale. Several reports on the synthesis and morphology of these materials can be found in literature, but they are often only a starting product in the preparation of lanthanide oxides and therefore not investigated in detail. Also the influence of organic ligands on the formation of carbonate particles has rarely been explored. Lechevallier et al. described lanthanide doped hydroxycarbonate nanoparticles with luminescence properties. In their article they reported the synthesis of amorphous Eu^{3+}: $Gd(OH)CO_3$ nanoparticles via a urea precipitation method, using nitrate salts as the lanthanide source.[1] The luminescence intensities of the hydroxycarbonate nanoparticles were high proving that some rare-earth carbonates might be promising matrixes for nanoparticles with optical properties. The Eu^{3+}: $Gd(OH)CO_3$ nanoparticles were found to have adequate characteristics for biolabeling (nanosized, water soluble, stable in suspension, strongly luminescent, $^5D_0$ luminescence lifetimes in the μs and ms range, non-toxic). Inspired by this work, and the lack of further research in this field, the aim was to carry out an extensive research on the synthesis of nanosized, water stable particles of the carbonate family, and most of all explore their luminescence properties.

In this chapter Eu^{3+} and Tb^{3+} doped hydroxycarbonates and oxycarbonate hydrate particles are presented. Eu^{3+} and Tb^{3+} ions were chosen because they show strong emission in the visible region. Additionally, as mentioned before in the introduction to the thesis, the Eu^{3+} ion is often used as structural probe because of its non-degenerated ground state $^7F_0$ and non-overlapping $^{2S+1}L_J$ multiplets. Two different

reaction conditions were employed: hydrothermal (autoclave reaction at 120°C) and mild (85-90°C). All the reactions were water based and easy in preparation. By substituting nitrate salts with acetate salts it was possible to reduce the size of hydroxycarbonates greatly (30-50 nm). Glucose and fructose were employed as stabilizing ligands in the synthesis of hydroxycarbonate and oxycarbonate hydrate particles and their influence on the final products was observed. D-glucose and D-fructose are rather different from conventional ligands used to assist nanoparticle synthesis, as they do not have carboxylic acid groups. They are highly sensitive to the pH value giving either a cyclic or acyclic form. Employing glucose and fructose as stabilizing ligands should cause the particles to be highly water dispersible due to the large number of hydroxyl groups in these ligands. The biocompatibility of glucose makes these nanoparticles available for bio-imaging.

4.2. Synthesis

4.2.1. Preparation of Eu^{3+} and Tb^{3+} doped $LaOHCO_3$

$LaOHCO_3$ particles were synthesized in an autoclave at 120 °C, at a temperature rise speed of 1 °C/min. The reaction was prepared by mixing water solutions of 3 mmol $Ln(OAc)_3 \cdot 2H_2O$ or $Ln(NO_3)_3 \cdot 5H_2O$ (Ln = La^{3+}, Eu^{3+}, Tb^{3+}) and 30 mmol urea or 3 mmol Na_2CO_3 and stirring for 10 minutes on a magnetic stirrer. The total volume of the solution was 50 mL. Next the solution was transferred to an autoclave and heated for 12 h. The autoclave was allowed to cool down naturally, after which the obtained products were washed three times with methanol and dried at 60°C.

$LaOHCO_3$ particles were also synthesized using the urea homogenous precipitation method (referred to as 'mild' reaction conditions). The reaction was prepared by mixing water solutions of 3 mmol $Ln(OAc)_3$ (Ln = La^{3+}, Eu^{3+}, Tb^{3+}) and 30 mmol urea

and stirring for 10 minutes on a magnetic stirrer. The entire solution volume added up to 50 mL. The reaction was carried out for 3 h in a round-bottom flask tightly closed for aging at 85 °C in an oil bath. The resulting white suspension was centrifuged and the product washed three times with ethanol and dried at 60 °C.

4.2.2. Preparation of Eu^{3+} and Tb^{3+} doped $Ln_2O(CO_3)_2 \cdot H_2O$ (Ln = La^{3+}, Ce^{3+})

To prepare $La_2O(CO_3)_2 \cdot H_2O$ particles in the absence of a stabilizing ligand a hydrothermal reaction at 120 °C was carried out. Water solutions of 3 mmol $Ln(OAc)_3 \cdot 2H_2O$ (Ln = La^{3+}, Eu^{3+}, Tb^{3+}) and 60 mmol urea were first stirred for 10 minutes on a magnetic stirrer. The total volume of the solution was 50 mL. Next the solution was transferred to an autoclave and heated for 12 h. The autoclave was allowed to cool down naturally, after which the obtained products were washed three times with methanol and dried at 60 °C. $La_2O(CO_3)_2 \cdot H_2O$ and $Ce_2O(CO_3)_2 \cdot H_2O$ particles could be prepared by employing mild reaction conditions in the absence of a stabilizing ligand. Aqueous solutions of 3 mmol $Ln(OAc)_3 \cdot 2H_2O$ (Ln=Ce^{3+}, Tb^{3+}) and 30 mmol urea were mixed for 10 minutes on a magnetic stirrer. The reaction was carried out for 3 h in a round-bottom flask tightly closed for aging at 85-90 °C in an oil bath. The obtained products were washed three times with methanol and dried at 60 °C.

4.2.3. Preparation of Eu^{3+} and Tb^{3+} doped $Ln_2O(CO_3)_2 \cdot H_2O$ (Ln = La^{3+}, Ce^{3+}) with stabilizing ligand (glucose and fructose)

$Ln_2O(CO_3)_2 \cdot H_2O$ particles were also prepared in the presence of glucose and fructose as stabilizing ligands. To an aqueous solution of 6 mmol glucose/fructose 3 mmol $Ln(NO_3)_3 \cdot 5H_2O$ or $Ln(OAc)_3 \cdot 2H_2O$ (Ln = La^{3+}, Ce^{3+}) solution and 30 mmol urea solution was added. The entire solution volume added up to 50 mL. The reaction was

carried out for 3 h in a round-bottom flask tightly closed for aging at 85 °C in an oil bath. The resulting white solution was centrifuged and the product washed three times with ethanol and dried at 60 °C.

4.3. Results and discussion

Table 1 summarizes the effect of the reaction conditions and the lanthanide source on the shape and size of the synthesized hydroxycarbonate and oxycarbonate hydrate particles characterized below. Symbols **A1**-**A16** have been assigned to the samples and will be used throughout this chapter. The shape and size of the obtained materials are indicated.

4.3.1. Characterization of $LaOHCO_3$ particles

The composition and phase purity of the products were first examined by XRD. Figure 4.1. shows the XRD pattern of sample **A1**. The diffraction peaks of the sample can be assigned to a pure hexagonal $LaOHCO_3$ phase.[2] The pure hexagonal phase of $LaOHCO_3$ is also obtained for other samples synthesized from urea (samples **A2** and **A4**). To further verify the formation of $LaOHCO_3$ DRIFTS infrared spectroscopy was used. Figure 4.2. shows a DRIFTS spectrum of sample **A1** as an example. The absorptions observed between 3300 and 3700 cm^{-1} are due to the stretching mode of OH. Peaks at 3617 cm^{-1} and 3488 cm^{-1} were assigned to structural OH and adsorbed water, respectively. The intense peaks in the 1500-1430 cm^{-1} region are attributed to the ν_3 mode of the carbonate CO_3^{2-} group. In addition bands around 1080 cm^{-1}, 850 cm^{-1}, 750 cm^{-1} can be distinguished in the spectrum. They are assigned to the ν_1, ν_2 and ν_4 modes of the carbonate ion. The bands at 2494 cm^{-1} and 2130 cm^{-1} are also due to the vibrations of the CO_3^{2-} group.[3] Similar observations were made for samples **A2** and **A4**. TEM and SEM images supplied information about the typical shape and size of the

obtained particles. The influence of reaction temperature and time on the phase and morphology of the particles were investigated. Also the presence of organic ligands was considered.

Table 4.1. Summary of the reaction parameters and corresponding results

Sample	Product	Lanthanide Source[a]	Carbonate source	Reaction conditions	Shape	Size
A1	$LaOHCO_3$	$La(OAc)_3$	urea	hydrothermal	sub-spheres	30-50 nm
A2	$LaOHCO_3$	$La(OAc)_3$	urea	mild	sub-spheres	30 nm
A3	$LaOHCO_3$	$La(OAc)_3$	Na_2CO_3	hydrothermal	spheres	100-200 nm
A4	$LaOHCO_3$	$La(NO_3)_3$	urea	hydrothermal	irregular sub-spheres	50-200 nm
A5	$La_2O(CO_3)_2{\cdot}H_2O$	$La(OAc)_3$	urea	mild	sub-spheres (aggregated)	50-100 nm
A6	$La_2O(CO_3)_2{\cdot}H_2O$	$La(OAc)_3$	urea	hydrothermal	sub-spheres	20-30 nm
A7	$Ce_2O(CO_3)_2{\cdot}H_2O$	$Ce(OAc)_3$	urea	mild	elongated spheroids	diameter x length 0.1-0.2 μm x 0.5 μm
A8	$Ce_2O(CO_3)_2{\cdot}H_2O$	$Ce(OAc)_3$	urea	hydrothermal	elongated spheroids	diameter x length 0.4-0.5 μm x 1 μm
A9	Gluc-$La_2O(CO_3)_2{\cdot}H_2O$	$La(NO_3)_3$	urea	mild	mixture of rectangular and hexagonal prisms	diameter x length 0.1-0.2 μm x 1-2 μm
A10	Gluc-$La_2O(CO_3)_2{\cdot}H_2O$	$La(OAc)_3$	urea	mild	elongated spheroids	50-200 nm

Table 4.1. (continued)

A11	Fruc-$La_2O(CO_3)_2 \cdot H_2O$	$La(NO_3)_3$	urea	mild	microrods	diameter x length 0.1-0.2 μm x 0.5-2 μm
A12	Fruc-$La_2O(CO_3)_2 \cdot H_2O$	$La(OAc)_3$	urea	mild	microspheres built from nanoplates	4 μm
A13	Gluc-$Ce_2O(CO_3)_2 \cdot H_2O$	$Ce(NO_3)_3$	urea	mild	hexagonal prisms	diameter x length 0.5-1 μm x 0.5-2 μm
A14	Gluc-$Ce_2O(CO_3)_2 \cdot H_2O$	$Ce(OAc)_3$	urea	mild	elongated spheroids	diameter x length 0.1 μm x 0.4-0.5 μm
A15	Fruc-$Ce_2O(CO_3)_2 \cdot H_2O$	$Ce(NO_3)_3$	urea	mild	stacks of nanodiscs	-
A16	Fruc-$Ce_2O(CO_3)_2 \cdot H_2O$	$Ce(OAc)_3$	urea	mild	mixture of irregular particles	-

[a] The salts were hydrated: $Ln(NO_3)_3 \cdot 5H_2O$ and $Ln(OAc)_3 \cdot 2H_2O$

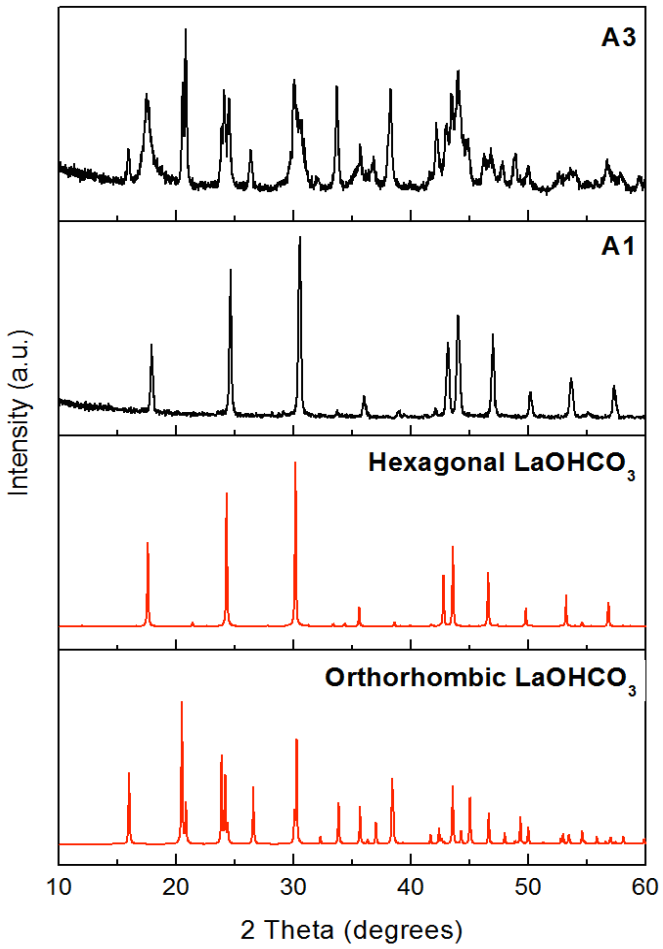

Figure 4.1: XRD patterns of samples A1 and A3. Sample A1 could be matched to the pure hexagonal $LaOHCO_3$. Sample A3 could be matched to a mixture of the hexagonal and orthorhombic phase of $LaOHCO_3$.

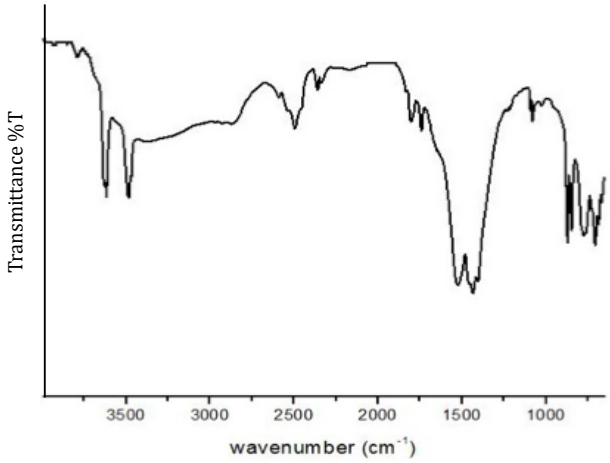

Figure 4.2: DRIFTS spectrum of sample C1, which represents the typical DRIFTS spectrum of $LaOHCO_3$ samples.

Figure 4.3. shows TEM and SEM images of the $LaOHCO_3$ particles synthesized in different reaction conditions. As can be seen from the TEM images particles of sample **A1**, formed in a hydrothermal reaction from urea decomposition in the presence of $Ln(OAc)_3$, are well monodispersed in their shape and size (Figure 4.3.a,b). The average diameter of the well-rounded sub-spherical particles is 30-50 nm. For sample **A2** (Figure 4.3.c), obtained in mild reaction conditions, the nanoparticles do not seem fully formed at these reaction conditions. Increasing the reaction time did not seem to give any significant changes in the morphology of the nanoparticles. Additionally XRD patterns showed lower crystallinity of the **A2** particles compared to **A1**. The effects of a different carbonate source – sodium carbonate – on the crystal structure and morphology of the product was also investigated (synthesis of sample **A3**). XRD clearly indicated that sample **A3** is a mixture of the hexagonal and orthorhombic $LaOHCO_3$ (see Figure 4.1.). By using electron microscopy it was determined that

spherically shaped nanoparticles, 100 – 200 nm in size, were formed (Figure 4.3.d). Unfortunately they had a very high tendency to aggregate and as a consequence did not form stable colloidal suspensions. Therefore **A3** particles were not further investigated. Synthesizing $LaOHCO_3$ from $La(NO_3)_3 \cdot 5H_2O$ and urea (sample **A4**) gave irregular sub-spherical particles around 50-200 nm in size (Figure 4.3.e,f). As employing $La(OAc)_3 \cdot 2H_2O$ as the lanthanide source gave smaller and more regular particles, therefore **A4** particles were not further investigated in this thesis work.

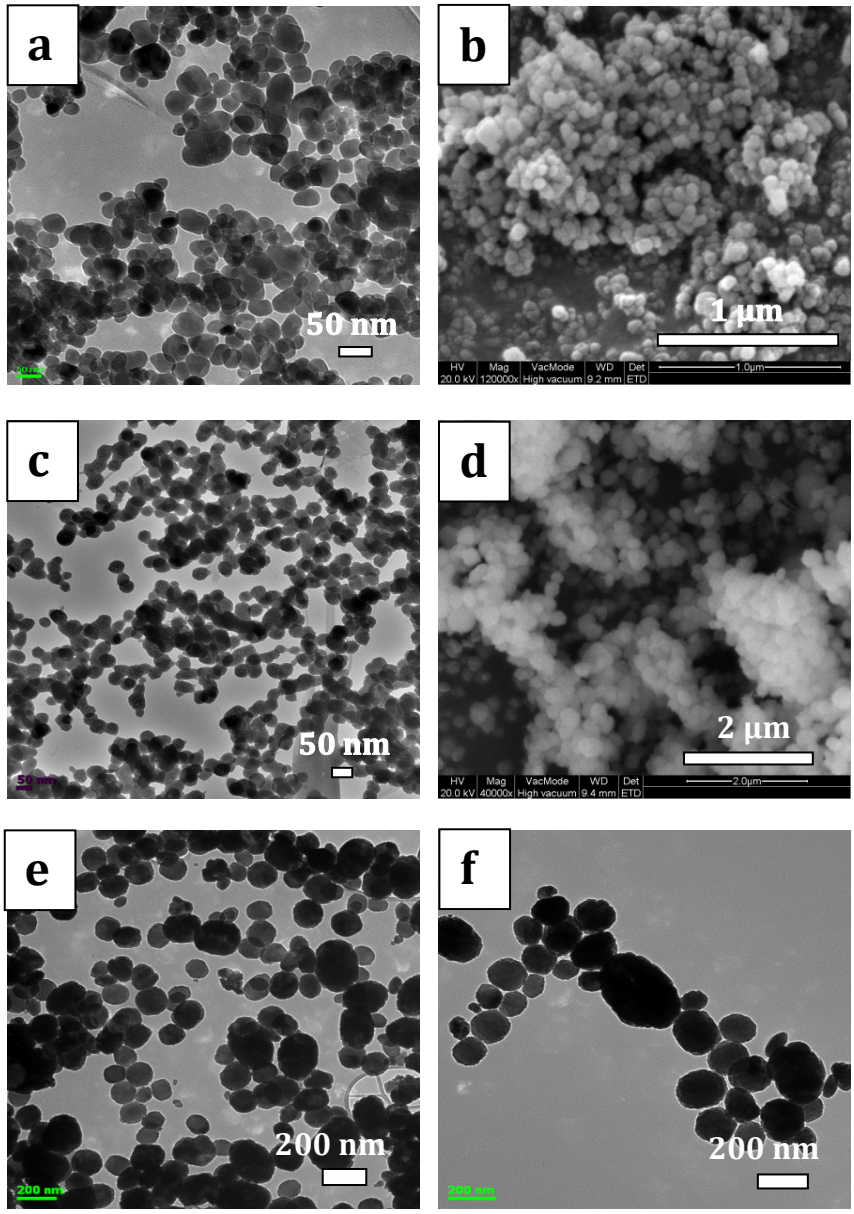

Figure 4.3: TEM and SEM images of $LaOHCO_3$ particles synthesized from different starting products and in different reaction conditions: (a) and (b) A1, (c) A2, (d) A3, (e) and (f) A4.

4.3.2. Characterization of $La_2O(CO_3)_2 \cdot H_2O$ particles

Lanthanum oxycarbonate hydrate particles were fabricated from $La(OAc)_3 \cdot 2H_2O$, in a supersaturated aqueous solution, at both mild and hydrothermal conditions. Figure 4.4. shows the XRD patterns of samples **A5** and **A6**, prepared in mild and hydrothermal reaction conditions, respectively. Both of the samples were assigned to the standard XRD pattern of lanthanum oxycarbonate hydrate. In the DRIFTS spectrum there are no peaks originating from OH vibrations around 3600 cm^{-1}, which were clearly visible in the spectra of the hydroxycarbonates (see Figure 4.2. and Figure 4.5.). A peak around 3500 cm^{-1} is present and can be assigned to adsorbed water. The intense peaks in the 1500-1430 cm^{-1} region are attributed to the ν_3 mode of the carbonate CO_3^{2-} group. Bands around 1080 cm^{-1}, 850 cm^{-1}, 750 cm^{-1} can be distinguished in the spectrum. They are assigned to the ν_1, ν_2 and ν_4 modes of the carbonate ion. The bands at around 2500 cm^{-1} and 2130 cm^{-1} are also due to the vibrations of the CO_3^{2-} group. TEM and SEM images show that sub-spherical nanoparticles, with uniform shape, and an average size of 20-30 nm were obtained (Figure 4.6.). When the reaction is carried out at lower temperature, particles less regular in their size were formed. A similar behaviour had been witnessed for the $LaOHCO_3$ nanoparticles described in the previous sub-chapter.

4.3.3. Characterization of $Ce_2O(CO_3)_2 \cdot H_2O$ particles

Cerium oxycarbonate particles were fabricated from $Ce(OAc)_3 \cdot 2H_2O$ at both mild (**A7**) and hydrothermal (**A8**) conditions. Both products gave crystalline X-ray patterns, similar to those observed for orthorhombic $La_2O(CO_3)_2$, and which could be assigned to the characteristic peaks of orthorhombic cerium oxycarbonate (JCPDS 43-0604).[4] The XRD pattern for **A7** has been presented in Figure 4.4. It was observed

that cerium oxycarbonate particles were obtained when using 30 mmol, as well as 60 mmol of urea (unlike in the case of lanthanum where the amount of urea used in the reaction gave two different products – the hydroxycarbonate or oxycarbonate hydrate). Samples **A7** and **A8** showed similar peaks in the DRIFTS spectrum to those observed for **A5** and **A6**. SEM images showed that in both reaction conditions elongated spheroid particles had formed (Figure 4.6.b). It was observed that the reaction carried out at 85-90 °C (**A7**) gave best results. A larger part of the particles were of similar size and shape. The average diameter was around 100-200 nm and length about 500 nm. Some small particles, which had just started to grow could be distinguished as well. When applying hydrothermal conditions (**A8**) the particles increase drastically in their size and form agglomerated chunks (Figure 4.6.c).

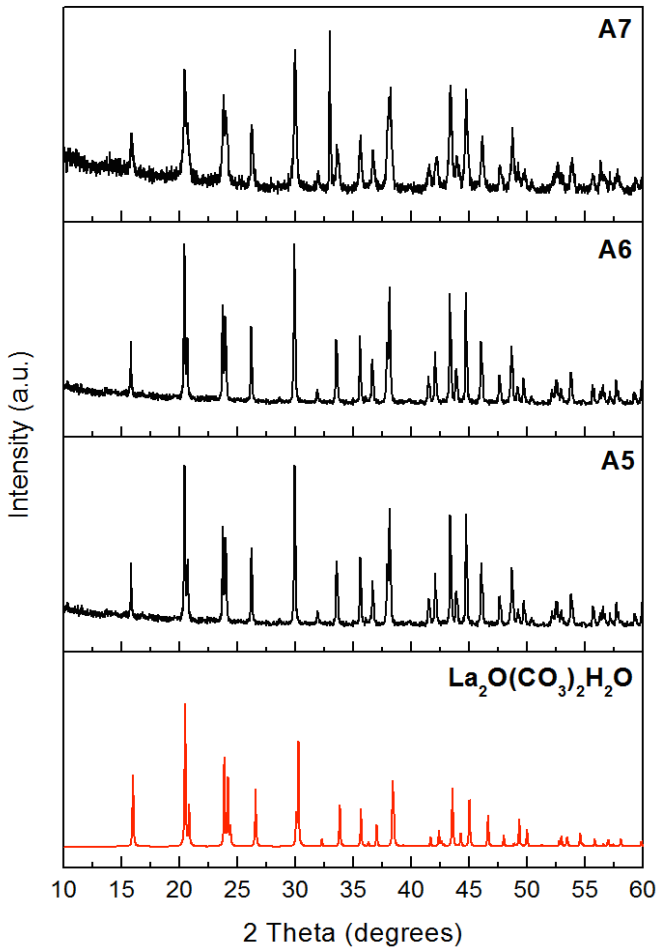

Figure 4.4: XRD patterns of samples A5, A6 and A7. Samples A5 and A6 could be matched to standard XRD pattern of the $La_2O(CO_3)_2 \cdot H_2O$ material. Sample A7 showed a similar XRD pattern and was assigned to the $Ce_2O(CO_3)_2 \cdot H_2O$ (no crystal structure of $Ce_2O(CO_3)_2 \cdot H_2O$ can be found in the ICSD database, therefore no standard pattern is shown).

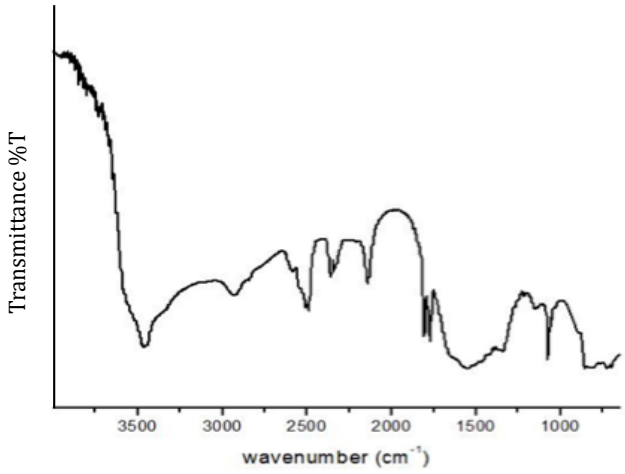

Figure 4.5: DRIFTS spectrum of sample A5, which represents the typical DRIFTS spectrum of $La_2O(CO_3)_2 \cdot H_2O$ samples.

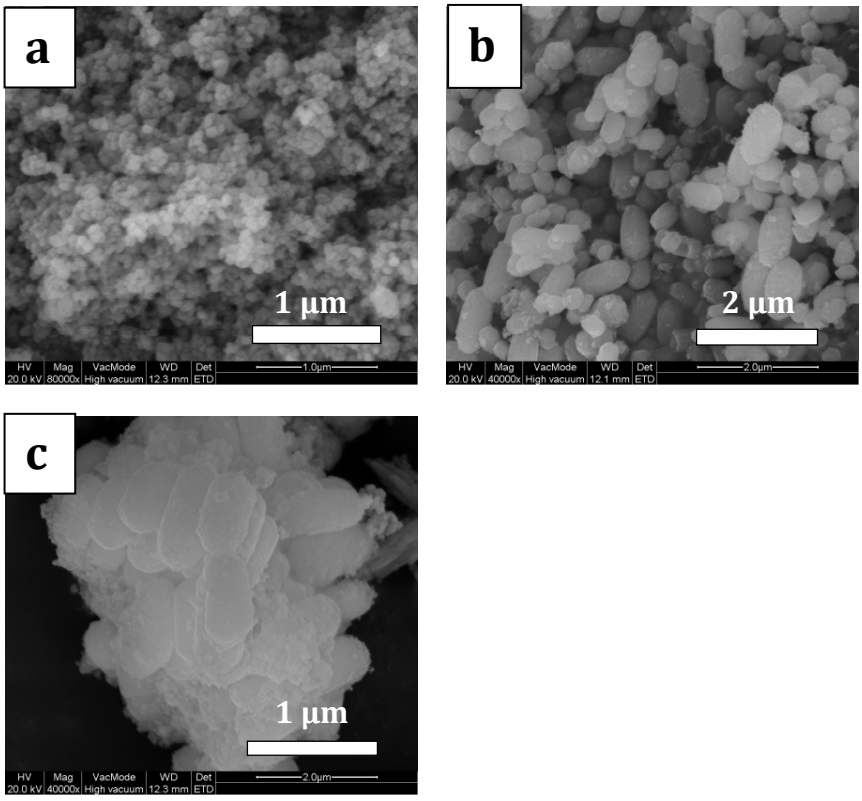

Figure 4.6: SEM images of (a) A6, (b) A7 and (c) A8.

4.3.4. Characterization of $La_2O(CO_3)_2 \cdot H_2O$ particles synthesized in the presence of glucose and fructose

For all the reactions carried out in the presence of glucose or fructose mild reaction conditions were applied and 6 mmol of the ligand were used. Using lower amounts of the ligand gave more agglomerated structures. Reactions were carried out in the presence of one of the ligands (glucose or fructose), urea and either $La(NO_3)_3 \cdot 5H_2O$ or $La(OAc)_3 \cdot 2H_2O$ giving rise to products **A9**, **A10**, **A11**, and **A12**. In all cases XRD (Figure 4.7.) and DRIFTS indicated that $La_2O(CO_3)_2 \cdot H_2O$ had formed. A reaction between $La(NO_3)_3 \cdot 5H_2O$ and urea, in the presence of glucose as stabilizing ligand, was

carried out giving product **A9**. SEM showed that a mixture of rectangular and hexagonal prisms around 1-2 μm long and 0.1-0.2 μm wide were formed in this reaction. The prisms showed a tendency to aggregate forming flower-like 3D structures (Figure 4.8.a,b). **A10** was obtained by substituting $La(NO_3)_3 \cdot 5H_2O$ with $La(OAc)_3 \cdot 2H_2O$, with all other reaction conditions unchanged. As can be seen from the SEM image (Figure 4.8.c) elongated spheroids, 50-200 nm in size, were formed. **A11** was formed when using fructose as organic ligand and $La(NO_3)_3 \cdot 5H_2O$ as lanthanide source. Microrods 0.5-2 μm in length and 0.1-0.2 μm wide were formed (Figure 4.8.d). Similarly to **A9** they had a tendency to aggregate into 3D architectures. When using fructose and $La(OAc)_3 \cdot 2H_2O$ as lanthanide source **A12** was produced. SEM showed that 3D microspheres around 4 μm in size, built from irregular nanoplates were formed (Figure 4.8.e,f).

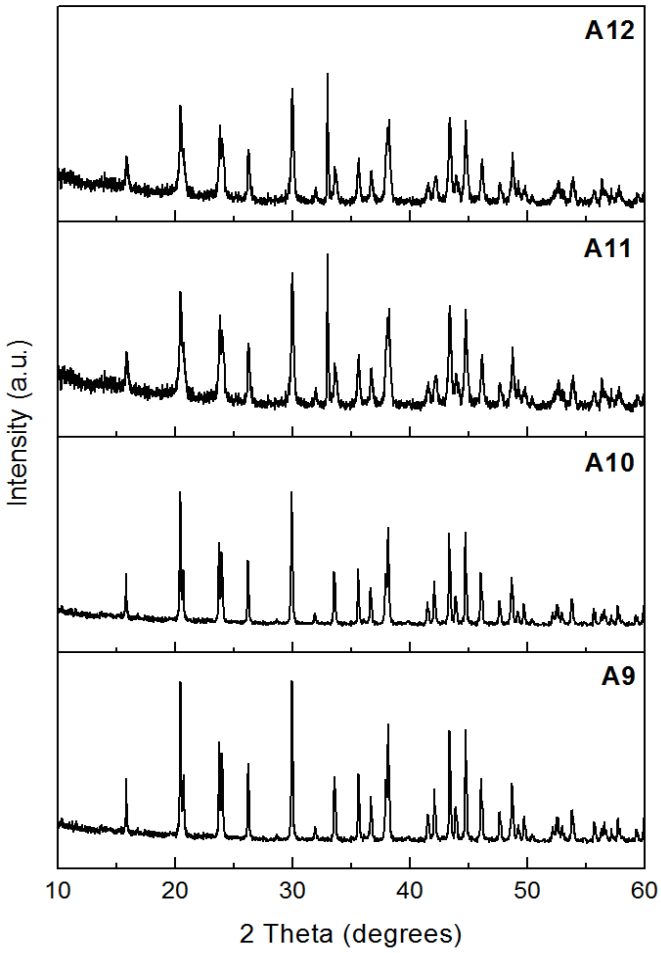

Figure 4.7: XRD pattern of samples A9, A10, A11 and A12.

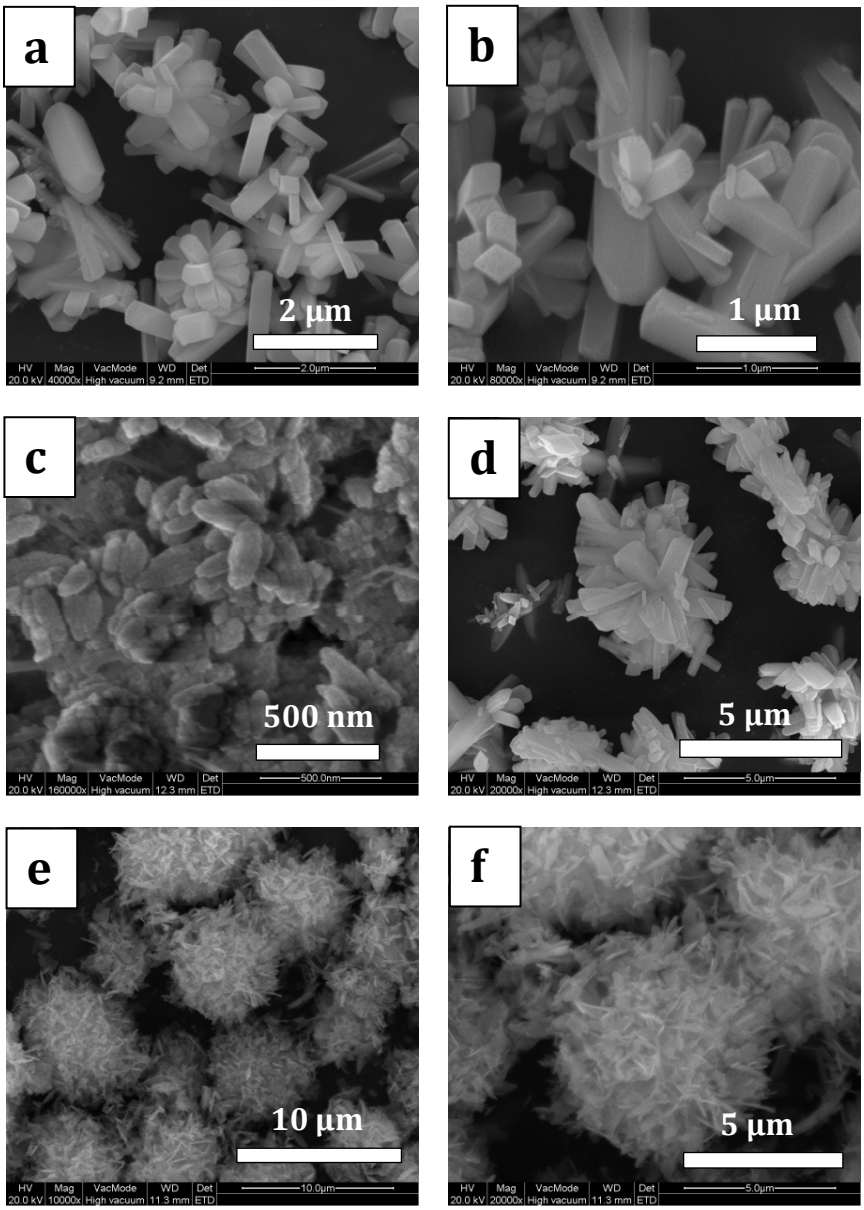

Figure 4.8: SEM images of (a) and (b) A9, (c) A10, (d) A11, (e) and (f) A12.

4.3.5. Characterization of $Ce_2O(CO_3)_2 \cdot H_2O$ particles synthesized in the presence of glucose and fructose

In the case of oxycarbonate hydrates synthesized without a stabilizing ligand a significant difference in the shape and size between lanthanum and cerium products could be witnessed. This was also true for oxycarbonate hydrate particles synthesized in the presence of glucose/fructose. A series of reactions similar to those described above, where two different sources of lanthanum were employed, were carried out using $Ce(NO_3)_3 \cdot 5H_2O$ or $Ce(OAc)_3 \cdot 2H_2O$ in the presence of glucose and fructose. In all cases XRD and DRIFTS infrared spectroscopy indicated that $Ce_2O(CO_3)_2$ had formed. In Figure 4.9. the XRD patterns of samples **A13**, **A14**, and **A15** have been presented. **A13** was produced in a reaction between $Ce(NO_3)_3 \cdot 5H_2O$ and urea in the presence of glucose. SEM showed that hexagonal prisms 0.5-2 μm in length and 0.5-1 μm wide were formed (see Figure 4.10.a). When using $Ce(OAc)_3 \cdot 2H_2O$ as cerium source, and with all other reaction conditions unchanged, elongated spheroids up to 500 nm long were produced (**A14**). They were very similar to particles **A7**. **A15** was formed when using fructose as organic ligand and $Ce(NO_3)_3 \cdot 5H_2O$ as cerium source. As can be seen from the SEM images stacks of nanodiscs, with a variety of sizes, were formed. **A16** was synthesized in the presence of fructose when using $Ce(OAc)_3 \cdot 2H_2O$ as the source of cerium giving rise to a mixture of irregular particles. The reaction was repeated several times, but no satisfying result, with particles of a uniform size and shape were obtained.

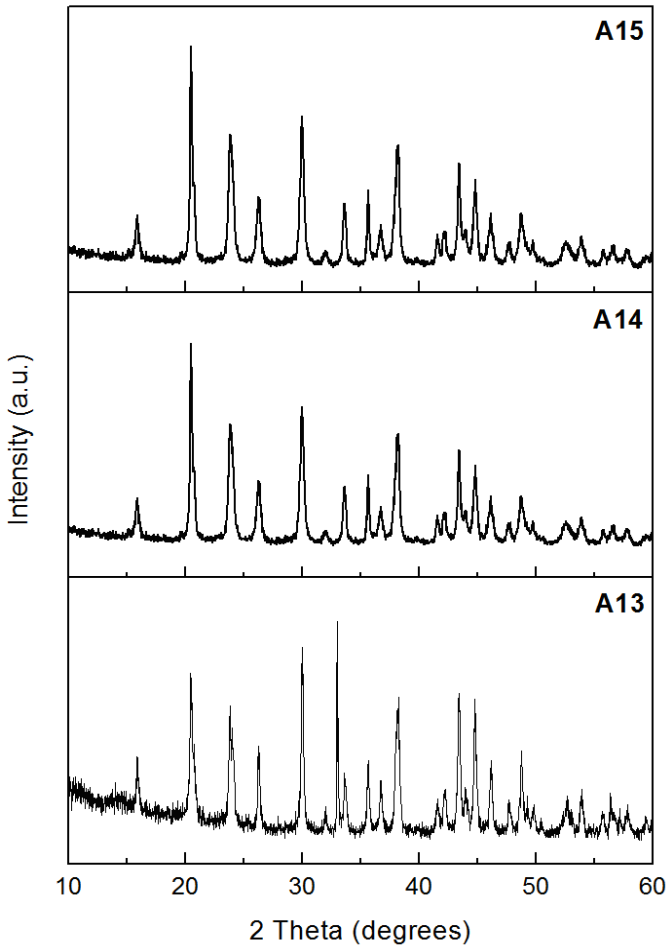

Figure 4.9: XRD patterns of samples and A13, A14 and A15.

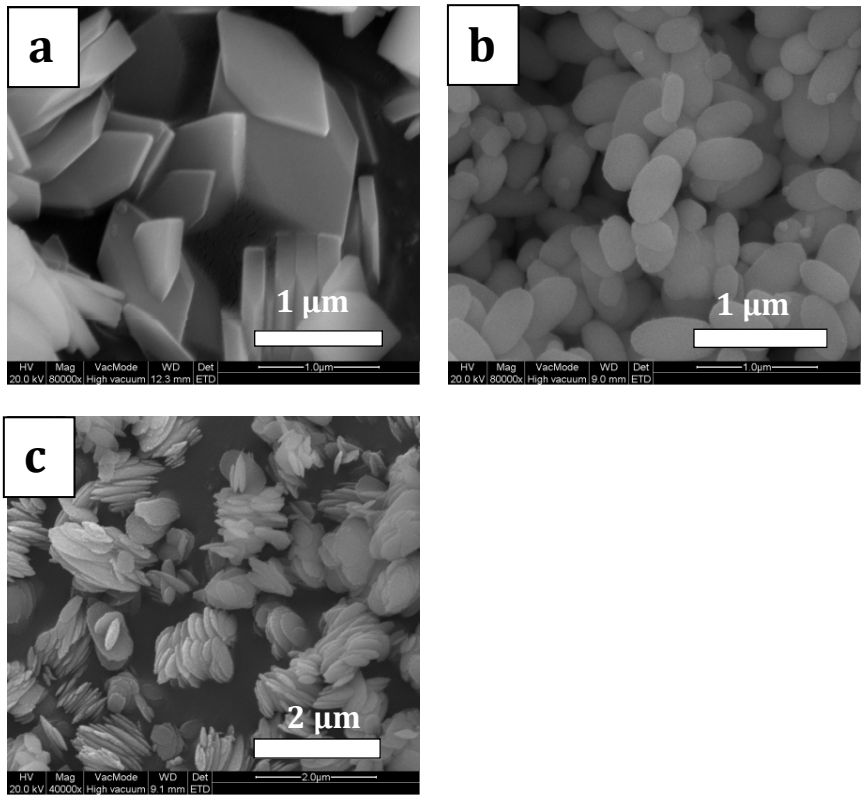

Figure 4.10: SEM images of (a) A13, (b) A14, and (c) A15.

4.3.6. Influence of the reaction conditions and organic ligands on the shape and size of the carbonate particles

On the basis of the above experimental results, it can be seen that the most important factors that affect the morphology of rare-earth carbonate materials are the lanthanide source, the molar ratio of urea to La^{3+}/Ce^{3+}, and the presence of an organic ligand. The temperature and time of a reaction were found to have a less significant impact on the morphology of the products. It was observed that most of the products were fully formed after 3 h and prolonging the reaction to 12 h or even up to 24 h gave no change in the morphology. Nanoparticles of hydroxycarbonate and

oxycarbonates hydrate prepared in the absence of a ligand at 90 °C were less uniform than nanoparticles prepared at 120 °C. However reactions at both temperatures gave particles of very similar shape and size. Therefore it can be established that in the formation of carbonate particles the time and temperature of the reaction have an impact on the morphology, but these are not the most significant factors. The impact of the lanthanide source on the morphology could clearly be seen in the case of glucose stabilized oxycarbonates. For example glucose stabilized $La_2O(CO_3)_2 \cdot H_2O$ synthesized from $La(NO_3)_3 \cdot 5H_2O$ gave a mixture of rectangular and hexagonal prisms 1-2 μm long (**A9**). Glucose stabilized $La_2O(CO_3)_2 \cdot H_2O$ synthesized from $La(OAc)_3 \cdot 2H_2O$ yielded elongated spheroids 50-200 nm in length (**A10**). It can clearly be stated that by changing the source of the lanthanide ion we can tune the size and shape of the carbonate products. The impact of glucose and fructose on the morphology of carbonate particles was investigated in this work. Ligands are commonly used to regulate the size and shape of inorganic crystals. They are known to form a complex with the metal ions and due to this they slow down the nucleation and growth of the crystals. Additionally their functional groups bind on the surface of the material and affect the growth rate of certain crystal facets. In the described experiments, the addition of glucose or fructose to the reaction solution obviously influences the morphology of the as-obtained $La_2O(CO_3)_2 \cdot H_2O$ and $Ce_2O(CO_3)_2 \cdot H_2O$ microcrystals. For example in the absence of a ligand sub-spherical $La_2O(CO_3)_2 \cdot H_2O$ nanoparticles 20 – 30 nm in size were obtained (**A6**). Elongated spheroids 50 – 200 nm in size where obtained when 6 mmol glucose was added to the reaction solution, and all other reaction conditions remained unchanged (**A10**).

4.3.7. Luminescence properties

In this part of the research it was investigated whether lanthanum/cerium hydroxycarbonate and oxycarbonates hydrates were good host lattices for the luminescence of rare-earth ions. Eu^{3+} and Tb^{3+} doped $LaOHCO_3$ and $La_2O(CO_3)_2 \cdot H_2O$ particles were prepared and their emission, excitation, luminescence lifetimes and quantum yields (QYs) were measured. A 5% doping of Eu^{3+} or Tb^{3+} was chosen for all samples. This was based on the experiments performed for **A1** which was doped with 2%, 5%, 10% and 15% Eu^{3+} or Tb^{3+}. At first the luminescent intensity of Eu^{3+} and Tb^{3+} doped nanoparticles increased with increase in the dopant concentration and then it decreased. When the dopant concentration increased above a certain level (over 5%), self-quenching started to occur, resulting in lower emission intensities. For both Eu^{3+} and Tb^{3+} 5% doping showed the highest intensities of luminescence and longest $^5D_0$ and $^5D_4$ luminescence lifetimes, consequently 5% doped materials were prepared throughout this work.

Table 4.2. $^5D_0$ luminescence lifetime values of Eu^{3+} doped A1.

Sample	Lifetime [ms]
2% Eu	0.65
5% Eu	0.70
10% Eu	0.60
15% Eu	0.60

Table 4.3. $^5D_4$ luminescence lifetime values of Tb^{3+} doped A1.

Sample	Lifetime [ms]
2% Tb	1.40
5% Tb	1.95
10% Tb	1.80
15% Tb	1.75

4.3.7.1. Luminescence properties of 5% Eu^{3+} and Tb^{3+} doped $LaOHCO_3$ **(A1)**

The room temperature combined emission and excitation spectrum of **5% Eu^{3+} doped A1** has been presented in Figure 4.11. All of the peaks have been assigned to the appropriate electronic transitions in Table 4.4.[5] The excitation spectrum of **5% Eu^{3+} doped A1** (observed at 617.0 nm) contains a strong and broad band from 250.0 – 300.0 nm with a maximum at 275.0 nm, and a series of sharp excitation peaks. The broad band corresponds to the ligand-to-metal charge-transfer (CT) band. The sharp peaks can be assigned to the characteristic transitions of europium. The emission spectrum was obtained by exciting the sample at 395.0 nm, into the strongest transition peak ($^5L_6 \leftarrow ^7F_0$). The emission spectrum contains a series of sharp peaks, which can be assigned to the $^5D_0 \rightarrow ^7F_J$ (J = 1-4) transitions of europium. At 590.0 nm the $^5D_0 \rightarrow ^7F_1$ transition can be observed. The $^5D_0 \rightarrow ^7F_1$ transition peak splits into several peaks indicating low symmetry. It partially overlaps the $^5D_0 \rightarrow ^7F_0$ transition peak located at around 583.0 nm. At 617.0 nm the $^5D_0 \rightarrow ^7F_2$ transition is observed. The large intensity of this peak is also an indication of low symmetry. This transition is responsible for the red emission color of the **5% Eu^{3+} doped A1** sample. Principally transitions between 4f states in trivalent rare-earth ions are not affected by their environment owing to the shielding provided by the outer lying 5s and 5p electrons.

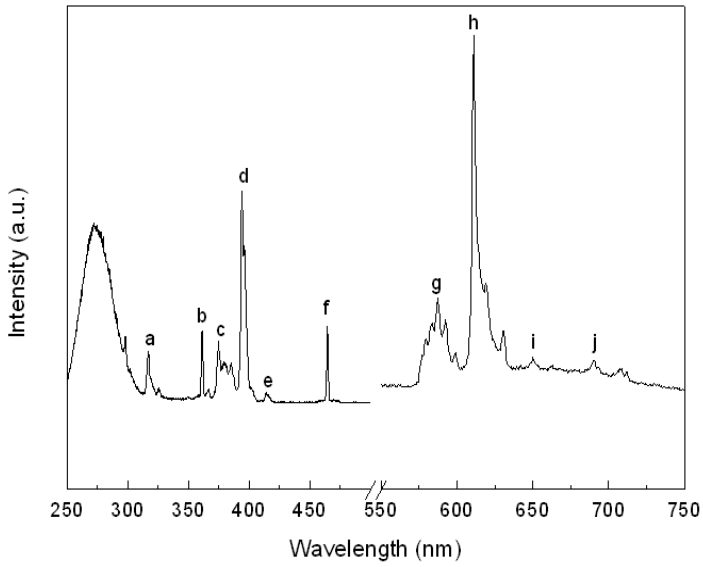

Figure 4.11: Excitation spectrum (monitored at 617.0 nm) and emission spectrum (excited at 395.0 nm) of 5% Eu doped A1 sample. The electronic transitions labeled a-j have been assigned in Table 4.4.

As the $^5D_0 \rightarrow {}^7F_2$ transition is known to be a hypersensitive transition, if europium resides in a center of symmetry, the intensity of this hypersensitive transition is small or absent.[6-8] As the site becomes more asymmetric the intensity of the $^5D_0 \rightarrow {}^7F_2$ transition peak increases. The $^5D_0 \rightarrow {}^7F_1$ transition is a magnetic dipole transition and therefore its intensity is not dependent of the Eu^{3+} environment and can be used as a reference point. The $(^5D_0 \rightarrow {}^7F_2)/(^5D_0 \rightarrow {}^7F_1)$ luminescence intensity ratio is commonly referred to as the hypersensitivity ratio and is used as a measure of the symmetry of the coordination sphere. The integrated area under each transition peak was determined using the trapezoidal rule. The value of the hypersensitive ratio – 2.86

indicates that the europium ions are located in an asymmetrical environment. The luminescence lifetime of **5% Eu^{3+} doped A1** was measured as 0.7 ms. This is a similar value to the luminescence lifetime previously reported for Eu^{3+} doped $GdOHCO_3$ nanoparticles.[1] The quantum yield of the sample was determined to be 12%. The CIE color coordinates of **5% Eu^{3+} doped A1** were calculated to be x = 0.62 and y = 0.37. The sample emitted a red color (see Figure 4.12 and Figure 4.16).

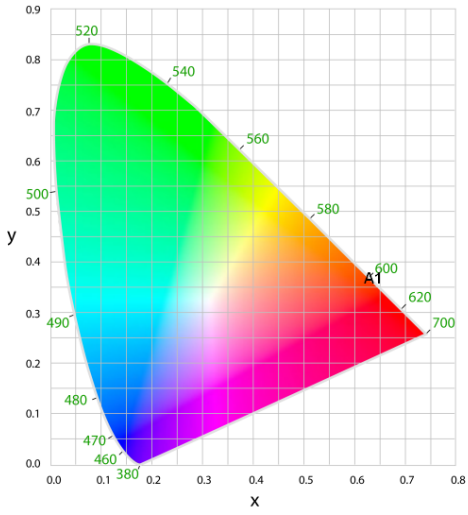

Figure 4.12: CIE chromaticity diagram presenting the color emitted by sample 5% Eu doped A1 (x = 0.62, y = 0.37).

Next, to study the stability of the **A1** particles in water the particles were dispersed in water to form a stable suspension. As can be noticed from Figure 4.13. the shape of the emission spectrum of the **5% Eu doped A1** colloidal suspension is very comparable to the shape of the emission spectrum of the **5% Eu doped A1** powder sample. The emission spectrum of the colloidal suspension is around 25% less intense than the emission spectrum of the powder. Also the luminescence lifetime of the colloidal suspension dropped to 655 µs (compared to 700 µs for the powder

sample). These observations prove that the **A1** particles are stable against chemical degradation in water. The colloidal suspension of the particles also emitted red luminescence under a laboratory UV lamp, at 365.0 nm excitation.

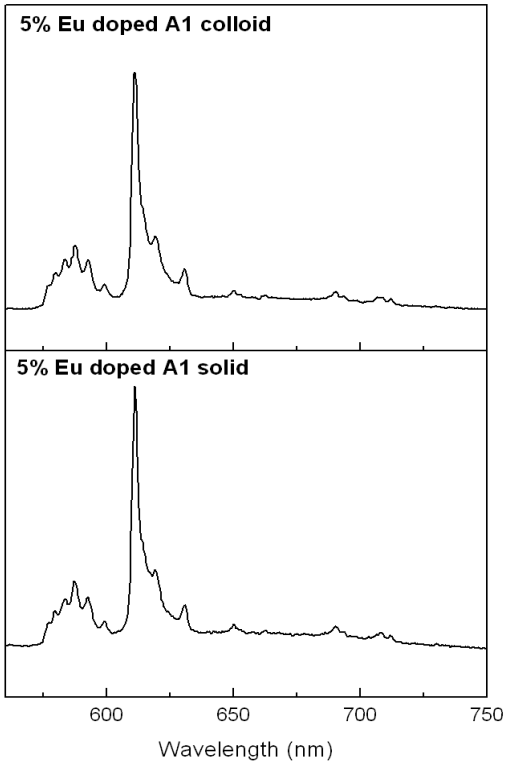

Figure 4.13: Emission spectra of 5% Eu doped A1 under 395.0 nm excitation for top: colloidal suspension, bottom: dried powder.

Figure 4.14. shows the room temperature combined emission and excitation spectrum of **5% Tb^{3+} doped A1**. The excitation spectrum (collected at 541.0 nm) contains a series of sharp excitation peaks. When the sample was excited at 351.0 nm, into the $^5L_9 \leftarrow {}^7F_6$ transition, the characteristic transition peaks of terbium ($^5D_4 \rightarrow {}^7F_J$, where J =

6-3) could be found in the spectrum. These peaks can be assigned to the following transitions of terbium in Table 4.4.[9-10] Also in this case the shape of the emission spectra of the powder and of the colloidal suspension is similar. For **5% Tb doped A1** sample luminescence lifetimes of 1605 μs (colloidal suspension) and 1750 μs (powder sample) were collected. A quantum yield of 7.5% was determined for the powder sample. The powder and the colloidal suspension of the particles both emitted green luminescence under a laboratory UV lamp (at 365.0 nm excitation). The $^5D_4 \rightarrow {}^7F_5$ transition is responsible for the green emission color (see Figure 4.15. and Figure 4.16).

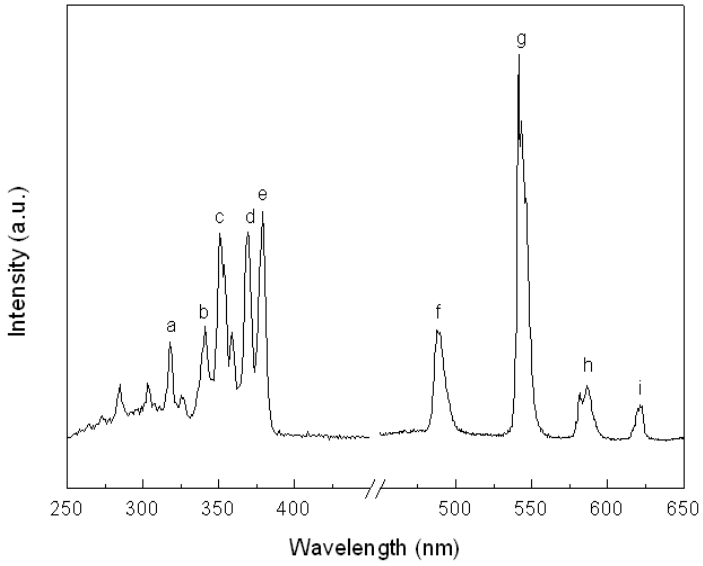

Figure 4.14: Excitation spectrum (monitored at 541.0 nm) and emission spectrum (excited at 351.0 nm) of 5% Tb doped A1 sample. The electronic transitions labeled a-i have been assigned in Table 4.4.

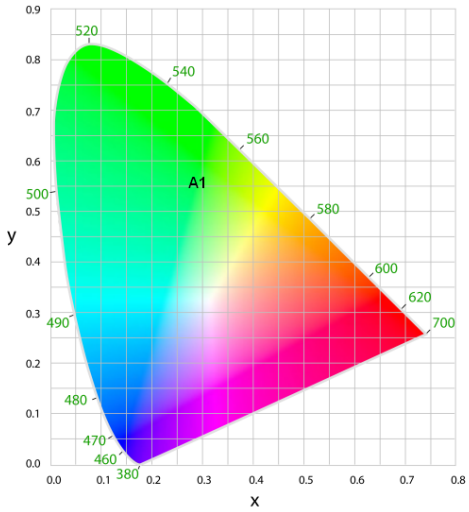

Figure 4.15: CIE chromaticity diagram presenting the color emitted by sample 5% Tb doped A1 (x = 0.29, y = 0.56).

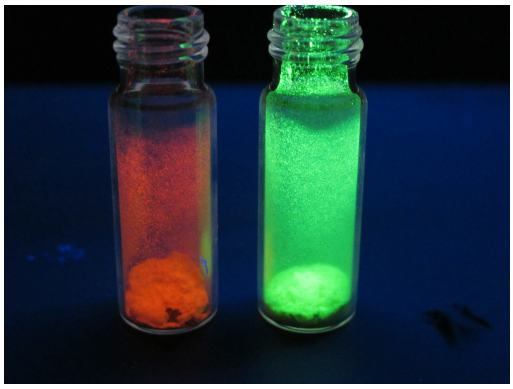

Figure 4.16: Photo of 5% Eu doped A1 (left) and 5% Tb doped A1 (right) powder samples taken when the samples was placed under a laboratory UV lamp (at a 365.0 nm excitation wavelength).

Table 4.4. Assignment of labeled transitions shown in Figures 4.11. and 4.14.

	Excitation					Emission		
	Wavelength (nm)	Energy (cm^{-1})	Transition			Wavelength (nm)	Energy (cm^{-1})	Transition
			5% Eu doped A1					
a	317.0	31546	$^5H_7$	$\leftarrow {}^7F_0$	**g**	590.0	16949	$^5D_0 \rightarrow {}^7F_1$
b	363.0	27548	$^5D_4$	$\leftarrow {}^7F_0$	**h**	617.0	16207	$^7F_2$
c	383.0	26110	$^5G_6$, $^5G_5$	$\leftarrow {}^7F_1$	**i**	652.0	15337	$^7F_3$
d	395.0	25316	$^5L_6$	$\leftarrow {}^7F_0$	**j**	690.0	14493	$^7F_4$
e	417.0	23981	$^5D_3$	$\leftarrow {}^7F_1$				
f	460.0	21739	$^5D_2$	$\leftarrow {}^7F_0$				
			5% Tb doped A1					
a	318.0	31447	$^5H_7$	$\leftarrow {}^7F_6$	**f**	488.0	20492	$^5D_4 \rightarrow {}^7F_6$
b	341.0	29325	$^5G_2$, $^5G_3$, $^5L_6$, $^5L_{7,8}$		**g**	541.0	18484	$^7F_5$
c	351.0	28490	$^5L_9$		**h**	586.0	17065	$^7F_4$
d	369.0	27100	$^5L_{10}$		**i**	622.0	16077	$^7F_3$
e	379.0	26385	$^5G_6$, $^5D_3$					

4.3.7.2. Luminescence properties of 5% Eu^{3+} and Tb^{3+} doped $La_2O(CO_3)_2 \cdot H_2O$ (**A6)**

Figure 4.17. presents the room temperature combined excitation and emission spectrum of **5% Eu doped A6**. The excitation spectrum, observed at an emission wavelength of 611.0 nm, consists of a strong and broad band from 250 – 300 nm, and a series of sharp excitation peaks is present. All of these sharp peaks have been assigned to Eu^{3+} transitions in Table 4.5. The strong CT excitation band indicates a sufficient oxygen-metal charge-transfer process. Figure 4.17. also presents the photoluminescence emission spectra of **5% Eu doped A6,** when exited at 395.0 nm. Excitation at this wavelength yields the characteristic emissions of europium (the peaks have been assigned to the appropriate transitions in Table 4.5.).

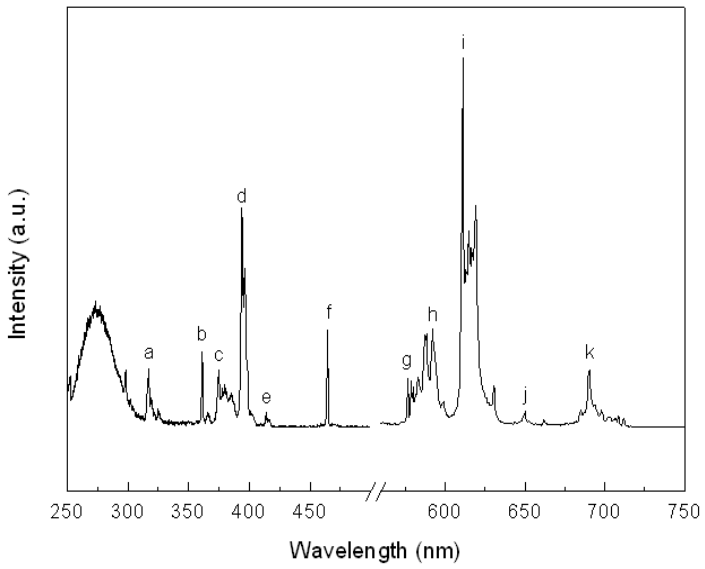

Figure 4.17: Excitation spectrum (monitored at 611.0 nm) and emission spectrum (excited at 395.0 nm) of 5% Eu doped A6 sample. The electronic transitions labeled a-k have been assigned in Table 4.5.

The emission peak at 576.0 nm corresponds to the $^5D_0 \rightarrow {}^7F_0$ transition. Similarly to the **5% Eu doped A1** emission spectrum it is observed that the $^5D_0 \rightarrow {}^7F_0$ transition peak partly overlaps with the 592.0 nm $^5D_0 \rightarrow {}^7F_1$ transition peak. The $^5D_0 \rightarrow {}^7F_1$ transition peak splits into more than three peaks indicating low symmetry and more than one crystallographic site. At 611.0 nm the $^5D_0 \rightarrow {}^7F_2$ transition is observed. Using the trapezoidal rule the $(^5D_0 \rightarrow {}^7F_2)/(^5D_0 \rightarrow {}^7F_1)$ ratio was calculated as 3.07 (calculated for the powder sample). This is an indication that the Eu^{3+} ions are located in an asymmetric environment. The **5% Eu doped A6** showed luminescence lifetimes of 705 µs for the powder sample and 655 µs for the colloidal suspension of these particles in water. Comparing this with the results obtained for the $LaOHCO_3$ matrix (**A1**) one can see that there is no significant difference in the decay times. Also in this case the shape of the emission spectrum of the powder sample is very comparable to the shape of the emission spectrum of the colloidal suspension (Figure 4.19.) Only a difference in intensity was observed,

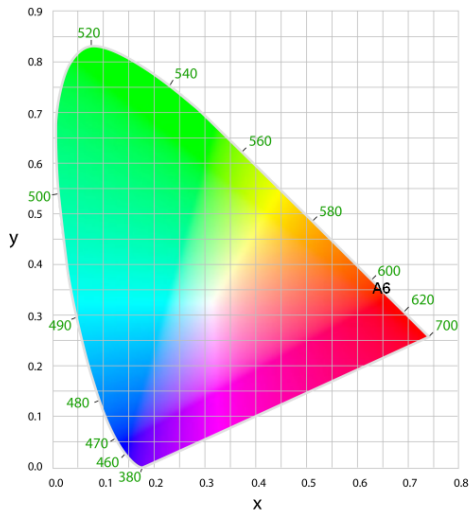

Figure 4.18: CIE chromaticity diagram of 5% Eu doped A6 (x = 0.64, y = 0.36).

Both the powder and the colloidal suspension of the particles emitted red luminescence under a hand-held laboratory UV lamp (Figure 4.22.). **5% Eu doped A6** showed a quantum yield of 6%, which was lower than that detected for **5% Eu doped A1** (QY = 12%). The CIE coordinates for sample **5% Eu doped A6** were calculated to be x = 0.64 and y = 0.36. (Figure 4.18.).

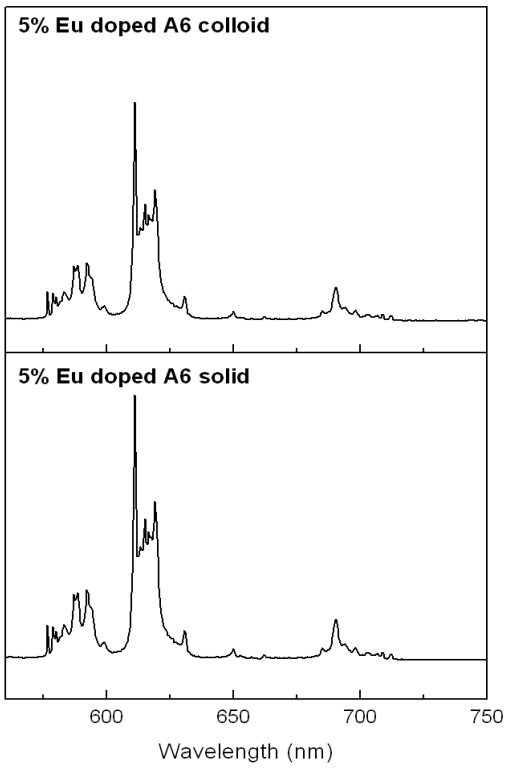

Figure 4.19: Emission spectra of 5% Eu doped A6 under 395.0 nm excitation for top: colloidal suspension, bottom: dried powder.

Figure 4.20. presents the room temperature combined excitation and emission spectrum of **5% Tb doped A6**. The excitation spectrum of **5% Tb doped A6**

(observed at 542.0 nm) contains a series of sharp excitation peaks. These peaks can be assigned to known terbium transitions (Table 4.5.). The emission spectrum (when the sample was excited at 351.0 nm) consists of four sharp emission peaks. The most intense peak at 540.0 nm corresponds to the $^5D_4 \rightarrow {}^7F_5$ transition. All of the peaks have been assigned to terbium transitions in Table 5.4. The powder sample showed a decay time of 1930 μs, whereas the colloidal suspension showed a decay time of 1605 μs. The measured luminescence lifetime of **5% Tb doped A6** (for powder sample) was slightly higher than that obtained for **5% Tb doped A1**. However in the colloidal suspension this difference was almost unnoticeable. It was observed that the shape of the emission spectrum of the powder sample and the shape of the emission spectrum of the colloidal suspension are comparable.

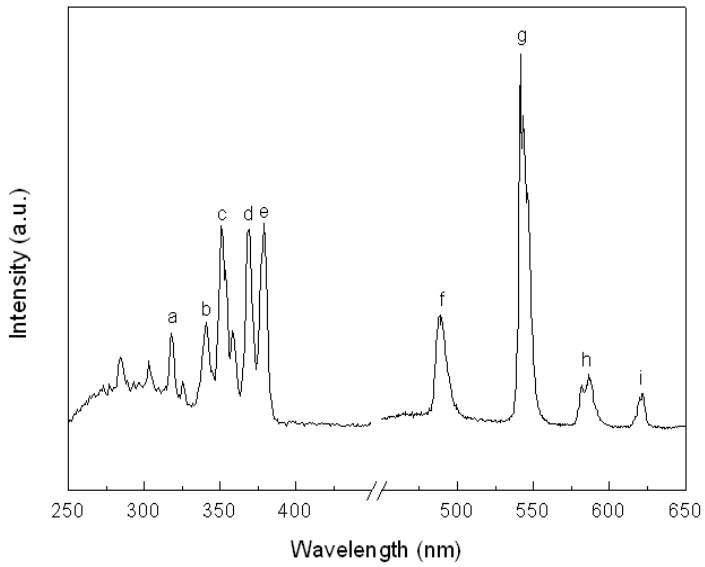

Figure 4.20: Excitation spectrum (monitored at 542.0 nm) and emission spectrum (excited at 351.0 nm) of 5% Tb doped A6 sample. The electronic transitions labeled a-i have been assigned in Table 4.5.

Both the powder and the colloidal suspension of **5% Tb doped A6** emit green luminescence under a UV lamp at an excitation wavelength of 365.0 nm (Figure 22.). A quantum yield of 5% was measured for the **5% Tb doped A6** powder sample. This is also lower than that recorded for **5% Tb doped A1** (QY = 7.5%). The CIE coordinates for **5% Tb doped A6** were calculated as x = 0.29 and y = 0.55. (Figure 4.21.).

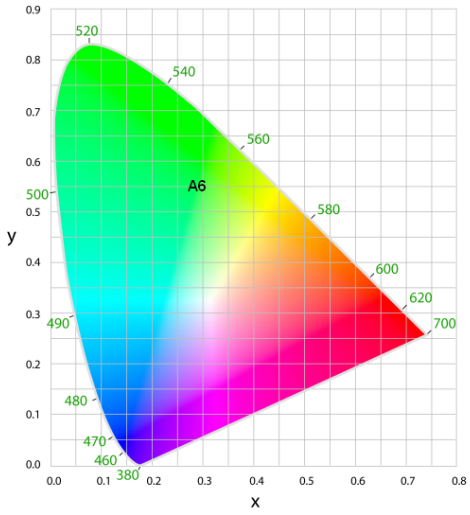

Figure 4.21: CIE chromaticity diagram of 5% Tb doped A6 (x = 0.29, y = 0.55).

Figure 4.22: Photo of 5% Eu doped A6 (front) and 5% Tb doped A6 (back) taken when the samples were placed under a laboratory UV lamp (at a 365.0 nm excitation wavelength).

Table 4.5. Assignment of labeled transitions shown in Figures 4.17. and 4.20.

	Excitation					Emission			
	Wavelength (nm)	Energy (cm^{-1})	Transition			Wavelength (nm)	Energy (cm^{-1})	Transition	
				5% Eu doped A6					
a	317.0	31546	$^5H_7$	$\leftarrow {}^7F_0$	**g**	576.0	17361	$^5D_0 \rightarrow$	$^7F_0$
b	361.0	27701	$^5D_4$	$\leftarrow {}^7F_0$	**h**	592.0	16892		$^7F_1$
c	37.0	26738	$^5G_6$, $^5G_5$	$\leftarrow {}^7F_1$	**i**	611.0	16367		$^7F_2$
d	395.0	25316	$^5L_6$	$\leftarrow {}^7F_0$	**j**	651.0	15361		$^7F_3$
e	415.0	24096	$^5D_3$	$\leftarrow {}^7F_1$	**k**	690.0	14493		$^7F_4$
f	464.0	21552	$^5D_2$	$\leftarrow {}^7F_0$					
				5% Tb doped A6					
a	318.0	31447	$^5H_7$	$\leftarrow {}^7F_6$	**f**	489.0	20450	$^5D_4 \rightarrow$	$^7F_6$
b	341.0	29325	$^5G_2$, $^5G_3$, $^5L_6$, $^5L_{7,8}$		**g**	541.0	18484		$^7F_5$
c	351.0	28490	$^5L_9$		**h**	586.0	17065		$^7F_4$
d	369.0	27100	$^5L_{10}$		**i**	622.0	16077		$^7F_3$
e	380.0	26316	$^5G_6$, $^5D_3$						

4.3.7.3. Luminescence properties of $Ce_2O(CO_3)_2 \cdot H_2O$ and Tb^{3+} doped $Ce_2O(CO_3)_2 \cdot H_2O$ (**A7)**

Figure 4.23. shows the room temperature emission spectra, in a powder and colloidal suspension form, of $Ce_2O(CO_3)_2$ particles obtained in a mild temperature reaction between $Ce(OAc)_3 \cdot 2H_2O$ and urea (**A7**). When the sample was excited at 292.0 nm (the excitation maximum) the maximum emission occurs at 370.0 nm (for the powder sample). For the colloidal suspension of **A7** in water the emission maximum shifted to 400 nm (see Figure 4.25.), which is due to the 5d-4f transitions of Ce^{3+} between the ^2D ($5d^1$) ground state and the $^2F_{5/2}$ ($4f^1$) state.[10-11]

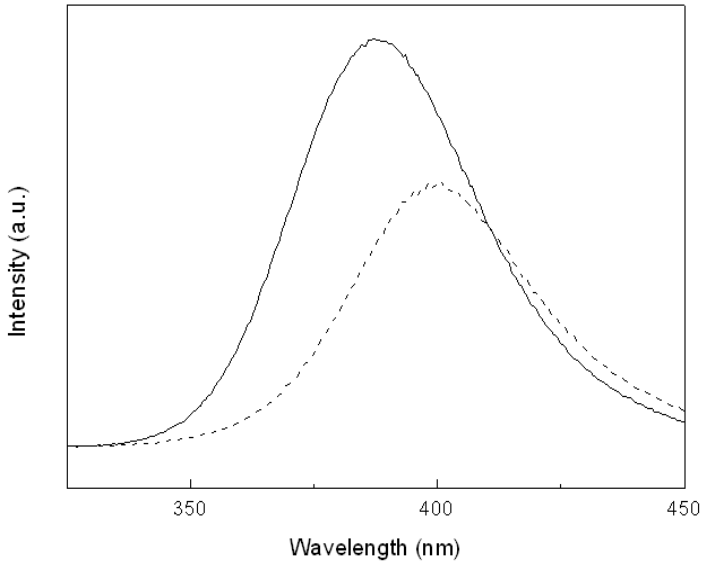

Figure 4.23: Emission spectra of $Ce_2O(CO_3)_2 \cdot H_2O$ powder sample (solid line) and of $Ce_2O(CO_3)_2 \cdot H_2O$ colloidal suspension (dashed line). Both spectra were recorded when excited at 292.0 nm.

The spectroscopy of Ce^{3+} is quite different from that of other trivalent lanthanide compounds. It has been observed that the emission spectrum can be shifted to longer wavelengths depending on the environment of the Ce^{3+} ion. This has been indicated to be a consequence of the interaction with cerium 5d orbitals.

Additionally the luminescence properties of **5% Tb doped A7** were investigated. The room temperature combined emission and excitation spectrum of **5% Tb doped A7** is presented in Figure 4.24.

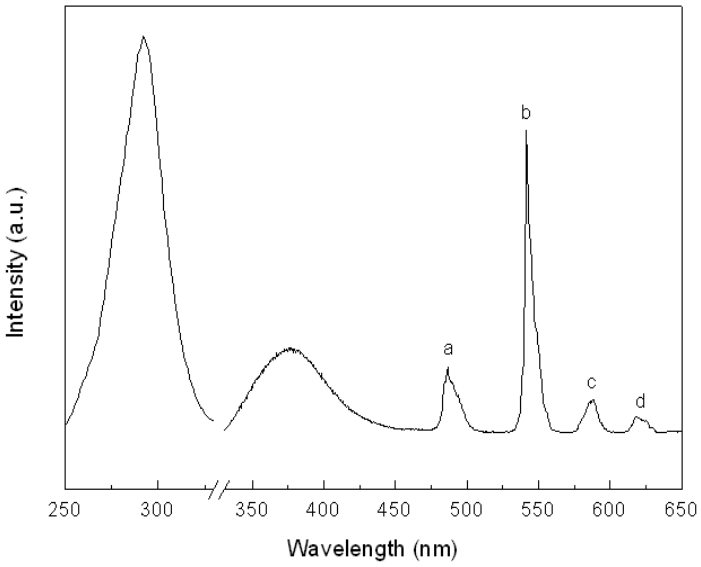

Figure 4.24: Excitation spectrum (monitored at 542.0 nm) and emission spectrum (excited at 292.0 nm) of 5% Tb doped A7 sample. Peaks labeled a-d have been assigned to the corresponding transitions in Table 4.6.

The emission spectrum shows narrow emission peaks resulting from the 4f-4f transitions within the terbium ions, with the most intensive peak at 542.0 nm corresponding to the $^5D_4 \rightarrow {}^7F_5$ transition. The terbium peaks have been assigned to the appropriate transitions in Table 4.6. Owing to the high concentration of Ce^{3+} in the particles (95%), the excited state of Ce^{3+} is not completely quenched by energy transfer to Tb^{3+} and therefore its emission can be seen as a broad band with a maximum around 375.0 nm (for powder sample). Here again we observed a shift of the cerium emission band towards longer wavelengths when performing measurements on the colloidal suspension of the particles (Figure 4.25).

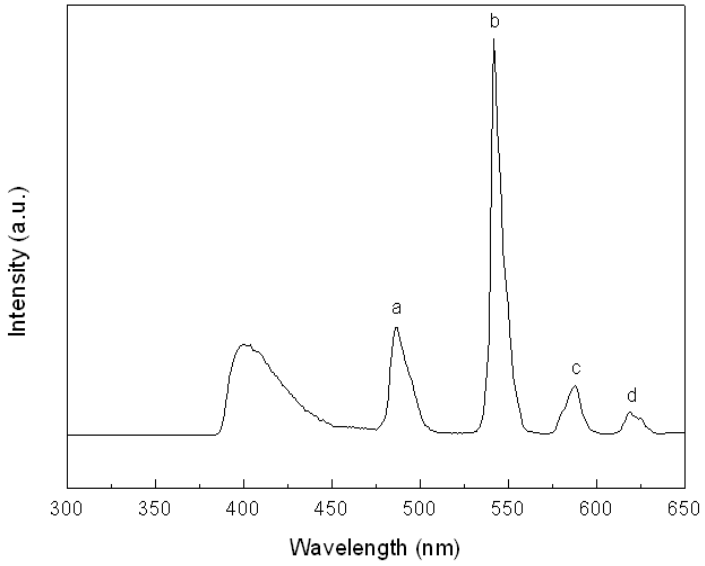

Figure 4.25: Emission spectrum of 5% Tb doped A7 in colloidal suspension (excited at 292.0 nm). Peaks labeled a-d have been assigned to the corresponding transitions in Table 4.6.

Apart from this shift the shape of the emission spectrum of the powder sample and the shape of the emission spectrum of the colloidal suspension are very similar. Luminescence lifetimes of 1405 μs and 1045 μs were recorded for the powder sample and colloidal suspension of **5% Tb doped A7**, respectively. Measurements showed a low quantum yield of around 1% for the **5% Tb doped A7** sample.

Table 4.6. Assignment of labeled transitions shown in Figures 4.26. and 4.27.

	Emission			
	Wavelength (nm)	Energy (cm^{-1})	Transition	
5% Tb doped A7 powder				
a	486.0	20576	$^5D_4 \rightarrow$	$^7F_6$
b	542.0	18450		$^7F_5$
c	588.0	17007		$^7F_4$
d	619.0	16155		$^7F_3$
5% Tb doped A7 colloidal suspension				
a	487.0	20534	$^5D_4 \rightarrow$	$^7F_6$
b	542.0	18450		$^7F_5$
c	588.0	17007		$^7F_4$
d	618.0	16181		$^7F_3$

The energy transfer process between cerium (sensitizer) and terbium (acceptor) can be explained in a simple way. First, Ce^{3+} ions are excited by UV irradiation, then energy transfer takes place from the $^5D_{3/2}$ ($5d^1$) state of Ce^{3+} to the acceptor energy states of Tb^{3+}, which decay nonradiatively to the $^5D_4$ state followed by radiative decay

to lower levels of ^7F_J (J=0-6).[12] The energy transfer process between cerium and terbium is schematically presented in Figure 4.26.

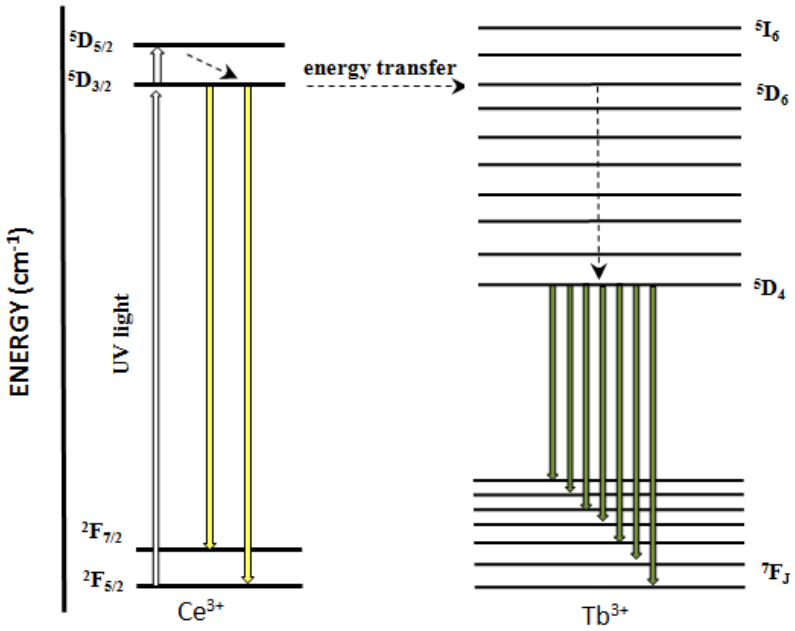

Figure 4.26: Scheme representing the energy transfer process between Ce^{3+} and Tb^{3+} in the 5% Tb doped A7 material.

4.3.7.4. Luminescence properties of 5% Tb^{3+} doped $La_2O(CO_3)_2{\cdot}H_2O$ synthesized in the presence of glucose (**A10)**

In order to investigate the luminescence properties of a Ln^{3+} doped $La_2O(CO_3)_2{\cdot}H_2O$ material synthesized in the presence of an organic ligand (glucose) the steady state luminescence properties, decay time, and quantum yield of **5% Tb doped A10** was studied. When excited at a wavelength of 351.0 nm the shape of the emission spectrum of the powder sample is very comparable to the shape of the emission spectrum of the colloidal suspension (Figure 4.27.). In both of the spectra

characteristic emission peaks of terbium can be detected. The most intense peak at around 540.0 nm corresponds to the $^5D_4 \rightarrow {}^7F_5$ transition. Three other peaks are observed: at around 490.0 nm ($^5D_4 \rightarrow {}^7F_6$), 580.0 nm ($^5D_4 \rightarrow {}^7F_4$), and 620.0 nm ($^5D_4 \rightarrow {}^7F_3$). Decay times of 1300 μs and 1200 μs were obtained for the powder sample and colloidal suspension, respectively. These lifetime values are significantly shorter than those measured for 5% Tb doped $La_2O(CO_3)_2 \cdot H_2O$ synthesized in the absence of glucose (**5% Tb doped A6**). In the **5% Tb doped A10** particles the photoluminescence of Tb^{3+} is most likely partially quenched by glucose, which is on the surface of the particles. Both the **5% Tb doped A10** powder sample and its colloidal suspension in water emitted visible green light, when held under a laboratory UV lamp (365.0 nm excitation). A decrease in the quantum yield was observed for the glucose-stabilized sample (QY = 2%).

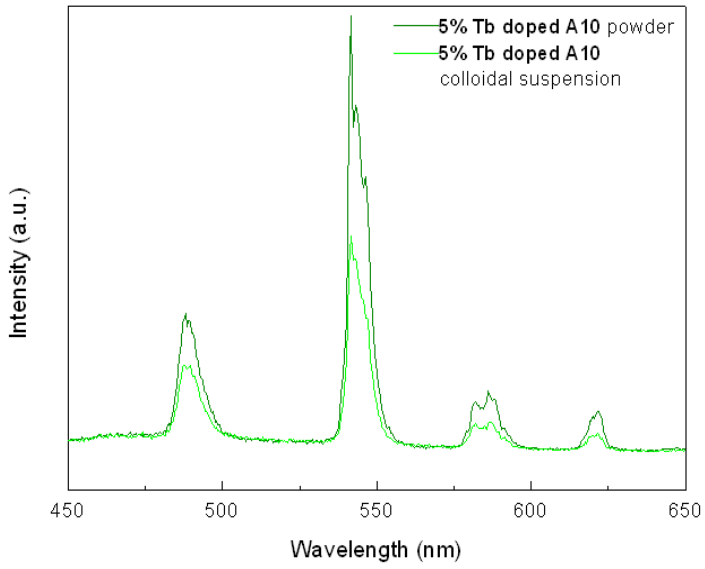

Figure 4.27: Emission spectra of 5% Tb doped A10 in powder and colloidal suspension form (excited at 351.0 nm).

4.3.7.5. Comparison between the luminescence properties of different rare-earth carbonate particles

Table 4.7. Luminescence lifetimes and quantum yield values of Eu^{3+} and Tb^{3+} doped rare-earth carbonate samples.

Product		Lifetime [ms]	Quantum yield[a] (%)
5% Eu doped A1	solid	0.70	12
	suspension	0.65	-
5% Eu doped A6	solid	0.70	6
	suspension	0.65	-
5% Tb doped A1	solid	1.75	7.5
	suspension	1.60	-
5% Tb doped A6	solid	1.95	5
	suspension	1.60	-
5% Tb doped A7	solid	1.40	0.8/1[b]
	suspension	1.05	-
5% Tb doped A10	solid	1.30	2
	suspension	1.20	

[a] Errors on the QY measurements are estimated to be up to 10%

[b] QY determined through excitation into the d-f transition of Ce^{3+}, all remaining QYs were determined based on excitation into the f-f transitions.

The luminescence lifetime values and quantum yields of all the measured samples have been collected in Table 4.7. Based on the luminescence measurements performed for 5% Eu^{3+} and 5% Tb^{3+} doped rare-earth hydroxycarbonates and rare-earth oxycarbonate hydrates the following conclusions can be drawn:

1) Eu^{3+} and Tb^{3+} doped $LaOHCO_3$ particles have higher QYs compared to Eu^{3+} and Tb^{3+} doped $La_2O(CO_3)_2 \cdot H_2O$ particles. It appears that this change in QY is caused by the change of radiative lifetime in the two matrices, as the luminescence lifetimes have comparable values.
2) Particles synthesized in the presence of the ligand show lower luminescence lifetime and QY compared to particles of the same carbonate material synthesized in the absence of the organic ligand. This decrease in luminescence lifetime and QY can most likely be explained by the quenching by OH groups from the ligand.
3) For both matrices, when comparing the emission intensity of the powder samples and colloidal suspensions a decrease of around 25% of emission intensity in the colloidal suspensions compared to the powder samples is observed.
4) When excited into the f-f transition (at 351.0 nm) Tb^{3+} doped $Ce_2O(CO_3)_2 \cdot H_2O$ has significantly lower emission intensity, decay time, and QY compared to Tb^{3+} doped $La_2O(CO_3)_2 \cdot H_2O$. This decrease could be caused by energy-transfer from Tb^{3+} to Ce^{3+}. When excited into the Ce^{3+} d-f transition (at 292.0 nm) the energy transfer from Ce^{3+} to Tb^{3+} is incomplete, which also results in low QY.

Table 4.8. presents the calculated CIE chromaticity coordinates and assigned color for Eu^{3+} and Tb^{3+} doped rare-earth carbonate samples discussed in this chapter.

Table 4.8. CIE chromaticity coordinates of 5% doped Eu^{3+} and Tb^{3+} samples and the assigned colors.

Sample	CIE (x)	CIE (y)	Color
5% Eu doped A1	0.63	0.37	red
5% Eu doped A6	0.64	0.36	red
5% Tb doped A1	0.29	0.56	green
5% Tb doped A6	0.29	0.55	green
5% Tb doped A7	0.28	0.49	green
5% Tb doped A10	0.29	0.55	green

4.4. Conclusions

In summary, a simple hydrothermal method was employed for the synthesis of sub-spherical lanthanum hydroxycarbonate nanoparticles 30-50 nm in size (**A1**). It was established that the acetate salt was a very good source of lanthanum for the synthesis of nanosized particles. When drastically increasing the amount of urea in the synthesis, with all other reaction conditions unchanged, 20-30 nm lanthanum oxycarbonate nanoparticles were formed (**A6**). Cerium oxycarbonate particles were found to be more dependent on the reaction time and temperature than other carbonate particles described in this work. Further, the influence of glucose and fructose as stabilizing ligands in the synthesis of lanthanum and cerium oxycarbonates was investigated. Depending on the applied ligand, and the source of lanthanum, particles of different shapes and sizes were collected. Particles obtained in the presence of glucose or fructose gave stable colloidal suspensions up to several days, yet a decrease in the luminescence lifetimes, compared to particles synthesized in the absence of the ligand, was observed. The Eu^{3+} and Tb^{3+} emission spectra, the luminescence lifetimes, and QYs in the carbonate matrices were measured and

compared. The particles were investigated in their powder form and as colloidal suspensions in water. It was observed that there was no significant change in shape of the emission spectrum and the luminescence lifetime before and after dispersion. Therefore we can conclude that the particles do not encounter any modifications after dispersion in water.

4.5. References

1. Lechevallier, S.; Lecante, P.; Mauricot, R.; Dexpert, H.; Dexpert-Ghys, J.; Kong, H.-K.; Law, G.-L.; Wong, K.-L. *Chem. Mater.* **2010**, 22, 6153.

2. Bergerhoff, G.; Brown, I. D. Crystallographic Databases, edited by Allen, F. H. et al.; International Union of Crystallography, Chester, 1987.

3. Jeevanandam, P.; Koltypin, Y.; Palchik, O.; Gedanken, A. *J. Mater. Chem.,* **2001**, 11, 869.

4. Oikawa, M.; Fujihara, S. *J. Solid. State Chem*., **2005**, 178, 2036.

5. Carnall, W.T.; Fields, P.R.; Rajniak, K. *J. Chem. Phys.*, **1968**, 49, 4450.

6. Sudarsan, V.; van Veggel F.C.J.M.; Herring, A.; Raudsepp, M. *J. Mater. Chem*., **2005**, 15, 1332.

7. Dejneka, M.; Snitzer, E.; Riman, R.E. *J. Lumin.*, **1995**, 65, 227.

8. Rosa, I.L.V.; Maciel, A.P.; Longo, E.; Leite, E.R.; Varela, J.A. *Mater. Res. Bull*., **2006**, 41, 1791.

9. Carnall, W.T.; Fields, P.R.; Rajniak, K. *J. Chem. Phys.*, **1968**, 49, 4447.

10. Couwenberg, I.; Binnemans, K.; De Leebeeck,H.; Gorller-Walrand, C. *J. Alloys Compd*., **1998**, 274, 157.

11. Vogler, A.; Kunkely, H. *Inorg. Chim. Acta*, **2006**, 359, 4130.

12. Pankratov, V.; Popov, A.I.; Chernov, S.A.; Zharkouskaya, A.; Feldmann, C. *Phys. Status Solidi B*, **2010**, 247, 2252.

Chapter 5: Tuning the architecture and properties of Ln^{3+}- doped $Y(WO_3)_2(OH)_3$ (Ln = Eu^{3+}, Tb^{3+}, and Dy^{3+}) microstructures built from nanobuilding blocks

In this chapter the hydrothermal synthesis of $Y(WO_3)_2(OH)_3$ nano- and micro-structures has been reported. The architecture of these materials could be tuned by varying the reaction time, source of rare-earth, and the amount of dioctyl sodium sulfosucciate (DSS) surfactant. Eu^{3+}, Tb^{3+}, and Dy^{3+} ions were incorporated into the $Y(WO_3)_2(OH)_3$ materials obtained after different reaction times and the luminescence was investigated for the material before and after heat treatment. It was observed that some of the Dy^{3+} doped $Y(WO_3)_2(OH)_3$ samples emitted white light.

The N_2 adsorption measurements presented in this chapter were performed by Ying-Ya Liu from COMOC lab.

The results presented in this chapter were published as part of the publication: 'Tuning the architecture and properties of micro structured yttrium tungstate oxide hydroxide and lanthanum tungstate' Anna M. Kaczmarek, Ying-Ya Liu, Pascal Van Der Voort, Rik Van Deun, *Dalton Trans.*, **2013**, *42*, 5471-5479.

5.1. Introduction

There is a continuous demand for new and efficient white light emitting materials in advanced technological applications. Interest in inorganic materials with controlled morphology, and well-defined size and shape originates from the observation that the chemical and physical properties of a material depend on its composition, as well as structure, crystal phase, shape, size and dimensionality.[1] Therefore by tuning the materials morphology one can obtain new, desired properties, such as luminescence properties. Rare-earth tungstates are known to be good matrixes due to their high chemical and thermal stability.[2]

This research was undertaken to synthesize $Y(WO_3)_2(OH)_3$ nano- and micro-structures, to investigate their formation mechanism and the different factors that affect it. The influence of heat treatment, reaction time, source of the rare-earth, and amount of the surfactant were studied. X-ray powder diffraction (XRD), scanning electron microscopy (SEM), and N_2 adsorption were employed to characterize the obtained products. The luminescence properties of the $Y(WO_3)_2(OH)_3$ nano- and micro- structures, after doping them with Eu^{3+}, Tb^{3+}, Dy^{3+} were explored. Luminescence measurements showed an efficient charge transfer from the WO_4^{2-} groups to Ln^{3+} ions.

5.2. Synthesis of Ln^{3+} doped $Y(WO_3)_2(OH)_3$ (Ln = Eu^{3+}, Tb^{3+}, Dy^{3+})

All chemicals were of analytical grade and used without further purification. In a typical procedure different amounts of DSS surfactant (0.25 - 1.25 mmol) were dissolved in 30 mL distilled water. A water solution of 1 mmol of $Y(NO_3)_3 \cdot 5H_2O$ was added to the DSS solution and vigorously stirred for 15 minutes. Next 1 mmol Na_2WO_4 dissolved in water was added, and the pH value of the solution was adjusted to 5 by

adding diluted HNO_3 or NaOH. The total volume of the solution was 40 mL. After 10 minutes it was transferred into an autoclave, sealed and heated at 200 °C for different amounts of time (1 - 24 h). The autoclave was cooled naturally to room temperature, the precipitate separated by centrifugation, and the product washed three times with ethanol and dried at 80 °C. The as-synthesized product was heat treated in air at 900 °C for 3 h.

5.3. Results and discussion

5.3.1. Characterization of $Y(WO_3)_2(OH)_3$ particles

The reaction parameters, corresponding morphologies and symbols, which have been assigned to the samples, are summarized in Table 5.1.

Table 5.1. A brief summary of the experimental conditions, the corresponding product morphologies, and assigned sample symbols which will be used throughout Chapter 5.[a]

Sample	RE source[b]	DSS [mmol]	Morphology of product
B1	$Y(NO_3)_3$	0	microsphere assembled by nanodiscs
B2	$Y(OAc)_3$	0	microsphere assembled by nanodiscs
B3	$Y(NO_3)_3$	0.25	mixture of microsphere assembled by nanodiscs and nanorods
B4	$Y(NO_3)_3$	0.5	microsphere assembled by nanorods with an addition of microspheres assembled by nanodiscs
B5	$Y(NO_3)_3$	0.75	microsphere assembled by nanorods
B6	$Y(NO_3)_3$	1.0	microsphere assembled by nanorods
B7	$Y(NO_3)_3$	1.25	irregular microsphere assembled by nanorods
B8	$Y(OAc)_3$	0.25	microsphere assembled by nanorods with an addition of microspheres assembled by nanodiscs
B9	$Y(OAc)_3$	0.5	microsphere assembled by nanorods
B10	$Y(OAc)_3$	0.75	irregular microsphere assembled by nanorods
B11	$Y(OAc)_3$	1.0	irregular microsphere assembled by nanorods
B12	$Y(OAc)_3$	1.25	irregular microsphere assembled by nanorods

[a] In all cases the reaction was carried out at pH 5 for 24 h at 200 °C

[b] The salts were hydrated: $Y(NO_3)_3 \cdot 5H_2O$ and $Y(OAc)_3 \cdot 2H_2O$

The composition and phase purity of the products were first examined by XRD. Figure 5.1. shows the typical XRD patterns of the samples obtained from an yttrium salt and sodium tungstate at pH 5 in the absence of DSS (after heat treatment at 900 °C for 3h). Strong and sharp diffraction peaks indicated good crystallinity of the samples. No additional peaks of impurities could be detected, indicating the high purity of the samples. The diffraction peaks of the products are in good agreement

with the standard values of monoclinic $Y(WO_3)_2(OH)_3$ (JCPDS 25-1245) (no crystal structure of $Y(WO_3)_2(OH)_3$ has been deposited in the ICSD database, therefore the JCPDS database was used in this case).[3] When $Y(WO_3)_2(OH)_3$ samples were synthesized in the presence of DSS the diffraction peaks of the precursors could not be indexed to a certain phase found in the JCPDS database. Only after heat treatment the products were in good agreement with the standard values of monoclinic $Y(WO_3)_2(OH)_3$ (Figure 5.2.).

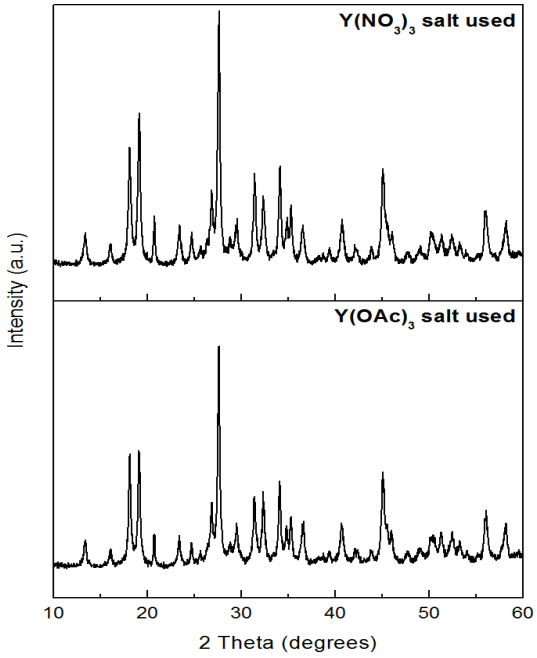

Figure 5.1: XRD patterns of samples B1 (top) and B2 (bottom) after heat treatment at 900 °C for 3 h.

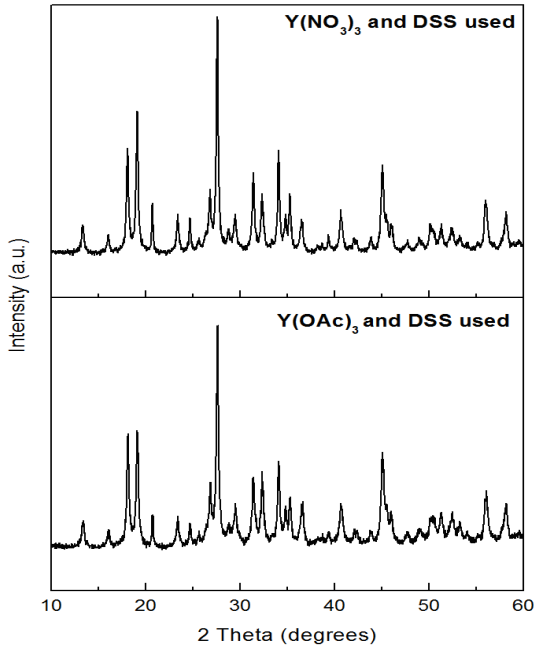

Figure 5.2: XRD patterns of samples B6 (top) and B11 (bottom) after heat treatment at 900 °C for 3 h.

It was observed that when the hydrothermal reaction was carried out at 200 °C for 24 h, at pH 5, in the absence and presence of DSS spherical microstructures built from nanobuilding blocks – either nanodiscs or nanorods were obtained. The nanobuilding blocks were aligned perpendicularly taking on a flower-like appearance. Similar spherical micro architectures constructed from nanorods or nanodiscs/nanoplates have been recently reported for several tungstate[4-6] and molybdate[7] compounds. Xu *et al.* had previously reported the formation of $YW_2O_6(OH)_3$ microstructures, synthesized from $Y(NO_3)_3{\cdot}5H_2O$ at pH 2 and 3 in the absence of a surfactant.[3] At pH 2 spherical microstructures having a 2-5 μm diameter were reported. They were built from multiple 1D prismatic nanorods (200-300 nm) aligned perpendicularly giving a

waxberry-like appearance. It could be observed that some of the nanorods were linked together by sharing a common edge. At pH 3 flower-like architectures, with a size in the range of 2-4 μm, were obtained. The microflowers were constructed from numerous nanoflakes (100-300 nm) with sword-like morphology. In this research work two sources of yttrium were used (nitrate and acetate salts) and DSS was employed as the surfactant. Figure 5.3. shows the typical SEM images of $Y(WO_3)_2(OH)_3$ microstructures obtained after 24 h hydrothermal treatment (200 °C), at pH 5, in the absence of surfactant. All SEM images presented in the chapter are images of the heat treated samples (the unheat treated samples are not shown as there were no significant changes in the morphology before and after heat treatment). These spherical microstructures, synthesized from both $Y(NO_3)_3{\cdot}5H_2O$ (**B1)** and $Y(OAc)_3{\cdot}2H_2O$ (**B2**), are built from irregular nanodiscs arranged perpendicularly.

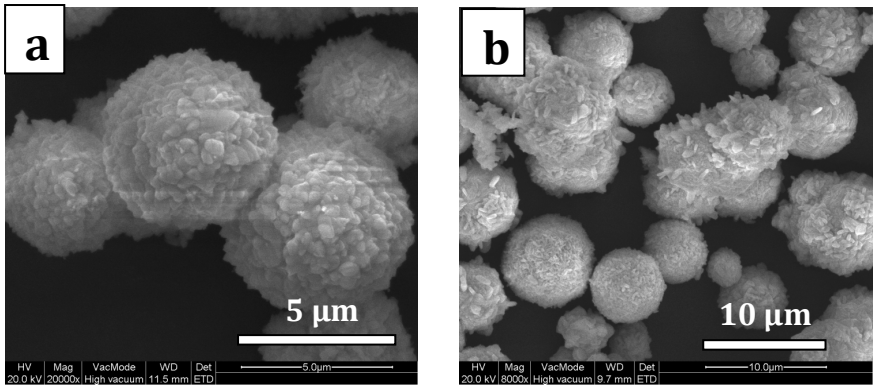

Figure 5.3: SEM images of samples B1 (a) B2 (b) after heat treatment.

When DSS was used in the reaction, the agglomeration of nanostructures into microstructures was found to be different than that for microstructures synthesized in the absence of surfactant. This has been shown in Figure 5.4. for sample **B6**. When

the reaction was ended after 1 h a large amount of irregular nanoparticles was observed. After 3 h of hydrothermal treatment nanorods (300-500 nm), which had formed bundle like aggregates, were observed.

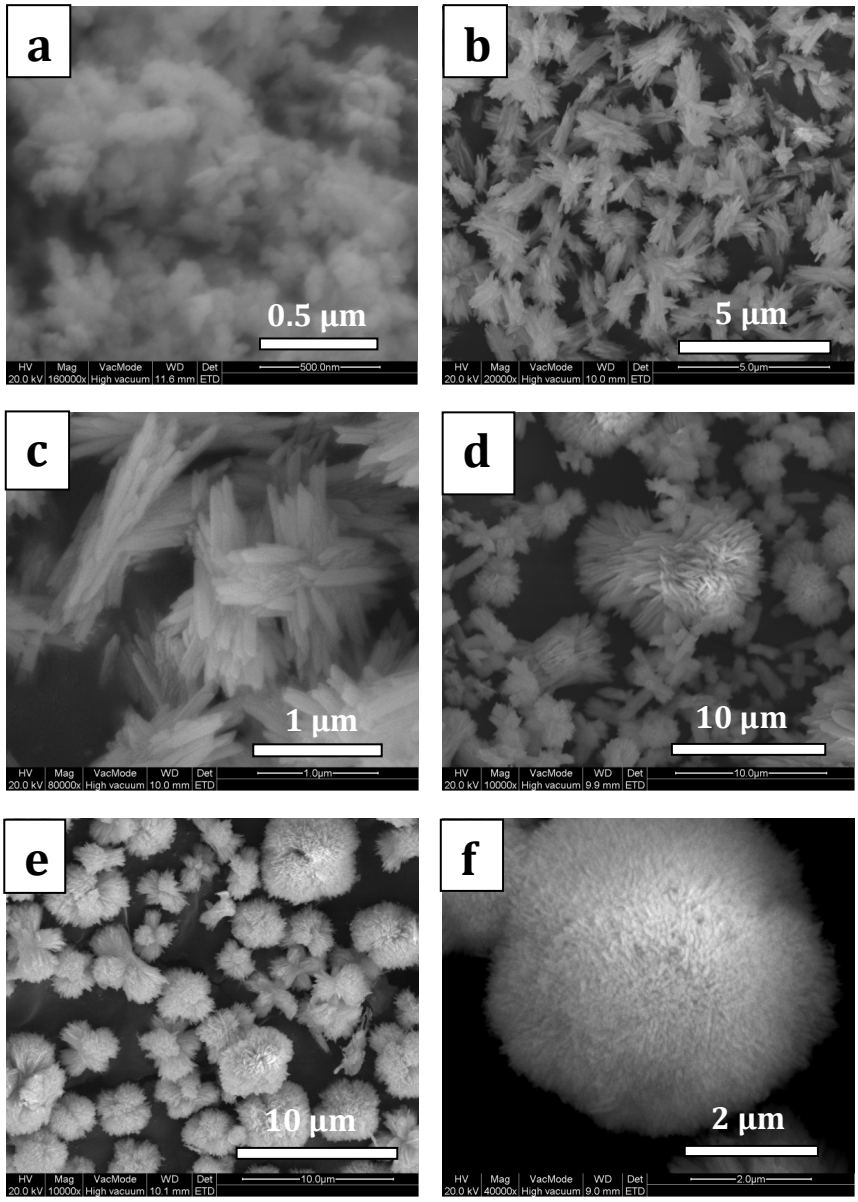

Figure 5.4: SEM images of B6 after a reaction time of (a) 1 h, (b, c) 3 h, (d) 6 h, (e) 12 h, (f) 24 h after heat treatment.

When the time was increased to 6 h and then 12 h the bundles continued to grow forming spherical microstructures. After 24 h of hydrothermal treatment only completely formed spherical microstructures in the range of 4-5 μm could be detected under the SEM.

To understand the effect of DSS on the crystal formation of the products, a series of experiments was carried out, where the amount of the DSS surfactant was varied and all other reaction conditions remained unchanged. First, the formation of $Y(WO_3)_2(OH)_3$ particles synthesized from $Y(NO_3)_3{\cdot}5H_2O$ were investigated (see Appendix.). When the reaction was carried out from $Y(NO_3)_3{\cdot}5H_2O$ the best reaction outcome was recorded when using 1.0 mmol DSS (**B6**). When employing 0.25 mmol (**B3**) or 0.5 mmol (**B4**) DSS in the reaction some spheres similar to those formed in the absence of the surfactant were detected additionally with some microplates aggregated together. Using 1.25 mmol (**B7**) of the surfactant gave spherical structures irregular in their size (often with cracks on their surface).

The formation process of **B9** (Figure 5.5.) was different than that of **B6**. When $Y(OAc)_3{\cdot}2H_2O$ was used in the synthesis after 1 h small spherical particles were formed, which seemed to be the precursors for the formation of shrubby like structures built from numerous nanorods eradiating from the 'trunk'. Next these shrubby like structures aggregated forming 4–5 μm spherical microstructures. After 6 h some incomplete intermediate forms could be detected. After 12 h completely formed spherical microstructures, around 4 μm in size, could be observed under the SEM. Prolonging the reaction to 24 h gave no significant difference in the morphology or size of the material. It was noted that **B9** formed very regular microspheres, whereas employing higher amounts of DSS gave two different types of microspheres

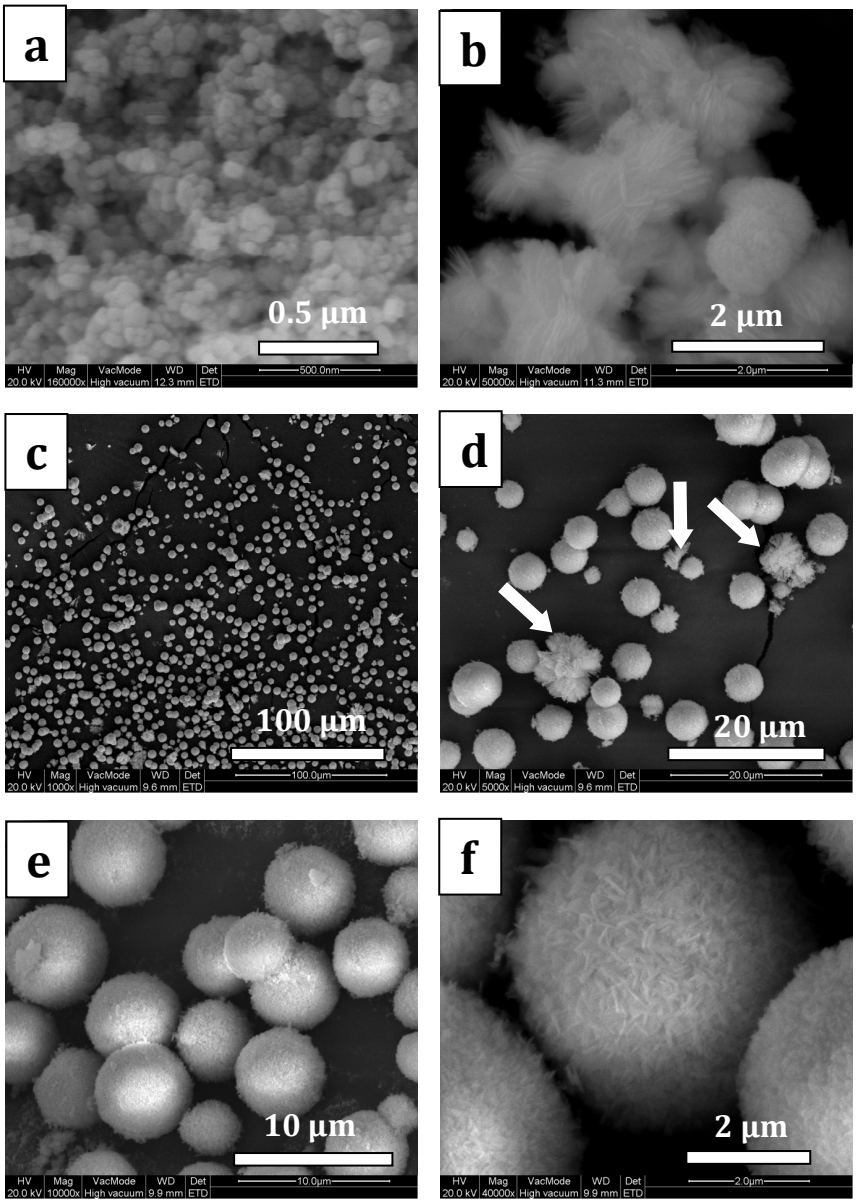

Figure 5.5: SEM images of B9 after a reaction time of (a) 1 h, (b) 3 h, (c, d) 6 h, (e, f) 12 h. Arrows in image (d) point at examples of incomplete, shrubby like structures.

in size and morphology. Using 0.25 mmol of DSS (**B8**) gave some spheres similar to those formed in the absence of the surfactant. Therefore it can be concluded that applying 0.5 mmol DSS when synthesizing $Y(WO_3)_2(OH)_3$ from $Y(OAc)_3{\cdot}2H_2O$ gave the best outcome.

Additionally nitrogen adsorption–desorption measurements were performed to investigate the porous structure of the $Y(WO_3)_2(OH)_3$ microstructures synthesized in the absence and presence of DSS. Four samples were investigated: **B1**, **B2**, **B6**, and **B9**. These samples were chosen in order to not only show the influence of DSS on the morphology, but also to show the influence of the Y^{3+} ion source on the products morphology. All of the samples were measured after heat treatment. As the microspheres are composed of a large number of nanorods/nanodiscs, the porous structure is contributed both from the packing of the nanobuilding blocks, as well as packing of the microspheres. The adsorption and desorption isotherms of nitrogen on samples **B1** and **B6** are shown in Figure 5.6. The Brunauer–Emmett–Teller (BET) specific surface area of **B1**, calculated from N_2 isotherms, is 10.6 m^2g^{-1}. The sample shows a typical H3 hysteresis loop according to the IUPAC classification, which is characteristic for a mesoporous material with plate-like particles giving rise to slit-shaped pores. These pores presumably arise from the voids between the nanodiscs within their spheres, indicating that the nanodiscs are loosely packed. The calculated BET specific surface area of **B6** is 5.2 m^2g^{-1}. Like in the case of **B1** there is a visible hysteresis loop observed in the relative pressure (P/P_0) range of 0.5–1.0. This implies the presence of slit-shaped mesopores in the sample. The adsorption and desorption isotherms of nitrogen on samples **B2** and **B9** are presented in Figure 5.7. The BET specific surface area of **B2**, calculated from N_2 isotherms, is 18.0 m^2g^{-1}. This indicates

a porous structure. The sample has a significant hysteresis loop observed in the relative pressure (P/P_0) range of 0.7–1.0, which implies the presence of mesopores. In this case the hysteresis loop is not type H3 (that typically always closes at $P/P_0 = 0.42$) but resembling more a type H1 hysteresis, indicating that the system consists of agglomerates of approximately uniform spheres. Sample **B9** hardly adsorbs any nitrogen, suggesting a very compact packing of the nanorods within the spheres. As a result it has a relatively low BET surface area of 3.4 m^2g^{-1}. In both cases, the nitrogen sorption experiments clearly showed that the $Y(WO_3)_2(OH)_3$ microspheres built in the absence of DSS (**B1** and **B2**) are more porous than those built in the presence of DSS (**B6** and **B9**). This implies that the nanodiscs are packed tighter into microspheres than the nanorods.

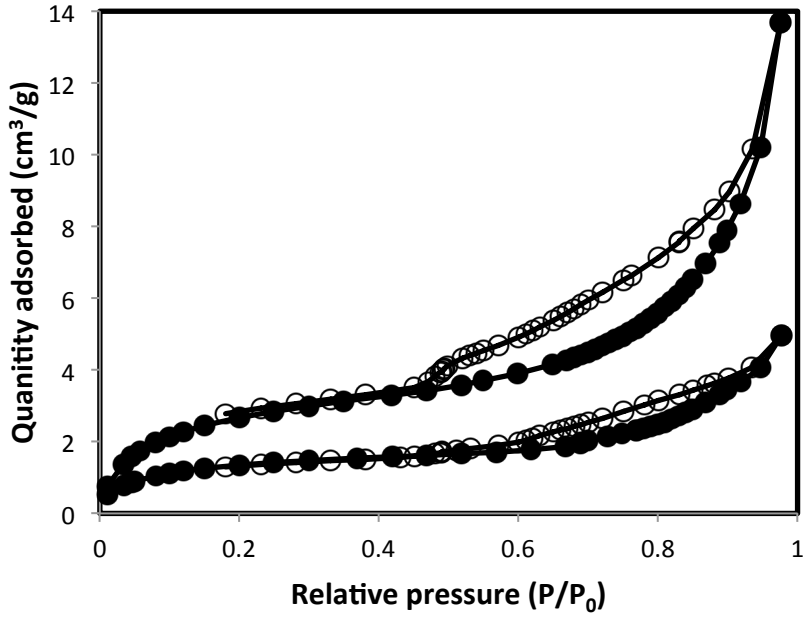

Figure 5.6: N_2 adsorption-desorption isotherms of B1 (top) and B6 (bottom).

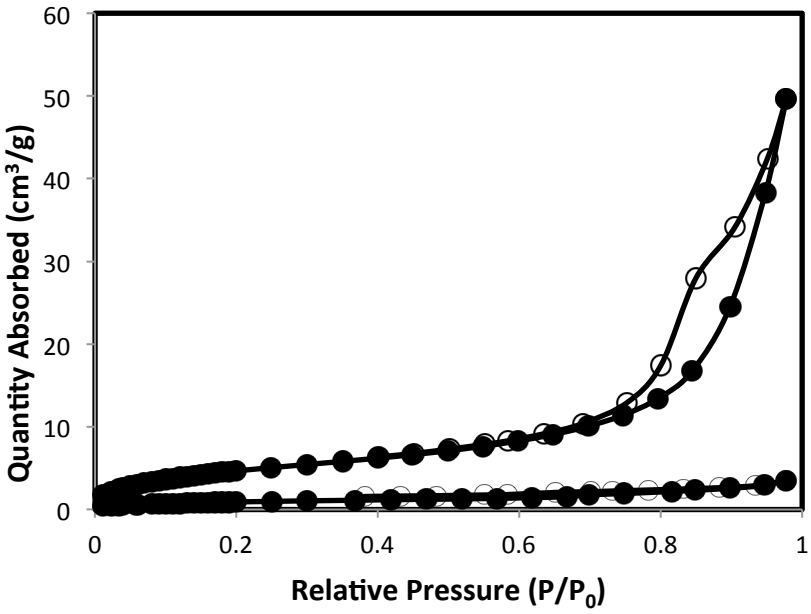

Figure 5.7: N_2 adsorption-desorption isotherms of B2 (top) and B9 (bottom).

5.3.2. Luminescence properties of Ln^{3+} doped $Y(WO_3)_2(OH)_3$ (Ln = Eu^{3+}, Tb^{3+}, Dy^{3+})

Undoped tungstates emit blue-green light under ultraviolet excitation. The excited tungstate groups may effectively transfer energy to doped rare-earths such as trivalent europium, terbium or dysprosium. Due to the similar chemical properties of Y^{3+} and Eu^{3+}, Tb^{3+}, and Dy^{3+} ions, doping 5% of the lanthanide ions into $Y(WO_3)_2(OH)_3$ did not influence the morphologies. In this subchapter the luminescence properties of 5% Ln^{3+} doped $Y(WO_3)_2(OH)_3$ prepared from the nitrate salts, in the presence of 1 mmol DSS, at pH 5 were investigated (sample **B6**). Both the precursor materials, as well as the heat treated samples, were investigated. The heat treated products showed higher emission intensities compared to the precursor products. This can most likely be explained by the fact that any luminescence quenchers, such as the

ligand are decomposed and adsorbed water molecules are desorbed upon heat treatment. Also the higher emission may be a result of improved crystallinity.

5.3.2.1. Luminescence properties of Eu^{3+} doped $Y(WO_3)_2(OH)_3$

Figure 5.8. presents the room temperature combined excitation-emission spectrum of **5% Eu doped B6 precursor** obtained after a reaction time of 1 h (will be referred to as **5% Eu doped B6 precursor_1h**). All of the peaks have been assigned to the appropriate electronic transitions in Table 5.2.

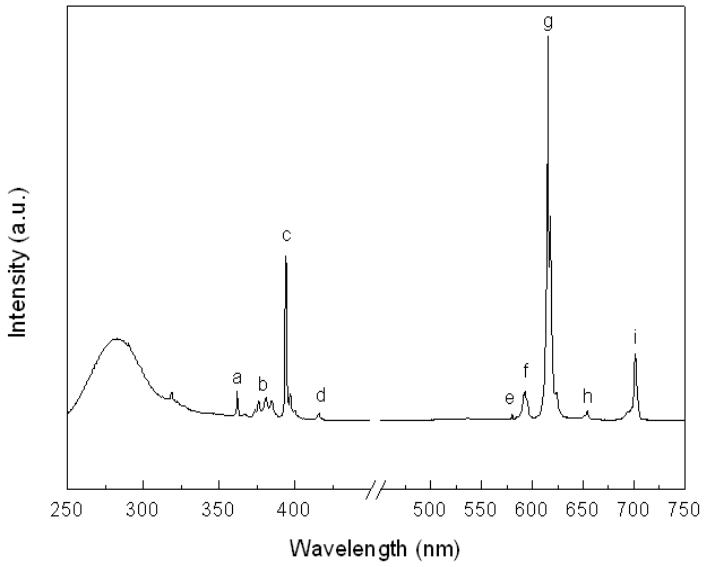

Figure 5.8: Excitation spectrum (monitored at 616.2 nm) and emission spectrum (excited at 282.0 nm) of 5% Eu doped B6 precursor_1h sample. The electronic transitions labeled a–i have been assigned in Table 5.2.

The excitation spectrum of **5% Eu doped B6 precursor_1h** (observed at 616.2 nm) contains a broad band in the region 250.0 – 320.0 nm with a maximum at 282.0 nm, and a series of sharp excitation peaks, which can be assigned to the typical intra 4f transitions of Eu^{3+}.[10] The broad band corresponds to the charge transfer absorption from the 2p orbitals of the oxygens to the 5d orbitals of the tungsten in the tungstate groups.[2] In the emission spectrum a series of peaks is observed, which can be assigned to the $^5D_0 \rightarrow {}^7F_J$ (J = 0 - 4) transitions of the Eu^{3+} ions. Figure 5.9. presents both the room temperature combined excitation-emission spectrum of **5% Eu doped B6 precursor** obtained after a reaction time of 3 h (will be referred to as 5**% Eu doped B6 precursor_3h**) and the room temperature combined excitation-emission spectrum of **5% Eu doped B6 precursor** obtained after a reaction time of 24 h (will be referred to as 5**% Eu doped B6 precursor_24h**). All of the peaks have been assigned to the appropriate electronic transitions in Table 5.2. The excitation spectra of **5% Eu doped B6 precursor_3h** and **5% Eu doped B6 precursor_24h** (observed at 617.0 nm) contain broad bands in the region 250.0 – 320.0 nm, and series of sharp excitation peaks, which can be assigned to the typical intra 4f transitions of Eu^{3+}. The broad band corresponds to the W-O charge transfer band. In the emission spectra series of sharp peaks are observed, which can be assigned to the $^5D_0 \rightarrow {}^7F_J$ (J = 0 - 4) transitions of the Eu^{3+} ions. Additionally a broad O-W bands with a maximum at 505.0 nm is present in the **5% Eu doped B6 precursor_24h** sample.

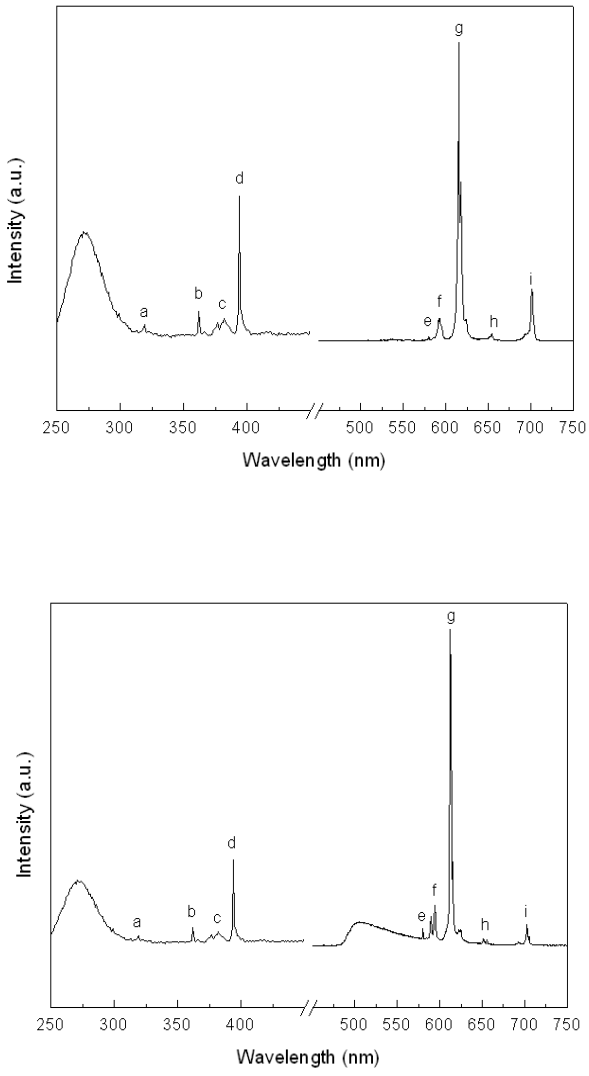

Figure 5.9: Top - excitation spectrum (monitored at 614.5 nm) and emission spectrum (excited at 275.0 nm) of 5% Eu doped B6 precursor_3h sample. Bottom - excitation spectrum (monitored at 612.7 nm) and emission spectrum (excited at 275.0 nm) of 5% Eu doped B6 precursor_24h sample. The electronic transitions labeled a–i have been assigned in Table 5.2.

In the **5% Eu doped B6 precursor** sample the different reaction times gave materials which emitted a variety of colors ranging from red to yellow. Figure 5.10. presents the CIE chromaticity diagram of **5% Eu doped B6 precursor_1h**, **5% Eu doped B6 precursor_3h** and **5% Eu doped B6 precursor_24h**.

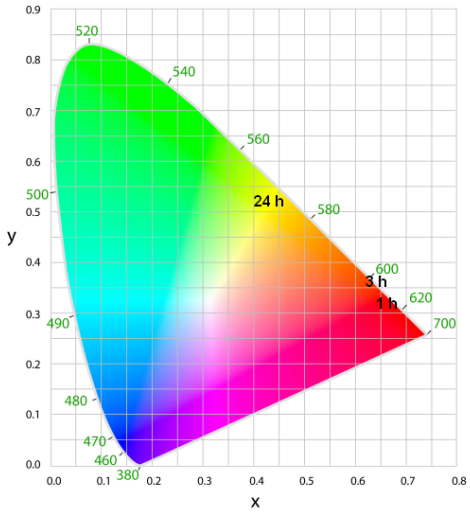

Figure 5.10: CIE chromaticity diagram presenting the colors emitted by samples: 5% Eu B6 precursor_1h (x = 0.65, y = 0.34), 5% Eu B6 precursor_3h (x = 0.63, y = 0.36), and 5% Eu B6 precursor_24h (x = 0.41, y = 0.52).

To investigate the influence of the ion doping percentage the **B6 precursor_24h** sample was additionally doped with 1% and 3% of Eu^{3+} ions. With the decrease in Eu^{3+} concentration from 5% to 1% the intensity of the broad charge transfer band increases and the emission of Eu^{3+} ions becomes weaker (see Figure 5.11.).

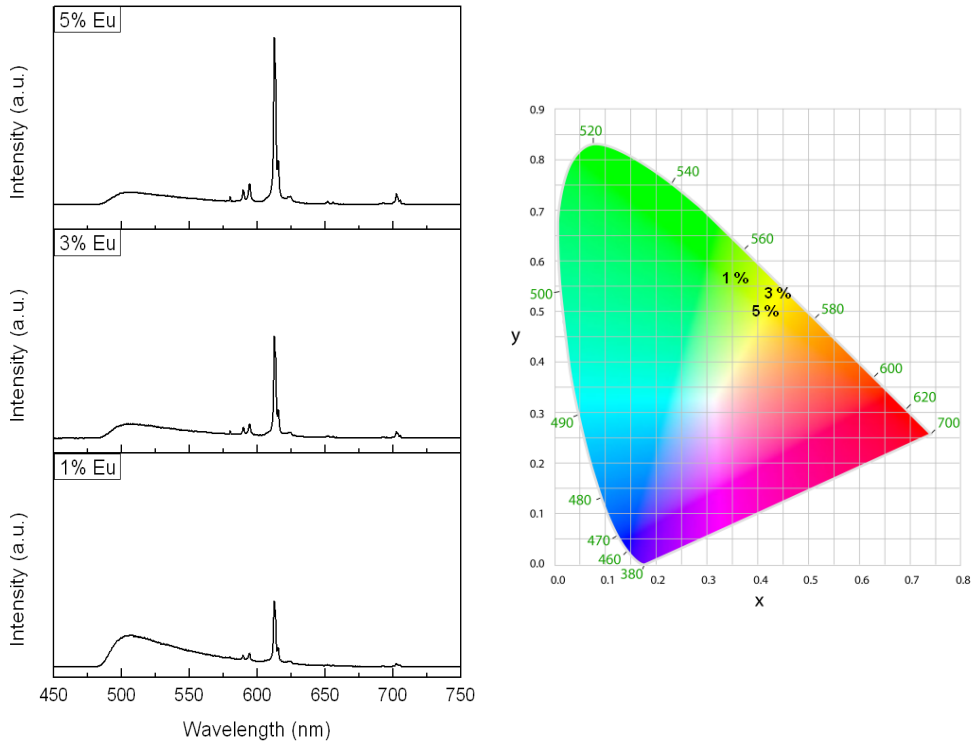

Figure 5.11: Right – emission spectra of 1%, 3%, and 5% doped B6 precursor_24h sample. Left – CIE chromaticity diagram showing the change of color when a different doping % of Eu is used (1% Eu_B6 precursor_24h: x = 0.33, y = 0.58; 3%_ B6 precursor_24h: x = 0.41, y = 0.53; 5% Eu_B6 precursor_24h: x = 0.41, y = 0.51).

For the **5% Eu doped B6_24h** sample the heat treated excitation and emission spectra have been presented in Figure 5.12. The excitation spectrum of the heat treated **5% Eu doped B6_24h** sample is similar to the **5% Eu doped B6 precursor_24h** sample. A shift of the broad O-W charge transfer band can be observed. The maximum of the band moves from 273.0 nm to 308.0 nm. A change in

the intensity of the $^5D_2 \leftarrow {}^7F_0$ transition (peak c in the spectrum) is also noticeable. This can be explained by the fact that it is a hypersensitive transition.[11] In the emission spectrum (when exciting the sample at 308.0 nm) the charge transfer band is so weak that it can barely be noticed. Also changes in the $^5D_0 \rightarrow {}^7F_1$ and $^5D_0 \rightarrow {}^7F_2$ transition peaks are observed. The $^5D_0 \rightarrow {}^7F_1$ transition peak splits into more than three peaks indicating low symmetry. The peak splitting of transition $^5D_0 \rightarrow {}^7F_0$ indicates the presence of more than one europium site.[12]

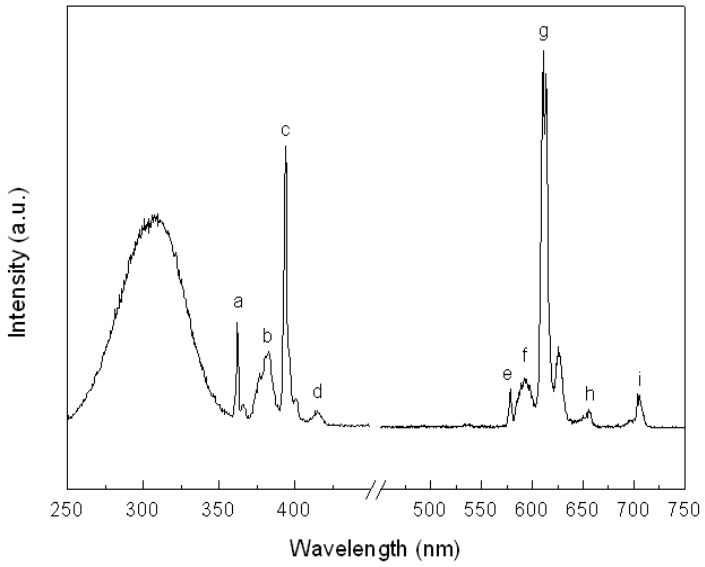

Figure 5.12: Excitation spectrum (monitored at 612.7 nm) and emission spectrum (excited at 308.0 nm) of 5% Eu doped B6_24h sample. The electronic transitions labeled a–i have been assigned in Table 5.2.

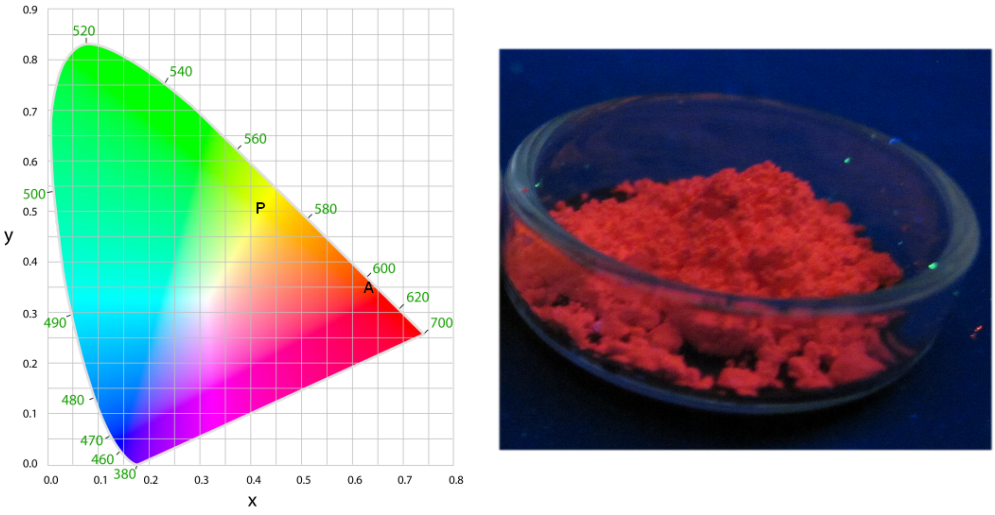

Figure 5.13: Left - CIE chromaticity diagram presenting the colors emitted by samples: 5% Eu B6 precursor_24h (P: x = 0.41, y = 0.51) and 5% Eu B6_24h (A: x = 0.63, y = 0.35) to show the difference in emitted color for a sample before and after heat treatment. Right – picture of 5% Eu B6_24h taken when the sample was placed under a laboratory UV lamp (at 302.0 nm excitation wavelength).

Table 5.2. Assignment of labeled transitions shown in Figures 5.8., 5.9., and 5.12.

	Excitation				Emission			
	Wavelength (nm)	Energy (cm^{-1})	Transition		Wavelength (nm)	Energy (cm^{-1})	Transition	
			5% Eu doped B6 precursor_1h					
a	361.4	27670	$^5D_4$	$\leftarrow {}^7F_0$	**e** 580.9	17215	$^5D_0 \rightarrow$	$^7F_0$
b	380.8	26260	$^5G_6$, $^5G_5$	$\leftarrow {}^7F_1$	**f** 592.4	16880		$^7F_1$
c	394.5	25349	$^5L_6$	$\leftarrow {}^7F_0$	**g** 616.2	16228		$^7F_2$
d	416.2	24027	$^5D_3$	$\leftarrow {}^7F_1$	**h** 655.0	15267		$^7F_3$
					i 701.1	14263		$^7F_4$
			5% Eu doped B6 precursor_3h					
a	318.9	31358	$^5H_6$	$\leftarrow {}^7F_0$	**e** 580.4	17229	$^5D_0 \rightarrow$	$^7F_0$
b	362.0	27624	$^5D_4$	$\leftarrow {}^7F_0$	**f** 593.3	16855		$^7F_1$
c	382.5	26144	$^5G_6$, $^5G_5$	$\leftarrow {}^7F_1$	**g** 614.5	16273		$^7F_2$
d	394.3	25361	$^5L_6$	$\leftarrow {}^7F_0$	**h** 654.7	15274		$^7F_3$
					i 701.8	14249		$^7F_4$

Table 5.2. (continued)

5% Eu doped B6 precursor_1h								
a	319.0	31348	$^5H_6$	$\leftarrow {}^7F_0$	**e**	580.9	17215	$^5D_0 \rightarrow {}^7F_0$
b	361.4	27670	$^5D_4$	$\leftarrow {}^7F_0$	**f**	593.3	16855	$^7F_1$
c	382.6	26137	$^5G_6$, $^5G_5$	$\leftarrow {}^7F_1$	**g**	612.7	16321	$^7F_2$
d	393.8	25394	$^5L_6$	$\leftarrow {}^7F_0$	**h**	651.6	15347	$^7F_3$
					i	702.0	14245	$^7F_4$
5% Eu doped B6_24h								
a	361.4	27670	$^5D_4$	$\leftarrow {}^7F_0$	**e**	577.4	17319	$^5D_0 \rightarrow {}^7F_0$
b	383.2	26096	$^5G_6$, $^5G_5$	$\leftarrow {}^7F_1$	**f**	592.4	16880	$^7F_1$
c	393.8	25394	$^5L_6$	$\leftarrow {}^7F_0$	**g**	612.7	16321	$^7F_2$
d	414.5	24125	$^5D_3$	$\leftarrow {}^7F_1$	**h**	655.1	15265	$^7F_3$
					i	705.5	14174	$^7F_4$

5.3.2.2. Luminescence properties of Tb^{3+} doped $Y(WO_3)_2(OH)_3$

Figure 5.14. shows the room temperature combined excitation-emission spectrum of **5% Tb doped B6 precursor_1h** sample.

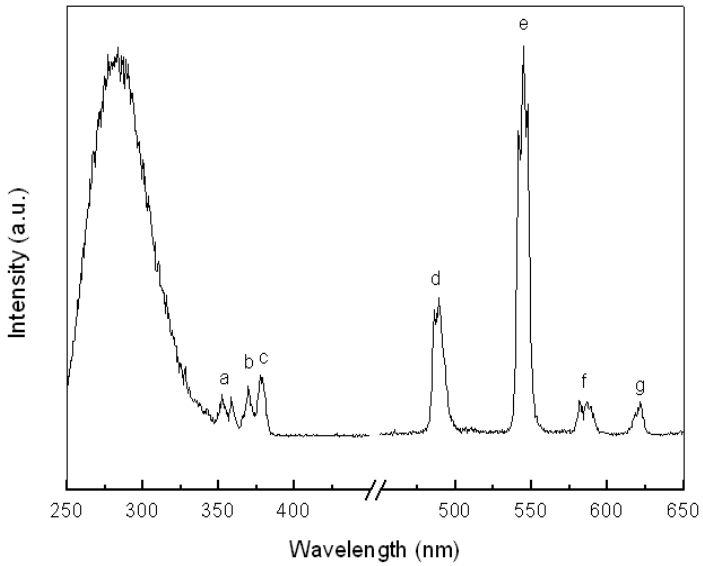

Figure 5.14: Excitation spectrum (monitored at 544.5 nm) and emission spectrum (excited at 284.0 nm) of 5% Tb doped B6 precursor_1h sample. The electronic transitions labeled a–g have been assigned in Table 5.3.

The excitation spectrum contains a strong broad band from 250 - 320 nm with a maximum at 284 nm, and a series of sharp excitation peaks, which can be assigned to the typical intra 4f transitions of Tb^{3+}.[13] In the emission spectrum a series of peaks is observed, which can be assigned to the $^5D_4 \rightarrow {}^7F_J$ (J = 6 - 3) transitions of the Tb^{3+} ions. The different reaction times (1 h, 3 h, 24 h) seemed to influence only the emission intensity of the Tb^{3+} ions (Figure 5.15). No W-O charge transfer band was present in

any of the emission spectra. All the terbium doped samples (before and after heat treatment) emitted green light under a UV lamp. Because of the lack of color change the heat treated **5% Tb doped B6** samples were not further analyzed in this project.

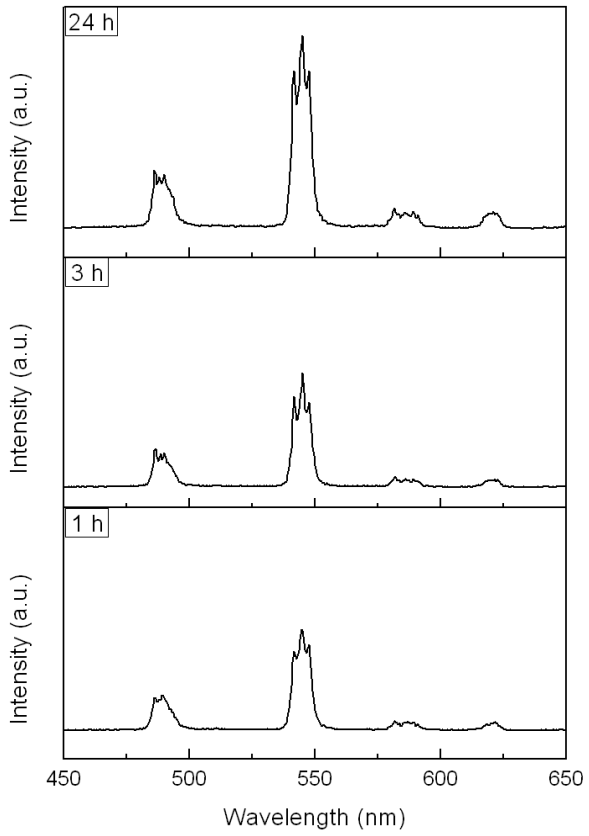

Figure 5.15: Emission spectra of samples 5% Tb doped B6 precursor_1h, 5% Tb doped B6 precursor_3h, and 5% Tb doped B6 precursor_24h (all excited at 284.0 nm).

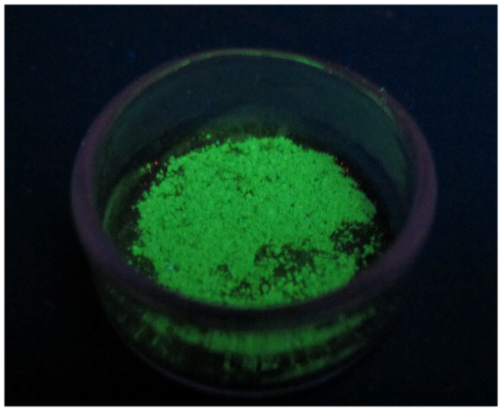

Figure 5.16: Photograph of 5% Tb doped B6 precursor_24h when placed under a laboratory UV lamp (at a 302.0 m, excitation wavelength).

Table 5.3. Assignment of labeled transitions shown in Figure 5.14.

	Excitation				Emission			
	Wavelength (nm)	Energy (cm^{-1})	Transition		Wavelength (nm)	Energy (cm^{-1})	Transition	
			5% Tb doped B6 precursor_1h					
a	352.0	28409	$^5L_9$	← $^7F_6$	**d** 489.3	20437	$^5D_4$ →	$^7F_6$
b	370.2	27012	$^5L_{10}$		**e** 544.5	18365		$^7F_5$
c	377.3	26504	$^5G_6$, $^5D_3$		**f** 581.5	17196		$^7F_4$
					g 621.5	16090		$^7F_3$

5.3.2.3. Luminescence properties of Dy^{3+} doped $Y(WO_3)_2(OH)_3$

Figure 5.17. shows the room temperature combined excitation-emission spectrum of **5% Dy doped B6 precursor_1h** sample. The excitation spectrum contains a broad band around 250 – 320 nm (with a maximum at 271.0 nm), and a series of sharp excitation peaks which can be assigned to the typical intra 4f transitions of Dy^{3+}.[14] In

the emission spectrum of Dy^{3+} a series of peaks is observed, which can be assigned to the transitions of the Dy^{3+} ions. At 484.1 nm the $^4F_{9/2} \rightarrow {}^6H_{15/2}$ transition peak can be distinguished. It is responsible for the blue component of the yellow-green emission of dysprosium. The blue light component is emphasized in this material due to the charge-transfer band. The hypersensitive $^4F_{9/2} \rightarrow {}^6H_{13/2}$ transition peak (at 574.0 nm) is responsible for the yellow emission. The small $^4F_{9/2} \rightarrow {}^6H_{11/2}$ transition peak (at 662.3 nm) is responsible for the red color.

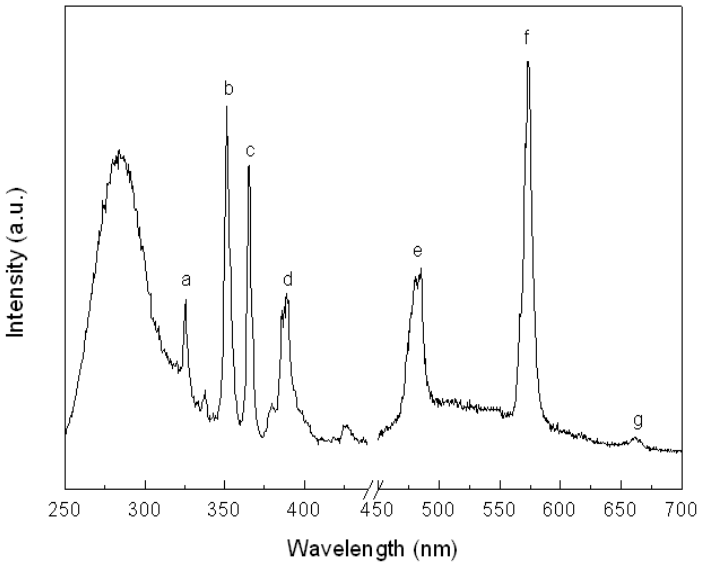

Figure 5.17: Excitation spectrum (monitored at 574.0 nm) and emission spectrum (excited at 271.0 nm) of 5% Dy doped B6 precursor_1h sample. The electronic transitions labeled a–g have been assigned in Table 5.4.

Figure 5.18. presents the emission spectra of **5% Dy doped B6 precursor** samples after different reaction times: 1 h, 3 h, and 24 h. As can be seen from the spectra a

change in the intensity of the charge transfer band can be observed. This also influences the color emitted by the material (see CIE diagrams in Figure 5.18.). The **5% Dy doped B6 precursor_24h** sample emitted almost ideal white light (coordinates of ideal white light are: x = 0.33, y = 0.33). The color temperature of this white light emitting sample was determined as 7393 K. This is referred to as a bluish white color. A photo of the **5% Dy doped B6 precursor_24h** sample taken under a UV laboratory lamp at an excitation wavelength of 302.0 nm has been presented in Figure 5.19.

The **5% Dy doped B6 precursor_1h** and **5% Dy doped B6 precursor_3h** samples both emitted near white light. Their color temperatures were calculated to be 5988 K ad 5708 K, respectively. These samples show a more yellowish than bluish tone.

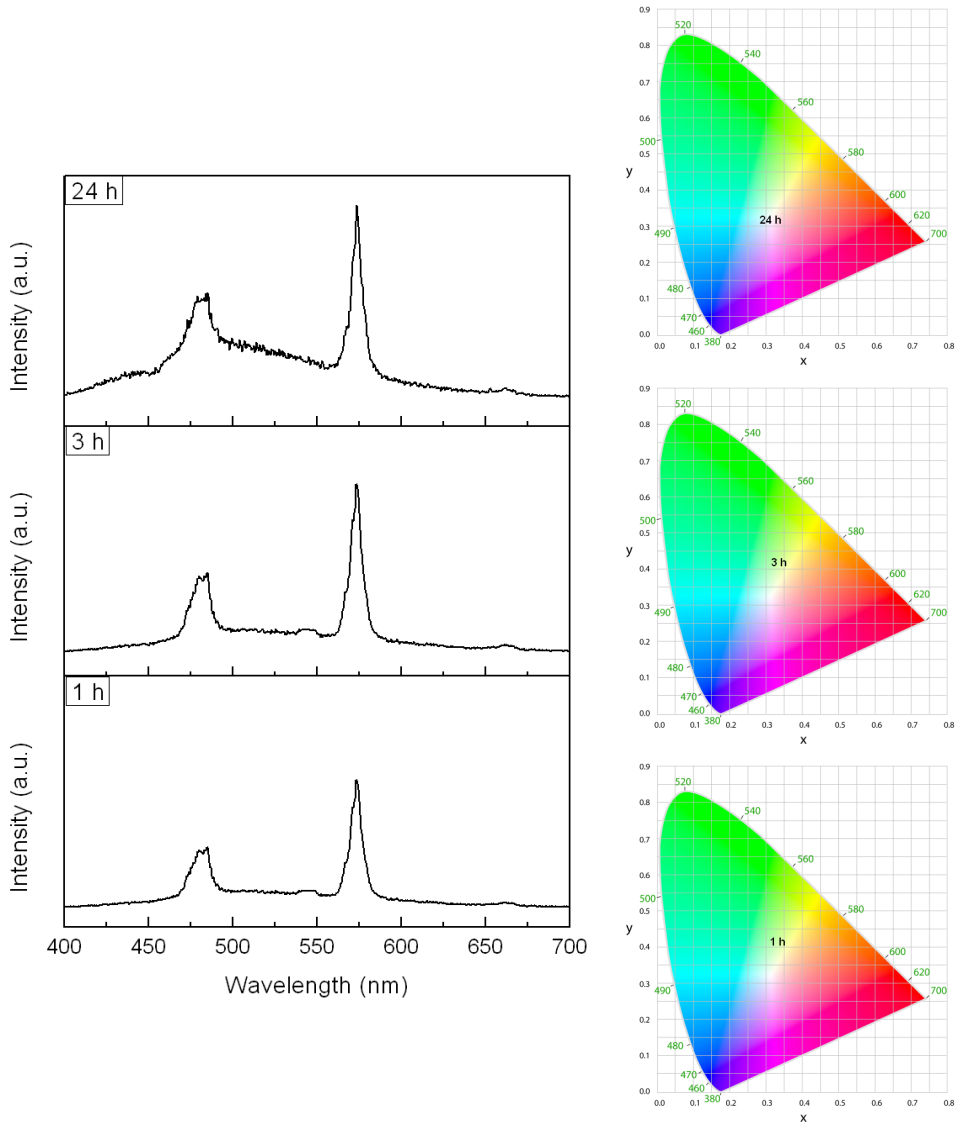

Figure 5.18: Left – emission spectra of 5% Dy doped B6 precursor_1h, 5% Dy doped B6 precursor_3h, and 5% Dy doped B6 precursor_24h. Right – CIE chromaticity diagrams presenting the colors emitted by the samples obtained after different reaction times (1 h: x = 0.32, y = 0.41; 3 h: x = 0.33, y = 0.41; 24 h: x = 0.29, y = 0.32).

Figure 5.19: Photograph of 5% Dy doped B6 precursor_24h taken under a UV laboratory lamp (at a 302.0 nm excitation wavelength). The sample shows cool white light emission.

Figure 5.20. presents the room temperature combined emission and excitation spectrum of **5% Dy doped B6_24h** sample (after heat treatment). As can be seen from this example after heat treatment the Dy doped materials show a much weaker charge transfer band than in the precursor samples. This inclines that there is a more efficient transfer of energy from the tungstate groups to the Dy^{3+} in the heat treated sample. The CIE color coordinates and color temperature were calculated for the **Dy doped B6_24h** sample. The CIE coordinates are x = 0.39, y = 0.42, whereas the color temperature is 5998 K. This material emits a rather cool white light with a bit of yellow tone in it.

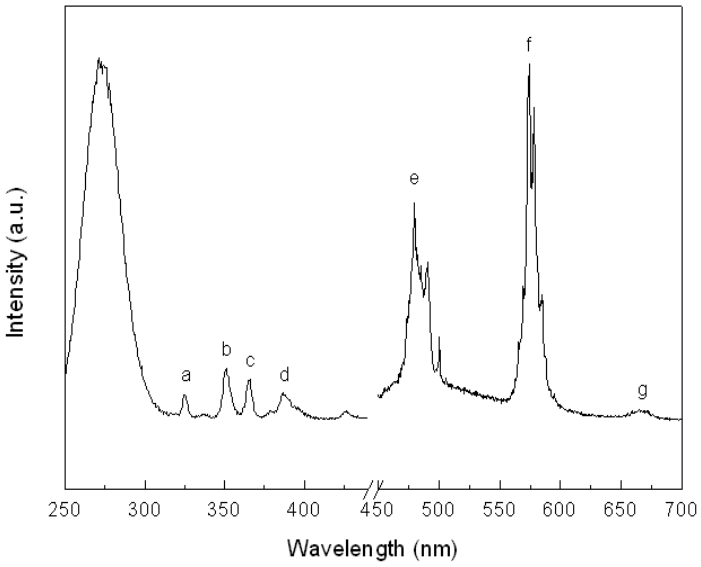

Figure 5.20: Excitation spectrum (monitored at 573.9 nm) and emission spectrum (excited at 270.0 nm) of 5% Dy doped B6_24h sample. The electronic transitions labeled a–g have been assigned in Table 5.4.

Table 5.4. Assignment of labeled transitions shown in Figures 5.17. and 5.20.

	Excitation				Emission			
	Wavelength (nm)	Energy (cm^{-1})	Transition		Wavelength (nm)	Energy (cm^{-1})	Transition	
			5% Dy doped B6 precursor_1h					
a	326.3	30647	$^6P_{3/2}$	$\leftarrow {}^6H_{15/2}$	**e** 484.1	20657	$^4F_{9/2} \rightarrow$	$^6H_{15/2}$
b	350.8	28506	$^6P_{7/2}$		**f** 574.0	17422		$^6H_{13/2}$
c	365.0	27397	$^6P_{5/2}$, $^4P_{3/2}$, $^4D_{3/2}$, $^4M_{19/2}$		**g** 662.3	15099		$^6H_{11/2}$
d	389.1	25700	$^4I_{13/2}$, $^4F_{7/2}$					
			5% Dy doped B6_24h					
a	325.2	30750	$^6P_{3/2}$	$\leftarrow {}^6H_{15/2}$	**e** 480.1	20829	$^4F_{9/2} \rightarrow$	$^6H_{15/2}$
b	350.8	28506	$^6P_{7/2}$		**f** 573.9	17425		$^6H_{13/2}$
c	365.0	27397	$^6P_{5/2}$, $^4P_{3/2}$, $^4D_{3/2}$, $^4M_{19/2}$		**g** 666.7	14999		$^6H_{11/2}$
d	387.1	25833	$^4I_{13/2}$, $^4F_{7/2}$					

5.4. Conclusion

In summary, a simple hydrothermal method was employed to synthesize precursor materials for $Y(WO_3)_2(OH)_3$. After heat treatment at 900 °C for 3 h the precursors were successfully transformed into $Y(WO_3)_2(OH)_3$, inheriting the morphology of the precursors. The influence of the DSS surfactant on the size and morphology of these samples was studied. It was shown that the presence of DSS (and its amount) significantly changed the shape of the nanobuilding blocks, and consequently the architecture of the microstructures. Additionally it was established that the rare-earth ion source (nitrate or acetate salt) had an impact on the size and shape of the nanobuilding blocks of the material. N_2 absorption-desorption measurements gave additional insight into the packing of the microstructures $Y(WO_3)_2(OH)_3$. It could be clearly seen from these measurements that the $Y(WO_3)_2(OH)_3$ microspheres built in the absence of DSS were more porous, revealing that the nanodiscs are loosely packed compared to the nanorods. These measurements also confirmed that there is a difference in the structure of the microspheres when two different sources of Y^{3+} ions are employed.

In the second part of this work the luminescence properties of Eu^{3+}, Tb^{3+} and Dy^{3+} doped $Y(WO_3)_2(OH)_3$ samples, and their precursor samples were investigated. Upon excitation into the tungstate charge transfer band the doped materials gave a range of emitted colors (the heat treatment and reaction time had a large impact of the emitted colors of Eu^{3+} and Dy^{3+} doped samples). Several of the Dy^{3+} doped samples gave white light emission with a range of different color temperatures.

5.5. References

1. Colfen, H.; Mann, S. *Angew. Chem., Int. Ed.*, **2003**, 42, 2350.

2. Kaczmarek, A. M.; Van Deun, R. *Chem. Soc. Rev.* **2013**, 42, 8835.

3. Xu, L.; Lu, C.; Shen, J.; Chen, Y.; Zhang, Z.; Hou, W. *CrystEngComm*, **2009**, 11, 1323.

4. Lei, F.; Yan, B. *J. Mater. Res.*, **2011**, 26, 88.

5. Tian, Y.; Chen, B.; Hua, R.; Yu, N.; Liu, B.; Sun, J.; Cheng, L.; Zhong, H.; Li, X.; Zhang, J.; Tian, B.; Zhong, H. *CrystEngComm*, **2012**, 14, 1760.

6. Xu, L.; Yang, X.; Zhai, Z.; Hou, W. *CrystEngComm*, **2011**, 13, 7267.

7. Xu, L.; Yang, X.; Zhai, Z.; Gu, D.; Pang, H.; Hou, W. *CrystEngComm*, **2012**, 14, 7330.

8. Sing, K.S.W. *Pure Appl. Chem*., **1982**, 54, 2201.

9. Bavykin, D.V.; Parmon, V.N.; Lapkin, A.A.; Walsch, F.C. *J. Mater. Chem*., **2004**, 14, 3370.

10. Carnall, W.T.; Fields, P.R.; Rajniak, K. *J. Chem. Phys.*, **1968**, 49, 4450.

11. Binnemans, K. *Chem. Rev.* **2009**, 109, 4283.

12. Nockemann, P.; Thijs, B.; Lunstroot, K.; Parac-Vogt, T.N.; Gorller-Walrand, C.; Binnemans, K.; Van Hecke, K.; Van Meervelt, L.; Nikitenko, S.; Daniels, J. Hennig, C.; Van Deun, R. *Chem. Eur. J.*, **2009**, 15, 1449.

13. Carnall, W.T.; Fields, P.R.; Rajniak, K. *J. Chem. Phys.*, **1968**, 49, 4447.

14. Carnall, W.T.; Fields, P.R.; Rajniak, K. *J. Chem. Phys.*, **1968**, 49, 4424.

Chapter 6: Enhanced luminescence in Ln^{3+}-doped Y_2WO_6 (Ln = Sm^{3+}, Eu^{3+}, Dy^{3+}) 3D microstructures through Gd^{3+} co-doping

In this chapter the synthesis and luminescence properties of a Sm^{3+}, Eu^{3+}, and Dy^{3+} doped Y_2WO_6 material is presented. At hydrothermal conditions and in the presence of sodium dodecyl sulfate (SDS) surfactant spherical 3D microstructures built from nanosized particles were formed when choosing the right pH of the reaction. A detailed luminescence, decay time and quantum yield study of the Ln^{3+} doped Y_2WO_6 material is shown. The influence of different lanthanide ion concentrations on luminescence properties was investigated. For the optimal lanthanide ion concentrations the systems were co-doped with 2% and 10% of Gd^{3+} ions to test the possible enhancement of luminescence through energy transfer from W-O and/or Gd^{3+} to Ln^{3+}. A significant increase of luminescence intensities, decay times and quantum yields was observed.

The results were published in the publication 'Enhanced luminescence in Ln^{3+}- doped Y2WO6 (Sm, Eu, Dy) 3D microstructures through Gd^{3+} co-doping' Anna M. Kaczmarek, Kristof Van Hecke, Rik Van Deun, *Inorg. Chem.*, **2014**, 53, 9498-9508.

6.1. Introduction

Despite a growing amount of research on lanthanide doped rare-earth tungstate materials there is still a lack of detailed luminescence data beyond recorded emission and excitation spectra, as well as calculated CIE coordinates. The quantum yields and luminescence lifetimes are quite rarely reported for lanthanide doped rare-earth tungstate materials. Most articles containing this data have been published in 2014. In one such report the quantum yields of the Eu^{3+} doped $RE_2(WO_4)_2$ (RE = Y^{3+}, La^{3+}, Gd^{3+}, Lu^{3+}) were reported to be very high, especially for Eu^{3+} doped $Lu_2(WO_4)_2$ (95%) and Eu^{3+} doped $Y_2(WO_4)_2$ (90%).[1] Also high quantum yield values for double rare-earth silver tungstate materials $AgRE(WO_4)_2$ (RE = Y^{3+}, La^{3+}, Gd^{3+}, Lu^{3+}) have been recently reported.[2] These promising results highlight the need for more detailed luminescence investigations of lanthanide doped rare-earth tungstate materials.

This research was undertaken with two motivations. First, it was intended to investigate the absolute quantum yield values of a different lanthanide doped tungstate material for which these values have not yet been reported in literature. Y_2WO_6 doped with different concentrations of lanthanides which emit light in the visible region was chosen for this study. The second motivation was to try to enhance the luminescence of these materials by co-doping Gd^{3+} ions into the matrix.

6.2. Synthesis of Ln^{3+} doped Y_2WO_6 (Ln = Sm^{3+}, Eu^{3+}, Gd^{3+}, Dy^{3+})

Samples were synthesized hydrothermally in the presence of SDS. 1 mmol of SDS was first dissolved in 20 mL distilled water. 1 mmol of $RE(NO_3)_3{\cdot}5H_2O$ salts at the right percentage amounts were weighed off and dissolved together in 10 mL of water. The water solution was slowly added to the SDS solution while stirring on a magnetic stirrer. After 15 minutes 1 mmol Na_2WO_4 dissolved in 10 mL water was slowly added,

and the pH value of the solution was adjusted to 3, 7 or 10 by adding diluted HNO_3 or NaOH. The total volume of the solution was adjusted to 50 mL by adding the right amount of water. After 10 minutes it was transferred into an autoclave, sealed and heated at 200 °C for 24h (at an oven heating rate of 1 °C per minute). The autoclave was cooled naturally to room temperature, the precipitate separated by centrifugation, and the product washed two times with water and two times with ethanol and dried at 60 °C in a vacuum oven. The as prepared samples are referred to as the 'precursors' throughout this chapter. Next the synthesized products were heat treated in air at 1100 °C for 3 h.

6.3. Results and discussion

6.3.1. Characterization of Y_2WO_6 particles

Table 6.1. summarizes the effect of the reaction pH on the phase of the yttrium tungstate material, as well as its shape. The different materials have been labeled **C1**-**C3**.

Table 6.1. Summary of the reaction parameters and corresponding results.

Sample	Ln source[a]	SDS [mmol]	Reaction pH	Morphology of product
C1	$Y(NO_3)_3$	1	3	Spherical microstructures (2-5 μm) built from regular nano-sized building blocks
C2	$Y(NO_3)_3$	1	7	Spherical microstructures (1-3 μm) built from irregularly shaped nano building blocks
C3	$Y(NO_3)_3$	1	10	Spherical microstructures (4-5 μm) built from regular rods stacked together (occasionally some of the microspheres had larger rods growing out from the core of these structures)

[a] The salt was hydrated: $Y(NO_3)_3 \cdot 5H_2O$

The XRD patterns of the **C1**-**C3** precursor samples could not be matched with any standard XRD patterns found in the JCPDS database. It is often reported that rare-earth tungstate precursor materials synthesized in the presence of surfactants cannot be matched with known XRD patterns.[3-4] Figure 6.1. shows the XRD patterns of the **C1**-**C3** samples prepared at pH = 3, 7, and 10 after annealing at 1100 ° C. The annealing temperature of 1100 ° C was chosen based on the observations made by Wang et al.[5] In their study they showed that lower annealing temperatures (650 or 750 °C) gave metastable forms of Y_2WO_6. As can be seen from the XRD pattern in Figure 6.1. when the reaction is carried out at pH = 3 a pure monoclinic Y_2WO_6 phase with no additional peaks is obtained. When the reaction solution is adjusted to neutral pH characteristic XRD patterns of a monoclinic Y_2WO_6 phase can be distinguished, yet the XRD pattern is noisy and some additional peaks are present. When the reaction was carried out at pH = 10 the obtained XRD pattern could not be matched to a known phase.

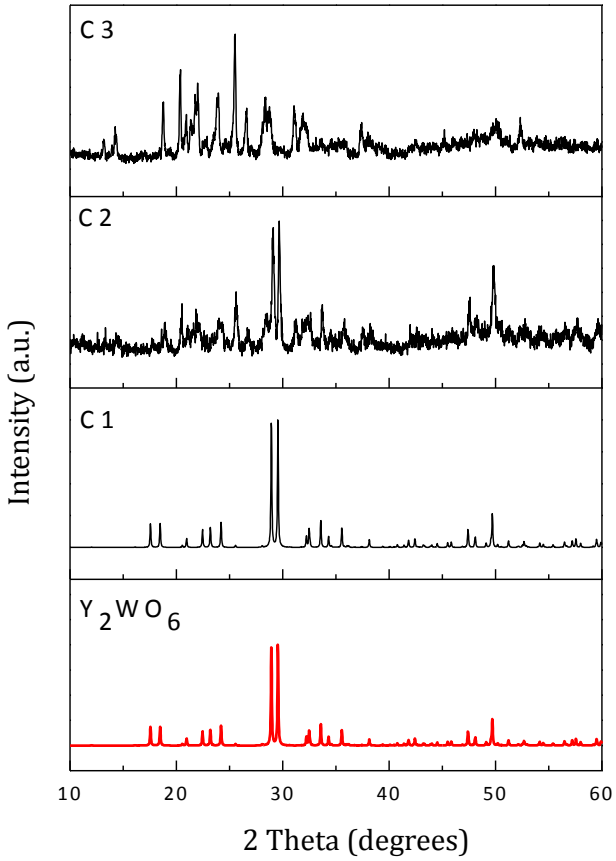

Figure 6.1: XRD patterns of Y_2WO_6 materials obtained at different pH values (C1 pH = 3, C2 pH = 7, C3 pH = 10) and annealed at 1100 °C for 3 h.

The morphologies of the **C1**-**C3** samples were characterized by SEM (Figure 6.2. and Figure 6.3.). All of the presented SEM images are of samples after annealing. For the synthesis of these materials an amount of 1 mmol of the surfactant was chosen based on our previous experience with rare-earth tungstate syntheses in the presence of a surfactant.[4] Preliminary experiments showed that amounts lower than 1 mmol caused the microstructures to be more aggregated. Using higher amounts usually did not show any differences. Occasionally some cracks could be visible on the surface of the

microstructures. Figure 6.2. shows that when the synthesis was carried out at pH = 3 spherical microstructures composed of nanosized building blocks were obtained as the product. The diameter of these microspheres was mostly between 2–5 μm, therefore they had quite a broad size distribution. It can be observed that the nanobuilding blocks are regular and are very tightly packed together.

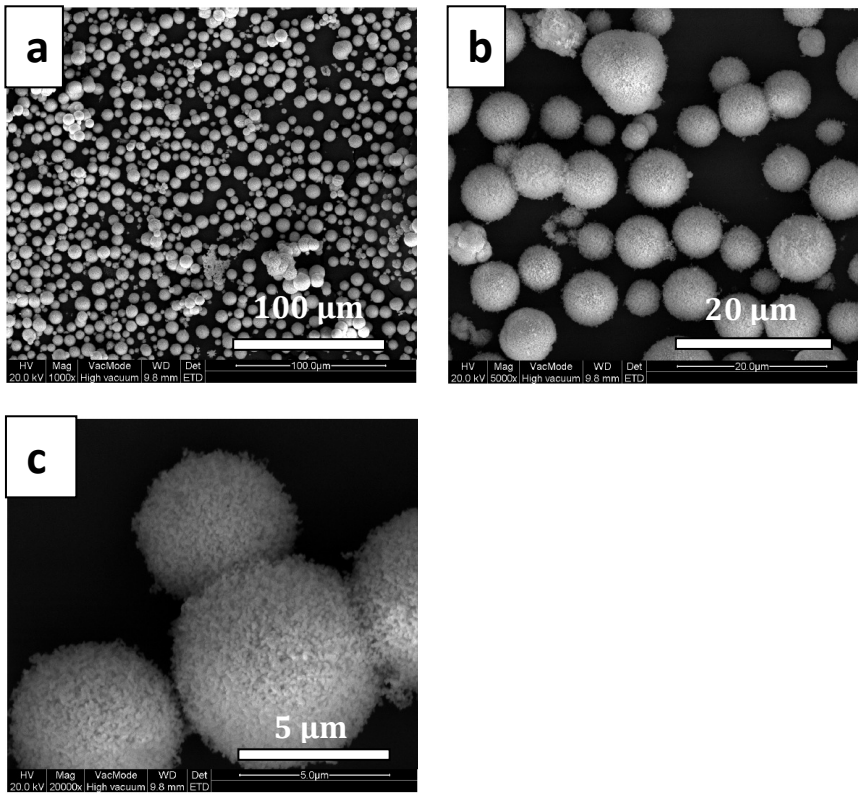

Figure 6.2: SEM images of sample C1 at different magnifications.

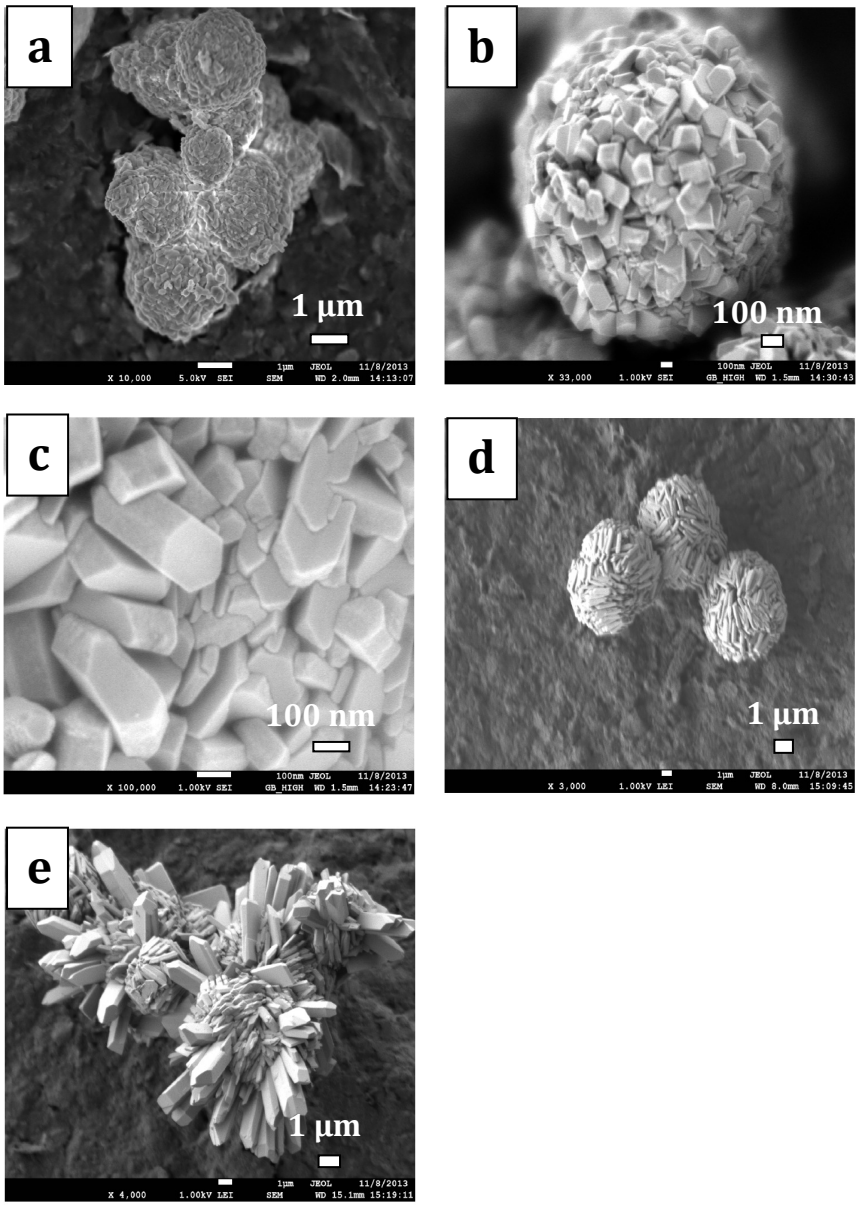

Figure 6.3: SEM images of (a) – (c) C2 and (d) – (e) C3.

When the pH of the reaction was raised to 7 also microspheres were formed. The products have been presented in Figures 6.3.a-c. These microstructures are built from irregularly shaped nanosized building blocks. The building blocks are varied in their size and shape and are tightly packed to form the spherical structures. The microstructures have an average diameter between 1-3 μm. When the pH of the reaction was adjusted to pH = 10 microspheres several microns in size were formed (Figures 6.3.e-f). They are built from regular rods stacked together to form the microspheres. Although these architectures were quite regular in their size occasionally some of the microspheres had larger rods growing out from the core of these structures.

Based on the observed XRD patterns as well as SEM images the microstructures synthesized at pH = 3 were chosen for further studies on the photoluminescence properties of Ln^{3+} doped Y_2WO_6. As only the **C1** material was further studied, it will be referred to as **Y_2WO_6** throughout the chapter.

6.3.2. Luminescence properties of Ln^{3+} doped Y_2WO_6 materials (Ln = Sm^{3+}, Eu^{3+}, Gd^{3+}, Dy^{3+})

In this subchapter the luminescence properties of Sm^{3+}, Eu^{3+}, Gd^{3+} and Dy^{3+} doped Y_2WO_6 samples prepared from nitrate salts, in the presence of 1 mmol SDS, at pH 3, before and after heat treatment at 1100 °C, were investigated. Concentrations of 2.5%, 5%, and 10% of the Ln^{3+} ions were doped into the Y_2WO_6 matrix. For the optimal lanthanide ion concentrations the systems were co-doped with either 2% or 10% Gd^{3+} ions to test the possible enhancement of luminescence through energy transfer from W-O and/or Gd^{3+} to Ln^{3+}.

6.3.2.1. Luminescence properties of Ln^{3+} doped Y_2WO_6 materials (**C1**) (Ln = Sm^{3+}, Eu^{3+}, Dy^{3+})

Room temperature combined excitation-emission spectra of 2.5% Ln^{3+} doped Y_2WO_6 (Ln = Sm^{3+}, Eu^{3+}, Dy^{3+}) samples after heat treatment at 1100 °C are presented in Figure 6.4., Figure. 6.5. and Figure 6.6. All of the peaks have been assigned to the appropriate electronic transitions in Table 6.1.[6-8] All of the excitation spectra contain a strong and broad band in the region 250 – 350 nm, and a series of sharp excitation peaks (they are much lower in intensity compared to the broad band), which can be assigned to typical intra-4f transitions of lanthanide ions. The broad band corresponds to the charge transfer absorption from the 2p orbitals of the oxygens to the 5d orbitals of tungsten. The emission spectra were obtained upon excitation into the O-W charge transfer band at 302.0 nm. The emission spectra consist of sharp emission peaks characteristic for Eu^{3+}, Sm^{3+}, and Dy^{3+} ions respectively. In the case of Sm^{3+} and Dy^{3+} weak broad O-W bands can additionally be observed in the emission spectra (the Eu doped Y_2WO_6 emission spectrum is presented from 550 nm as there was no broad band in the region of 400–550 nm). The fact that these charge transfer bands are so weak, or not present at all indicates that there is an efficient transfer of energy from the tungstate groups to the doped lanthanide ions. In the emission spectrum of **2.5% Eu:Y_2WO_6** sample the $^5D_0 \rightarrow {}^7F_1$ transition peak (peak e in Figure 6.3.) splits into more than three peaks indicating that more than one Y^{3+} crystallographic site is occupied by Eu^{3+} ions.[9]

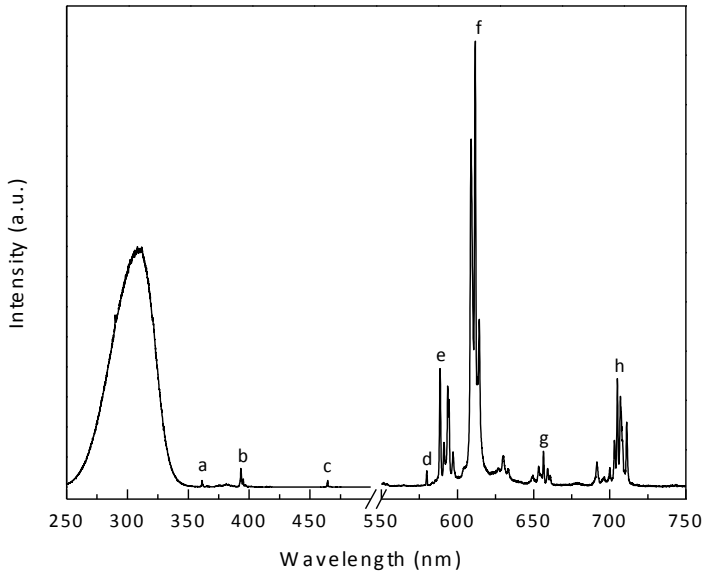

Figure 6.4: Excitation spectrum (monitored at 611.6 nm) and emission spectrum (excited at 302.0 nm) of 2.5% Eu: Y_2WO_6 sample. The electronic transitions labeled a–h have been assigned in Table 6.1.

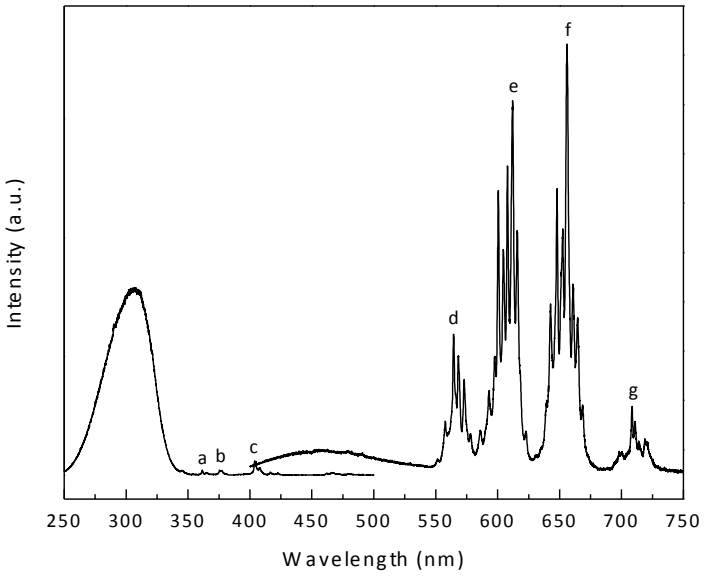

Figure 6.5: Excitation spectrum (monitored at 655.9 nm) and emission spectrum (excited at 302.0 nm) of 2.5% Sm: Y_2WO_6 sample. The electronic transitions labeled a–g have been assigned in Table 6.1.

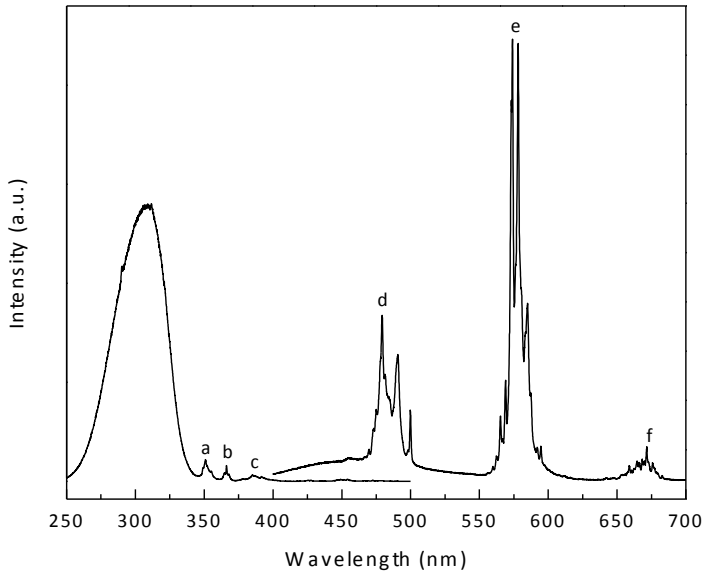

Figure 6.6: Excitation spectrum (monitored at 574.0 nm) and emission spectrum (excited at 302.0 nm) of 2.5% Dy: Y_2WO_6 sample. The electronic transitions labeled a–f have been assigned in Table 6.1.

Table 6.1. Assignment of labeled transitions shown in Figures 6.4. – 6.6.

	Excitation				Emission			
	Wavelength (nm)	Energy (cm^{-1})	Transition		Wavelength (nm)	Energy (cm^{-1})	Transition	
			2.5% Eu_Y_2WO_6					
a	361.2	27686	$^5D_4$	← $^7F_0$	**d** 579.9	17244	$^5D_0$ →	$^7F_0$
b	393.3	25426	$^5L_6$		**e** 588.6	16989		$^7F_1$
c	464.6	21524	$^5D_2$		**f** 611.8	16345		$^7F_2$
					g 656.5	15232		$^7F_3$
					h 705.0	14184		$^7F_4$
			2.5% Sm_Y_2WO_6					
a	361.6	27655	$^4D_{5/2}$, $^6P_{5/2}$, $^4D_{3/2}$	← $^6H_{5/2}$	**d** 564.4	17718	$^4G_{5/2}$ →	$^6H_{5/2}$
b	376.3	26574	$^6P_{7/2}$		**e** 612.1	16337		$^6H_{7/2}$
c	403.7	24771	$^6P_{3/2}$		**f** 656.2	15239		$^6H_{9/2}$
					g 708.4	14116		$^6H_{11/2}$

Table 6.1. (continued).

				2.5% Dy_Y_2WO_6				
a	350.9	28498	$^6P_{7/2}$	$\leftarrow {}^6H_{15/2}$	**d**	479.3	20864	$^4F_{9/2} \rightarrow$ $^6H_{15/2}$
b	366.2	27308	$^6P_{5/2}$, $^4P_{3/2}$, $^4D_{3/2}$, $^4M_{19/2}$		**e**	574.0	17422	$^6H_{13/2}$
c	385.2	25961	$^4I_{13/2}$, $^4F_{7/2}$		**f**	671.6	14890	$^6H_{11/2}$

The luminescence decay curves of 2.5% Eu, Sm, and Dy doped Y_2WO_6 were measured when excited at 302.0 nm and monitored at the appropriate wavelength. The decay curves could be well fitted using the single exponential equation. The luminescence lifetime of **2.5% Eu: Y_2WO_6** was found to be 559 µs. For **2.5% Sm: Y_2WO_6** the lifetime was calculated to be 272 µs and 112 µs for **2.5% Dy: Y_2WO_6**. The QY of **2.5% Eu: Y_2WO_6** was determined to be 53%. QYs for **2.5% Sm: Y_2WO_6** and **2.5% Dy: Y_2WO_6** were found to be 8% and 17%, respectively.

When the samples were placed under a laboratory UV lamp, choosing an excitation wavelength of 302.0 nm, the 2.5% Eu, Sm, Dy doped samples showed a red, orange-pink, and white color, respectively (Figure 6.7).

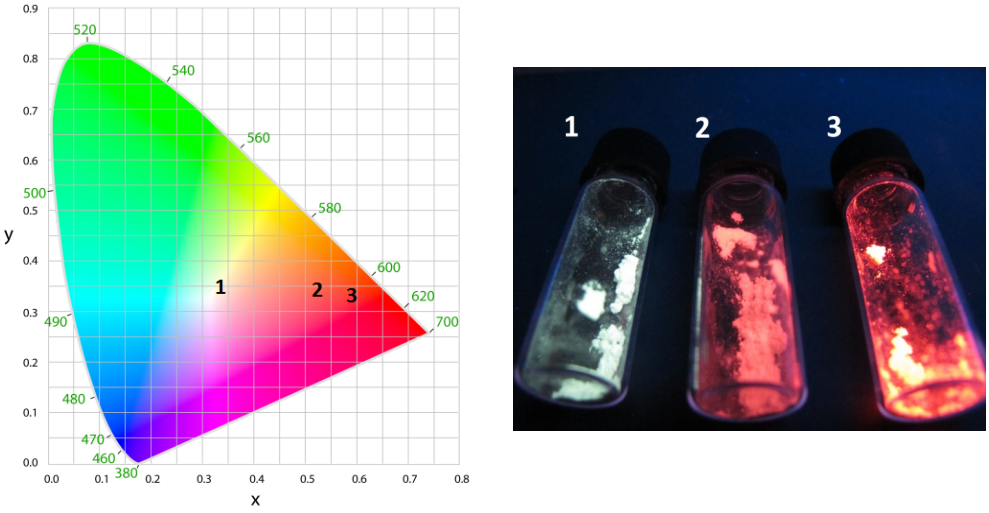

Figure 6.7: CIE color coordinate diagram (left) and photograph (right) of (1) 2.5% Dy: Y_2WO_6, (2) 2.5% Sm: Y_2WO_6, (3) 2.5% Eu: Y_2WO_6. The photograph was taken when the samples were placed under a laboratory UV lamp (at a 302.0 nm excitation wavelength).

Figure 6.7. also presents the CIE chromaticity diagram of these samples calculated based on the emission spectra data and color matching functions issued by CIE in 1931. The CIE coordinates for **2.5% Eu: Y_2WO_6** were determined to be x = 0.581, y = 0.338. The CIE coordinates for **2.5% Sm: Y_2WO_6** were determined to be x = 0.510, y = 0.344. For the **2.5% Dy: Y_2WO_6** sample the CIE coordinates were calculated to be x = 0.324, y = 0.353. These coordinates of the **2.5% Dy: Y_2WO_6** sample are close to the standard white light (x = 0.333, y = 0.333). The color temperature of the white emitting **2.5% Dy: Y_2WO_6** sample was determined to be 4428 K. The color temperature is a measurement in degrees Kelvin that indicates the tone of a specific type of light source. The **2.5% Dy: Y_2WO_6** sample falls under the category of neutral white light (neutral white light sources reveal a clear, white light with little blue or red tones). This type of white light is most often used in office areas.

The influence of the doping percentage of the Ln^{3+} ion on the luminescence properties of these materials was investigated. Besides the 2.5% doped Y_2WO_6 samples materials with 5% and 10% Ln^{3+} doping were synthesized. It was observed that for the Eu: Y_2WO_6 material with the increase of Eu^{3+} ion concentration the emission intensity, decay time and QY values increase (when increasing the Eu^{3+} doping concentration above 10% the emission intensity, decay time and QY values started to drop). The intensity of the emission spectra of Eu: Y_2WO_6 samples with different doping concentrations have been compared in Figure 6.8. Figure 6.9. and Figure 6.10. show analogous graphs for Sm^{3+} and Dy^{3+} samples, respectively. The decay times as well as QYs have been collected in Table 6.2. Figure 6.11. presents the decay curves of Eu: Y_2WO_6 samples with different doping concentrations. As can be seen the **10% Eu: Y_2WO_6** has the longest decay time. Also the **10% Eu: Y_2WO_6**

material shows a QY as high as 68%. Unlike for the Eu^{3+} doped materials, the Sm doped Y_2WO_6 and Dy doped Y_2WO_6 samples showed a different tendency. The 2.5% doped samples (**2.5% Sm: Y_2WO_6** and **2.5% Dy: Y_2WO_6**) were found to have the strongest luminescence emission, longest decay times, and highest QY values. With the rise of dopant concentration these values gradually decreased. The exact decay times and QYs can also be found in Table 6.2. For some of the samples with the change of dopant ion concentration there was a slight change in the emitted colors. As has been mentioned previously the **2.5% Dy: Y_2WO_6** material emitted white light under 302.0 nm excitation. The 5% and 10% Dy^{3+} doped samples showed white-yellow light instead of pure white light. The color temperature for the **5% Dy: Y_2WO_6** and **10% Dy: Y_2WO_6** samples were calculated to be 4428 K and 3880 K, respectively.

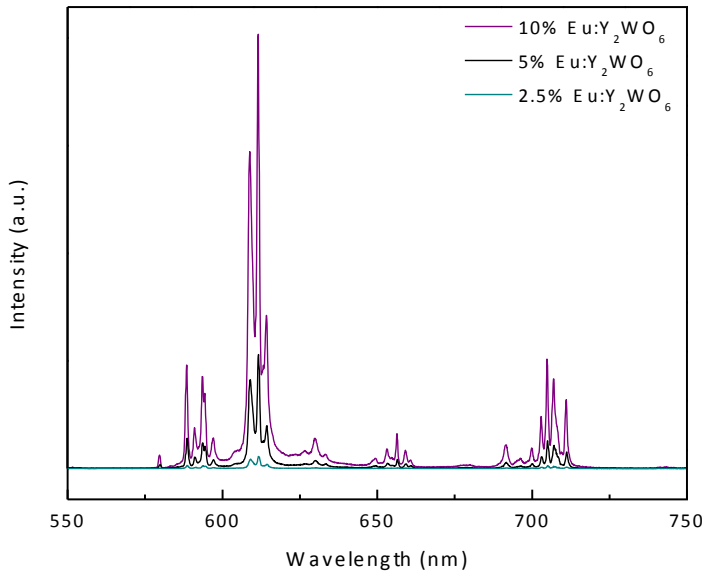

Figure 6.8: Emission spectra of Eu^{3+} (2.5%, 5%, and 10%) doped Y_2WO_6 microstructures excited at 302.0 nm.

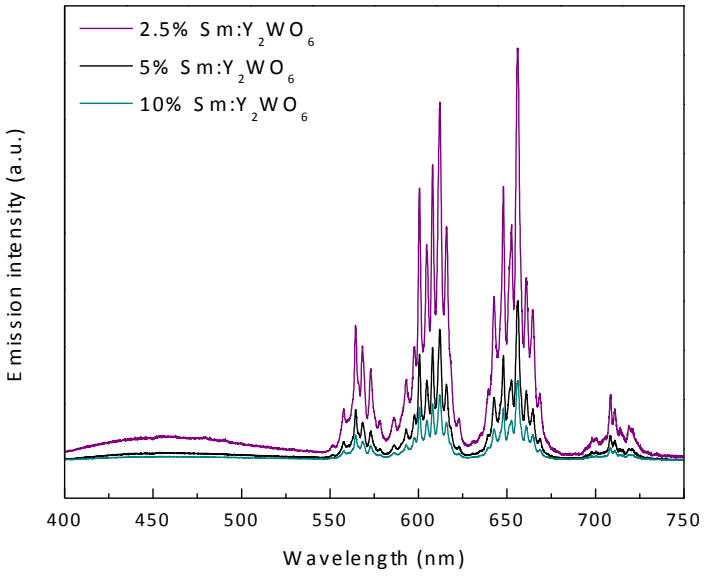

Figure 6.9: Emission spectra of Sm^{3+} (2.5%, 5%, and 10%) doped Y_2WO_6 microstructures excited at 302.0 nm.

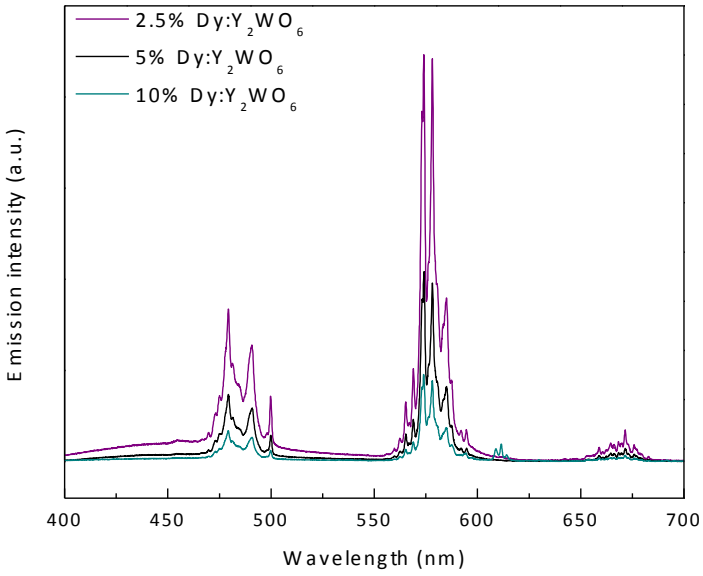

Figure 6.10: Emission spectra of Dy^{3+} (2.5%, 5%, and 10%) doped Y_2WO_6 microstructures excited at 302.0 nm.

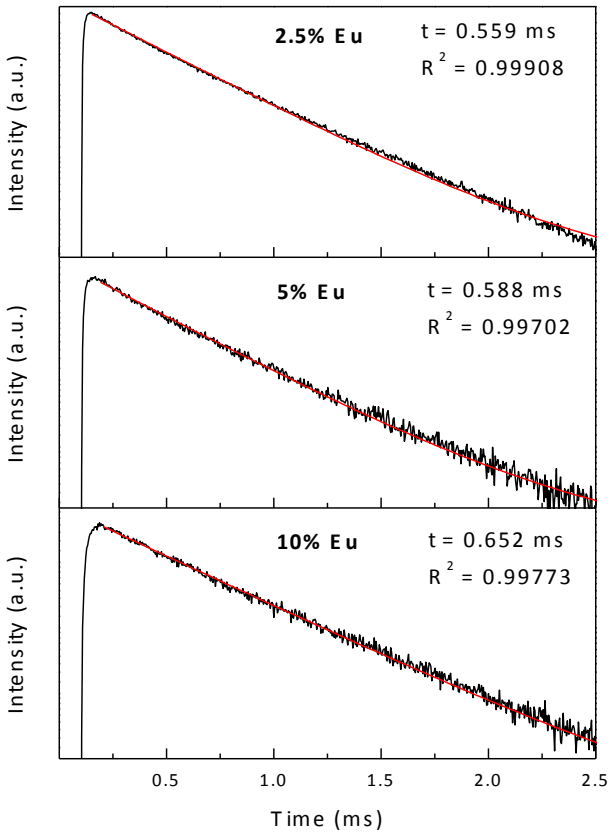

Figure 6.11: Luminescence decay curves for Eu: Y_2WO_6 (2.5%, 5%, and 10%), λ_{ex} = 302.0 nm, λ_{em} = 611.6 nm. Red solid lines represent the fitting results.

Table 6.2. Luminescence decay times and QY values of studied Y_2WO_6 doped samples (samples after heat treatment).

Sample	Luminescence decay time (μs)	Quantum Yield (%)
2.5% Eu:Y_2WO_6	559	53
5% Eu:Y_2WO_6	588	56
10% Eu:Y_2WO_6	652	68
2.5% Eu_2% Gd:Y_2WO_6	651	62
2.5% Eu_10 % Gd:Y_2WO_6	582	37
10% Eu_2% Gd:Y_2WO_6	701	79
10% Eu_10% Gd:Y_2WO_6	566	33
2.5% Sm:Y_2WO_6	272	8
5% Sm:Y_2WO_6	180	3
10% Sm:Y_2WO_6	114	1
2.5% Sm_2% Gd:Y_2WO_6	320	11
2.5% Sm_10% Gd:Y_2WO_6	420	19
2.5% Dy:Y_2WO_6	119	17
5% Dy:Y_2WO_6	78	4
10% Dy:Y_2WO_6	56	2
2.5% Dy_2% Gd:Y_2WO_6	155	21
2.5% Dy_10% Gd:Y_2WO_6	160	22

It is normally expected that with the increase of Ln^{3+} ion concentration the decay times decrease due to concentration quenching. As has been presented in the results discussed above the optimal concentration of Eu^{3+} in the Y_2WO_6 material is 10%, whereas for Sm^{3+} and Dy^{3+} the optimal concentration is 2.5%. After doping the Y_2WO_6

with more than 10% Eu^{3+} ions a decrease of these values is also observed. The low critical quenching concentration of the Sm^{3+} and Dy^{3+} ions (compared to Eu^{3+} ions) may be due to the cross-relaxation effect of these ions.[10] Eu^{3+} ions have a higher quenching concentration as no such cross-relaxation effect exists for these ions (in general the cross-relaxation effect will cause the activator ion to have a low quenching concentration).

In order to further deepen the understanding of these materials the luminescence properties of the precursor materials (as synthesized materials without annealing at 1100 °C) were investigated and compared with the Y_2WO_6 materials after heat treatment. In all the cases the excitation spectra of the precursor samples are similar to the heat treated ones, yet a shift of the broad O-W charge transfer band towards shorter wavelengths can be observed in the precursor samples. As an example the excitation spectra of **2.5% Eu: Y_2WO_6** material before and after heat treatment at 1100 °C have been compared (see Figure 6.12.). In the samples before heat treatment (precursor samples) from the relative intensities of the f-f transitions compared to the broad charge transfer band it can be estimated that the energy transfer is less efficient then in the heat treated systems. This may be due to the conversion from distorted tungstate groups in the precursor material to regular tungstate groups in the heat treated material. Differences are also observed in the emission spectra. In the precursor samples of **2.5% Sm: Y_2WO_6** and **2.5% Dy: Y_2WO_6** the characteristic f-f transition peaks of these lanthanides are partially overlapped with strong broad charge transfer bands (Figure 6.13.). The presence of these bands indicates that the transfer of energy from the tungstate groups to the Ln^{3+} ions is not as efficient as in the heat treated samples. Because of the presence of this strong broad band there is a

significant difference in the color that the Sm^{3+} doped precursor samples emit compared to the heat treated samples (the broad band gives a blue-green color component). The **2.5% Sm: Y_2WO_6 precursor**, **5% Sm: Y_2WO_6 precursor**, and **10% Sm: Y_2WO_6 precursor** samples all gave white light when excited with a 302.0 nm laboratory lamp. After heat treatment in all cases the emission color changed to orange-pink. The Dy^{3+} doped precursor samples (**2.5% Dy: Y_2WO_6 precursor**, **5% Dy: Y_2WO_6 precursor**, and **10% Dy: Y_2WO_6 precursor**) also showed white light emission at the three investigated ion concentrations (according to the CIE color diagram the samples gave a bluish-white light, though the blue component was not visible when exciting the samples with a UV lamp). As can be seen from Table 6.3. all the Ln^{3+} doped Y_2WO_6 precursor materials have decay times significantly shorter from the corresponding materials after heat treatment (see Table 6.2. for comparison with the heat treated samples). Also the QYs are notably lower compared to the annealed materials.

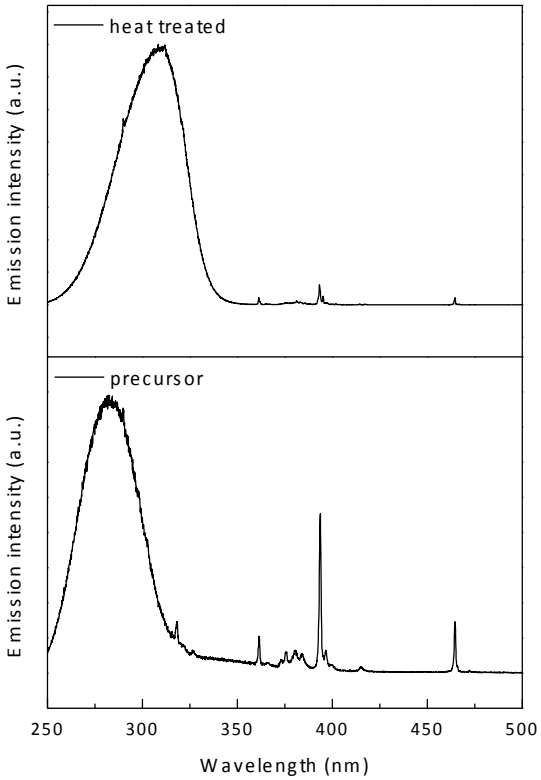

Figure 6.12. Excitation spectra of 2.5% Eu: Y_2WO_6 sample before (bottom) and after heat treatment (top).

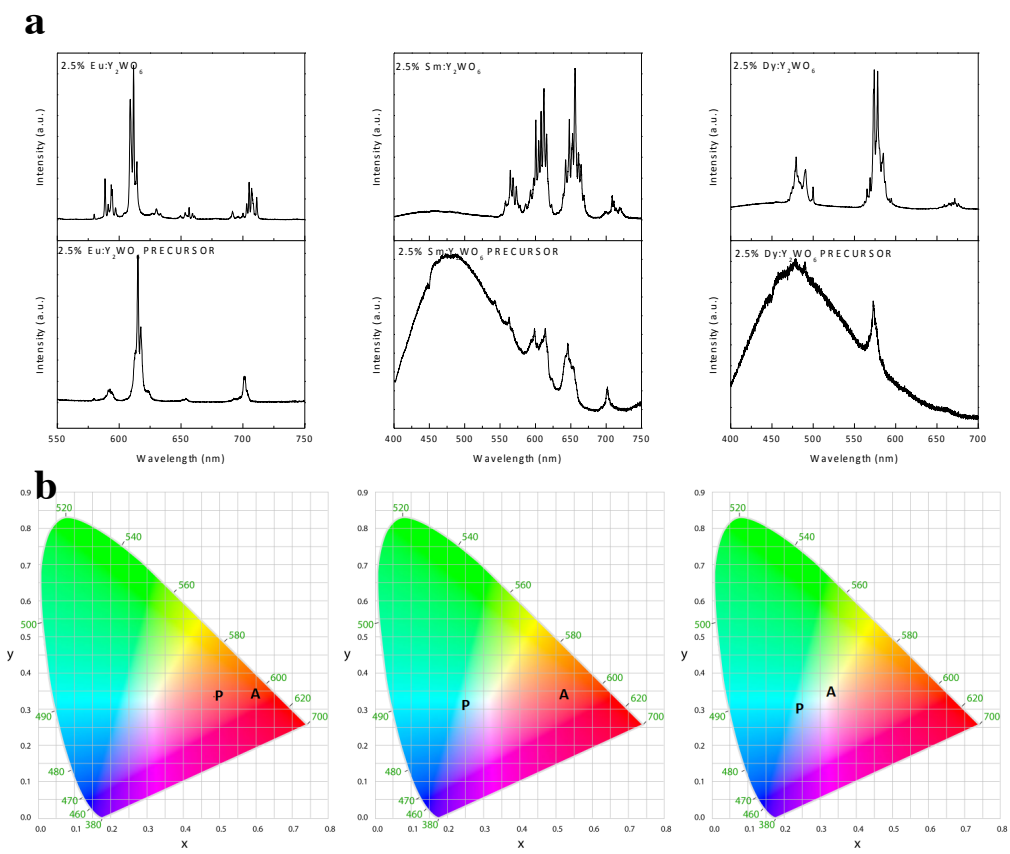

Figure 6.13: a) Comparison of the emission spectra of 2.5% Eu, Sm and Dy doped Y_2WO_6 samples before (bottom) and after heat treating at 1100 °C (top). The precursor samples were excited at 283.0 nm, whereas the heat treated samples were excited at 302.0 nm (corresponding to the maximum of the O-W charge transfer band in each case). b) The CIE coordinates are shown on the color diagrams: precursor (P) and annealed sample (A).

Table 6.3. Decay times and QY values of studied Y_2WO_6 doped samples (samples before heat treatment).

Sample	Luminescence decay time (μs)	Quantum Yield (%)
2.5% Eu:Y_2WO_6 precursor	417	12
5% Eu:Y_2WO_6 precursor	424	19
10% Eu:Y_2WO_6 precursor	449	27
2.5% Sm:Y_2WO_6 precursor	138	3
5% Sm:Y_2WO_6 precursor	77	< 1
10% Sm:Y_2WO_6 precursor	56	<1
2.5% Dy:Y_2WO_6 precursor	84	5
5% Dy:Y_2WO_6 precursor	62	<1
10% Dy:Y_2WO_6 precursor	50	<1

6.3.2.2. Luminescence properties of Gd^{3+} co-doped Ln^{3+}: Y_2WO_6 materials (Ln = Sm^{3+}, Eu^{3+}, Dy^{3+})

It is known from literature that co-doping certain ions (for example Gd^{3+}, Ba^{2+}, Bi^{3+}, Li^+, K^+, Na^+) into a phosphor matrix can improve its luminescence properties.[11-13] In the research work presented in this chapter it was observed that incorporating Gd^{3+} ions into the matrix does not cause any changes in the excitation spectra. A different situation is observed for example for Bi^{3+} ions, where co-doping them into a phosphor material leads to a shift of the excitation band towards longer wavelengths.[12] The reasoning for the improvement of luminescence properties of a Ln^{3+} doped material after co-doping with Gd^{3+} ions is still not quite understood and different energy transfer mechanisms have been proposed by researchers.[14-16] It is likely that the

presence of the Gd^{3+} ions in the material increases the luminescence properties of Eu^{3+}, Sm^{3+} and Dy^{3+} doped Y_2WO_6 due to the fact that Gd^{3+} ions have better matching energy levels to accept the energy from the tungstate matrix and subsequently pass it on to the Eu^{3+}, Sm^{3+} or Dy^{3+} ions. One could also assume that the increase in luminescence could be due to the change of local crystal field of the Ln^{3+} ions after co-doping Gd^{3+} ions into the matrix. Yet, in the case of a change in the local crystal field of the Eu^{3+} ions we would expect to see a difference in the peak splitting when comparing the Eu^{3+}: Y_2WO_6 materials with the Gd^{3+}_Eu^{3+}: Y_2WO_6 materials. This was not observed in the materials synthesized during this PhD. While it was observed that incorporating Gd^{3+} ions into the Ln^{3+}: Y_2WO_6 matrix did not have effect on the peak splitting and relative peak intensities in the excitation and emission spectra, a significant change in the photoluminescence intensity was visible. For the Eu^{3+}: Y_2WO_6 material the 10% Eu^{3+} doped sample (**10% Eu: Y_2WO_6)** was chosen to test the effect of co-doping Gd^{3+} ions, because the 10% Eu^{3+} doping in this material showed the strongest luminescence. The QY of **10% Eu_2% Gd: Y_2WO_6** was calculated to be 79%. Therefore there was an increase in QY compared to the **10% Eu: Y_2WO_6** material (QY = 68%). When the amount of co-doped Gd^{3+} ions was increased to 10% (**10% Eu_10% Gd: Y_2WO_6**) a drop in emission intensity, as well as decay time and QY value was observed. The QY dropped to 33% in this system (see Figures 6.14. – 6.16. and Table 6.4.). This can most likely be explained by quenching effects when the co-doping percentage of Gd^{3+} ions is so high.[16] Concentration quenching is a manifestation of the Förster non-radiative energy transfer phenomenon.[17-18] It is characterized by a decrease in the QY value as the concentration of the dopant is increased. This phenomenon is most likely caused by the rise in the number of non-radiative decay

channels. Additionally the **2.5% Eu: Y_2WO_6** material was also co-doped with 2% and 10% Gd^{3+} ions. In the case of **2.5% Eu_2% Gd: Y_2WO_6** an increase in luminescence intensity, decay time, and QY were observed (QY = 62%). Co-doping the system with 10% Gd^{3+} (**2.5% Eu_10% Gd: Y_2WO_6**) again caused these values to decrease (QY = 37%). From these experiments it can be concluded that for Eu^{3+}: Y_2WO_6 the **10% Eu_2% Gd: Y_2WO_6** system is the most efficient.

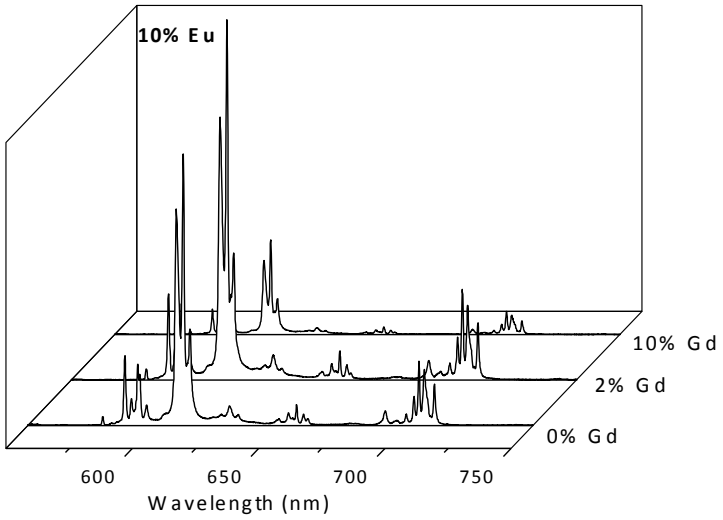

Figure 6.14: Change in emission intensity observed for 10% Eu: Y_2WO_6 co-doped with 0%, 2%, and 10% Gd^{3+} ions.

The 2.5% doped Sm^{3+} and Dy^{3+} materials were also co-doped with Gd^{3+} ions. The 2.5% ion doped samples were chosen for this experiment as for the Sm^{3+} and Dy^{3+} doped Y_2WO_6 materials they showed the largest emission intensity, longest decay times and highest QYs. In both cases with the incorporation of both 2% and 10% Gd^{3+} ions the

luminescence efficiency increased. The highest QY values were measured for the **2.5% Sm_10% Gd: Y_2WO_6** and **2.5% Dy_10% Gd: Y_2WO_6** samples: 19% and 22%, respectively. This means that the QY of the **2.5% Sm_10% Gd: Y_2WO_6** is approximately 2.4 times larger than that in the **2.5% Sm: Y_2WO_6** material.

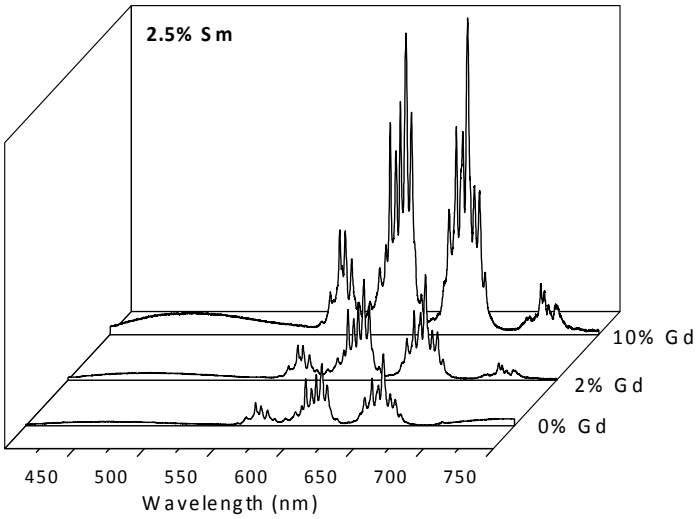

Figure 6.15: Change in emission intensity observed for 2.5% Sm: Y_2WO_6 co-doped with 0%, 2%, and 10% Gd^{3+} ions.

For the 2.5% Dy doped material the increase is not that significant. Some slight changes in the emitted colors were also visible. This was especially noticeable for the Dy^{3+} system where after co-doping with Gd^{3+} the sample emitted pale yellow (although a shade of blue is visible when the sample is observed under a 302.0 nm UV lamp) instead of white light. The color temperature of **2.5% Dy_10% Gd: Y_2WO_6** sample was determined to be 3591 K (compared to 4428 K for the sample with no co-

doped Gd^{3+} ions). Therefore, co-doping the **2.5% Dy: Y_2WO_6** sample with 10% Gd^{3+} ions shifts the color towards warm white (halogen white). Table 6.2. summarizes the decay times and QY values of all the discussed materials. Table 6.4. presents the calculated CIE coordinates and colors assigned to these coordinates for all the materials discussed in this chapter.

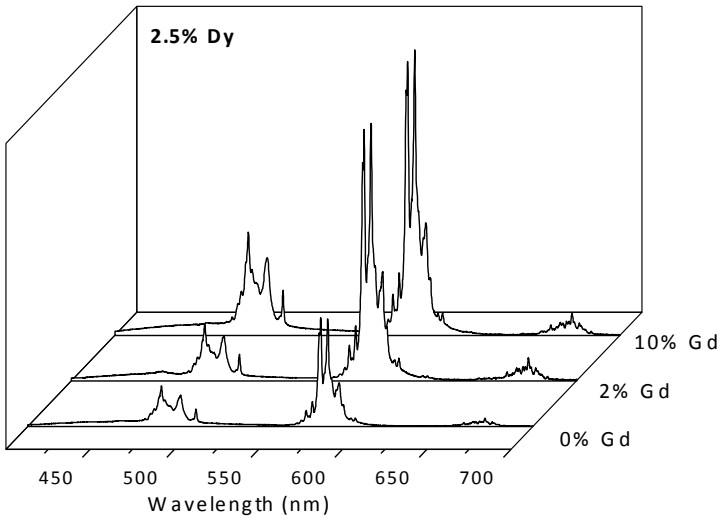

Figure 6.16: Change in emission intensity observed for 2.5% Dy: Y_2WO_6 co-doped with 0%, 2%, and 10% Gd^{3+} ions.

Figure 6.17: Photo presenting the most efficient doped Y_2WO_6 systems as seen under a 302.0 nm UV lamp (from left to right): 10% Eu_2% Gd: Y_2WO_6, 2.5% Sm_10% Gd: Y_2WO_6, 2.5% Dy_10% Gd: Y_2WO_6.

Table 6.4. Comparison of CIE chromaticity coordinates for Ln^{3+} doped Y_2WO_6 samples and Ln^{3+} doped Y_2WO_6 precursor samples.

Doped ion	Material	CIE (x)	CIE (y)	Color
Eu^{3+}	**2.5% Eu:Y_2WO_6 precursor**	0.48	0.33	orange-pink
	2.5% Eu:Y_2WO_6	0.58	0.34	red
	2.5% Eu_2% Gd:Y_2WO_6	0.59	0.33	red
	2.5% Eu_10% Gd:Y_2WO_6	0.65	0.35	reddish orange
	5% Eu:Y_2WO_6 precursor	0.57	0.34	red
	5% Eu:Y_2WO_6	0.64	0.34	reddish orange
	10% Eu:Y_2WO_6 precursor	0.63	0.33	reddish orange
	10% Eu:Y_2WO_6	0.64	0.35	reddish orange
	10 % Eu_2% Gd:Y_2WO_6	0.64	0.35	reddish orange
	10% Eu_10% Gd:Y_2WO_6	0.64	0.34	reddish orange

Table 6.4. (continued)

Sm^{3+}	**2.5% Sm:Y_2WO_6 precursor**	0.24	0.30	white
	2.5% Sm:Y_2WO_6	0.51	0.34	orange-pink
	5% Sm:Y_2WO_6 precursor	0.24	0.31	white
	5% Sm:Y_2WO_6	0.52	0.35	orange-pink
	10 % Sm:Y_2WO_6 precursor	0.27	0.32	white
	10% Sm:Y_2WO_6	0.54	0.35	orange-pink
	2.5% Sm_2% Gd:Y_2WO_6	0.52	0.34	orange-pink
	2.5% Sm_10% Gd:Y_2WO_6	0.44	0.33	orange-pink
Dy^{3+}	**2.5% Dy:Y_2WO_6 precursor**	0.24	0.31	white
	2.5% Dy:Y_2WO_6	0.32	0.35	white
	5% Dy:Y_2WO_6 precursor	0.24	0.31	white
	5% Dy:Y_2WO_6	0.37	0.39	white
	10 % Dy:Y_2WO_6 precursor	0.24	0.31	white
	10% Dy:Y_2WO_6	0.39	0.39	white
	2.5% Dy_2% Gd:Y_2WO_6	0.41	0.41	white
	2.5% Dy_10% Gd:Y_2WO_6	0.37	0.39	white

6.4. Conclusions

In this chapter Eu^{3+}, Sm^{3+}, and Dy^{3+} doped Y_2WO_6 materials were synthesized hydrothermally in the presence of SDS surfactant, which was used as a structure directing agent. Only at pH 3 a pure phased material – monoclinic Y_2WO_6 – was obtained. 3D spherical microstructures built from irregular nanosized building blocks were formed in these reaction conditions. By varying the dopant ion concentration and by co-doping the Y_2WO_6 materials with different concentrations of Gd^{3+} ions the

emission intensities, decay times, quantum yields and colors emitted by the samples could be changed. Some of the obtained samples were shown to give white light. For example the **2.5% Dy: Y_2WO_6** sample emitted white light when excited at 302.0 nm. The QY of this white emitting material was evaluated to be 17%. The most efficient system was observed for **10% Eu_2% Gd: Y_2WO_6** where the QY reached 79%. Doping 10% Gd^{3+} ions into the 2.5% Sm: Y_2WO_6 material gave a QY approximately 2.4 times larger than of the material with no Gd^{3+} ions. Among the studied systems the Sm^{3+}, Gd^{3+} co-doped system showed the highest increase of efficiency compared to the system without co-doped Gd^{3+} ions. Co-doping Gd^{3+} ions was shown to be a successful way of increasing the luminescence properties, as well as tuning the emitted light color, of the lanthanide doped Y_2WO_6 material.

6.5. References

1. Zhou, Y.; Yan, B. *CrystEngComm* **2013**, 15, 5694.

2. Zhou, Y.; Yan, B.; He, X.-H. *J. Mater. Chem. C* **2014**, *2*, 848.

3. Huang, S.; Zhang, X.; Wang, L.; Bai, L.; Xu, J.; Li, C.; Yang, P. *Dalton Trans*. **2012**, 41, 5634.

4. Kaczmarek, A. M.; Liu, Y.-Y.; Van Der Voort, P.; Van Deun, R. *Dalton Trans.* **2013**, 42, 5471.

5. Wang, J;. Zhang, Z.-J.; Zhao, J.-T.; Chen, H.-H.; Yang, X.-X.; Tao, Y.; Huang, Y. *J. Mater. Chem*. **2010**, 20, 10894.

6. Carnall, W.T.; Fields, P.R.; Rajniak, K. *J. Chem. Phys.*, **1968**, 49, 4450.

7. Carnall, W.T.; Fields, P.R.; Rajniak, K. *J. Chem. Phys.*, **1968**, 49, 4447.

8. Carnall, W.T.; Fields, P.R.; Rajniak, K. *J. Chem. Phys.*, **1968**, 49, 4424.

9. Binnemans, K. Görller-Walrand, C. *J. Rare Earth*, **1996**, 14, 174.

10. Li, Y.-C.; Chang, Y.-H.; Lin, Y.-F.; Chang, Y.-S.; Lin, Y.-J. *J. Alloy Compd*., **2007**, 439, 367.

11. Singh, B. P.; Parchur, A. K.; Ningthoujam, R.S.; Ansari, A. A.; Singh, P.; Rai, S. B. *Dalton Trans*. **2014**, 43, 4779.

12. Devi, Ch. V.; Phaomei, G.; Yaiphaba, N.; Rajmuhon Singh N. *J. Alloys Compd.* **2014**, 583, 259.

13. Ryba-Romanowski, W.; Gołąb, S.; Dominiak-Dzik, G.; Solarz, P. *Appl. Phys. A* **2002**, 74, 581.

14. Debasu, M. L.; Ananias, D.; Rocha, J.; Malta, O. L.; Carlos, L. D. *Phys. Chem. Chem. Phys.* **2013**, 5, 15565.

15. Li, Y.-C.; Chang, Y.-H.; Chang, Y.-S.; Lin, Y.-J.; Laing, C.-H. *J. Phys. Chem. C* **2007**, 111, 10682.

16. Pu, Y.; Tang, K.; Zhu, D.-C.; Han, T.; Zhao, C.; Peng, L.-L. *Nano-Micro Letters* **2013**, 5, 117.

17. Förster, *T. Discuss. Faraday Soc*. **1959**, 27, 7.

18. Carnall, W. T.; Fields, P. R.; Rajnak, K. *J. Chem. Phys.* **1968**, *49*, 4443.

Chapter 7: Luminescence of Tb^{3+} doped $Ce_2(WO_4)_3$ and $Ce_{10}W_{22}O_{81}$ 3D microstructures

In this chapter the synthesis and luminescence properties of Tb^{3+} doped $Ce_2(WO_4)_3$ and $Ce_{10}W_{22}O_{81}$ materials are presented. The materials were obtained at hydrothermal conditions, in the presence and absence of dioctyl sodium sulfosuccinate (DSS) surfactant. $Ce_2(WO_4)_3$ material was obtained when the pH of the reaction was not adjusted (pH = 8-9), and 1 : 1.5 molar ratios of Ce : W were used. Changing the pH to 7, and the molar ratio of Ce : W to 1 : 1, gave a different material - $Ce_{10}W_{22}O_{81}$. The luminescence of these materials was tested after doping Tb^{3+} ions into the matrixes. They were shown to be efficient green and blue light emitting phosphors.

7.1. Introduction

Although quite a large amount of rare-earth tungstate materials has been reported (for example Y_2WO_6, $Gd_2(WO_4)_3$, $Y_2(WO_4)_3$, $NaY(WO_4)_2$)[1], reports on 3D structured cerium tungstate materials cannot be found in literature. Up until now only nanosized $Ce_2(WO_4)_3$ particles, obtained in a reversed microemulsion synthesis, have been reported by Pramanik et al.[2] A $Ce_{10}W_{22}O_{81}$ nano- or microsized material has not been reported so far.

This research was undertaken with two motivations. First, it was intended to synthesize 3D structured $Ce_2(WO_4)_3$ and $Ce_{10}W_{22}O_{81}$ materials, built from nano- or micro- sized building blocks. By varying reaction conditions, such as the source of Ce^{3+} ions and the presence of a structure directing agent (DSS surfactant), four $Ce_2(WO_4)_3$ materials with different 3D architectures were obtained. By changing the pH value from 8-9 to pH 7 a $Ce_{10}W_{22}O_{81}$ material was obtained instead (only when $Ce(NO_3)_3{\cdot}5H_2O$ was used as the source of cerium ions). The second motivation was to incorporate Tb^{3+} ions into the cerium tungstate matrixes and investigate the luminescence properties of the material. Tb^{3+} ions were chosen because it is known that it is feasible to excite Tb^{3+} ions by energy-transfer from Ce^{3+} ions (indirect excitation).

7.2. Synthesis

7.2.1. Synthesis of Tb^{3+}:$Ce_2(WO_4)_3$

Samples were synthesized hydrothermally in the presence and absence of DSS surfactant. When DSS was used first 1 mmol of DSS was dissolved in 20 mL distilled water. 1 mmol of $RE(NO_3)_3{\cdot}5H_2O$ or $RE(OAc)_3{\cdot}2H_2O$ (RE = Ce^{3+}, Tb^{3+}) salts at the right percentage amounts were weighed off and dissolved together in 10 mL of water.

The dissolved salts were slowly added to the DSS solution while stirring on a magnetic stirrer. After 10 minutes 1.5 mmol Na_2WO_4 dissolved in 10 mL water was slowly added. The pH of the solution was left without adjusting. After 10 minutes the suspension was transferred into an autoclave and heated at 200 °C for 24h (at an oven heating rate of 1 °C per minute). After the end of the heating time the autoclave was cooled naturally to room temperature, the precipitate centrifuged, and the product washed two times with water and two times with ethanol. The product was dried in a vacuum oven at 60 °C. To obtain the final product the precursor material (as prepared product) was heat treated in air at 900 °C for 3h.

7.2.2. Synthesis of Tb^{3+}:$Ce_{10}W_{22}O_{81}$

Samples were synthesized hydrothermally in the presence and absence of DSS surfactant. When DSS was used first 1 mmol of DSS was dissolved in 20 mL distilled water. 1 mmol of $RE(NO_3)_3 \cdot 5H_2O$ or $RE(OAc)_3 \cdot 2H_2O$ (RE = Ce^{3+}, Tb^{3+}) salts at the right percentage amounts were weighed off and dissolved together in 10 mL of water. The dissolved salts were slowly added to the DSS solution while stirring on a magnetic stirrer. After 10 minutes 1.5 mmol Na_2WO_4 dissolved in 10 mL water was slowly added. The pH of the solution was adjusted to pH 7 by adding a few drops of diluted HNO_3. After 10 minutes the suspension was transferred into an autoclave and heated at 200 °C for 24h (at an oven heating rate of 1 °C per minute). After the end of the heating time the autoclave was cooled naturally to room temperature, the precipitate centrifuged, and the product washed two times with water and two times with ethanol. The product was dried in a vacuum oven at 60 °C. To obtain the final product the precursor material (as prepared product) was heat treated in air at 900 °C for 3h.

7.3. Results and discussion

7.3.1. Characterization of $Ce_2(WO_4)_3$ and $Ce_{10}W_{22}O_{81}$ materials

Table 7.1. summarizes the effect of the reaction conditions and the cerium source on the morphology and phase of the synthesized materials characterized below. Symbols **D1**-**D8** have been assigned to the samples and will be used throughout this chapter.

Table 7.1. Summary of the reaction parameters and corresponding results

Sample	Ln source[a]	DSS [mmol]	Reaction pH	Morphology of product
D1	$Ce(NO_3)_3$	0	8-9	Irregular flower-like microspheres around 2–3 μm in diameter assembled from nanorods (nanoparticles additionally present)
D2	$Ce(NO_3)_3$	1	8-9	Flower-like microspheres around 10 μm in diameter assembled from microrods (ribbon-like microstructures additionally present)
D3	$Ce(OAc)_3$	0	8-9	Passion flower-like microstructures 30–50 μm in size
D4	$Ce(Oac)_3$	1	8-9	Microsized spheres assembled from irregular nanorods with rough edges
D5	$Ce(NO_3)_3$	0	7	Irregular microsized assemblies of nanosheets
D6	$Ce(NO_3)_3$	1	7	Flower-like structures up to 10 μm in size built from nanosheets
D7	$Ce(OAc)_3$	0	7	-
D8	$Ce(OAc)_3$	1	7	-

[a] The salts were hydrated: $Ce(NO_3)_3 \cdot 5H_2O$ or $Ce(OAc)_3 \cdot 2H_2O$

As a first step in the analysis of the obtained materials XRD patterns of the **D1**-**D8** precursor samples (as prepared, before heat treating them at 900 °C) were recorded. Similarly to previous observations the XRD patterns of the precursor samples could not be matched with any standard patterns found in the JCPDS database.[3-4] Figure 7.1. presents the XRD patterns of samples **D1**-**D4** after heat treating them at 900 °C for 3h in air. These XRD patterns can be well matched to the standard monoclinic $Ce_2(WO_4)_3$ phase found in the ICSD database.[5] Figure 7.2. shows the XRD patterns of samples **D5**-**D6** after heat treatment (same conditions as samples **D1**-**D4**). These samples can be well matched with the standard orthorhombic $Ce_{10}W_{22}O_{81}$ phase found in the ICSD database.[6] In all cases it was observed that the presence of the DSS surfactant did not influence the formed phase. Samples **D7** and **D8** did not give a pure phase of any known material, and were not further analyzed. It can be concluded that changing the reaction pH from 8-9 to neutral pH changed the phase from $Ce_2(WO_4)_3$ to $Ce_{10}W_{22}O_{81}$. Yet, this was only true for the reactions where $Ce(NO_3)_3 \cdot 5H_2O$ was used as the source of Ce^{3+} ions. When $Ce(OAc)_3 \cdot 2H_2O$ was employed in the reaction and the pH was adjusted to 7, the XRD patterns could not be matched to any known pure phase. For this reason samples **D7**-**D8** were not further studied.

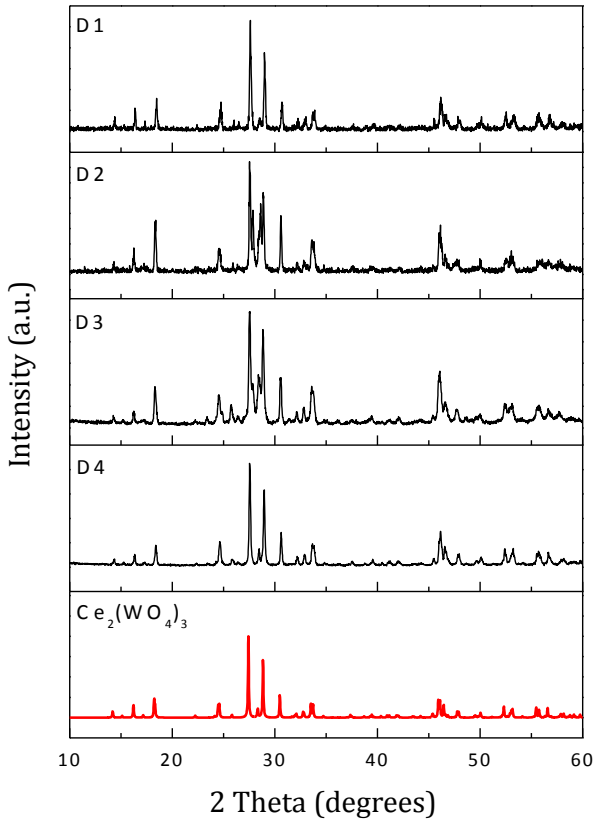

Figure 7.1: XRD patterns of samples D1-D4 after heat treatment. All of the samples could be matched to the pure monoclinic $Ce_2(WO_4)_3$ phase.

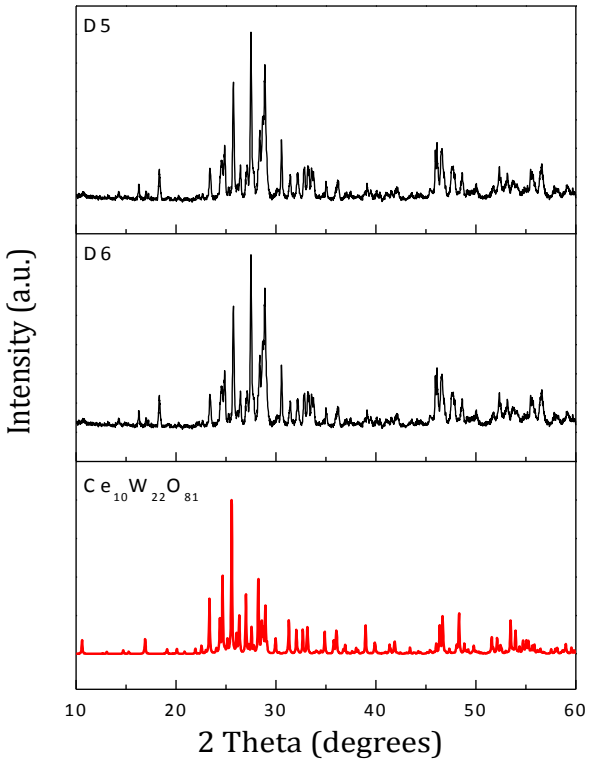

Figure 7.2: XRD patterns of samples D5-D6 after heat treatment. The samples could be matched to the pure orthorhombic $Ce_{10}W_{22}O_{81}$ phase.

The samples were further characterized through DRIFTS. Figure 7.3. shows the DRIFTS spectrum of sample **D1**. Because no vibrations attributed to the O-H stretch vibrations are present in the spectrum one can assume that after heat treatment all of the water molecules present on the surface of the material have been removed. Also no organic bands, which could be attributed to the presence of the DSS surfactant, can be detected in samples **D2** and **D4**. Therefore it can be concluded that the surfactant is also completely burned off during the heat treatment process. In all the samples below 1000 cm^{-1} the characteristic tungstate vibrations are visible. For example for sample **D1** the bands at 955 cm^{-1} and 884 cm^{-1} are attributed to the W-O stretch

vibrations, and the band at 746 cm^{-1} is attributed to the asymmetric stretch vibrations of W-O-W bridges.[7] Similar peaks (sometimes with slightly shifted wavenumbers) are observed for samples **D2**-**D4**. Figure 7.4. presents the DRIFTS spectrum of sample **D6**. In both sample **D5** and **D6** at around 1622-1633 cm^{-1} there is a small peak, which can be assigned to the O-H stretch vibrations. This means that some small amounts of water may be present on the surface of these materials. No organic bands which could be assigned to the DSS surfactant are present in sample **D6**. The samples also show the characteristic W-O and W-O-W bands below 1000 cm^{-1}.

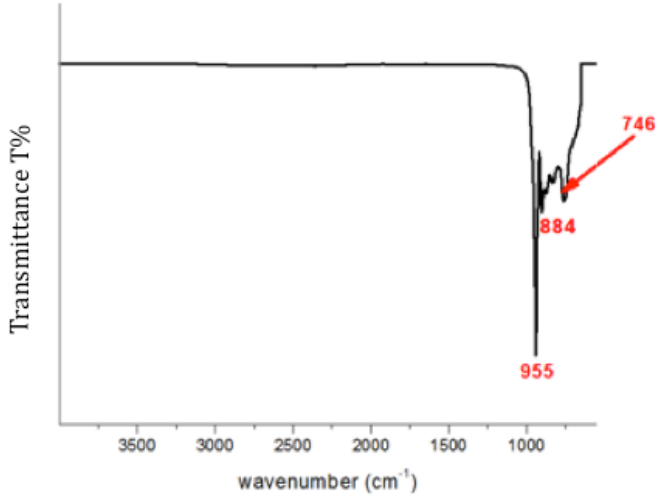

Figure 7.3: DRIFTS spectrum of sample D1.

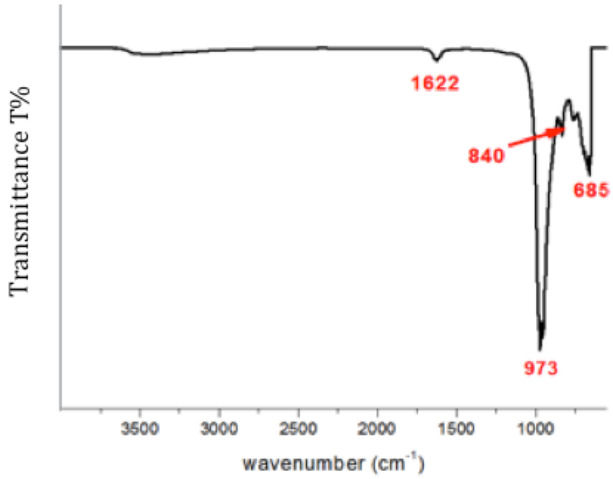

Figure 7.4: DRIFTS spectrum of sample D6.

The morphology of samples **D1**-**D6** were characterized by SEM. Figure 7.5. presents the morphology of the cerium tungstate samples obtained from $Ce(NO_3)_3 \cdot 5H_2O$, where 1 mmol of the Ce^{3+} salt and 1.5 mmol of Na_2WO_4 was used, at pH = 8-9, both in the presence and absence of DSS (samples **D1** and **D2**). When no DSS was used in the reaction (sample **D1,** Figure 7.5.a,b) irregular flower-like microspheres around 2–3 μm in diameter were formed. These microstructures were built from nanosized rods assembled together to form flower-like morphologies. Sometimes nanosized spherical particles were additionally present on the surface of the microstructures. When DSS was used in the reaction flower-like microspheres around 10 μm in diameter, assembled from microrods were obtained (sample **D2**, Figure 7.5.c,d). In this case besides the flower-like microstructures also ribbon-like microstructures could be found. Based on these observations it can be said that when $Ce(NO_3)_3 \cdot 5H_2O$ was used in the synthesis, although a pure phased material was obtained, the material did not show completely uniform morphology. Fig. 7.6. presents the morphology of the

cerium tungstate samples obtained from $Ce(OAc)_3 \cdot 2H_2O$, where 1 mmol of the Ce salt and 1.5 mmol of Na_2WO_4 was used, at pH = 8-9, both in the presence and absence of DSS. When no DSS is present in the reaction microstructures, which can be best compared to passion flowers, were formed (sample **D3**, Figure 7.6.a,b). These structures were quite large – usually between 20-50 μm. Employing DSS in the reaction led to microspheres, usually around 5 μm in size. They were built from irregular nanorods with rough edges (sample **D4**, Fig. 7.6.c,d). The nanorods were packed very tightly together to form the microstructures.

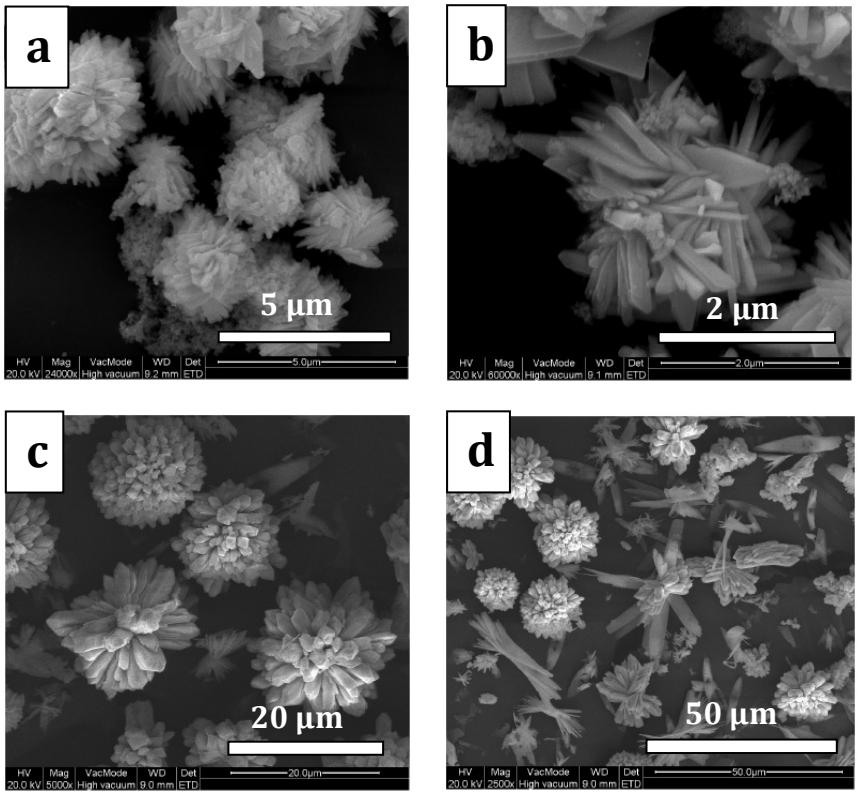

Figure 7.5: SEM images at different magnifications of samples D1 (a), (b) and D2 (c), (d).

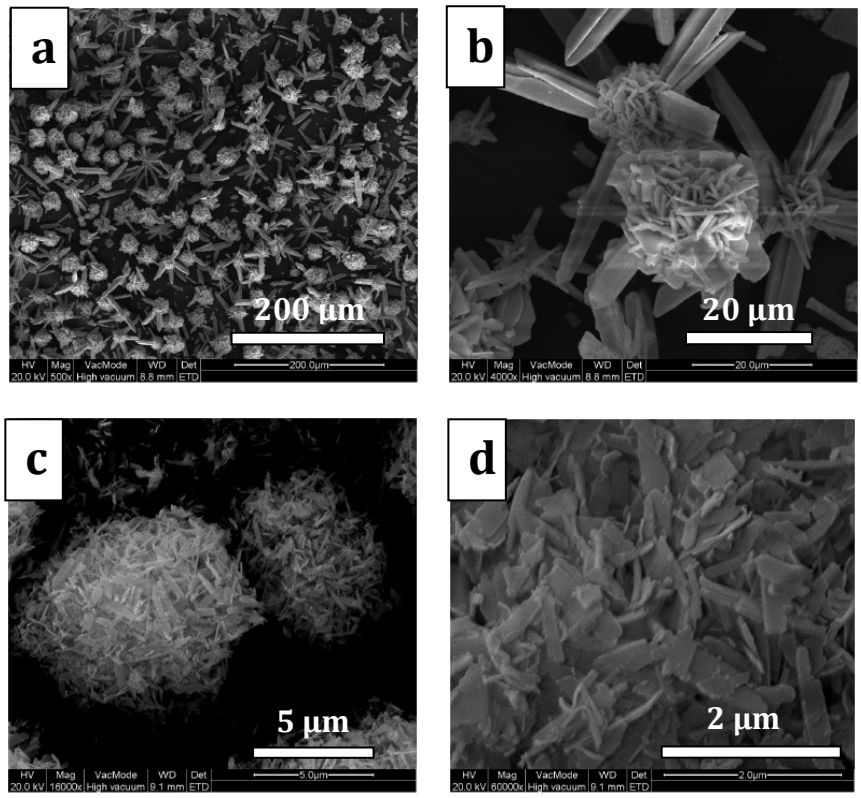

Figure 7.6: Fig. 8 SEM images at different magnifications of samples D3 (a), (b) and D4 (c), (d).

When the molar ratio of the Ce^{3+} salt to Na_2WO_4 was changed from 1.5 : 1 to 1 : 1, and additionally the pH of the reaction was changed to 7, samples **D5** and **D6** were formed. Their morphology is presented in Figure 7.7. When no DSS was used in the reaction irregular microstructures composed of nanosheets were obtained (sample **D5**, Figure 7.7.a,b). Depending on the packing of the nanosheet building blocks some of them formed bowknot-like structures. When DSS was employed flower-like structures up to 10 µm in size were obtained (sample **D6**, Figure 7.7.c,d). These microstructures are built of nanosheets layered on top of each other. As mentioned earlier in this chapter, when $Ce(OAc)_3 \cdot 2H_2O$ was employed in the reaction and the pH

adjusted to 7 (molar ratio of $Ce(OAc)_3 \cdot 2H_2O$ to Na_2WO_4 was 1 : 1) the XRD patterns could not be matched to any known pure phase. Because of this the morphology of these materials was not studied.

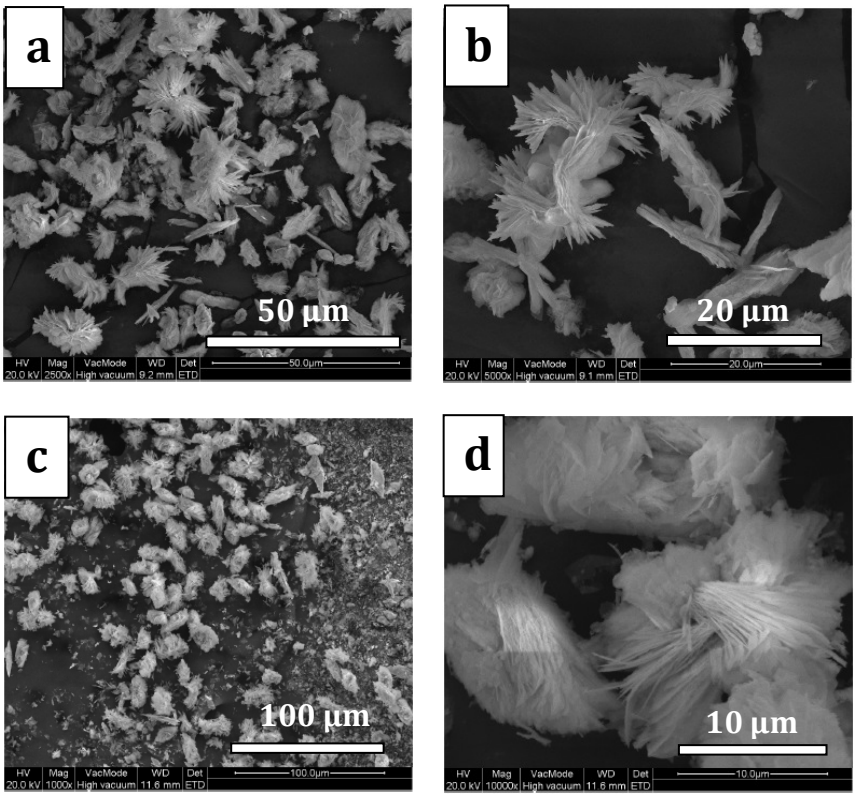

Figure 7.7: SEM images at different magnifications of samples D5 (a), (b) and D6 (c), (d).

7.3.2. Luminescence properties of 5% Tb^{3+} doped $Ce_2(WO_4)_3$ and $Ce_{10}W_{22}O_{81}$ (**D1** – **D6**)

In the previous two chapters it has been shown that rare-earth tungstates are good host lattices for the luminescence of lanthanide ions. When the materials were excited into the tungstate charge transfer band energy could be effectively transferred to the doped lanthanide ions. If the transfer of energy from the tungstate groups to the lanthanide ions was not complete the tungstate groups emitted blue-green light themselves. This blue-green light in combination with the light emitted by the lanthanide ion could lead to white light emitting samples. Lanthanum and yttrium tungstate compounds are suitable hosts, because their 4f shells are empty, and unless other light emitting components are present, no f-f transitions are possible.[8] This is not the case with cerium compounds, which emit a broad band in the blue-green region. In this subchapter the luminescence properties of the $Ce_2(WO_4)_3$ and $Ce_{10}W_{22}O_{81}$ micromaterials doped with trivalent terbium ions are presented. Terbium ions were chosen among the lanthanides, as it is known that an efficient energy transfer can occur between the Ce^{3+} and Tb^{3+} ions. Several articles can be found where a Tb^{3+} doped material is additionally co-doped with Ce^{3+} ions to enhance the luminescence.[9-12]

Figure 7.8. presents the room-temperature combined excitation and emission spectrum of **5% Tb doped D1** sample, after annealing at 900 °C. In the excitation spectrum a strong and broad band with a maximum at around 260.0 nm is visible. This band can be assigned to the charge-transfer from the 2p orbitals of the oxygens to the 5d orbitals of the tungsten. No characteristic bands of the Tb^{3+} or broad band of Ce^{3+} can be detected in the excitation spectrum. In the emission spectrum the four

characteristic emission peaks of Tb^{3+} are present.[13] Peak a can be assigned to the $^5D_4 \rightarrow {}^7F_6$ transition, peak b to the $^5D_4 \rightarrow {}^7F_5$ transition, peak c to the $^5D_4 \rightarrow {}^7F_4$ transition, and peak d to the $^5D_4 \rightarrow {}^7F_3$ transition. The wavelength and wavenumber values of the peaks are presented in Table 7.2. No broad emission peaks, which could be appointed either to the Ce^{3+} ions of the tungstate band, are visible in the spectrum.

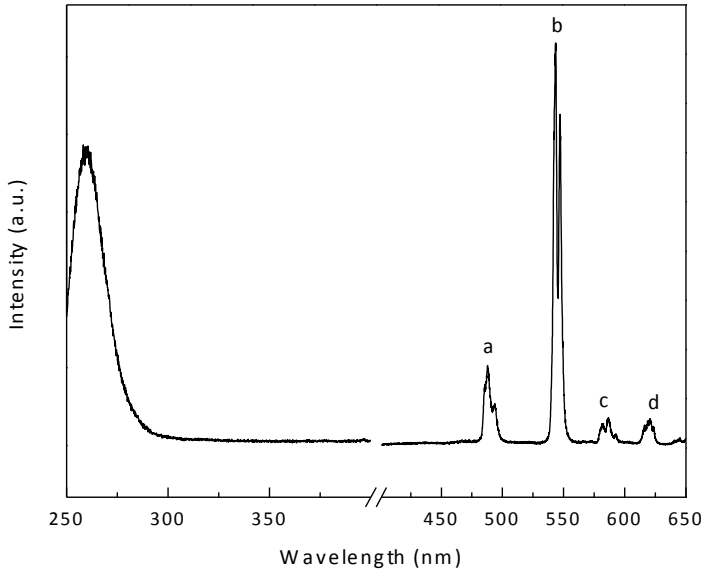

Figure 7.8: Excitation spectrum (monitored at 543.6 nm) and emission spectrum (excited at 260.0 nm) of 5% Tb doped D1. The electronic transitions labelled a-d have been assigned in Table 7.2.

Figure 7.9. presents the emission spectrum of **5% Tb doped D1** with a rainbow curve fitted underneath to show the different color components, as well as the CIE color diagram with the x and y coordinates of the sample shown on the diagram.

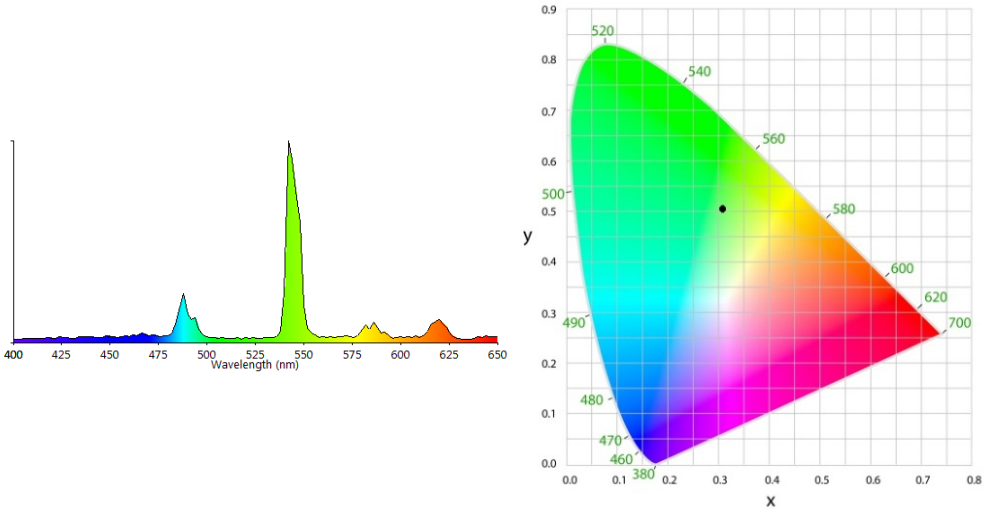

Figure 7.9: Left: emission spectrum of 5% Tb doped D1 (excited at 260.0 nm) with rainbow plotted under curve to show the different color components. Right: CIE color diagram; the black dot shows the x and y color coordinates of the sample (x = 0.31, y = 0.51).

Figure 7.10. compares the emission spectra of **5% Tb doped D1-D4** when excited at 260.0 nm. In the emission spectra only the characteristic peaks of Tb^{3+} can be observed The different intensities of the peaks in the excitation and emission spectra, as well as slight peak shifts and some small changes in the peak splitting indicate different environment around the ions (which can be explained by the different morphologies of the four $Ce_2(WO_4)_3$ materials). **5% Tb doped D3** has the weakest emission intensity. As can be seen from the SEM images this material has particles the biggest in size. In all cases a strong broad band, with a maximum around 260.0 nm was visible in the excitation spectra (similar to that for **5% Tb doped D1** sample). No other peaks were present in these excitation spectra. Figure 7.11. presents the room-temperature combined excitation-emission spectrum of **5% Tb doped D6**. In the

excitation spectrum two broad bands are present, one with a maximum at around 260.0 nm, and the other at around 366.0 nm. The first one can be assigned to the W-O charge transfer band, while the other has been assigned to be Ce^{3+} band. When excited into the W-O band the material shows all of the characteristic peaks of Tb^{3+}, which unlike in the spectra of the Tb: $Ce_2(WO_4)_3$ are embedded on a broad band ranging from around 400–550 nm. This broad band can be assigned to the 5d-transitions of Ce^{3+} between the $^2F_{5/2}$ ($4f_1$) ground state and the ^2D ($5d_1$) state,[14] as well as the W-O band.

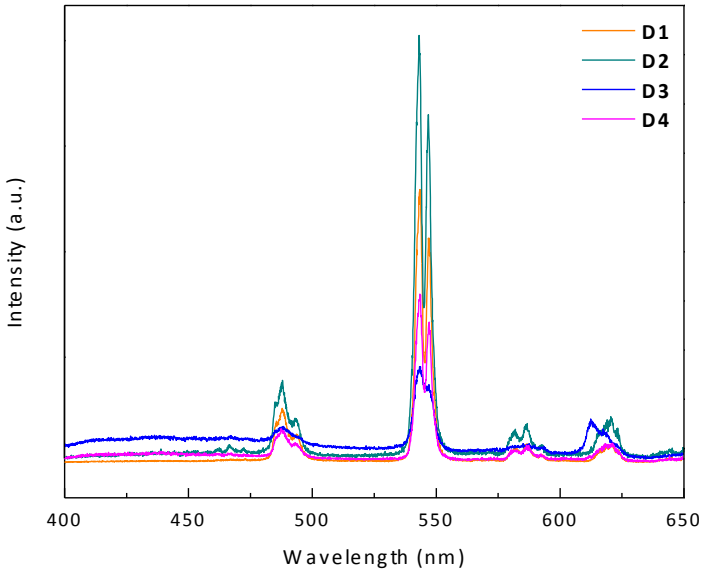

Figure 7.10: Emission spectra of 5% Tb doped D1, D2, D3, and D4 when excited at 260.0 nm.

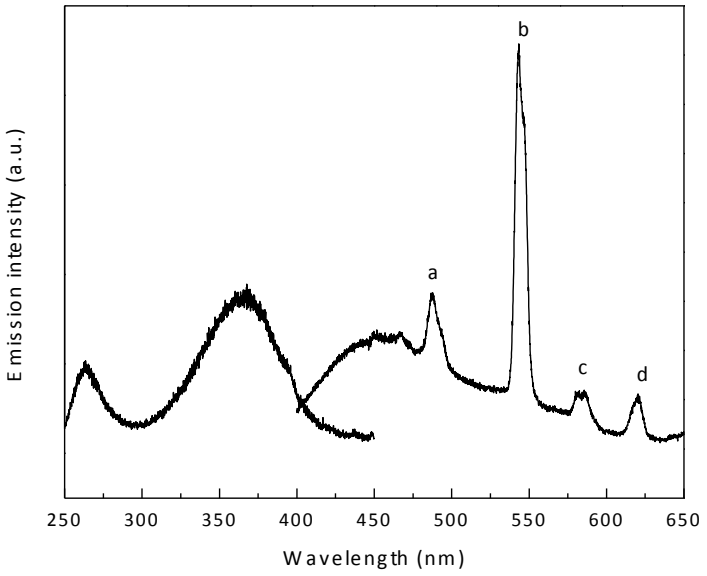

Figure 7.11: Excitation spectrum (monitored at 543.4 nm) and emission spectrum (excited at 270.0 nm) of 5% Tb doped D6. The electronic transitions labeled a-d are assigned in Table 7.2.

Figure 7.12. presents the emission spectrum of **5% Tb doped D6** with a rainbow curve underneath to show the different color components, as well as the CIE color diagram with the x and y coordinates of the sample shown on the diagram. When the material is excited at 366.0 nm (into the Ce^{3+} band) only a strong, broad band is observed in the emission spectrum (Figure 7.13.). The band has a maximum at around 460.0 nm. No peaks of terbium are present in the emission spectrum. The **5% Tb doped D5** sample showed a similar excitation and emission spectrum. Table 7.3. gathers the CIE color coordinates for **5%Tb doped D1-D6** samples.

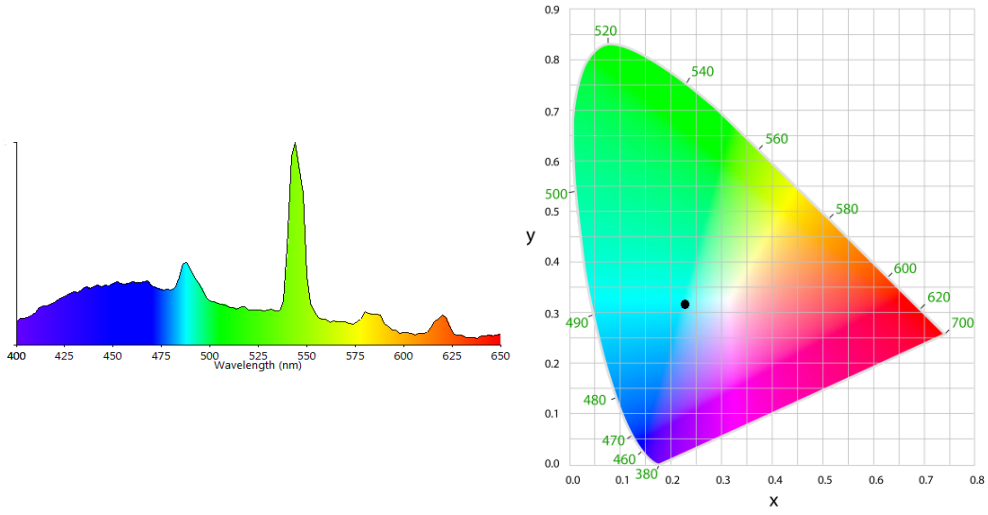

Figure 7.12: Left: emission spectrum of 5% Tb doped D6 (excited at 270.0 nm) with rainbow plotted under curve to show the different color components. Right: CIE color diagram; the black dot shows the x and y color coordinates of the sample (x = 0.23, y = 0.32).

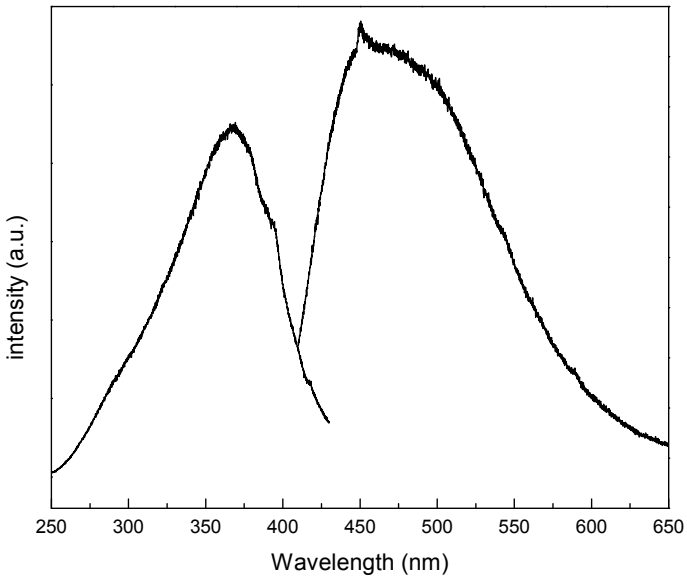

Figure 7.13: Excitation spectrum (monitored at 430.0 nm) and emission spectrum (excited at 366.0 nm) of 5% Tb doped D6.

Table 7.2. Assigment of labeled transitions shown in Figure 7.8. and Figure 7.11.

	Emission		
Wavelength (nm)	Energy (cm^{-1})	Transition	
5% Tb doped D1			
a 488.3	20479	$^5D_4 \rightarrow$	$^7F_6$
b 543.6	18396		$^7F_5$
c 586.9	17039		$^7F_4$
d 620.4	16119		$^7F_3$
5% Tb doped D6			
a 486.7	20547	$^5D_4 \rightarrow$	$^7F_6$
b 543.4	18403		$^7F_5$
c 585.9	17068		$^7F_4$
d 620.3	16121		$^7F_3$

Table 7.3. CIE chromaticity coordinates for 5% Tb^{3+} doped D1-D6 materials.

Sample	CIE (x)	CIE (y)	Color
5% Tb doped D1	0.31	0.51	green
5% Tb doped D2	0.32	0.51	green
5% Tb doped D3	0.30	0.52	green
5% Tb doped D4	0.31	0.50	green
5% Tb doped D5	0.25	0.37	blue-green
5% Tb doped D6	0.23	0.32	blue

7.4. Conclusions

In this chapter two cerium tungstate materials ($Ce_2(WO_4)_3$ and $Ce_{10}W_{22}O_{81}$) with microsized 3D architectures were successfully synthesized. A simple hydrothermal synthesis was employed to obtain the precursor materials. After heat treatment at 900 °C for 3 h, the precursors were transformed into the desired materials. The influence of the lanthanide source and DSS surfactant on the size and morphology of these materials was studied in this work. The results showed that the presence of DSS significantly changed the shape of the building blocks, and consequently the final architecture of the microstructure. It could be established that the source of the cerium ions (nitrate or acetate salt) plays an important role in the size and shape formation of the microstructures. In the second part of this work the luminescence properties of 5% Tb doped $Ce_2(WO_4)_3$ and $Ce_{10}W_{22}O_{81}$ materials were investigated. Depending on the morphology the materials showed some changes in the luminescence spectra. The CIE color coordinates of the materials were calculated. It was observed that the $Ce_2(WO_4)_3$ microstructures emitted green light, whereas the $Ce_{10}W_{22}O_{81}$ microstructures emitted either blue or blue-green light.

7.5. References

1. Kaczmarek, A.M.; Van Deun, R. *Chem. Soc. Rev.,* **2013**, 42, 8835.

2. Pramanik, S.; Bhattacharya, S.C.; *Mater. Chem. Phys*., **2010**, 121, 125.

3. Kaczmarek, A.M.; Van Hecke, K.; Van Deun, R. *Inorg. Chem.,* **2014**, 53, 9498.

4. Kaczmarek, A.M.; Liu, Y.-Y.; Van Der Voort, P.; Van Deun, R. *Dalton Trans.*, **2013**, 42, 5471.

5. T. Gressling, Hk. Müller-Buschbaum *Z. Naturforschung*, **1995**, 50b, 1513.

6. Barker, R.S.; Evans, I.R. *Acta Cryst*., **2008**, B64, 708.

7. Lei, F.; Yan, B. *J. Mater. Res.*, **2011**, 26, 88.

8. Van Deun, R. *Advanced Inorganic Chemistry*, **2012**.

9. Ghosh, P.; Kar, A.; Patra, A. *Nanoscale*, **2010**, 2, 1196.

10. Seed Ahmed, H.A.A.; Ntwaeaborwa, O.M.; Kroon, R.E. *Curr. Appl. Phys*., **2013**, 13, 1264.

11. Pankratov, V.; Popov, I.; Chernov, S.A.; Zharkouskaya, A.; Feldmann, C. *Phys. Status Solidi B*, **2010**, 247, 2252

12. Rabouw, F.T.; den Hartog, S.A.; Senden, T.; Meijerink, A. *Nature Comm.*, **2014**, doi:10.1038/ncomms4610

13. Carnall, W.T.; Fields, P.R.; Rajniak, K. *J. Chem. Phys.*, **1968**, 49, 4447.

14. Uysal Satilmis, S.; Ege, A.; Ayvacikli, M.; Khatab, A.; Ekdal, E.; Popovici, E.J.; Henini, M.; Can, N. *Opt. Mater.* **2012**, 34, 1921.

Chapter 8: General conclusions

Two types of materials – rare-earth carbonates and rare-earth tungstates were described in this thesis. This choice was based on the relatively small amount of published results compared to other inorganic matrices at the beginning of this PhD work.

Chapter 4 described the synthesis and characterization of several rare-earth carbonate materials: $LaOHCO_3$, $La_2O(CO_3)_2{\cdot}H_2O$ and $Ce_2O(CO_3)_2{\cdot}H_2O$. Some of the $La_2O(CO_3)_2{\cdot}H_2O$ and $Ce_2O(CO_3)_2{\cdot}H_2O$ materials were synthesized both in the presence and absence of stabilizing ligands (glucose and fructose) to compare their influence of the materials morphology. Two different synthetic techniques were employed to obtain these materials: a low temperature urea homogenous precipitation method and a hydrothermal method. Other factors, such as the source of the lanthanide ions (nitrate or acetate salt), and the source of carbonate ions were also changed in order to obtain materials with a variety of morphologies. For example when the $LaOHCO_3$ material was synthesized hydrothermally from $La(OAc)_3$ and urea small nanoparticles 30-50 nm in size were obtained. When urea was substituted for Na_2CO_3, and all other reaction conditions remained unchanged, larger spheres 100-200 nm in size were formed. When glucose and fructose were used as stabilizing ligands for the synthesis of $La_2O(CO_3)_2{\cdot}H_2O$ it was observed that materials with very different morphologies were obtained. In a low temperature urea homogenous precipitation synthesis, where $La(OAc)_3$ was used as the source of lanthanum and glucose was present in the reaction, elongated spheroids 50-200 nm in size were observed under the SEM. When fructose was used instead of glucose 4 μm microspheres built from nanoplates were

formed. Therefore it can be concluded that all of these factors had a significant impact in tuning the morphology of rare-earth carbonate particles.

An important part of this work was investigating in detail the luminescence properties of Eu^{3+} and Tb^{3+} doped rare-earth carbonate materials in solid state and as colloidal suspensions. It was observed that the luminescence properties of the Eu^{3+}/Tb^{3+} doped $LaOHCO_3$ particles were quite different from those of the Eu^{3+}/Tb^{3+} doped $La_2O(CO_3)_2 \cdot H_2O$ particles. Especially differences in peak splitting in the emission spectra, as well as the quantum yield (QY) values, were observed. Most likely the change in QY is caused by the change of radiative lifetime in the two matrices, as the luminescence lifetimes have comparable values. As could be expected particles synthesized in the presence of a ligand showed lower luminescence lifetimes and QYs compared to particles of the same carbonate material synthesized in the absence of the organic ligand. This decrease in luminescence lifetime and QY can most likely be explained by the quenching of OH groups from the ligand. When comparing the emission spectra measured in the solid state and colloidal suspension only a drop of intensity (about 25%) was visible, whereas the shape and relative peak intensities were very similar. No significant changes in the length of the luminescence lifetimes were observed. Therefore it can be concluded that the particles do not encounter any modifications after dispersion in water. All of the Eu^{3+} and Tb^{3+} doped rare-earth carbonate samples showed strong red and green emission, respectively after exciting them with a laboratory UV lamp at an excitation wavelength of 365.0 nm. As several of these particles form stable colloidal suspensions in water and are non-toxic to the human body, they could be promising candidates for use in biolabeling.

Chapters 5, 6, and 7 present the synthesis, characterization, and luminescence properties of several Ln^{3+} doped rare-earth tungstate materials ($Y(WO_3)_2(OH)_3$, Y_2WO_6, $Ce_2(WO_4)_3$ and $Ce_{10}W_{22}O_{81}$).

$Y(WO_3)_2(OH)_3$ 3D structured micromaterials were obtained in hydrothermal syntheses (200 °C) in the presence and absence of dioctyl sodium sulfosucciate surfactant (DSS). This study showed that the morphology of the $Y(WO_3)_2(OH)_3$ material can be tuned by the following factors: reaction time, amount of surfactant, and source of Y^{3+}. Significant changes in the luminescence properties of the materials were additionally observed for samples which were heat treated at 900 °C for 3 h and when changing the doping percentage of the Ln^{3+} ion. Additionally it was observed that a decrease of Eu^{3+} ion concentration from 5% to 1% the intensity of the broad charge transfer band increases and the emission of Eu^{3+} ions becomes weaker. A change of emitted color was observed.

Among other tungstate materials, which were presented in this thesis are Ln^{3+} doped Y_2WO_6 materials synthesized hydrothermally in the presence of sodium dodecyl sulfate surfactant (SDS). This material was shown to be very sensitive to the reaction pH and only at an appropriate reaction pH a pure phased material could be obtained. At pH=3 spherical microstructures (2-5 μm), built from regular nanosized building blocks, were observed under the SEM.

The detailed luminescence properties of Sm^{3+}, Eu^{3+}, and Dy^{3+} doped Y_2WO_6 spherical 3D microstructures built from nanosized particles were studied. Additionally the enhancement of luminescence through co-doping with Gd^{3+} ions was explored for this material. Several white light emitting materials, with quite high QY values, were obtained. For example for Dy: Y_2WO_6 samples doped with 2.5%, 5% and 10% Dy^{3+},

before and after heat treatment, all showed white light emission. As the longest lifetime and quantum yield was observed for the 2.5% Dy^{3+} doped sample it was further co-doped with Gd^{3+} ions to investigate their influence on the luminescence properties. The 2.5% Dy, 10% Gd doped Y_2WO_6 sample showed the highest QY of 22% and a decay time of 160 μs. The color temperature of this sample was calculated to be 3591 K. The 2.5% Dy^{3+} doped sample, without co-doped Gd^{3+} ions showed a color temperature of 4428 K, therefore co-doping the sample shifted the emitted color toward warm white (halogen white).

In chapter 7 the synthesis and luminescence properties of 5% Tb^{3+} doped $Ce_2(WO_4)_3$ and $Ce_{10}W_{22}O_{81}$ materials was presented. These materials were obtained in a hydrothermal synthesis, in the presence and absence of dioctyl sodium sulfosuccinate surfactant (DSS), by varying the pH and Ce : W molar ratio. All of these materials revealed an efficient charge transfer from the tungstate groups to the Tb^{3+} ions. They showed green, blue or green-blue emission under UV excitation. The different energy transfer mechanisms for these materials were suggested in the thesis.

Therefore, based on the study carried out for several rare-earth tungstate materials it can be concluded that by varying factors such as reaction time, sources of the rare-earth ions, presence and amount of ligand the morphology of these materials could be tuned. Additionally by changing the doping percentage of the lanthanide, heat treatment and co-doping with Gd^{3+} ions, new luminescence properties of the Ln^{3+} doped rare-earth tungstate materials could be obtained. These observations can be employed for controlling the morphologies and luminescence of other lanthanide doped rare-earth phosphors.

Appendix: Additional SEM images

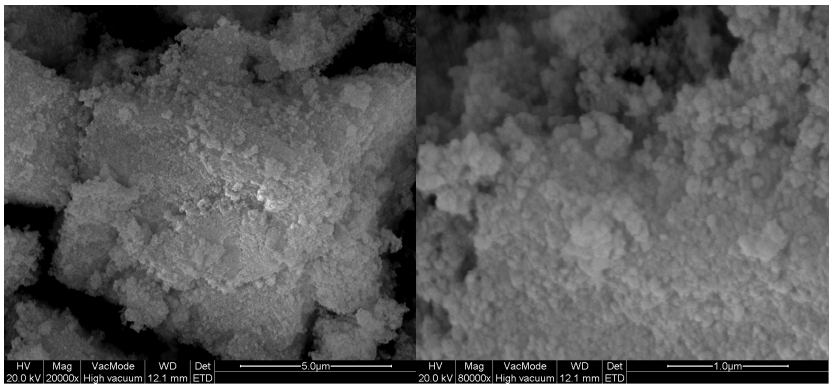

Figure S4.1: SEM images of A5 samples.

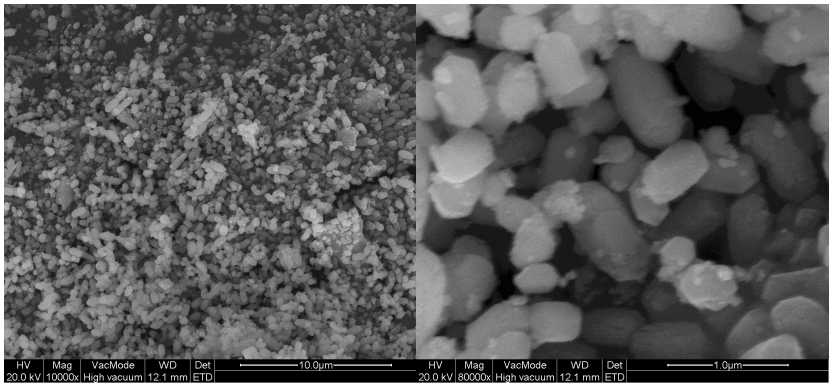

Figure S4.2: SEM images of A7 samples.

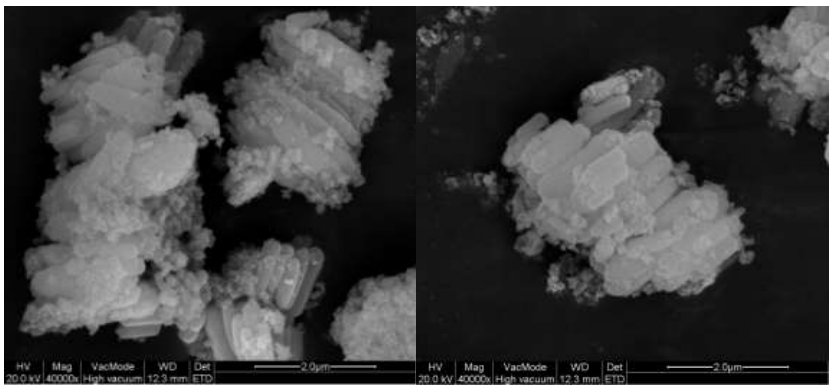

Figure S4.3: SEM images of A8 sample.

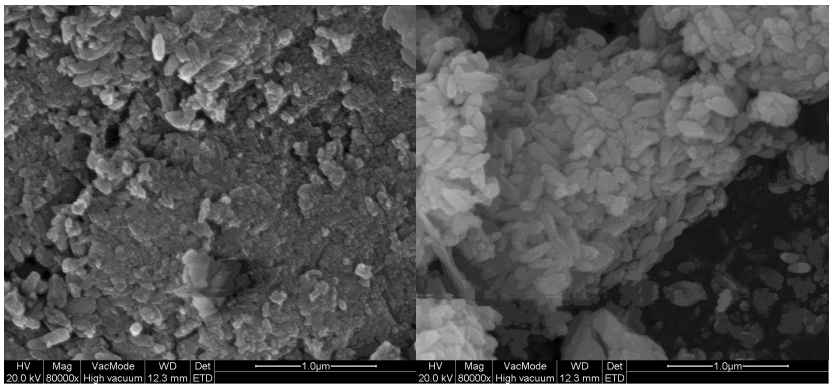

Figure S4.4: SEM images of A10 sample.

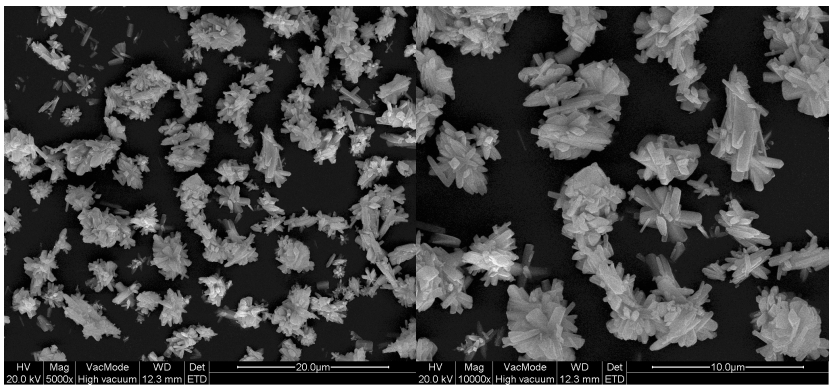

Figure S4.5: SEM images of A11 sample.

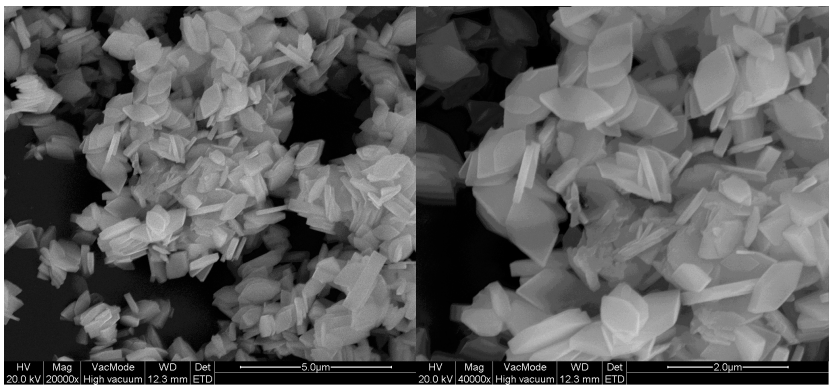

Figure S4.6: SEM images of A13 sample.

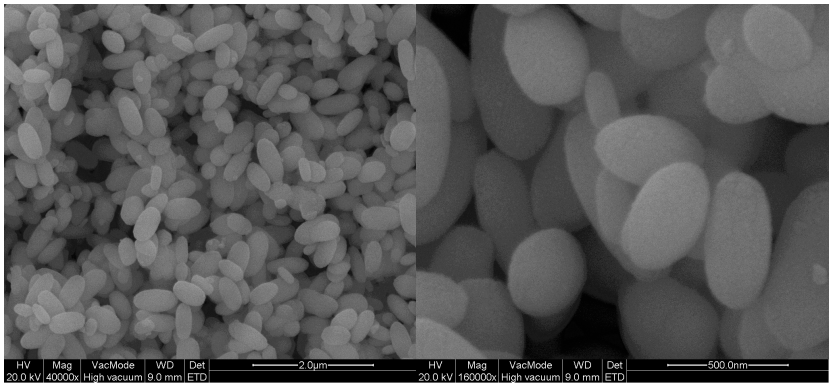

Figure S4.7: SEM images of A14 sample.

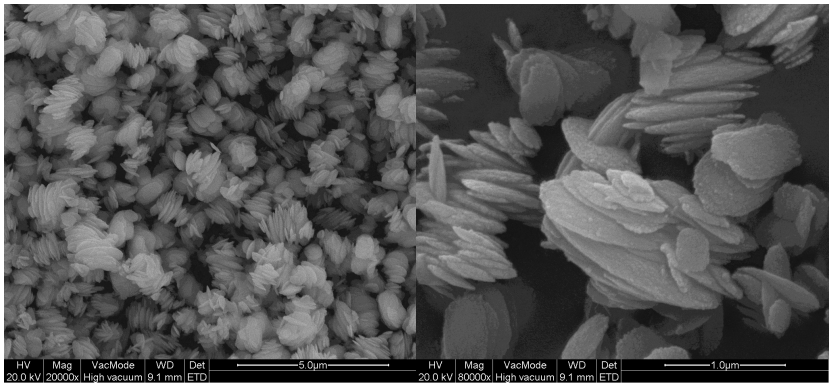

Figure S4.8: SEM images of A15 sample.

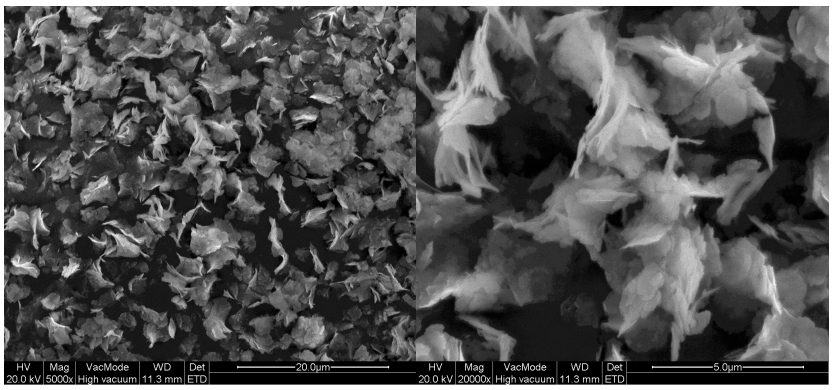

Figure S4.9: SEM images of A16 sample.

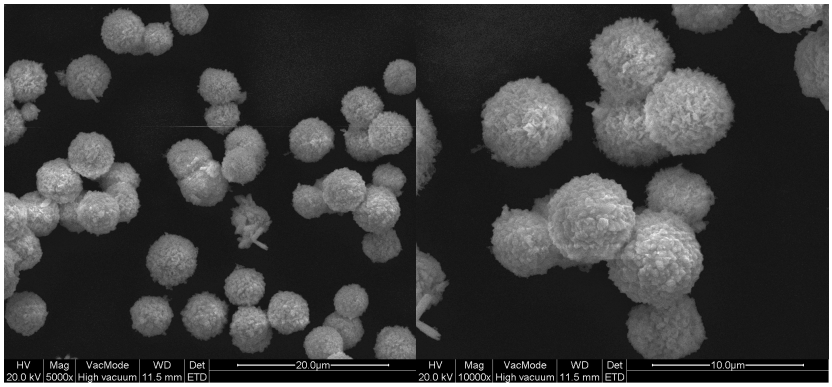

Figure S5.1: SEM images of B1 sample.

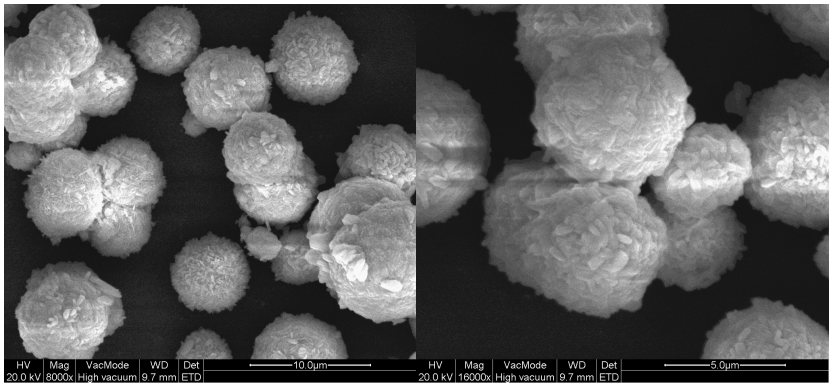

Figure S5.2: SEM images of B2 sample.

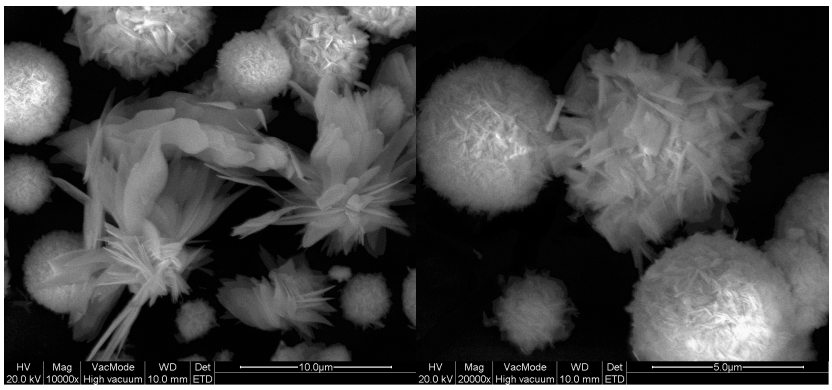

Figure S5.3: SEM images of B3 sample.

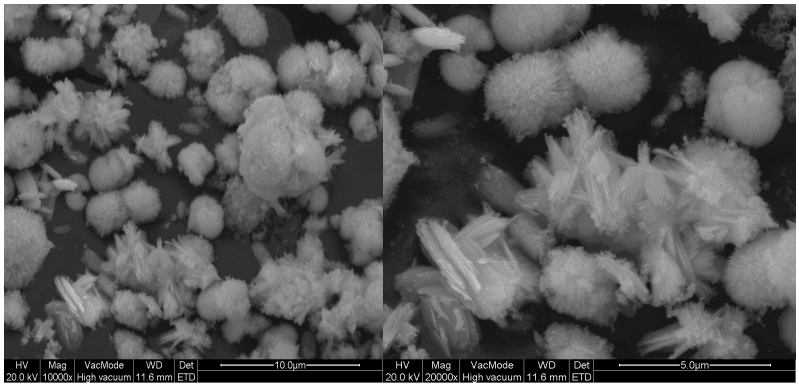

Figure S5.4: SEM images of B4 sample.

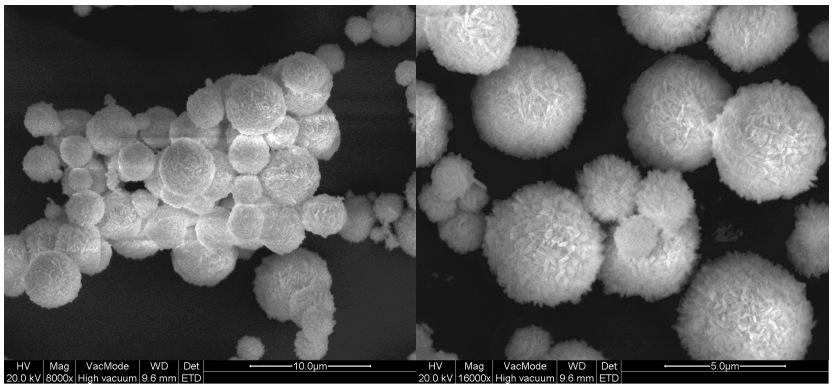

Figure S5.5: SEM images of B5 sample.

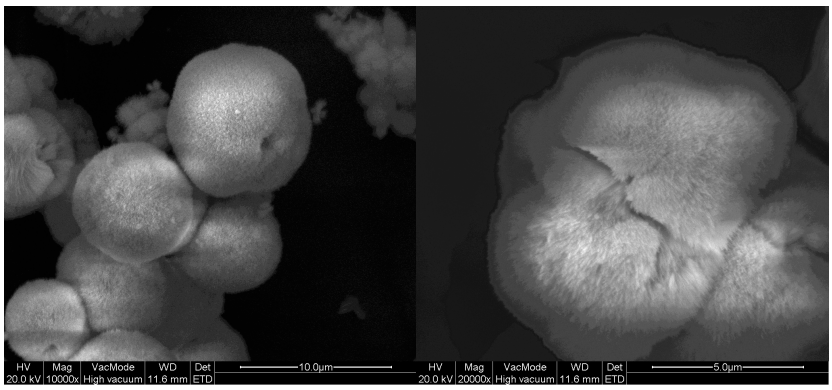

Figure S5.6: SEM images of B7 sample.

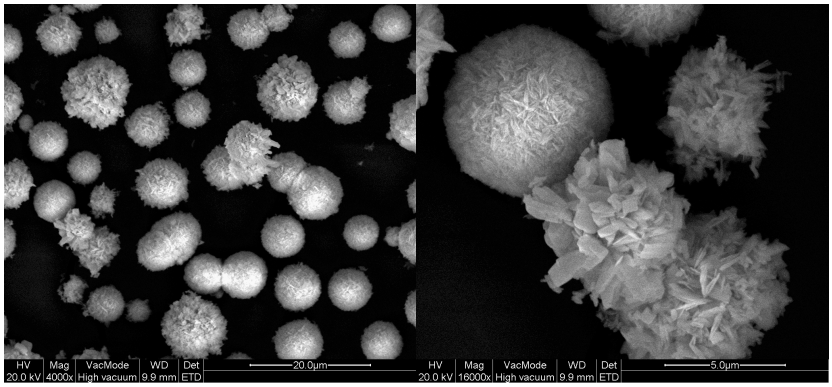

Figure S5.7: SEM images of B8 sample.

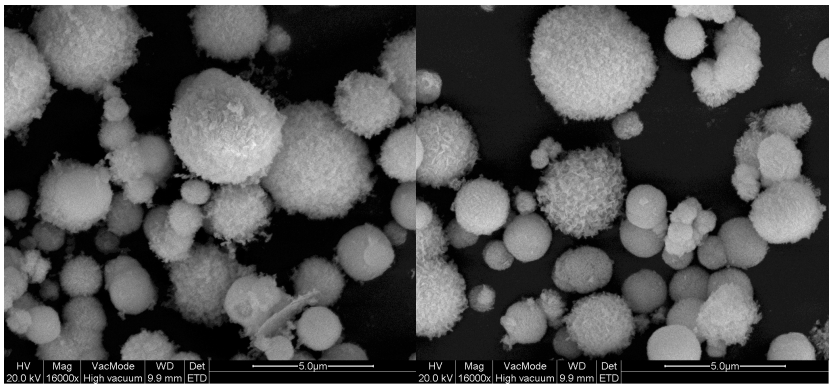

Figure S5.8: SEM images of B10 sample.

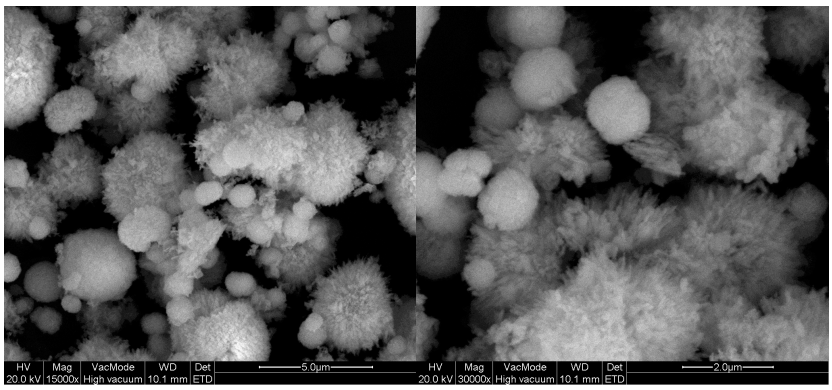

Figure S5.9: SEM images of B11 sample.

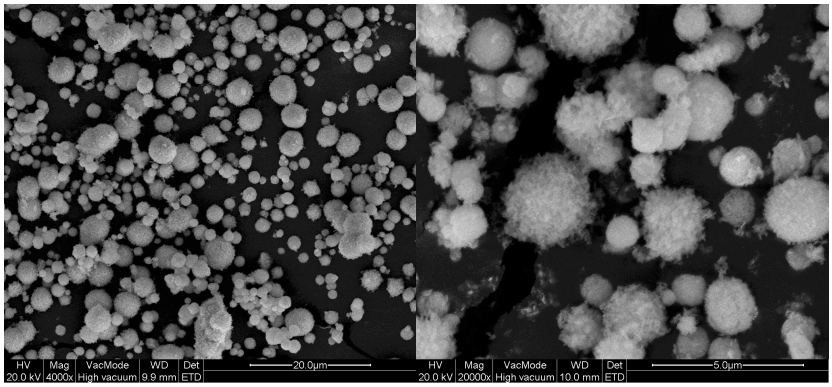

Figure S5.10: SEM images of B12 sample.